University of Alberta

Bonding Patterns in New Intermetallic Antimonides

by

Allison M. Mills ©

A thesis submitted to the Faculty of Graduate Studies and Research in partial fulfillment
of the requirements for the degree of Doctor of Philosophy

Department of Chemistry

Edmonton, Alberta

Spring 2001

Canada

Abstract

Bonding in intermetallic compounds has eluded description by a simple overall scheme. Although electron-counting rules have been developed for two limiting classes, the non-polar Hume-Rothery and the polar Zintl compounds, no clear bonding schemes exist between the two extremes. In this research, several new intermetallic antimonides have been synthesized through reaction of the elements, their crystal structures determined by X-ray diffraction, and their electronic structures calculated using the extended Hückel method. They possess structures featuring extensive homoatomic bonding networks that test the limits of current bonding theories.

$La_{13}Ga_8Sb_{21}$, $RE_{12}Ga_4Sb_{23}$ (RE = La–Nd, Sm), and $REGaSb_2$ (RE = La–Nd, Sm) adopt new structure types containing unusual Ga–Ga and Sb–Sb bonding patterns. Columnar triangular assemblies of face-sharing RE trigonal prisms occur in $La_{13}Ga_8Sb_{21}$ and $RE_{12}Ga_4Sb_{23}$. These trigonal prisms are centred by Ga or Sb atoms, resulting in isolated trigonal planar $GaSb_3$ units. Channels outlined by square Sb ribbons linked by either puckered Ga_6 rings (in $La_{13}Ga_8Sb_{21}$) or Ga_2 pairs (in $RE_{12}Ga_4Sb_{23}$) enclose the RE columns. In $REGaSb_2$, square nets of Sb atoms and two-dimensional $^2_\infty[GaSb]$ layers, within which zigzag Ga chains occur, are separated by RE atoms.

Networks of Ge–Ge and Sb–Sb bonding are found in the structures of $FeGe_{1-x}Sb_x$ ($0 \leq x \leq 0.33$). Honeycomb (6^3) Ge nets and kagomé (3636) nets of Fe atoms are stacked alternately, leaving open channels that are filled by isolated Ge atoms and Sb_2 dumbbells. Large voids in these structures can be filled by transition metal (R) atoms to give the new series of compounds $R_{1-x}(R,Fe)_6Ge_4(Ge,Sb)_2$ (R = Ti, Cr, Mn).

Homoatomic main-group element bonding predominates in the new antimonides. Pairs, rings, and chains containing strong covalent bonds coexist with ribbons and nets containing weaker delocalized bonds. By considering the Sb–Sb bonds within the square networks of $La_{13}Ga_8Sb_{21}$, $RE_{12}Ga_4Sb_{23}$, and $REGaSb_2$ as one-electron bonds, the Zintl concept can be extended to these relatively polar compounds. However, the Zintl concept fails for non-polar $FeGe_{1-x}Sb_x$ and $R_{1-x}(R,Fe)_6Ge_4(Ge,Sb)_2$.

Acknowledgements

Table of Contents

List of Tables

List of Figures

List of Crystallographic Abbreviations and Symbols

a, b, c	lengths of basis vectors, lengths of cell edges
α, β, γ	interaxial angles between b and c, a and c, and a and b axes, respectively
d_{hkl}	interplanar distance, or spacing, of neighbouring net planes (hkl)
F_c	calculated structure factor
F_o	observed structure factor
hkl	indices of the Bragg reflection (Laue indices) from the set of parallel equidistant net planes (hkl)
(hkl)	indices of a crystal face, or of a single net plane (Miller indices)
$[hkl]$	indices of a lattice direction
λ	wavelength
μ	linear absorption coefficient
P	experimental instability factor in weighting scheme (used in the calculation of $\sigma(I)$ to downweight intense reflections)
R	residual index
R_w	weighted residual index
R_{int}	residual index for averaged symmetry equivalent reflections
ρ	density
σ	standard deviation
U_{eq}	equivalent isotropic atomic displacement parameter
U_{ij}	elements of anisotropic atomic displacement parameter tensor
V	cell volume of the direct lattice
w	weighting factor applied to structure factor
x, y, z	coordinates of a point (location of an atom) expressed in units of a, b, and c
Z	number of formula units per unit cell

Chapter 1

Introduction

Chemical Bonding in Intermetallic Compounds

Most of the elements are metals or metalloids, and when these are combined intermetallic compounds result. Considering all of the possible compositions, only a fraction of which have been investigated, this class of compounds encompasses a huge number of members and displays a rich structural chemistry.[1] Intermetallic compounds range from simple close-packed binaries to complex quasicrystalline materials.[2] The physical properties exhibited by this class are equally varied. Some members have important technological applications as permanent magnets ($SmCo_5$), thermoelectric materials (Bi_2Te_3), superconductors (Nb_3Sn) and semiconductors ($GaAs$).[3] Despite their prevalence, intermetallic compounds have, for the most part, been neglected in mainstream chemistry. Although physicists and metallurgists have described and optimized the properties of technologically useful materials, basic questions concerning the chemical bonding in these phases remain unanswered.[4,5]

Background. Prior to the development of X-ray diffraction, the existence of intermetallic compounds with definite compositions and distinct structures was debatable. Historically, the reaction of metals was expected to produce alloys or "solid solutions" with simple structures and wide homogeneity ranges. But in 1839, Karsten noticed that

the action of acids on alloys of Cu and Zn differed at the equiatomic composition and, based on this observation, suggested the formation of an intermetallic compound, CuZn, the now-familiar β-brass. In the years that followed, several more examples were characterized. Chemists found these new intermetallic materials strange and disturbing because most failed to obey the ordinary valence rules that had been applied successfully to ionic and covalent compounds. Chemically based electron counting rules for intermetallic compounds were thought to be impossible.[3]

Since this time, thousands of intermetallic compounds with structures ranging from close-packed to remarkably complex ones have been identified.[1] Several classification systems have been devised to relate the structures by considering them as packings of spheres, stackings of nets, or assemblies of coordination poyhedra.[6–8] However, these geometric relationships, in general, neglect the importance of chemical bonding. The development of a theory relating structures and the character of interatomic interactions has been hindered by the fact that a given structure type can satisfy different types of bonding requirements. Compounds containing either primarily ionic or metallic interactions frequently crystallize in similar structure types built up from close-packed layers that accommodate the non-directional interactions. To further complicate the situation, ionic, metallic, and covalent bonding often coexist in the same structure. Owing to the complexity of the interactions involved, the chemical bonding in intermetallic compounds has eluded description by a simple overall scheme. However, well-developed electron-counting rules exist for two limiting classes of intermetallic compounds, the Hume-Rothery compounds[9] and the Zintl compounds.[10]

Electron Counting Schemes. In 1926, Hume-Rothery observed that the ratio of valence electrons to atoms, or valence electron concentration (*vec*), is a crucial variable in determining the structure type adopted by a large number of compounds.[3,9] In alloy systems involving Cu, Ag, and Au, and other metallic elements with similar electronegativities, a sequence of structures is formed at specific *vec*s, regardless of the particular elemental composition. For example, Cu_5Zn_8,[11] Cu_9Ga_4,[12] and $Cu_{41}Sn_{11}$[13] all have a *vec* of 1.6 and crystallize in the γ-brass (or a closely related) structure (Figure 1-1). Indeed, most binary compounds that adopt the γ-brass structure have a *vec* near 1.6. Many other phases with a similar dependence on the *vec* and different zones of permissible electron count are known, including the simple face-centred cubic, body-centred cubic, hexagonal close-packed, and the rather complex β-Mn structures.[9] These structures feature high symmetry, densely packed atoms, and large coordination numbers, characteristics typical of the elemental metals. The Hume-Rothery valence electron counting rule works well for intermetallic compounds in which the electronegativity difference for the components is small and non-directional bonding interactions predominate.

When the component atoms of an intermetallic compound have very different electronegativities, the Zintl concept is more appropriate as an electron counting rule.[10] In the early 1930s, Zintl studied compounds of the alkali metals and the post-transition metals that possessed properties that were unlike those of the more typically metallic Hume-Rothery compounds.[3,10] These polar intermetallic compounds were brittle and weakly conducting; their crystal structures contained directional bonds with normal single-bond lengths between the electronegative component atoms. Based on these

observations, Zintl suggested the coexistence of ionic and covalent interactions in these polar intermetallics, and proposed an electron counting scheme in which the electropositive atoms donate their valence electrons to the more electronegative atoms. The electronegative atoms then participate in homoatomic bonds, as necessary, to complete their valence shells. If we consider NaTl as an example, the Na atoms donate their valence electrons to Tl, resulting in a $[Tl]^{1-}$ network, isoelectronic to elemental C, that adopts the diamond structure (Figure 1-2).[14] For this new class of compounds, the structure adopted is determined by the *vec* of the anionic component.

Although the bonding and electronic structure of the Hume-Rothery and Zintl compounds can be explained using simple electron counting schemes, the factors that determine which of several feasible atomic arrangements is realized are still largely unknown. In the case of the Hume-Rothery compounds, more than one structure type may be formed at a specific *vec*, depending on the composition and the reaction conditions.[9] For instance, at a *vec* of 1.5, phases with the body-centred cubic, hexagonal close-packed or β-Mn structure are found in different binary systems. In some systems, all three structure types are observed within separate temperature ranges. The preference of one structure type over another at a given *vec* may depend on subtle size and electronic factors. This is also the case for the Zintl compounds, in which a remarkable variety of isoelectronic anionic substructures are observed.[5,10,15] In the compounds $CaSi_2$ and $BaSi_2$, for example, the anionic networks consist of corrugated hexagonal $[Si]^{1-}$ nets analogous to those in metallic As,[16] or of Si_4^{4-} tetrahedra that resemble the P_4 tetrahedra of white P,[17] respectively (Figure 1-3). The Zintl electron-transfer concept predicts only

the overall charge of the anionic substructure, but the actual geometry of the substructure is sensitive to the sizes and electronegativities of the component atoms.

Bonding Patterns in Antimonides. Of course, the Hume-Rothery and Zintl concepts are only applicable to certain limiting classes of intermetallic compounds in which the electronegativity differences between the metal or metalloid atoms are either small or large. No clear bonding schemes exist between the two extremes. It is in this uncharted territory that we expect to find new and unusual modes of bonding. Antimony, located at the boundary between the metals and non-metals in the periodic table, provides an entry point into this unexplored area. Antimony forms intermetallic antimonides with most of the metallic elements[1] and displays a broad flexibility in its homoatomic bonding. The most polar antimonides adhere to the Zintl concept and contain classical Sb substructures built up from normal two-electron single bonds. In compounds with reduced electronegativity differences, Sb networks with "non-classical" geometries become prevalent and the applicability of the Zintl concept is challenged. The various classical and more unusual non-classical Sb substructures found in intermetallic compounds have recently been reviewed by Papoian and Hoffmann.[18] The Sb networks appearing in metal-rich antimonides, in particular, have been surveyed by Kleinke.[19]

The alkali (A) and alkaline-earth (AE) metal antimonides A_3Sb (A = Li–Cs)[20] and Mg_3Sb_2,[21] with stoichiometries and structures typical of ionic salts, provide the most obvious manifestation of the Zintl concept. Assuming complete electron transfer from the electropositive metals, the isolated Sb atoms have completed valence shells, and are assigned an oxidation state of -3. At other compositions, classical covalently-bonded Sb substructures (Sb–Sb ~ 2.8–2.9 Å) predominate in the alkali and alkaline-earth metal

antimonides. The simplest classical substructure containing an Sb–Sb bond is the Sb_2 dumbbell found in numerous Zintl phases (Figure 1-4a). According to a Zintl analysis, each Sb atom of the pair must have three lone pairs of electrons, in addition to the shared bonding pair, to complete its valence octet, resulting in a −2 oxidation state. The anionic substructure in $K_2Ba_3Sb_4$ is an array of Sb_2 dumbbells which can be represented as $[(Sb_2{}^{4-})_2]^{8-}$, supporting the electron transfer hypothesis.[22] A more unusual classical structural feature is the Sb_4 square shown in Figure 1-4b. In this unit, each Sb^{1-} participates in two single bonds and possesses two non-bonding electron pairs, and the overall charge per Sb_4 square is −4. The structures of the alkaline earth antimonides $AE_{11}Sb_{10}$ (AE = Ca, Sr) contain one $Sb_4{}^{4-}$ square, as well as four $Sb_2{}^{4-}$ dumbbells and eight isolated Sb^{3-} anions per two formula units.[23] Based on these assignments, we arrive at the Zintl formulation $(AE^{2+})_{22}[(Sb_4{}^{4-})(Sb_2{}^{4-})_4(Sb^{3-})_8]$.

Chains of Sb atoms are also frequently encountered in the substructures of the alkali and alkaline-earth metal antimonides. Isolated Sb_6 zigzag segments (Figure 1-4c) are found in the compounds AE_2Sb_3 (AE = Sr, Ba).[24] Assuming completed octets for each of the chain atoms, the terminal and inner atoms are assigned as Sb^{2-} and Sb^{1-}, respectively. One $Sb_6{}^{8-}$ chain is found per two formula units, leading to the charge-neutral representation $(AE^{2+})_4[Sb_6]^{8-}$. Infinite one-dimensional zigzag chains occur in ASb (A = Na–Cs)[25] and $AESb_2$ (AE = Ca, Sr).[26] These chains are helical in the alkali metal antimonides, and planar in the alkaline-earth metal antimonides, presumably due to the effects of the different cation matrices (Figure 1-5). In both cases, the chain atoms are assigned an oxidation state of −1, and the one-dimensional substructure can be represented by $\frac{1}{\infty}[Sb]^{1-}$. The geometries of classical Sb substructures can also be

extended to two-dimensions. The structure of $BaSb_3$ contains puckered two-dimensional nets composed of interconnected 14-atom rings (Figure 1-6).[27] One third of the net atoms are three-connected neutral Sb^0. The remaining two-connected centres are assigned as Sb^{1-}, giving the overall formulation $^2_\infty[Sb_3]^{2-}$ for the substructure.

In antimonides involving the less electropositive rare-earth elements, more unusual non-classical multicentre Sb–Sb bonding interactions (~ 3.0–3.2 Å) which can be rationalized using an extended Zintl concept frequently appear.[18] The simplest of these is the linear Sb_3 unit that, along with isolated Sb atoms, is found in the anionic substructure of $Eu_{14}MnSb_{11}$ (Figure 1-7a).[28] Since structural and magnetic studies suggest that the Eu and Mn centres are in the +2 and +3 oxidation states, respectively, the composite Sb substructure must have a charge of -31 in order to maintain charge balance. There are eight isolated Sb^{3-} anions per formula unit; therefore, the linear Sb_3 unit is assigned a charge of -7, making it isoelectronic with I_3^{1-}.[29] The Sb_3^{7-} unit has been modelled as a hypervalent three-centre four-electron bonded structure.[18,30] This model assumes that, in the absence of significant s-p mixing, only the axial Sb p orbitals are involved in bonding. These atomic orbitals are combined to form three molecular orbitals (MOs): one bonding, one non-bonding, and one antibonding (Figure 1-8). At the electron count proposed for the Sb_3^{7-} unit, four electrons are involved in the axial p orbital system, and these fill the bonding and non-bonding orbitals. According to this MO picture, each of the Sb–Sb bonds in the Sb_3^{7-} anion may be considered as a half-bond, consistent with the longer $3.258(2)$ Å distances observed. By describing such intermediate Sb–Sb interactions as one-electron bonds, the Zintl electron transfer concept can be applied to antimonides that incorporate non-classical subnetworks.[18]

Other examples of hypervalent electron-rich bonding and long Sb–Sb bonds are found in one- and two-dimensional Sb substructures. Extended one-dimensional linear chains occur in the compounds RE_3MSb$_5$ (RE = La–Nd, Sm; M = Ti, Zr, Hf, Nb) (Figure 1-7b).[31] The model proposed for Sb$_3^{7-}$ can be extrapolated to this system: each Sb atom of the chain, participating in two one-electron bonds, requires three lone pairs to obtain a completed valence shell, and is assigned a –2 oxidation state. Considering La$_3$TiSb$_5$ as an example, the La^{3+} and Ti^{4+} cations donate a total of 13 electrons to the Sb substructure, which consists of three isolated Sb^{3-} anions and two $_\infty^1[$Sb$]^{2-}$ chains per formula unit, resulting in the formulation (La^{3+})$_3$(Ti^{4+})[(Sb^{3-})$_3$(Sb^{2-})$_2$]. If an infinite number of linear chains are brought together, two-dimensional sheets result. Many of the binary rare-earth diantimonides RESb$_2$ adopt either the SmSb$_2$ (RE = La–Nd, Sm)[32] or ZrSi$_2$ (RE = Yb)[33] structure type, both of which incorporate a square Sb net (Figure 1-7c). Following the reasoning applied to the one-dimensional Sb chains, each Sb atom of the two-dimensional sheet, now participating in four one-electron bonds, is assigned as Sb^{1-}. In the diantimonide structures, the square nets coexist with either Sb$_2^{4-}$ pairs (SmSb$_2$-type) or $_\infty^1[$Sb$]^{1-}$ zigzag chains (ZrSi$_2$-type), and charge balance is achieved if the rare-earth cation is assumed to be in the +3 oxidation state for RE = La–Nd, Sm or in the +2 oxidation state for Yb.

The simple Zintl electron transfer concept often breaks down for antimonides of the transition metals, which can exist in multiple oxidation states and may have electronegativities approaching that of Sb. Despite the difficulties involved in the application of the Zintl electron counting rule to many transition metal antimonides,

structural features that resemble those encountered in the Zintl phases persist. Nearly all of the first row transition metal diantimonides MSb$_2$ crystallize in structures, either CuAl$_2$-type (M = Ti, V)[34] or FeS$_2$-type (M = Cr, Fe–Ni),[35] containing Sb$_2$ pairs (Sb–Sb ~ 2.8–2.9 Å). According to our analysis above, the Sb$_2$ structural unit is assigned an overall charge of –4, leading to a +4 oxidation state for the transition metal. But a closer inspection of each of the structures reveals that there may be weaker bonding interactions between the Sb$_2$ pairs. The Sb$_2$ pairs in the CuAl$_2$-type structures are assembled at distances of ~ 3.3–3.5 Å into hexagonal nets (Figure 1-9a). In the FeS$_2$-type structures, the Sb$_2$ dumbbells are stacked in a ladder arrangement, with interpair Sb–Sb distances of ~ 3.2–3.8 Å (Figure 1-9b). If we consider the longer interpair Sb–Sb interactions as one-electron bonds, then we arrive at oxidation states of –1 and +2 for the Sb and transition metal atoms, respectively, in each structure. However, if we abandon our artificial restriction to integral values, the Sb and transition metal oxidation states may lie somewhere between the two proposed extremes, making our Zintl analysis of the transition metal diantimonides ambiguous.[18]

A similar uncertainty arises when the Zintl concept is applied to the low-temperature form of ZrSb$_2$.[36] At the classical limit, the anionic substructure in β-ZrSb$_2$ may be described as a one-dimensional $_\infty^1[\text{Sb}]^{1-}$ zigzag chain (Sb–Sb 2.890(1) Å) bordered by isolated Sb^{3-} anions. Alternatively, since the 3.146(1) Å Sb–Sb distance between the chains and the atoms that border them is typical of an intermediate bonding interaction, the Sb substructure may be modelled as a non-classical four-atom-wide square ribbon (Figure 1-10). Completing the Sb octets, we assign the inner four-connected ribbon atoms as Sb^{1-} and the terminal two-connected atoms as Sb^{2-}. The

limiting classical and non-classical interpretations of the Sb bonding network result in a +4 or +3 oxidation state for Zr, respectively. Although Zr^{4+} seems more reasonable, this assignment would neglect Sb–Sb interactions that surely possess at least partial bonding character. The unusual ribbon substructure of β-$ZrSb_2$ points to the existence of more complex Sb networks.

New Intermetallic Antimonides. The goal of this research is to expand the structural chemistry of antimony by synthesizing and structurally characterizing new ternary and quaternary antimonides. Since the most unusual and challenging Sb substructures are found in rare-earth and transition metal antimonides, our focus is the isolation of intermetallic compounds in these systems, with the expectation that new patterns of homoatomic Sb–Sb bonding will be encountered. These compounds will test the limits of the current bonding concepts and electron counting rules. In light of the many examples of intermetallic antimonides that exhibit interesting and technologically important properties, such as the binary III-V semiconductor InSb,[37] the ternary magnetoresistive material $Eu_{14}MnSb_{11}$,[38] and the quaternary thermoelectric material $LaFe_3CoSb_{12}$,[39] the physical properties of the new intermetallic antimonides will be measured. By relating structure and bonding to physical properties, in some cases using band structure calculations, we may gain a better understanding of how to design novel materials with desired characteristics.

Experimental Methods

Synthesis. The synthesis of intermetallic compounds typically entails extreme reaction conditions to overcome the huge kinetic barriers that impede the reaction

between solids.[40–42]   The most common method for the synthesis of solid-state compounds is by direct reaction. Extended annealing at high temperatures is used to overcome the slow solid-state reaction rates. Stoichiometric mixtures of the elements, usually in the form of powders, are combined in fused silica tubes. Because the desired products are non-oxides, the tubes are sealed under dynamic vacuum, then heated in a furnace for several days at temperatures between 700 and 1000 °C. Crystal growth may be encouraged by slowly cooling the reaction mixture. In some cases, an excess of a low-melting solid (a flux), such as elemental Sn (mp 232 °C), may be added to the reaction mixture to enhance the diffusion of the reactants and to promote the nucleation of crystallites. After the reaction is finished, the Sn is easily removed by treatment with HCl.   However, this method is not always applicable, because the Sn sometimes participates in the reaction, resulting in the formation of unwanted byproducts.

Since there is no simple way of monitoring the progress of these high-temperature reactions, very little is known about the reaction mechanisms involved. We must resort to trial and error for the determination of the correct loading compositions and reaction conditions. In the search for new compounds, the phase diagram of a particular ternary system at one temperature is explored by reacting various stoichiometries of the elements. Alternatively, a specific compound, for example, an unknown member of a structural family or a hypothetical structural variant, may be targeted. In this case, the reaction composition and heating program are selected based on the preparation of the known compound. An understanding of structural chemistry is a valuable tool in the design of new materials.

Characterization. Knowledge of the chemical composition and structure of a compound is essential for its description. For intermetallic compounds of the heavier elements, elemental compositions are routinely determined by X-ray fluorescence analysis.[40,43] An X-ray fluorescence spectrum is generated when the sample is bombarded with a high-energy electron beam in a scanning electron microscope. The incident electrons ionize some of the core electrons of the elements in the sample, and electrons from outer orbitals immediately drop down to fill the vacant levels. X-rays of characteristic energies and wavelengths are emitted during this process, and the emission spectrum obtained for the sample is analyzed to identify and quantify the elements present. In this research, an energy-dispersive spectrometer, which discriminates X-ray energies, is used, and the technique is described as energy-dispersive X-ray (EDX) analysis.

X-ray diffraction is the most powerful method for the structural characterization of intermetallic compounds.[40–42,44] With wavelengths ($\sim$ 1 Å) comparable to the interatomic spacings in crystals, X-rays incident on a sample are diffracted according to Bragg's Law

$$\lambda = 2d_{hkl}\sin\theta$$

where λ is the wavelength of the incident X-ray, d_{hkl} is the perpendicular distance between adjacent (hkl) planes, and θ is the angle at which the X-ray beam is diffracted. In the resulting diffraction pattern, the positions and intensities of the diffraction peaks depend on the size, symmetry and contents of the crystal's unit cell. Various photographic and digital techniques have been devised to collect the diffraction patterns

produced by powder or single-crystal samples. Structural information can be extracted from the patterns collected using technique-specific analytical methods.

A powder sample contains randomly-oriented crystallites. For each set of (hkl) planes, at least some crystallites will be oriented at the Bragg angle θ with respect to the incident X-ray beam. Since all possible crystallite orientations should be present, a cone of scattering will be formed for each set of planes. In the Guinier photographic technique used in this research,[42] a film intercepts the diffracted beam. Thus, every plane of the crystal is represented by a line on the film. The resulting powder pattern provides a characteristic fingerprint for the compound. In exploratory chemistry, the powder pattern of an unknown reaction product can be compared to a library of patterns for known compounds to determine whether these phases are present. However, if the product is identified, through a process of elimination, as a new phase, the determination of its structure based on powder diffraction alone is difficult, given the generally poor resolution of the diffraction lines. On the other hand, if the product adopts a known structure type, accurate cell parameters for the compound can be determined by indexing its powder pattern.

The structures of new intermetallic compounds are usually determined using single crystal X-ray diffraction.[44] In general, a single crystal is rotated in the incident X-ray beam, such that each set of (hkl) planes is brought into reflecting position. In photographic methods, such as the Weissenberg technique, the diffraction peaks are recorded on a film. Since it is difficult to quantify the intensities of the diffraction peaks on film, photographic techniques are mainly used to screen crystals for quality, and to determine preliminary cell parameters and symmetry information. Once a suitable single

crystal is found, an intensity data set containing several thousand reflections is collected on a diffractometer. In this method, a radiation detector measures the intensity of each reflection, and, based on this data, the crystal's symmetry and cell parameters can be established. In order to determine the identity and positions of the atoms contained in the unit cell, the intensity data must be converted into electron density data using mathematical procedures.

Physical Properties. Crystal structure, electronic structure, and transport properties are intimately related. Most intermetallic compounds, owing to the intermediate electronegativity differences between the component metals, are either semiconductors or metals. Classical Zintl compounds should, by definition, display semiconducting behaviour.[10] However, prediction of the transport behaviour for less polar intermetallics is not as straightforward. The measurement of electrical resistivity provides a way of testing the validity of bonding schemes and can serve as a window into the electronic structure of intermetallic compounds.

Resistivity. The electrical resistivity is an inherent property of a material that describes its ability to carry an electrical current. Experimentally, the resistivity of a sample can be determined using a four-probe technique (Figure 1-11).[42] For a needle-shaped crystal, four metal leads are attached at intervals along the length of the sample. A current (I) is driven through the two outer leads, and the voltage drop (V) across the inner leads is measured. The resistivity (ρ) of the material can be calculated by the relation

$$\rho = \frac{VA}{I\ell}$$

where A is the cross-sectional area of the sample, and ℓ is the distance between the two inner contacts.

The resistivity of a material can also be defined in terms of the number of charge carriers (n) per unit volume, the charge (Ze) of the carriers, and the carrier mobility (μ) according to

$$\rho = \frac{1}{nZe\mu}.$$

The value of Ze is constant for electrical conductors. However, the mobility of the carriers decreases, in general, with increasing temperature due to scattering by lattice vibrations. The temperature dependence of the carrier concentration depends on the type of material. Taking all of these factors into account, the resistivity of most materials varies with temperature. The magnitude and temperature dependence of the resistivity allow the classification of solids as insulators, semiconductors, or metals.[40,45]

For insulators and semiconductors, the resistivity increases exponentially at low temperatures (Figure 1-12a). The source of this behaviour can be traced to the band structures of these materials. In the electronic structures of insulators and semiconductors, a completely filled valence band and an empty conduction band are separated by a band gap. If the energy of the band gap is larger than ~ 3 eV, the material is classified as an insulator, and if smaller, as a semiconductor.[40] For both classes of compounds, conductivity results from the promotion of electrons to the empty conduction band. The room temperature resistivities of insulators are very large, typically greater than 10^{12} Ω cm.[40] For semiconductors, the room temperature resistivities, in the 10^{-2} to 10^5 Ω cm range,[40] indicate that a significant number of carriers occupy the conduction

band. As the temperature decreases, fewer electrons possess enough energy to be excited across the band gap and the resistivity increases.

The resistivity of metals, on the other hand, is dominated by carrier mobility, rather than concentration, and decreases with decreasing temperature (Figure 1-12b). In metals, the origin of conductivity is a partially filled band at the Fermi level. The number of carriers is large and effectively constant, resulting in a small room temperature resistivity on the order of 10^{-5} to $10~\Omega$ cm.[40] The temperature dependence of the resistivity is a result of changes in carrier mobility with temperature. Interactions with lattice vibrations and crystal imperfections impede the flow of electrons. At high temperatures, the scattering of charge carriers by lattice phonons is frequent, and the resistivity of the material is large. As the temperature decreases, phonon collisions become less frequent, and the resistivity is lowered. However, at very low temperatures, a limiting residual resistivity (ρ_0) is reached that is dependent on the purity and perfection of the sample. Collisions with impurity atoms and lattice defects prevent the resistivity of a normal metal from completely vanishing.

Superconductivity. In some materials, including many metals, the electrical resistivity does disappear completely below a critical temperature, T_c (Figure 1-12c). This behaviour indicates a transition to the superconducting state.[46,47] In a superconductor, electron-phonon interactions cause the pairing of conduction electrons. The resulting Cooper pairs, composed of electrons with opposite spins and momenta, become the charge carriers in the material. These electron pairs are highly correlated and move in a single coherent motion; when paired, both electrons must undergo exactly the

same scattering events. Since the probablity of simultaneous identical scattering is negligible, the Cooper pairs can move through the solid without any resistance.

In addition to zero resistivity, superconductors exhibit another distinctive and fundamental property: perfect diamagnetism. In any material, the magnetic induction (B) inside the sample, when placed in an external magnetic field (H), is given by

$$B = H + 4\pi M$$

where M is the magnetic moment per unit volume (magnetization) of the sample. Superconducting materials exclude or expel a magnetic field, provided the field is below the critical field strength H_c. Thus, theoretically, the magnetic induction should be zero inside the sample ($B = 0$), and the magnetic susceptibility (χ), defined as

$$\chi = \frac{M}{H},$$

should attain a limiting value of $-1/4\pi$. However, in real samples, the susceptibility reached below T_c is always lower in magnitude than the theoretical value, and the ratio of the two values gives the superconducting fraction of the sample.

In practice, two different types of experiments can be carried out to investigate the temperature dependence of the magnetic susceptibility. If the sample is cooled below T_c in zero field before measuring the susceptibility as a function of temperature in a small applied field, diamagnetic shielding, or flux exclusion, occurs. Alternatively, if the same measurement is made after cooling the sample in an external field, the Meissner effect, or flux expulsion, is observed. Because of flux pinning in the sample, the Meissner superconducting fraction is always lower than the shielding fraction.

Band Structure. Owing to the structural complexity of intermetallic compounds, semiempirical extended Hückel calculations are used to investigate electronic

structure.[48,49] In these calculations, a number of simplifying approximations are applied. Only valence electrons are considered, and the valence atomic orbitals are described by Slater-type orbitals with exponents obtained from first principles calculations on atoms. According to the tight-binding approximation, one-electron crystal orbitals (Bloch functions) are constructed, by making use of translational symmetry, from linear combinations of these atomic orbitals. The Hamiltonian matrix for the system is simplified by using the valence state ionization potentials of the atoms involved to determine the matrix elements.

Although limited by its dependence on the availability of accurate parameters, the extended Hückel method provides a simple and fast method for the calculation of the band structures of solids. The results extracted from these calculations, such as orbital interaction or density of states curves, can provide valuable insight into the nature of bonding in a compound and the origin of electron transport properties. Electronic structure calculations bridge the gap between crystal structure and physical properties, facilitating the development of structure-property relationships in intermetallic compounds.
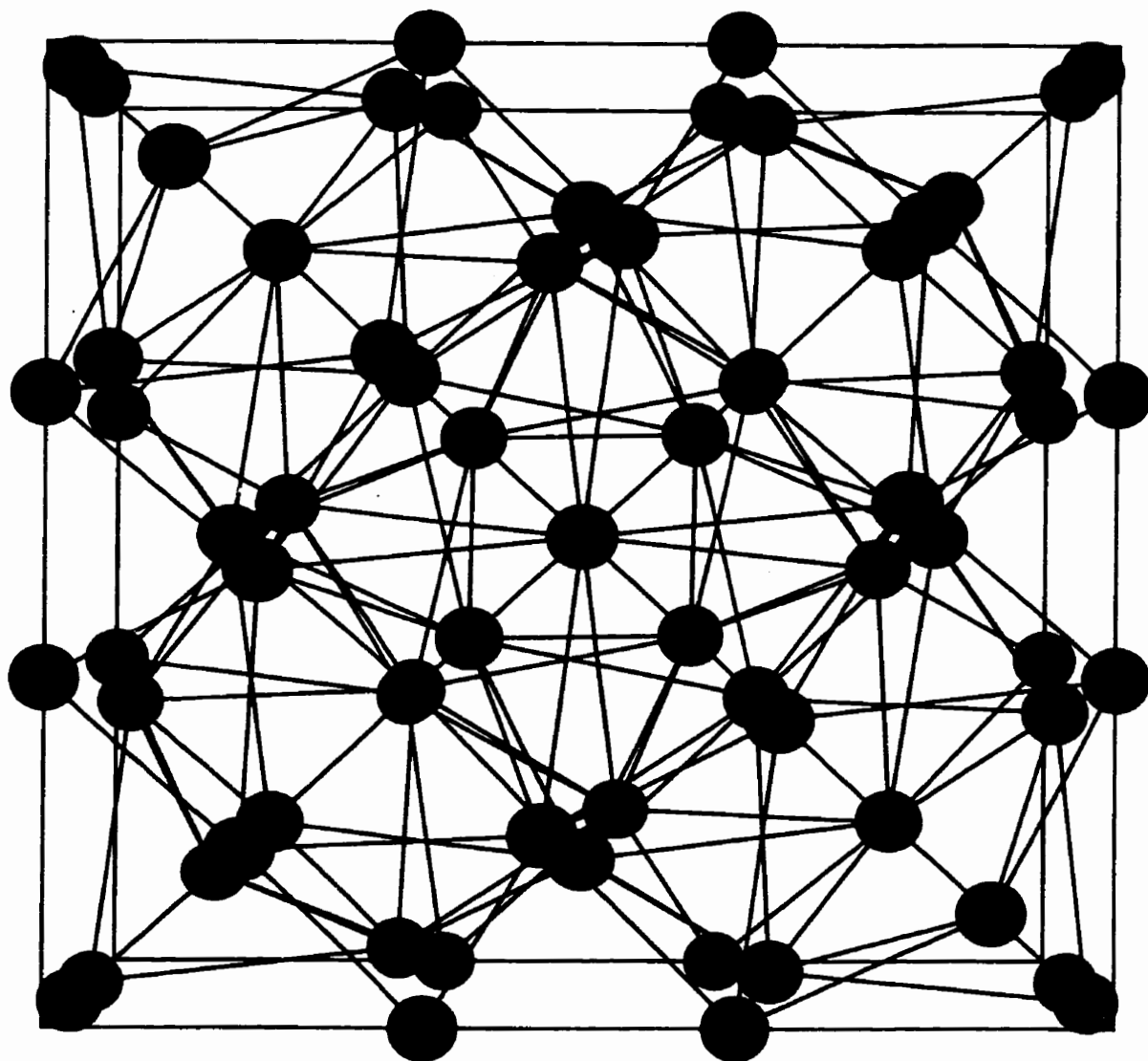
Figure 1-1. Structure of the Hume-Rothery compound Cu_5Zn_8, γ-brass. The lightly shaded circles are Cu atoms, and the solid circles are Zn atoms.
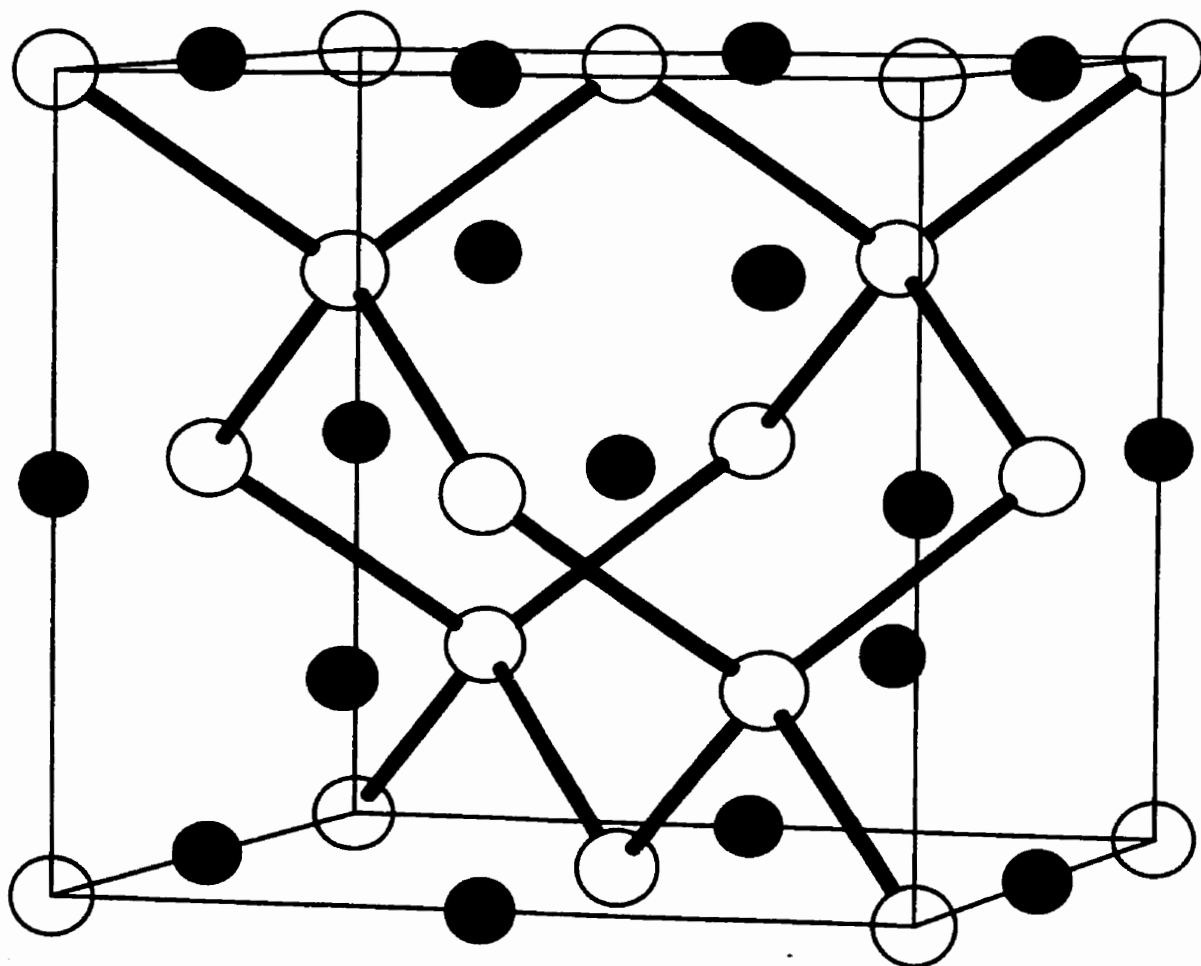
Figure 1-2. Structure of the Zintl compound NaTl. The small lightly shaded circles are Na atoms, and the large open circles are Tl atoms.

(a)

(b)
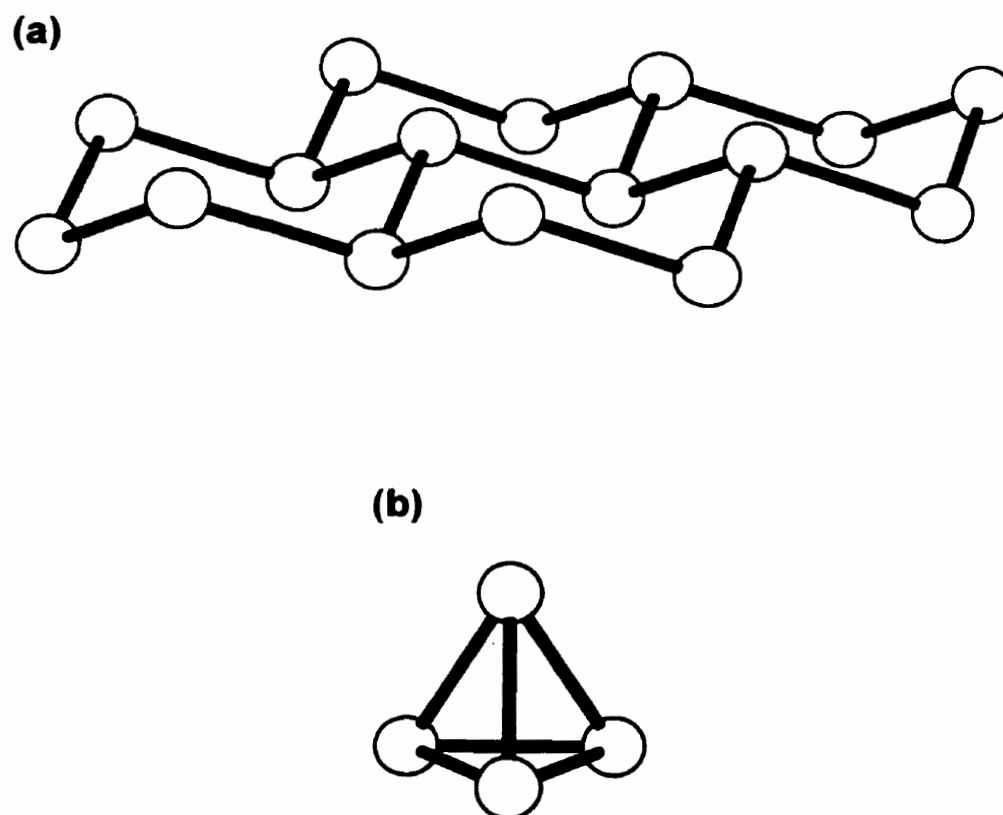
Figure 1-3. Isoelectronic (a) $[Si]^{1-}$ and (b) Si_4^{4-} substructures in $CaSi_2$ and $BaSi_2$, respectively.

(a)

(b)

(c)
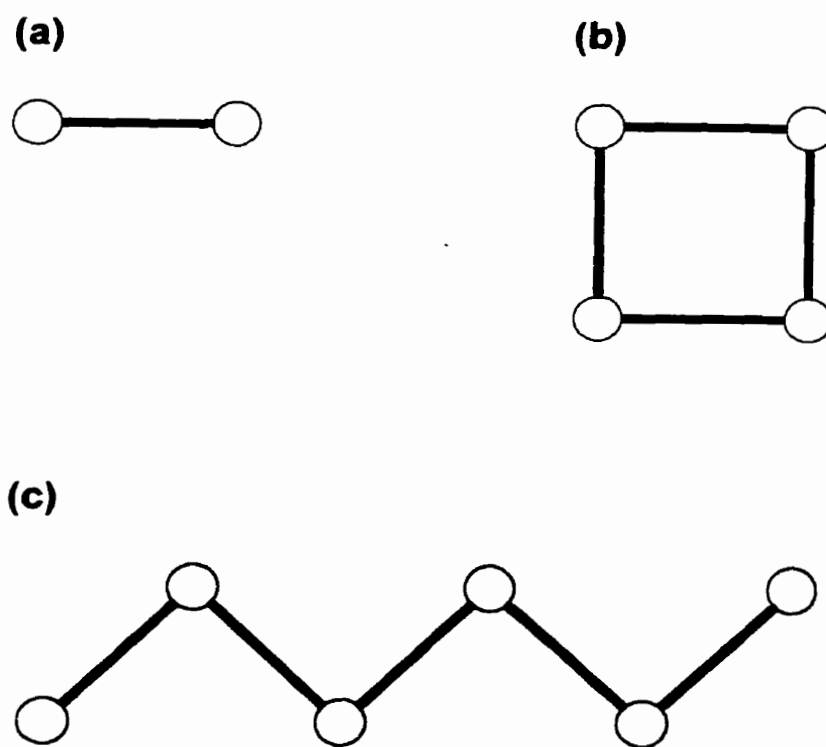
Figure 1-4. Examples of finite classical Sb networks: (a) Sb_2^{4-} dumbbell, (b) Sb_4^{4-} square, and (c) Sb_6^{8-} zigzag segment.

(a)　　　　　　　　　　　**(b)**
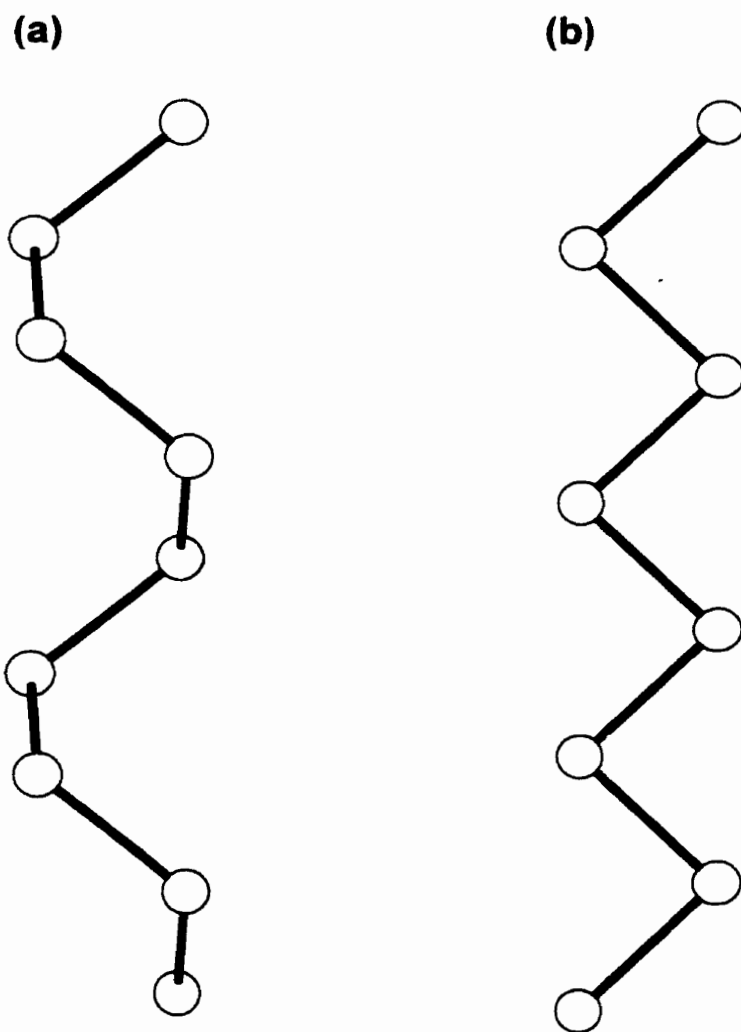
Figure 1-5. Examples of classical one-dimensional Sb networks: (a) helical and (b) planar zigzag $_\infty^1[\text{Sb}]^{1-}$ chains.
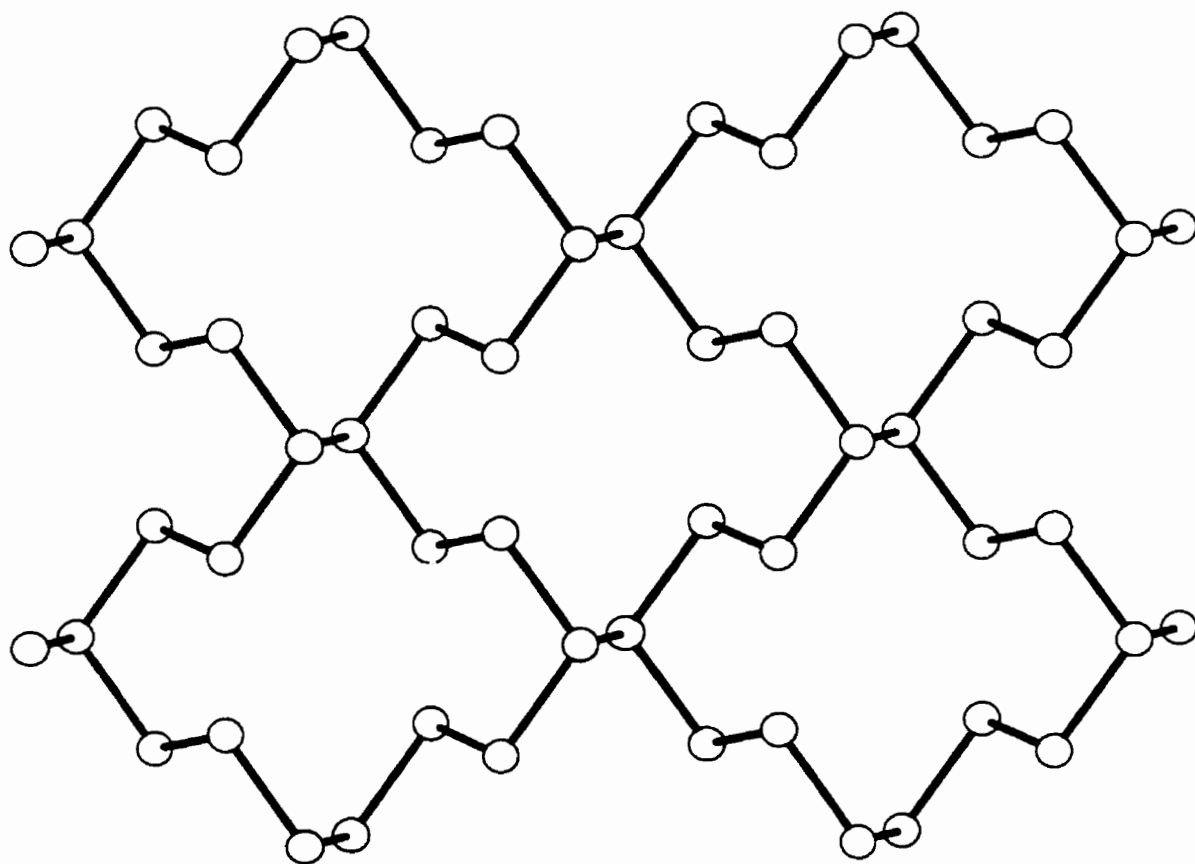
Figure 1-6. Classical two-dimensional $_{\infty}^{2}[\mathrm{Sb}_3]^{2-}$ substructure in BaSb$_3$.
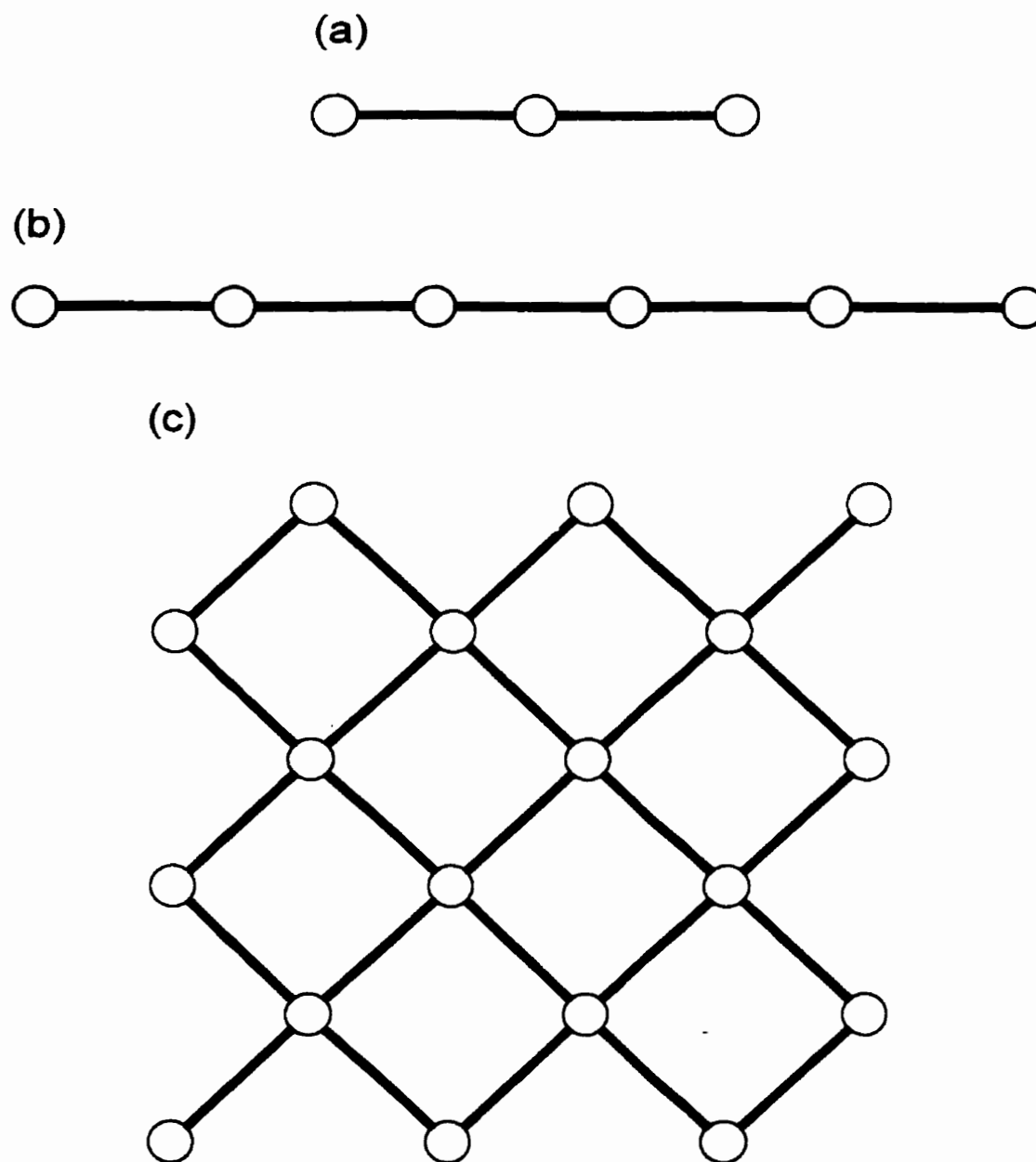
Figure 1-7. Examples of nonclassical Sb networks: (a) Sb_3^{7-} unit, (b) one-dimensional linear $^1_\infty[Sb]^{2-}$ chain, and (c) two-dimensional square $^2_\infty[Sb]^{1-}$ net.

antibonding

non-bonding
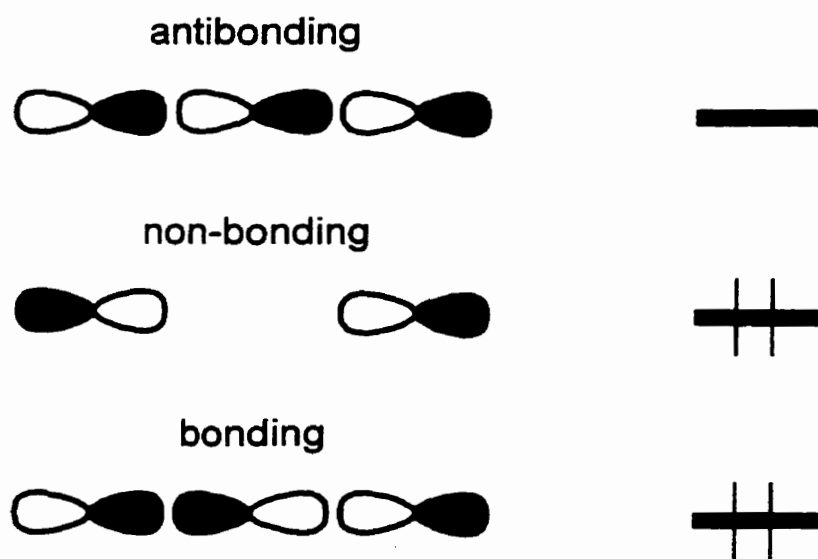
bonding

Figure 1-8. Molecular orbital (MO) scheme for the axial p orbital system of Sb_3^{7-}. The four electrons involved in hypervalent Sb–Sb bonding occupy the bonding and non-bonding orbitals.

(a)

(b)
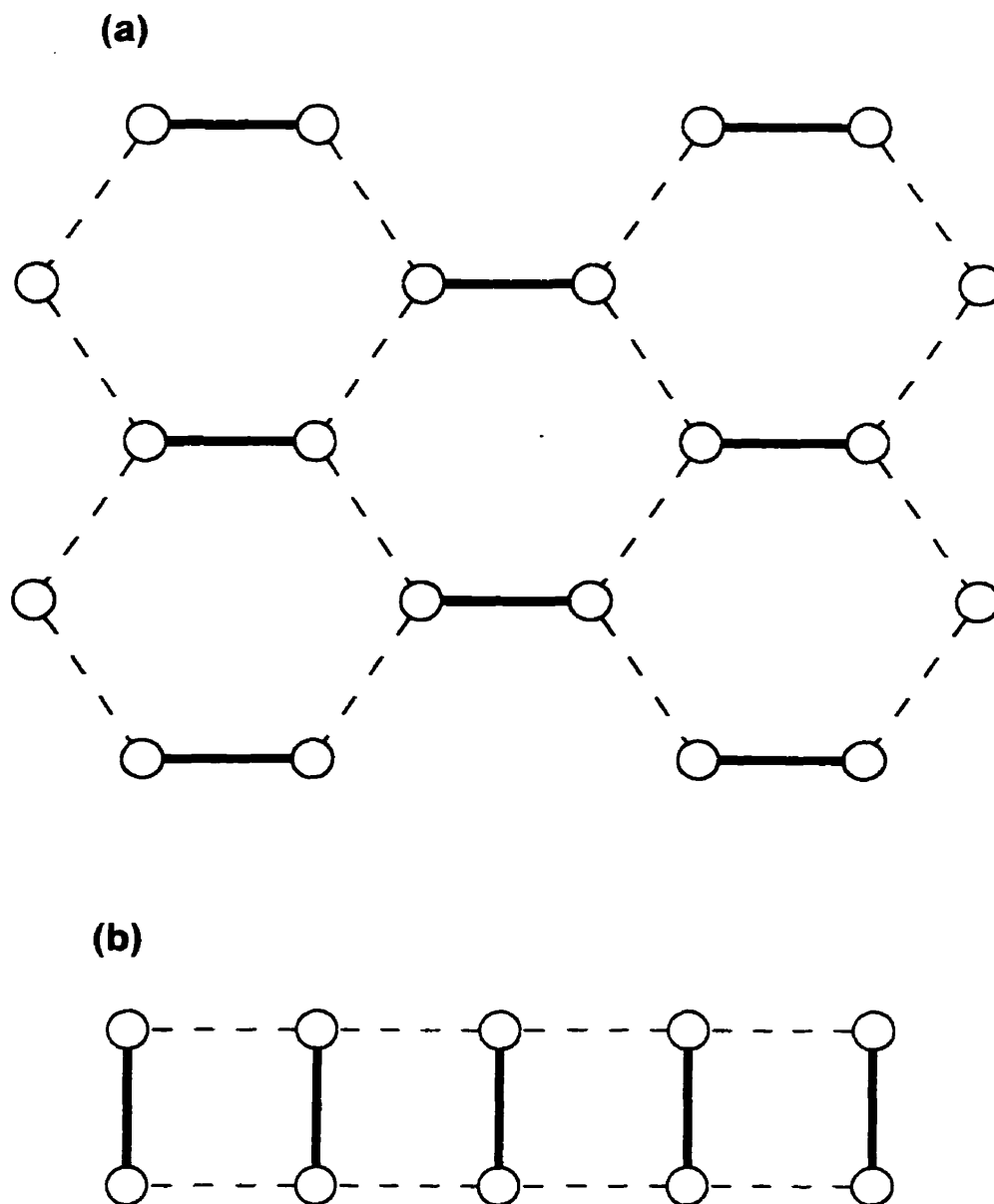
Figure 1-9. Examples of Sb networks for which the Zintl concept breaks down: (a) hexagonal net and (b) ladder network containing Sb_2 pairs connected by longer Sb–Sb interactions. The shorter ($\sim$ 2.8–2.9 Å) Sb–Sb bonds are represented by solid lines, and the longer ($\sim$ 3.2–3.8 Å) interactions are represented by dashed lines.
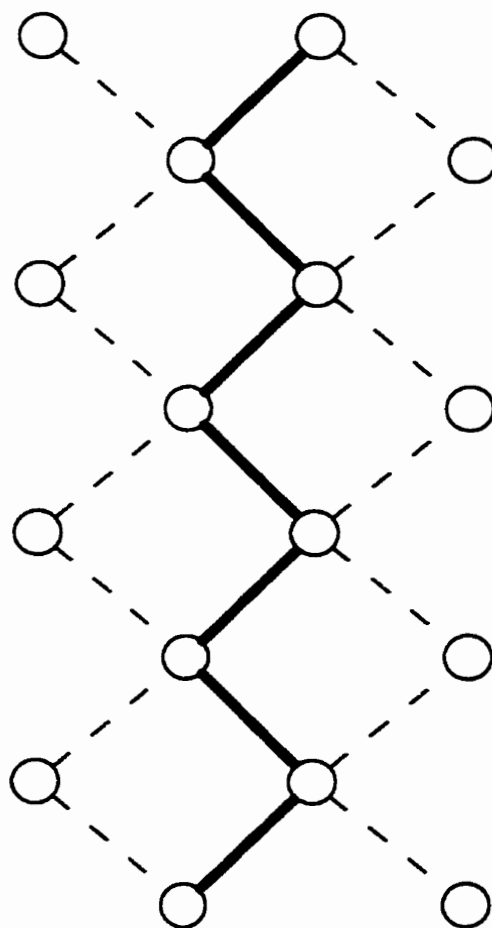
Figure 1-10. The four-atom-wide Sb ribbon in low-temperature β-ZrSb₂. The shorter (~ 2.9 Å) Sb–Sb bonds are represented by solid lines, and the longer (~ 3.1 Å) interactions are represented by dashed lines.
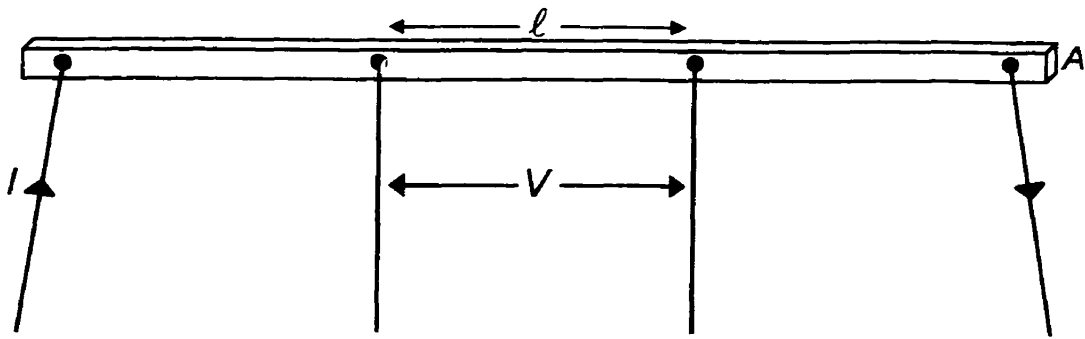
Figure 1-11. Four-probe arrangement for resistivity measurements. A current (I) is driven through the two outer leads, and the voltage drop (V) across the inner leads is measured. A is the cross-sectional area of the sample, and ℓ is the distance between the two inner contacts.

(a) insulator or semiconductor
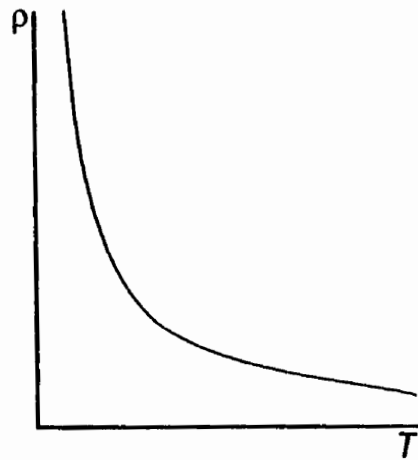
(b) metal
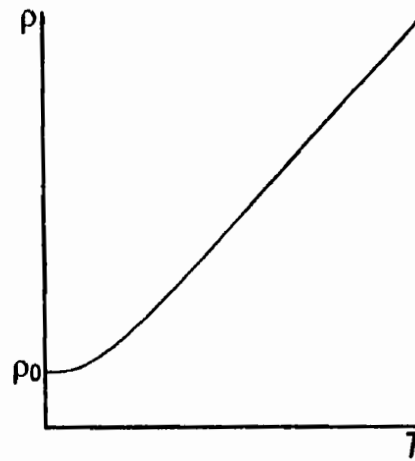
(c) superconductor
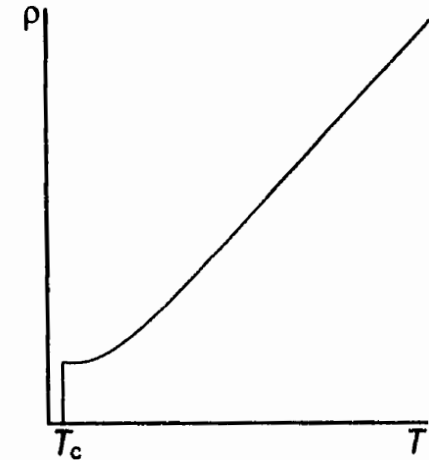
Figure 1-12. Temperature (T) dependence of the resistivity (ρ) of (a) an insulator or semiconductor, (b) a normal metal, and (c) a superconductor.

References

(1)   Villars, P. *Pearson's Handbook, Desk Edition: Crystallographic Data for Intermetallic Phases*; ASM International: Materials Park, OH, 1997.

(2)   Steinhardt, P. J. *Science*; **1987**, *238*, 1242.

(3)   *Intermetallic Compounds*; Westbrook, J. H., Ed. John Wiley and Sons: New York, 1967.

(4)   Nesper, R. *Angew. Chem. Int. Ed. Engl.* **1991**, *30*, 789.

(5)   Schäfer, H. *Ann. Rev. Mater. Sci.* **1985**, *15*, 1.

(6)   Hyde, B. G.; Andersson, S. *Inorganic Crystal Structures*; John Wiley and Sons: New York, 1989.

(7)   Pearson, W. B. *The Crystal Chemistry and Physics of Metals and Alloys*; John Wiley and Sons: New York, 1972.

(8)   Schubert, K. *Kristallstrukturen zweikomponentiger Phasen*; Springer-Verlag: Berlin, 1964.

(9)   Hume-Rothery, W.; Raynor, G. V. *The Structure and Bonding of Metals and Alloys*; Institute of Metals: London, 1962.

(10)   *Chemistry, Structure, and Bonding of Zintl Phases and Ions*; Kauzlarich, S. M., Ed. VCH Publishers: New York, 1996.

(11)   Bradley, A. J.; Gregory, C. H. *Philos. Mag.* **1931**, *12*, 143.

(12)   Stokhuyzen, R.; Brandon, J. K.; Chieh, P. C.; Pearson, W. B. *Acta Crystallogr. Sect. B: Struct. Crystallogr. Cryst. Chem.* **1974**, *30*, 2910.

(13)   Booth, M. H.; Brandon, J. K.; Brizard, R. Y.; Chieh, C.; Pearson, W. B. *Acta Crystallogr. Sect. B: Struct. Crystallogr. Cryst. Chem.* **1977**, *33*, 30.

(14)   Zintl, E.; Dullenkopf, W. *Z. Phys. Chem. Abt. B*; **1932**, *16*, 195.

(15)   Schäfer, H.; Eisenmann, B.; Müller, W. *Angew. Chem. Int. Ed. Engl.* **1973**, *12*, 694.

(16)   Janzon, K. H.; Schäfer, H.; Weiss, A. *Z. Naturforsch. B: Anorg. Chem. Org. Chem. Biochem. Biophys. Biol.* **1968**, *23*, 1544.

(17)   Schäfer, H.; Janzon, K. H.; Weiss, A. *Angew. Chem. Int. Ed. Engl.* **1963**, *2*, 393.

(18)   Papoian, G. A.; Hoffmann, R. *Angew. Chem. Int. Ed.* **2000**, *39*, 2408.

(19)   Kleinke, H. *Chem. Soc. Rev.* **2000**, *29*, 411.

(20)   (a) Brauer, G.; Zintl, E. *Z. Phys. Chem. Abt. B*; **1937**, *37*, 323. (b) Gnutzmann, G.; Dorn, F. W.; Klemm, W. *Z. Anorg. Allg. Chem.* **1961**, *309*, 210. (c) Dorn, F. W.; Klemm, W. *Z. Anorg. Allg. Chem.* **1961**, *309*, 189.

(21)   Zintl, E.; Husemann, E. *Z. Phys. Chem. Abt. B*; **1933**, *21*, 138.

(22)   Eisenmann, B.; Gieck, C.; Rößler, U. *Z. Anorg. Allg. Chem.* **1999**, *625*, 1331.

(23)   (a) Deller, K.; Eisenmann, B. *Z. Naturforsch. B: Anorg. Chem. Org. Chem.* **1976**, *31*, 29. (b) Rehr, A.; Kauzlarich, S. M. *Acta Crystallogr. Sect. C: Cryst. Struct. Commun.* **1994**, *50*, 1859.

(24)   (a) Eisenmann, B. *Z. Naturforsch. B: Anorg. Chem. Org. Chem.* **1979**, *34*, 1162. (b) Eisenmann, B.; Jordan, H.; Schäfer, H. *Z. Naturforsch. B: Anorg. Chem. Org. Chem.* **1985**, *40*, 1603.

(25)   (a) Cromer, D. T. *Acta Crystallogr.* **1959**, *12*, 41. (b) Busmann, E.; Lohmeyer, S. *Z. Anorg. Allg. Chem.* **1961**, *312*, 53. (c) Dorn, F. W.; Klemm, W. *Z. Anorg. Allg. Chem.* **1961**, *309*, 189.

(26)   (a) Deller, K.; Eisenmann, B. *Z. Anorg. Allg. Chem.* **1976**, *425*, 104. (b) Deller, K.; Eisenmann, B. *Z. Naturforsch. B: Anorg. Chem. Org. Chem.* **1976**, *31*, 1146.

(27)   Deller, K.; Eisenmann, B. *Z. Naturforsch. B: Anorg. Chem. Org. Chem.* **1978**, *33*, 676.

(28)   Rehr, A.; Kauzlarich, S. M. *J. Alloys Compd.* **1994**, *207/208*, 424.

(29)   Pimentel, G. C. *J. Chem. Phys.* **1951**, *19*, 446.

(30)   Gallup, R. F.; Fong, C. Y.; Kauzlarich, S. M. *Inorg. Chem.* **1992**, *31*, 115.

(31)   (a) Ferguson, M. J.; Hushagen, R. W.; Mar, A. *J. Alloys Compd.* **1997**, *249*, 191. (b) Bolloré, G.; Ferguson, M. J.; Hushagen, R. W.; Mar, A. *Chem. Mater.* **1995**, *7*, 2229.

(32)   Wang, R.; Steinfink, H. *Inorg. Chem.* **1967**, *6*, 1685.

(33)   Wang, R.; Bodnar, R.; Steinfink, H. *Inorg. Chem.* **1966**, *5*, 1468.

(34)   (a) Donaldson, J. D.; Kjekshus, A.; Nicholson, D. G.; Rakke, T. *J. Less-Common Met.* **1975**, *41*, 255. (b) Havinga, E. E.; Damsma, H.; Hokkeling, P. *J. Less-Common Met.* **1972**, *27*, 169.

(35)   (a) Holseth, H.; Kjekshus, A.; Andresen, A. F. *Acta Chem. Scand.* **1970**, *24*, 3309. (b) Holseth, H.; Kjekshus, A. *Acta Chem. Scand.* **1968**, *22*, 3273. (c) Rosenqvist, T. *Acta Metall.* **1953**, *1*, 761. (d) Kjekshus, A.; Rakke, T.; Andresen, A. F. *Acta Chem. Scand. Ser. A*; **1974**, *28*, 996.

(36)   (a) Garcia, E.; Corbett, J. D. *J. Solid State Chem.* **1988**, *73*, 452. (b) Garcia, E.; Corbett, J. D. *J. Solid State Chem.* **1988**, *73*, 440.

(37)   *Materials used in semiconductor devices*; Hogarth, C. A., Ed. John Wiley and Sons: New York, 1965.

(38)   Chan, J. Y.; Kauzlarich, S. M.; Klavins, P.; Shelton, R. N.; Webb, D. J. *Chem. Mater.* **1997**, *9*, 3132.

(39)   Sales, B. C.; Mandrus, D.; Williams, R. K. *Science*; **1996**, *272*, 1325.

(40)   West, A. R. *Basic Solid State Chemistry, Second Edition*; John Wiley and Sons: West Sussex, 1999.

(41)   Rao, C. N. R.; Gopalakrishnan, J. *New Directions in Solid State Chemistry, Second Edition*; Cambridge University Press: Cambridge, 1997.

(42)   *Solid State Chemistry: Techniques*; Cheetham, A. K.; Day, P., Eds. Oxford University Press: Oxford, 1987.

(43)   Flewitt, P. E. J.; Wild, R. K. *Physical Methods for Materials Characterization*; Institute of Physics Publishing: Bristol, 1994.

(44)   Stout, G. H.; Jensen, L. H. *X-ray Structure Determination: A Practical Guide, Second Edition*; John Wiley and Sons: New York, 1989.

(45)   Pollock, D. D. *Electrical Conduction in Solids: An Introduction*; American Society for Metals: Materials Park, OH, 1985.

(46)   *Chemistry of Superconductor Materials: Preparation, Chemistry, Characterization and Theory*; Vanderah, T. A., Ed. Noyes Publications: Park Ridge, NJ, 1992.

(47)   Cyrot, M.; Pavuna, D. *Introduction to Superconductivity and High-T_c Materials*; World Scientific Publishing: Singapore, 1992.

(48)   Hoffmann, R. *Solids and Surfaces: A Chemist's View of Bonding in Extended Structures*; VCH Publishers: New York, 1988.

(49)   Ren, J.; Liang, W.; Whangbo, M.-H. *Crystal and Electronic Structure Analysis Using CAESAR*; PrimeColor Software: Cary, NC, 1998.

Chapter 2

Rare-Earth Gallium Antimonides $La_{13}Ga_8Sb_{21}$ and $RE_{12}Ga_4Sb_{23}$ (RE = La–Nd, Sm): Linking Sb Ribbons by Ga_6 Rings or Ga_2 Pairs [†]

Introduction

Solid-state compounds of the post-transition metals and metalloids display a remarkable variety of structures that challenge our assumptions on what kinds of bonding are possible. There now exist many ternary compounds $M_xA_yB_z$ containing an electropositive component M (alkali or alkaline-earth metal) and two main-group elements A and B, classified as Zintl phases, in which an electron-precise formulation is possible and bonding is readily understood in terms of the fulfillment of closed-shell configurations through the formation, if necessary, of homoatomic bonds.[1] In general, it is the more electronegative main-group element B that participates in such additional homoatomic bonding. Thus, for instance, in the overwhelming majority of ternary alkali or alkaline-earth metal gallium antimonides, $M_xGa_ySb_z$, the less electronegative Ga atoms complete their octets almost invariably through heteroatomic Ga–Sb bonds, while the more electronegative Sb atoms do so through the presence of lone pairs or through the formation of homoatomic Sb–Sb bonds.[2] As a result, the most common building blocks

in these compounds are tetrahedral $GaSb_4$ and trigonal planar $GaSb_3$ units. These tetrahedra or trigonal planes may occur as isolated anions, or may be condensed via corner-sharing or through Sb–Sb bonds into oligomers, polymeric chains, or more extended networks. Standing in stark contrast, then, is the case of $Na_2Ga_3Sb_3$, the only compound in this system where Ga–Ga bonding is also present.[2a]

Substitution of the alkali or alkaline-earth metal by a rare-earth metal increases the complexity of the electronic structure, since it is not as obvious that the notion of full electron transfer by the rare-earth element is necessarily valid. Indeed, electronic structure calculations frequently suggest significant covalent character in bonds between rare-earth and main-group elements, although the approximation of a trivalent rare-earth cation is still useful.[3,4] New structural features occur, as seen in the rare-earth main-group element antimonides $REIn_{0.8}Sb_2$ (RE = La–Nd) and $RESn_{0.75}Sb_2$ (RE = La–Nd, Sm), which feature strong homoatomic In–In or Sn–Sn bonds, respectively, in one-dimensional chains, as well as extensive multicentre weak Sb–Sb bonds in two-dimensional square nets.[4,5] Extension to the heretofore unexplored RE–Ga–Sb system has led to the isolation of two compounds, $La_{13}Ga_8Sb_{21}$ and $Pr_{12}Ga_4Sb_{23}$, which represent the first examples of ternary rare-earth gallium antimonides. Their structures retain the characteristic $GaSb_3$ trigonal planes found in the alkali or alkaline-earth gallium antimonides, but, in a remarkable departure, they also contain puckered Ga_6 rings (in $La_{13}Ga_8Sb_{21}$) or Ga_2 pairs (in $Pr_{12}Ga_4Sb_{23}$) linking extended one-dimensional Sb ribbons. The results confirm earlier expectations for the existence of structures inversely related to a large family of intermetallic structures built up from trigonal prisms, but in which metalloid–metalloid bonding instead of metal–metal bonding is prevalent.[6]

Experimental Section

Synthesis. Starting materials were powders of the rare-earth elements (99.9%, Alfa-Aesar), Sb powder (99.995%, Aldrich), and Ga granules (99.99%, Alfa-Aesar or Cerac). Reactions were carried out on a 0.4-g scale in evacuated fused-silica tubes (8-cm length; 10-mm i.d.). Elemental compositions were determined by energy-dispersive X-ray (EDX) analysis on a Hitachi S-2700 scanning electron microscope. X-ray powder patterns were collected on an Enraf-Nonius FR552 Guinier camera (Cu $K\alpha_1$ radiation; Si standard) and analyzed with the Filmscan and Jade 3.0 software packages.[7]

Single grey needle-shaped crystals of $La_{13}Ga_8Sb_{21}$ (Anal. (mol%): La 34(1), Ga 20(1), Sb 46(1)% (average of 2 analyses)) were isolated from a reaction of La, Ga, and Sb in the ratio 1:2:2. The sample was heated at 900 °C for 3 days, cooled slowly to 500 °C over 4 days, and then cooled to 20 °C over 12 h. Numerous attempts at various temperatures and stoichiometries to substitute other rare-earth metals for La in $La_{13}Ga_8Sb_{21}$ were unsuccessful. All of the syntheses resulted, not in the expected $La_{13}Ga_8Sb_{21}$-type phase, but in a different phase which was subsequently identified as the $Pr_{12}Ga_4Sb_{23}$-type, also crystallizing as grey needles. The single crystals of $Pr_{12}Ga_4Sb_{23}$ (Anal. (mol%): Pr 32(1), Ga 10(1), Sb 58(1)% (average of 4 analyses)) used in the structure determination were originally obtained from a reaction of Pr, Ga, and Sb in the ratio 13:8:21 at 1000 °C for 3 days, followed by cooling to 20 °C over 18 h. In contrast to the $La_{13}Ga_8Sb_{21}$-type phase, which could only be prepared with La, rare-earth substitution is possible in $RE_{12}Ga_4Sb_{23}$ (*RE* = La–Nd, Sm). Mixtures of the elements *RE*, Ga, and Sb in the stoichiometric ratio 12:4:23, heated as before, resulted in reasonably pure products. The powder patterns of $RE_{12}Ga_4Sb_{23}$ were indexed, and the orthorhombic

cell parameters refined with the use of the program POLSQ[8] are given in Table 2-1. The observed and calculated interplanar distances, as well as intensities determined using the program LAZY-PULVERIX,[9] are listed in Tables A-1 to A-5.

Structure Determination. Pre-screening of crystals of $La_{13}Ga_8Sb_{21}$ and $Pr_{12}Ga_4Sb_{23}$ was important because of their similar colour and habit. Preliminary cell parameters were obtained from Weissenberg photographs. Final cell parameters for $La_{13}Ga_8Sb_{21}$ and $Pr_{12}Ga_4Sb_{23}$ were determined from least-squares analysis of the setting angles of 1146 or 3256 reflections, respectively, centred on a Bruker P4/RA/SMART–1000 CCD system. Intensity data were collected at 22 °C using a combination of ϕ rotations (0.3°) and ω scans (0.3°) in the range $2° \leq 2\theta(Mo\ K\alpha) \leq 61°$ for $La_{13}Ga_8Sb_{21}$ and $2° \leq 2\theta(Mo\ K\alpha) \leq 66°$ for $Pr_{12}Ga_4Sb_{23}$. Crystal data and further details of the data collections are given in Table 2-2. All calculations were carried out using the SHELXTL (Version 5.1) package.[10] Conventional atomic scattering factors and anomalous dispersion corrections were used.[11] Intensity data were reduced and averaged, and face-indexed numerical absorption corrections were applied in XPREP. Initial atomic positions were located by direct methods using XS, and refinements were performed by least-squares methods using XL.

Weissenberg photographs of $La_{13}Ga_8Sb_{21}$ revealed hexagonal Laue symmetry $6/mmm$ and no systematic extinctions. Upper-level photographs exhibited six-fold rotational symmetry, ruling out trigonal space groups. On the basis of intensity statistics and the successful structure solution, the centrosymmetric space group $P6/mmm$ was chosen. Initial positions for all atoms of $La_{13}Ga_8Sb_{21}$, except Ga(2), were found by direct methods. A first refinement revealed considerable electron density at the site $\frac{1}{3}$, $\frac{2}{3}$, 0,

located at the centre of a La_6 trigonal prism and coordinated by three coplanar Sb atoms. This site was assigned to Ga, given the trigonal planar coordination geometry of the site and reasonable Ga–Sb and Ga–La bond lengths. In early refinements, the thermal ellipsoids for Ga(1) and Ga(2) were quite elongated along the c direction, suggesting that these sites should each be split into two positions. Shifting Ga(1) and Ga(2) off the x, y, ½ and x, y, 0 mirror planes, respectively, led to close Ga(1)–Ga(1) and Ga(2)–Ga(2) contacts (0.50 and 0.58 Å), which demand that the Ga(1) and Ga(2) positions each have a maximum occupancy of 50%. Reasonable, if still somewhat elongated, thermal ellipsoids resulted for both atoms. The possibility that the disorder in the Ga positions is a consequence of improper choice of space group was considered; however, the close Ga positions are also present when the structure was refined in lower symmetry space groups such as $P\bar{3}$.

A series of refinements allowing the occupancies of successive atoms to vary freely revealed partial occupancies of 86(1)%, 47.1(5)%, and 47.8(9)% for La(3), Ga(1) and Ga(2), respectively, and essentially full occupancy for all other atoms. The resulting formula is "$La_{12.85(1)}Ga_{7.56(6)}Sb_{21}$" (with Z = 1), which is close to the ideal formulation "$La_{13}Ga_8Sb_{21}$" and consistent with EDX analyses. The final refinement for $La_{13}Ga_8Sb_{21}$ led to reasonable values for the anisotropic displacement parameters and a featureless difference electron density map ($\Delta\rho_{max}$ = 3.80, $\Delta\rho_{min}$ = –2.59 e Å^{-3}).

Weissenberg photographs of $Pr_{12}Ga_4Sb_{23}$ displayed Laue symmetry mmm and systematic extinctions (hkl: $h + k + l = 2n + 1$) consistent with the orthorhombic space groups $Immm$, $Imm2$, $I222$ and $I2_12_12_1$. Intensity statistics and satisfactory averaging (R_{int} = 0.044) favoured the centrosymmetric space group $Immm$. Initial positions of all atoms

were found by direct methods followed by subsequent difference Fourier syntheses. Once all atomic positions, except for Ga(2), were found, a refinement assuming the ideal formula "$Pr_{12}Ga_4Sb_{23}$" proceeded satisfactorily. However, the difference Fourier map revealed a small amount of residual electron density ($\Delta\rho_{max} = 8.24$, $\Delta\rho_{min} = -2.56$ e $Å^{-3}$) at a site coordinated by a tetrahedron of Sb atoms (Sb(1) at 2.23(3) Å ($\times 2$), Sb(7) at 2.70(4) Å ($\times 2$)), analogous to the site partially occupied by Mn atoms in the related structure of La_6MnSb_{15}.[12] This site was assigned to Ga(2), on the basis of the reasonable Ga(2)–Sb(7) and Ga(2)–Pr(1) bond lengths. However, the short Ga(2)–Sb(1) distance precludes the Ga(2) and Sb(1) sites from being simultaneously occupied. The occupancies of Ga(2) and Sb(1) were thus refined with the constraint that their sum be 100% and with the restraint that the displacement parameters be approximately equal (with a standard deviation of 0.003 Å), given significant correlation in the refinement of parameters of closely spaced sites. Refinements in which the occupancies of successive atoms were allowed to vary resulted in essentially 100% occupancy for all atoms, except for Ga(1), Ga(2) and Sb(1), whose occupancies converged to 96.4(7)%, 2.7(2)%, and 97.3(2)%, respectively.

Alternatively, the Ga(2) site may conceivably be assigned to O, since the distance to the two closest Sb(1) atoms is reasonable for an Sb–O bond. Reasonable displacement parameters for O are obtained only if this site is partially occupied (~ 50%), giving a hypothetical "$Pr_{12}Ga_{3.9}Sb_{23}O$" structure which would have the O atom bridging two Sb atoms of a kinked square sheet. EDX analyses of several $RE_{12}Ga_4Sb_{23}$ crystals were inconclusive, giving variable O content (from 0 to ~ 10 %) likely arising from surface oxidation of the crystals. However, chemical arguments do not support this model;

although several antimonide oxides have been reported, the O atoms in these structures are coordinated to the electropositive metals, never to the more electronegative antimony atoms.[13]

If the original model is accepted, the final formula is "$Pr_{12}Ga_{3.98(1)}Sb_{22.90(1)}$" (with $Z = 2$), close to the ideal formula "$Pr_{12}Ga_4Sb_{23}$" and in excellent agreement with the elemental analysis. The final refinement led to a featureless electron density map ($\Delta\rho_{max}$ = 4.79, $\Delta\rho_{min}$ = −2.59 e $Å^{-3}$) and reasonable displacement parameters for all atoms, except Ga(1). The thermal ellipsoid of this site is somewhat elongated along a, suggesting that the Ga(1) atom may be tending to displace randomly slightly above or slightly below the mirror plane at 0, x, y, a situation similar, but less pronounced, to that discussed for $La_{13}Ga_8Sb_{21}$ above. Solution of the structure in the lower symmetry space group $I2mm$ led to a similar elongated thermal ellipsoid for Ga(1), rather than a single well-behaved site.

The atomic positions of $La_{13}Ga_8Sb_{21}$ and $Pr_{12}Ga_4Sb_{23}$ were standardized with the program STRUCTURE TIDY.[14] Final values of the positional and displacement parameters are given in Table 2-3, and the interatomic distances are listed in Table 2-4. Anisotropic displacement parameters are listed in Table A-6.

Results and Discussion

Structures. Examples of ternary rare-earth main-group element antimonides were previously limited to $REIn_{0.8}Sb_2$ and $RESn_{0.75}Sb_2$.[4,5] The RE–Ga–Sb system is particularly rich, yielding $La_{13}Ga_8Sb_{21}$ and $Pr_{12}Ga_4Sb_{23}$, which are new structure types, in addition to a REGaSb$_2$ phase, to be reported separately, which is analogous to the In and

Sn compounds.[15] The $La_{13}Ga_8Sb_{21}$ phase is distinctly more difficult to prepare than the $Pr_{12}Ga_4Sb_{23}$ phase, requiring an excess of Ga to succeed. There may be structural reasons, evident later, for why this phase could only be prepared for RE = La. In contrast, the competing $RE_{12}Ga_4Sb_{23}$ phase forms readily with diverse starting compositions and temperatures. A plot of the unit cell volume for $RE_{12}Ga_4Sb_{23}$ (RE = La–Nd, Sm) (Figure 2-1) shows a monotonic decrease consistent with the lanthanide contraction and a +3 oxidation state for RE in all cases.

As shown in Figures 2-2 and 2-3, respectively, the structures of $La_{13}Ga_8Sb_{21}$ (down the c axis) and $Pr_{12}Ga_4Sb_{23}$ (down the a axis) bear striking similarities and can be fruitfully discussed together. Both structures contain extended networks of Sb and Ga atoms forming large channels that are occupied by columns of face-sharing trigonal prisms of RE atoms. We discuss first the overall connectivity in these structures, and then consider in turn the coordination around the Sb, Ga, and RE atoms.

In $La_{13}Ga_8Sb_{21}$ (Figure 2-2), the channels are outlined by 21-membered rings which are formed by five-atom-wide ribbons of Sb atoms (Sb(2)–Sb(3)–Sb(4)–Sb(3)–Sb(2)) that are bordered by Ga(1) atoms and linked by Ga(1)–Ga(1) bonds. The Ga(1)–Ga(1) bonds result in puckered Ga_6 rings which sandwich La(3) atoms at the origin of the unit cell. Four trigonal prisms whose vertices are La(1) and La(2) atoms share rectangular faces to form a larger triangular assembly residing within the channels. The three outer trigonal prisms are filled by Sb(1) atoms, while the central prism is filled by a Ga(2) atom, generating trigonal planar $GaSb_3$ units. These trigonal prismatic columnar assemblies $^1_\infty[La_6GaSb_3]$ extend along the c direction such that they are in

registry with each other in adjacent channels, the La atoms being positioned directly across from each other on opposite sides of common square faces within the Sb ribbons.

The change from the hexagonal symmetry of $La_{13}Ga_8Sb_{21}$ (Figure 2-2) to the pseudohexagonal orthorhombic symmetry of $Pr_{12}Ga_4Sb_{23}$ (Figure 2-3) results from a loss of equivalence in the three Ga/Sb segments that together outline the anionic channels, as shown in Figure 2-4. The channels within $Pr_{12}Ga_4Sb_{23}$ are also enclosed by 21 atoms, but now they are built up from isolated five-atom-wide Sb ribbons (Sb(7)–Sb(6)–Sb(8)–Sb(6)–Sb(7)) and six-atom-wide Sb ribbons (Sb(1)–Sb(4)–Sb(3)–Sb(3)–Sb(4)–Sb(1)) that are connected by Ga(3) atoms. The five-atom-wide Sb ribbons are parallel to (001) and the six-atom-wide Sb ribbons are approximately parallel to (011) or (01$\bar{1}$). The topological transformation involves taking the Ga atoms that border one of the five-atom-wide Sb ribbons in $La_{13}Ga_8Sb_{21}$ (Figure 2-4a) and twisting them outwards to form the isolated five-atom-wide Sb ribbons in $Pr_{12}Ga_4Sb_{23}$ (Figure 2-4b). Note that Ga atoms are also replaced by Sb atoms to form the six-atom-wide Sb ribbons in $Pr_{12}Ga_4Sb_{23}$. Another way to consider the channel-defining substructure in $Pr_{12}Ga_4Sb_{23}$ is through the stacking of strongly kinked two-dimensional Sb square sheets perpendicular to the b direction; where the folds occur to produce the kinks, Sb atoms are replaced by Ga atoms. The kinked sheets are then linked by Ga(3)–Ga(3) bonding, completing large channels. In $Pr_{12}Ga_4Sb_{23}$, Ga_2 pairs occur, in contrast to the Ga_6 rings in $La_{13}Ga_8Sb_{21}$. Isolated five-atom-wide ribbons divide the large channels into smaller 21-atom channels.

The channels of $Pr_{12}Ga_4Sb_{23}$ enclose columns of four trigonal prisms that have Pr atoms (Pr(1), Pr(2), Pr(3), Pr(4)) at their vertices and that are grouped together in the same manner as in $La_{13}Ga_8Sb_{21}$. Likewise, the Pr_6 trigonal prisms are filled by Ga(1),

Sb(5), and two Sb(2) atoms that together constitute trigonal planar GaSb$_3$ units. However, in Pr$_{12}$Ga$_4$Sb$_{23}$, the $^1_\infty$[Pr$_6$GaSb$_3$] columnar assemblies in adjacent channels separated by the six-atom-wide Sb ribbons are shifted by half the unit cell length along a with respect to each other. Correspondingly, the Pr atoms on opposite sides of the kinked sheets are positioned in an alternating "checkerboard" fashion, an arrangement in which no two Pr atoms share the same square face. With respect to the isolated five-atom-wide Sb ribbon, adjacent $^1_\infty$[Pr$_6$GaSb$_3$] columnar assemblies remain in registry, and the Pr atoms are situated directly across from each other on opposite sides of square faces.

The one-dimensional five- or six-atom-wide Sb ribbons that enclose the channels in La$_{13}$Ga$_8$Sb$_{21}$ and Pr$_{12}$Ga$_4$Sb$_{23}$ may be viewed as segments cut from the infinite two-dimensional square nets of Sb atoms commonly found in many binary and ternary antimonides. Five-atom-wide Sb ribbons occur in both La$_{13}$Ga$_8$Sb$_{21}$ and Pr$_{12}$Ga$_4$Sb$_{23}$, but the Sb–Sb bonds follow a long-short-short-long pattern in La$_{13}$Ga$_8$Sb$_{21}$, while they are essentially identical in Pr$_{12}$Ga$_4$Sb$_{23}$ (Figure 2-5a). Six-atom-wide Sb ribbons occur in Pr$_{12}$Ga$_4$Sb$_{23}$, where the Sb–Sb bonds follow an alternating long-short-long-short-long pattern (Figure 2-5b). These Sb–Sb distances, which range from 3.0085(7) to 3.134(1) Å, are longer than the intralayer Sb–Sb bond length (2.908 Å) and shorter than the weakly bonding interlayer distance (3.355 Å) in elemental Sb.[16] Rather, they are comparable to the Sb–Sb distances occurring in the Sb square sheets in LaSb$_2$ (3.087–3.157 Å),[17] LaIn$_{0.8}$Sb$_2$ (3.119(3)–3.142(3) Å),[4] or LaZn$_{0.52}$Sb$_2$ (3.097(2) Å),[18] which have been interpreted as one-electron half-bonds.[4,5] Ga atoms are then located at the fringes of these five- or six-atom-wide Sb ribbons so that they may be considered to be the terminal atoms of 7- or 8-atom-wide ribbons, respectively. In the case of Pr$_{12}$Ga$_4$Sb$_{23}$, the Ga(2)

site is occupied to such a small extent (2.7(2)%) that the description of isolated five-atom-wide Sb ribbons made earlier is probably more useful, although for the purpose of comparison, the partially occupied Ga(2) sites are portrayed in Figure 2-5a.

In $La_{13}Ga_8Sb_{21}$, Ga(1) resides at a site that is 0.50 Å distant from a symmetry-equivalent position across a mirror plane, so that only one of these can be occupied locally. One short (2.766(7) Å) and one long (3.131(7) Å) Ga(1)–Sb(2) bond form (Figure 2-5a). Each Ga(1) atom is additionally coordinated to two other Ga(1) atoms of neighbouring ribbons to complete a distorted $Ga(Ga_2Sb_2)$ tetrahedron (Figure 2-6a). The shorter Ga(1)–Sb(2) distance is slightly greater than the Ga–Sb single bond distances observed in the isolated $GaSb_4^{9-}$ tetrahedra found in the Zintl phase $Na_3Sr_3GaSb_4$ (2.709(2)–2.752(5) Å)[2c] or in the corner-sharing $GaSb_4$ tetrahedra found in GaSb (2.64 Å).[19] However, the longer Ga(1)–Sb(2) distance must indicate a considerably weaker bonding interaction. Together, these two contacts may be viewed as a 3-centre-2-electron bond with unequal distribution of electron density between the three atoms. The Ga(1)–Ga(1) bonding that connects adjacent Sb ribbons results in a Ga_6 ring (Figure 2-8). It is assumed that the Ga_6 ring adopts a chair conformation (Ga–Ga–Ga 115.9(3)°) since this choice of local site occupation leads to intraring Ga(1)–Ga(1) distances of 2.422(5) Å, precluding the unreasonably shorter 2.371(4) Å distances that would occur in any other ring conformation. Even the 2.422(5) Å Ga(1)–Ga(1) distance is somewhat shorter than the Ga–Ga distances found in the intermetallic compounds GaTe (2.431(2)–2.437(3) Å),[20] $LaGa_2$ (2.494 Å),[21] and $Na_{22}Ga_{39}$ (2.435(7)–2.989(7) Å).[22] However, single Ga–Ga distances as short as 2.333(1) Å (in [(tBu)NCHCHN(tBu)]GaGa[(tBu)NCHCHN(tBu)])[23] have been observed in organometallic complexes. The occurrence of this unusually short

Ga–Ga bond may explain why the $La_{13}Ga_8Sb_{21}$ phase has only been found with the largest RE so far. Substitution of a smaller RE for La would contract the structure and shrink the $^1_\infty[RE_6GaSb_3]$ columnar assemblies to such an extent that the Ga–Ga bonds linking the Sb ribbons would become unreasonably short. In the $Pr_{12}Ga_4Sb_{23}$ structure, the Ga–Sb bonds at two corners of the channels have been broken, and only one Ga–Ga bond remains (Figure 2-4); the relaxed steric requirements permit a larger range of RE trigonal prism sizes within the channels.

In $Pr_{12}Ga_4Sb_{23}$, Ga(3) is bonded to four Sb(1) atoms at a distance of 2.9020(7) Å, which is longer than typical Ga–Sb single bonds in Zintl compounds,[2] but is consistent with a Ga–Sb half-bond, analogous to one-electron Sb–Sb bonds within square sheets. The Ga_2 pairs which link together kinked sheets are formed when Ga(3) bonds with a neighbouring Ga(3) atom at a distance of 2.586(4) Å, longer than that found in $La_{13}Ga_8Sb_{21}$, but comparable to typical values in other solid-state compounds ($e.g.$, 2.541(3) Å in $Na_2Ga_3Sb_3$).[2a] These coordinating atoms around Ga(3) thus complete a $Ga(GaSb_4)$ square pyramid, with Ga at the apical and Sb at the basal positions (Figure 2-6b). For comparison, a $GaGa_5$ square pyramidal coordination is encountered in binary $BaAl_4$-type gallide phases such as $BaGa_4$.[24] It has been proposed that, in $BaGa_4$, a full single bond forms to the apical Ga atom, but multicentre bonding takes place to the four basal Ga atoms in a $GaGa_5$ square pyramid, a bonding situation similar to the suggestion above for the $Ga(GaSb_4)$ square pyramid in $Pr_{12}Ga_4Sb_{23}$.[25-27]

Common to both $La_{13}Ga_8Sb_{21}$ and $Pr_{12}Ga_4Sb_{23}$ are the $GaSb_3$ units which result from filling the RE_6 trigonal prisms (Figures 2-2 and 2-3). Similarly filled four-prism assemblies are found in the Zintl compound Cs_6GaSb_3,[2d] while larger filled nine-prism

assemblies are found in $K_{10}Ga_3Sb_{6.33}$.[2c] The Ga–Sb bond distances of the $Ga(2)Sb(1)_3$ unit of $La_{13}Ga_8Sb_{21}$ (2.6200(16) Å) and the $Ga(1)Sb(2)_2Sb(5)$ unit of $Pr_{12}Ga_4Sb_{23}$ (2.6011(11)–2.620(2) Å) are comparable to those of the trigonal planar $GaSb_3^{6-}$ units found in Cs_6GaSb_3 (2.608(5)–2.676(5) Å)[2d] and of the cyclic $Ga_3Sb_6^{9-}$ anions found in $K_{20}Ga_6Sb_{12.66}$ (2.552(4)–2.632(4) Å).[2c] Three-coordinate Ga may seem unusual in other contexts, but does occur in many of the alkali or alkaline-earth metal gallium antimonides. Partial double-bond character has been invoked to explain the somewhat shorter Ga–Sb bonds in the trigonal planar $GaSb_3$ units of these compounds;[2c] however, it must be realized that the surrounding RE atoms will also no doubt exert strong matrix effects. Unlike the anions in these Zintl compounds which are rigorously planar, the Ga atoms of the $GaSb_3$ units in $La_{13}Ga_8Sb_{21}$ and $Pr_{12}Ga_4Sb_{23}$ are shifted slightly above or below the plane of the Sb atoms. Two close Ga(2) positions, each approximately 0.3 Å off the plane of the Sb atoms, are resolved in $La_{13}Ga_8Sb_{21}$, while in $Pr_{12}Ga_4Sb_{23}$, this tendency toward pyramidalization is expressed as an elongated Ga(1) thermal ellipsoid. Such behaviour may imply that additional electron density is localized at the Ga centres in question.

The RE atoms at the vertices of the trigonal prisms share similar coordination numbers (CN 9 or 10) and environments in both $La_{13}Ga_8Sb_{21}$ and $Pr_{12}Ga_4Sb_{23}$. As is typical in ternary rare-earth antimonides containing Sb square sheets, the RE atoms reside at the centres of capped square antiprisms.[4,5,12,17,18] With a–h designating the eight corners of a square antiprism, two additional coordinating sites i and j are found, either both capping the same square face (Figure 2-7a), or one capping a square face and another capping a triangular face of the square antiprism (Figure 2-7b). The RE

environments then differ in the placement and identity of coordinating atoms. In the first type of arrangement, which applies to La(1) in $La_{13}Ga_8Sb_{21}$ and to Pr(2) and Pr(3) in $Pr_{12}Ga_4Sb_{23}$, two Ga atoms cap one square face of a square antiprism of Sb atoms. The Ga sites around La(1) are split in a manner reminiscent of the situation in $LaSn_{0.75}Sb_2$, where the capping Sn atom can reside in several closely-spaced partially occupied sites.[5] In the second type of arrangement, atoms from a Ga_2 pair occupy sites **h** and **i**, forcing an Sb atom to occupy the capping site **j** in the square antiprisms around La(2) in $La_{13}Ga_8Sb_{21}$ and Pr(4) in $Pr_{12}Ga_4Sb_{23}$. In the case of Pr(1), **h** and **i** are too close for them to be occupied simultaneously by Sb and Ga, respectively; if site **i** is ignored, then the commonly observed nine-coordinate monocapped square antiprism of Sb atoms results. The *RE*–Sb and *RE*–Ga distances (Table 2-4) in both structures are reasonable when compared with those found in the binary compounds $LaSb_2$ (3.183–3.432 Å),[17] $PrSb_2$ (3.151–3.377 Å),[28] $LaGa_2$ (3.335 Å),[21] and $PrGa_2$ (3.278 Å).[29]

The coordination environment of La(3), which is sandwiched between Ga_6 rings at the origin of the unit cell in $La_{13}Ga_8Sb_{21}$, is quite different from the square antiprismatic geometries of the other *RE* atoms in the structure. Each La(3) atom is coordinated by twelve Ga(1) atoms of two puckered Ga_6 rings, six at the short distance of 3.051(6) Å, and six at the longer distance of 3.386(7) Å (Figure 2-8). Assuming that the Ga_6 rings adopt a chair conformation, two possibilities exist for the local coordination geometry of La(3). The puckered rings may be parallel, with all inter-ring Ga(1)–Ga(1) distances being 4.338(9) Å; this arrangement is similar to that found in the $CeCd_2$ structure type adopted by Gd_5CuGa_9.[30] Alternatively, the rings may be inverted with respect to one another, in such a manner that three short (3.843(8) Å) and three long

inter-ring Ga(1)–Ga(1) distances result. Although this relative ring orientation resembles that between the puckered 6^3 layers of the $CaIn_2$ structure type, the shortest inter-ring Ga(1)–Ga(1) distance is much longer than the bonding interlayer Ga–Ga distance of 2.961 Å found in $CaIn_2$-type $YbGa_2$.[31] It is unclear whether the disorder results from a random occupation of the Ga(1) sites without any preferred relative ring orientation, or whether local ordering exists along each 6-fold axis (with the Ga_6 rings all either parallel or inverted) and the disorder results from the random distribution of these axes.

Bonding. The variety of main-group element substructures present in these rare-earth gallium antimonides, absent in the alkali or alkaline-earth gallium antimonides, is remarkable. It is of interest to see how far the Zintl concept can be used to account for these complex substructures, especially given the presence of non-classical bonding patterns such as the Sb ribbons. Inherent in the Zintl concept is the assumption that full electron transfer takes place from the electropositive to the electronegative elements, but it would be thought that this is rendered less applicable because of the reduced electronegativity differences between rare-earth and main-group elements (compared to electronegativity differences between alkali or alkaline-earth elements and main-group elements).

Assuming, then, that the rare-earth atoms adopt a +3 oxidation state, the donated electrons contribute to the formation of bonds in the remaining framework, giving the formulations $(La^{3+})_{13}[Ga_8Sb_{21}]^{39-}$ and $(Pr^{3+})_{12}[Ga_4Sb_{23}]^{36-}$. The ambiguity lies in the valence state of the Ga atoms, so we will satisfy closed-shell requirements for the more electronegative Sb atoms first. Any electrons that remain once the Sb octets have been satisfied may then be used by the Ga atoms, either as lone pairs, or for homoatomic

Ga–Ga bonding. Three types of Sb atoms are present in both structures: isolated Sb^{3-} atoms centring the RE_6 trigonal prisms, interior Sb^{1-} atoms participating in four Sb–Sb half-bonds within the ribbons, and terminal Sb^{2-} atoms participating in only two Sb–Sb half-bonds at the ribbon edges. The idea of weak one-electron Sb–Sb bonds has now gained acceptance and is supported on firm theoretical grounding.[3–5,32] As shown earlier in Figure 2-5, there is some distortion of the Sb atoms away from ideal square planar geometries. A similar, but more asymmetrical, pattern is observed in the narrower three-atom-wide Sb ribbons found in La_6MnSb_{15}, and has been traced to a second-order Peierls distortion.[3,12] It is likely that a similar electronic driving force is responsible for the distortions of the five- and six-atom-wide Sb ribbons in $La_{13}Ga_8Sb_{21}$ and $Pr_{12}Ga_4Sb_{23}$, although understanding the more complicated patterns found here will require a more detailed analysis.

In our electron counting exercise, we now arrive at the formulations $[(La^{3+})_{13}(Ga^0)_8(Sb^{3-})_6(Sb^{2-})_6(Sb^{1-})_9]$ and $[(Pr^{3+})_{12}(Ga^{1.25+})_4(Sb^{3-})_6(Sb^{2-})_6(Sb^{1-})_{11}]$. In the case of $La_{13}Ga_8Sb_{21}$, the Ga atoms of $La_{13}Ga_8Sb_{21}$ must have an oxidation state of 0, on average, in order to maintain charge balance. This implies that 24 electrons (3 electrons/Ga atom × 8 Ga atoms) are distributed over the six Ga(1) and two Ga(2) atoms per formula unit. Twelve of these electrons are used to form the six single bonds of the Ga(1)$_6$ rings. For the problem of localizing the twelve remaining electrons (or 1.5 electrons/Ga atom), perhaps some provocative suggestions can be made. The Ga–Ga distance within the Ga(1)$_6$ rings is short (2.422(5) Å) and is comparable to the value of 2.420(1) Å found in $[(^tBu_3Si)_2GaGa(Si^tBu_3)]$ or 2.441(1) Å found in the cyclic molecule $[\{(Mes_2C_6H_3)Ga\}_3]^{2-}$, where formal Ga–Ga bond orders of 1.5 and 1.33, respectively, are

proposed and partial π overlap is presumably involved.[33–35] Equally, π overlap may be involved in the Ga–Sb bonds of the trigonal planar $GaSb_3$ units.[2c] As well, the tetrahedral or trigonal planar coordination geometries of Ga(1) and Ga(2), respectively, are both distorted in a manner that could indicate the stereochemical activity of a lone pair of electrons. Lastly, further reduction of the Sb ribbons is possible without severe structural consequences, since the square nets from which they are excised can act as electron "sinks,"[36] effectively allowing Sb–Sb bond orders that need not be exactly 0.5.

In the case of $Pr_{12}Ga_4Sb_{23}$, the Ga atoms must have an average oxidation state of +1.25. Seven electrons (1.75 electrons/Ga atom $\times$ 4 Ga atoms) are distributed over the two Ga(1) and two Ga(3) atoms per formula unit. Two of these electrons form the Ga(3)–Ga(3) single bond that links the kinked Sb sheets. Five electrons (1.25 electrons/Ga atom) remain. As in the case of $La_{13}Ga_8Sb_{21}$, the distribution of these remaining electrons, whether localized on Ga(1) and Ga(3), or participating in further orbital overlap, cannot be determined conclusively at this stage. It is hoped that electronic band structure calculations will clarify this picture. However, extrapolating from the electronic structure of the related La_6MnSb_{15}, where kinked Sb square sheets are also found, leads to a simple explanation for why the corresponding sheets in $Pr_{12}Ga_4Sb_{23}$ are kinked only where Ga has been substituted for Sb.[3] Atoms residing at the kinked sites have some degree of s-p hybridization. Since lighter elements undergo such hybridization more readily than heavier elements (the usually cited reason of closer energetic separation of s and p orbitals is disputable),[35,37] it is not surprising that the Ga atoms are the ones occupying the kinked sites instead of Sb atoms in the square sheets.

Structural Relationships. Superficially, the structures of $La_{13}Ga_8Sb_{21}$ and $Pr_{12}Ga_4Sb_{23}$ resemble the hexagonal structures of a large family of metal-rich compounds, generally phosphides and silicides, composed of differently sized triangular groupings of trigonal prisms.[38-40] The $Ho_6Ni_{20}P_{13}$ structure $(P6_3/m)$[41] and its antitype $Ba_{0.8}Hf_{12}As_{17.7}$ $(P6_3/m)$[6] are most similar to $La_{13}Ga_8Sb_{21}$ and $Pr_{12}Ga_4Sb_{23}$: all four structures contain four-prism-large triangular assemblies of trigonal prisms separated by ribbons cut from square nets. Generally, metal–metal bonding networks predominate in compounds such as $Ho_6Ni_{20}P_{13}$,[41] but in $La_{13}Ga_8Sb_{21}$ and $Pr_{12}Ga_4Sb_{23}$ we see the emergence of inversely-related structures, first recognized in $Ba_{0.8}Hf_{12}As_{17.7}$, in which metalloid–metalloid (As–As or Sb–Sb) bonding is a prominent feature.[6]

There exists a simpler structure, $Cs_6SnAs_3O_{0.5}$, in which assemblies of four trigonal prisms appear (Figure 2-9a).[42] In $Ba_{0.8}Hf_{12}As_{17.7}$ (Figure 2-9b) and $La_{13}Ga_8Sb_{21}$ (Figure 2-9c), however, extended hexagonal channel networks of As–As or Sb–Sb bonds, respectively, separate the trigonal prism assemblies. In $Ba_{0.8}Hf_{12}As_{17.7}$, six-atom-wide ribbons of As atoms form 18-atom channels that enclose assemblies of Hf_6 trigonal prisms, the outermost ones being filled by As atoms and the central one vacant. The effect of the 6_3 screw axes present in $Ba_{0.8}Hf_{12}As_{17.7}$ is to translate neighbouring columnar assemblies of Hf_6 trigonal prisms by $c/2$ along the column axis with respect to one another. Likewise, the As ribbons are also mutually displaced. In $La_{13}Ga_8Sb_{21}$, seven-atom-wide ribbons composed of Sb and Ga separate triangular groupings of larger La_6 prisms. In contrast to $Ba_{0.8}Hf_{12}As_{17.7}$, the structure of $La_{13}Ga_8Sb_{21}$ does not contain a 6_3 axis and, consequently, there is no mutual displacement of the Ga/Sb ribbons. This arrangement of the ribbons results in a near-planar Ga_6 ring around each corner of the

unit cell. It also forces the La atoms on either side of the ribbons to share the same square face of atoms, preventing any translation of the assemblies of trigonal prisms relative to one another.

The structure of $Pr_{12}Ga_4Sb_{23}$ is more closely related to the La_6MnSb_{15} structure type adopted by RE_6MSb_{15} (RE = La, Ce; M = Mn, Cu, Zn).[12] The single-prism columns of La_6 trigonal prisms that are filled by isolated Sb atoms in La_6MnSb_{15} (Figure 2-10a) are replaced by larger four-prism triangular groupings in $Pr_{12}Ga_4Sb_{23}$ (Figure 2-10b). A corresponding enlargement of the pseudohexagonal channels surrounding the column of trigonal prisms in La_6MnSb_{15} also takes place. The two-dimensional Sb sheets of La_6MnSb_{15} are folded at every fifth diagonal to allow intersheet Sb–Sb bonding, while in $Pr_{12}Ga_4Sb_{23}$, kinks in the sheets occur along every seventh diagonal, where Ga atoms replace Sb atoms. The three-atom-wide Sb ribbons in La_6MnSb_{15} (drawn isolated in Figure 2-10a) are replaced by five-atom-wide Sb ribbons in $Pr_{12}Ga_4Sb_{23}$. In La_6MnSb_{15}, there are Mn atoms at 50% occupancy in sites at the edge of the isolated Sb strip, but in $Pr_{12}Ga_4Sb_{23}$, these sites remain essentially vacant (2.7(2)% Ga). In the same manner that the hexagonal metal-rich structures such as $Ho_6Ni_{20}P_{13}$ can be regarded as belonging to a homologous series with increasingly larger triangular assemblies of trigonal prisms,[41] it is evident that La_6MnSb_{15} and $Pr_{12}Ga_4Sb_{23}$ form the first two members of a series of pseudohexagonal orthorhombic metalloid-rich structures, with the general formula $(RE)_{(n+1)(n+2)}(A)_{n(n-1)+2}(Sb)_{n(n+7)+5}$. Neglecting the partially occupied Mn site and recognizing that an Sb_2 pair in La_6MnSb_{15} takes the place of the Ga_2 pair in $Pr_{12}Ga_4Sb_{23}$, we can rewrite the formula of the n = 1 member as $RE_6A_2Sb_{13}$, where A = Sb. The n = 2 member is $RE_{12}A_4Sb_{23}$, exemplified by $Pr_{12}Ga_4Sb_{23}$. It would seem worthwhile, then, to

attempt the syntheses of "$RE_6Ga_2Sb_{13}$" ($n = 1$) or "$RE_{20}Ga_8Sb_{35}$" ($n = 3$), although the small increments in the stoichiometric ratios and similar predicted X-ray diffraction patterns will make this a challenging task. Equally worthwhile would be to attempt substitutions of Ga with another main-group element, such as Al, Si, or Ge.

Table 2-1. Cell parameters for ternary $RE_{12}Ga_4Sb_{23}$ compounds.

Compound	a (Å)	b (Å)	c (Å)	V (Å^3)
$La_{12}Ga_4Sb_{23}$	4.344(2)	19.750(7)	26.860(11)	2305(1)
$Ce_{12}Ga_4Sb_{23}$	4.308(2)	19.509(9)	26.667(12)	2241(1)
$Pr_{12}Ga_4Sb_{23}$	4.283(3)	19.394(10)	26.553(16)	2206(1)
$Nd_{12}Ga_4Sb_{23}$	4.268(1)	19.308(6)	26.425(8)	2177.6(8)
$Sm_{12}Ga_4Sb_{23}$	4.213(3)	19.120(10)	26.099(15)	2103(1)

Table 2-2. Crystallographic data for $La_{13}Ga_8Sb_{21}$ and $Pr_{12}Ga_4Sb_{23}$.

Formula	$La_{12.85(1)}Ga_{7.56(6)}Sb_{21}$	$Pr_{12}Ga_{3.98(1)}Sb_{22.90(1)}$
Formula mass (amu)	4868.83	4756.48
Space group	D_{6h}^1-P6/mmm (No. 191)	$D_{2h}^{25}-Immm$ (No. 71)
a (Å)	17.657(2) [a]	4.2612(3) [b]
b (Å)	17.657(2) [a]	19.4070(13) [b]
c (Å)	4.3378(7) [a]	26.3972(18) [b]
V (Å^3)	1171.2(3)	2183.0(3)
Z	1	2
T (°C)	22	22
Diffractometer	Bruker P4/RA/SMART–1000 CCD	Bruker P4/RA/SMART–1000 CCD
ρ_{calc} (g cm^{-3})	6.903	7.236
Crystal dimensions (mm)	Needle, $0.10 \times 0.01 \times 0.01$	Needle, $0.410 \times 0.004 \times 0.002$
Radiation	Graphite-monochromated Mo $K\alpha$, $\lambda = 0.71073$ Å	Graphite-monochromated Mo $K\alpha$, $\lambda = 0.71073$ Å
μ(Mo $K\alpha$) (cm^{-1})	275.41	293.79
Transmission factors [c]	0.6457–0.8095	0.8733–0.9220
Scan type	Mixture of ϕ rotations (0.3°) and ω scans (0.3°)	Mixture of ϕ rotations (0.3°) and ω scans (0.3°)
2θ limits	$2° \le 2\theta$(Mo $K\alpha$) $\le 61°$	$2° \le 2\theta$(Mo $K\alpha$) $\le 66°$
Data collected	$-23 \le h \le 22, -22 \le k \le 23, -5 \le l \le 2$	$-2 \le h \le 6, -28 \le k \le 29, -39 \le l \le 39$
No. of data collected	7046	9014
No. of unique data, including $F_o^2 < 0$	671 ($R_{int} = 0.110$)	2178 ($R_{int} = 0.044$)
No. of unique data, with $F_o^2 > 2\sigma(F_o^2)$	404	1554
No. of variables [d]	39	75 (6 restraints)
$R(F)$ for $F_o^2 > 2\sigma(F_o^2)$ [e]	0.034	0.030
$R_w(F_o^2)$ [f]	0.085	0.072
Goodness of fit [g]	0.92	0.98
$\Delta\rho_{max}, \Delta\rho_{min}$ (e Å^{-3})	3.8, -2.6	4.8, -2.6

Table 2-2. Crystallographic data for $La_{13}Ga_8Sb_{21}$ and $Pr_{12}Ga_4Sb_{23}$ (continued).

[a] Obtained from a refinement constrained so that $a = b$, $\alpha = \beta = 90°$, and $\gamma = 120°$.

[b] Obtained from a refinement constrained so that $\alpha = \beta = \gamma = 90°$.

[c] A numerical face-indexed absorption correction was applied, with the use of programs in the SHELXTL package (Sheldrick, G. M. *SHELXTL Version 5.1*; Bruker Analytical X-ray Systems: Madison, WI, 1997).

[d] Including an extinction coefficient.

[e] $R(F) = \Sigma \left\| F_o \right| - \left| F_c \right\| / \Sigma \left| F_o \right|$.

[f] $R_w(F_o^2) = \left[\Sigma \left[w(F_o^2 - F_c^2)^2 \right] / \Sigma wF_o^4 \right]^{1/2}$; $w^{-1} = \left[\sigma^2(F_o^2) + (aP)^2 + bP \right]$ where $P = \left[\max(F_o^2, 0) + 2F_c^2 \right] / 3$. For $La_{13}Ga_8Sb_{21}$, $a = 0.0389$, $b = 0.0000$; for $Pr_{12}Ga_4Sb_{23}$, $a = 0.0302$, $b = 0.0000$.

[g] $GooF = \left[\Sigma \left[w(F_o^2 - F_c^2)^2 \right] / (n - p) \right]^{1/2}$ where n is the number of reflections and p is the total number of parameters refined.

Table 2-3. Positional and equivalent isotropic displacement parameters for $La_{13}Ga_8Sb_{21}$ and $Pr_{12}Ga_4Sb_{23}$.

Atom	Wyckoff position	Occupancy	x	y	z	U_{eq} (Å^2) [a]
			$La_{13}Ga_8Sb_{21}$			
La(1)	6m	1	0.58274(4)	0.16547(8)	1/2	0.0073(3)
La(2)	6m	1	0.16800(4)	0.33600(7)	1/2	0.0079(3)
La(3)	1a	0.859(13)	0	0	0	0.0229(14)
Ga(1)	12n	0.471(5)	0.1343(2)	0	0.443(2)	0.030(3)
Ga(2)	4h	0.478(9)	1/3	2/3	0.0663(11)	0.011(2)
Sb(1)	6l	1	0.24818(5)	0.49636(10)	0	0.0086(3)
Sb(2)	6j	1	0.24697(7)	0	0	0.0102(3)
Sb(3)	6k	1	0.37508(8)	0	1/2	0.0167(4)
Sb(4)	3f	1	1/2	0	0	0.0088(4)
			$Pr_{12}Ga_4Sb_{23}$			
Pr(1)	8l	1	0	0.27695(3)	0.40559(2)	0.00798(12)
Pr(2)	8l	1	0	0.38900(3)	0.26312(2)	0.00777(11)
Pr(3)	4j	1	1/2	0	0.09340(3)	0.00822(15)
Pr(4)	4j	1	1/2	0	0.38118(3)	0.00953(15)
Ga(1)	4i	0.964(7)	0	0	0.18986(7)	0.0225(6)
Ga(2)	4h	0.027(2)	0	0.181(3)	1/2	0.0126(17)
Ga(3)	4g	1	0	0.43337(9)	0	0.0134(3)
Sb(1)	8l	0.973(2)	0	0.11138(4)	0.43300(3)	0.01520(19)
Sb(2)	8l	1	0	0.11584(3)	0.14030(2)	0.00912(13)
Sb(3)	8l	1	0	0.22151(3)	0.28669(2)	0.00875(13)
Sb(4)	8l	1	0	0.33456(3)	0.14421(2)	0.00908(14)
Sb(5)	4i	1	0	0	0.28911(3)	0.00957(18)
Sb(6)	4h	1	0	0.38335(5)	1/2	0.01313(19)
Sb(7)	4g	1	0	0.23336(5)	0	0.01133(19)
Sb(8)	2a	1	0	0	0	0.0088(2)

[a] U_{eq} is defined as one-third of the trace of the orthogonalized U_{ij} tensor.

Table 2-4. Selected interatomic distances (Å) in $La_{13}Ga_8Sb_{21}$ and $Pr_{12}Ga_4Sb_{23}$.

$La_{13}Ga_8Sb_{21}$			
La(1)–Ga(2)	3.182(3) (×2)	La(3)–Ga(1)	3.051(6) (×6)
La(1)–Sb(4)	3.3326(9) (×2)	La(3)–Ga(1)	3.386(7) (×6)
La(1)–Sb(3)	3.3567(14) (×2)	Ga(1)–Ga(1)	2.422(5) (×2)
La(1)–Sb(1)	3.3749(8) (×4)	Ga(1)–Sb(2)	2.766(7)
La(2)–Sb(1)	3.2737(15) (×2)	Ga(1)–Sb(2)	3.131(7)
La(2)–Ga(1)	3.314(3) (×2)	Ga(2)–Sb(1)	2.6200(16) (×3)
La(2)–Sb(2)	3.3632(6) (×4)	Sb(2)–Sb(3)	3.1338(14) (×2)
La(2)–Sb(3)	3.3648(11) (×2)	Sb(3)–Sb(4)	3.0934(11) (×2)

$Pr_{12}Ga_4Sb_{23}$			
Pr(1)–Ga(2)	3.11(3)	Pr(4)–Ga(3)	3.3925(10) (×2)
Pr(1)–Sb(2)	3.2150(6) (×2)	Pr(4)–Sb(5)	3.2322(9) (×2)
Pr(1)–Sb(6)	3.2365(8)	Pr(4)–Sb(4)	3.2800(7) (×2)
Pr(1)–Sb(7)	3.2849(4) (×2)	Pr(4)–Sb(1)	3.3290(7) (×4)
Pr(1)–Sb(1)	3.2936(9)	Ga(1)–Sb(2)	2.6011(11) (×2)
Pr(1)–Sb(4)	3.3091(6) (×2)	Ga(1)–Sb(5)	2.620(2)
Pr(1)–Sb(3)	3.3180(8)	Ga(2)–Sb(7)	2.70(4) (×2)
Pr(2)–Ga(1)	3.2743(8) (×2)	Ga(3)–Ga(3)	2.586(4)
Pr(2)–Sb(3)	3.2966(7) (×2)	Ga(3)–Sb(1)	2.9020(7) (×4)
Pr(2)–Sb(3)	3.3095(8)	Sb(1)–Sb(4)	3.1296(7) (×2)
Pr(2)–Sb(4)	3.3119(8)	Sb(3)–Sb(4)	3.0085(7) (×2)
Pr(2)–Sb(2)	3.3239(7) (×2)	Sb(3)–Sb(3)	3.0844(9) (×2)
Pr(2)–Sb(5)	3.3287(6) (×2)	Sb(6)–Sb(8)	3.1088(7) (×2)
Pr(3)–Ga(1)	3.3201(15) (×2)	Sb(6)–Sb(7)	3.1095(10) (×2)
Pr(3)–Sb(8)	3.2585(6) (×2)		
Pr(3)–Sb(2)	3.3356(6) (×4)		
Pr(3)–Sb(6)	3.3472(9) (×2)		
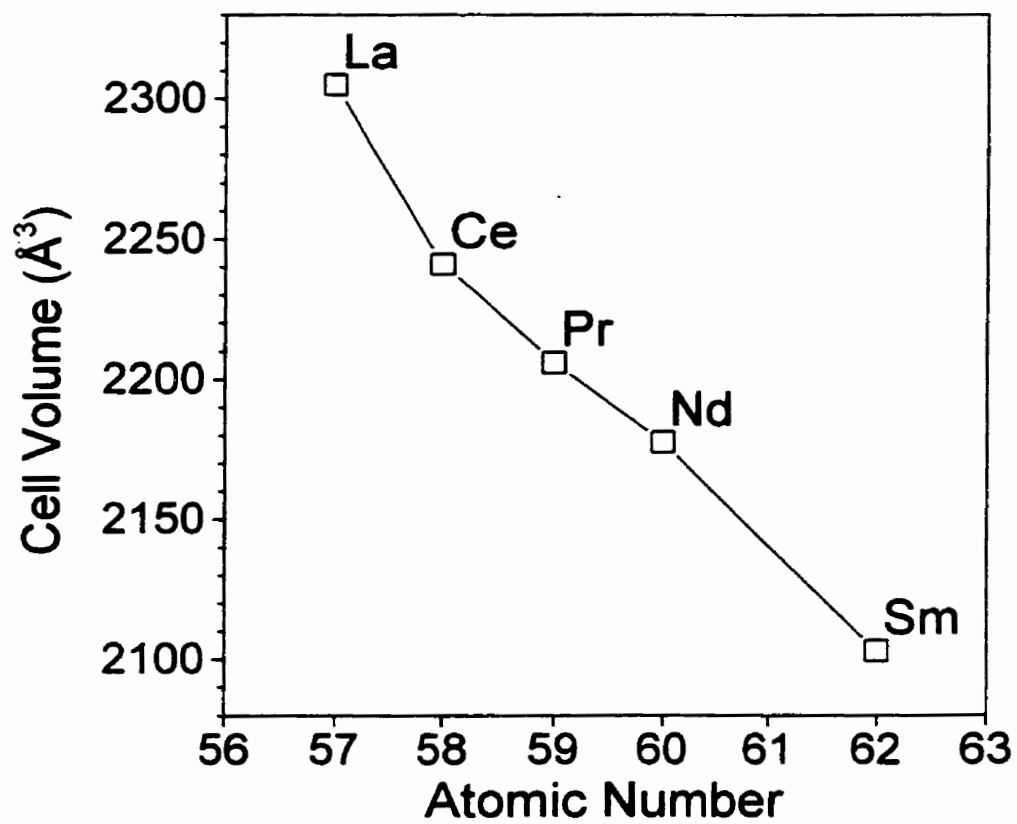
Figure 2-1. Plot of unit cell volume for $RE_{12}Ga_4Sb_{23}$ compounds. The lines are drawn only for guidance.
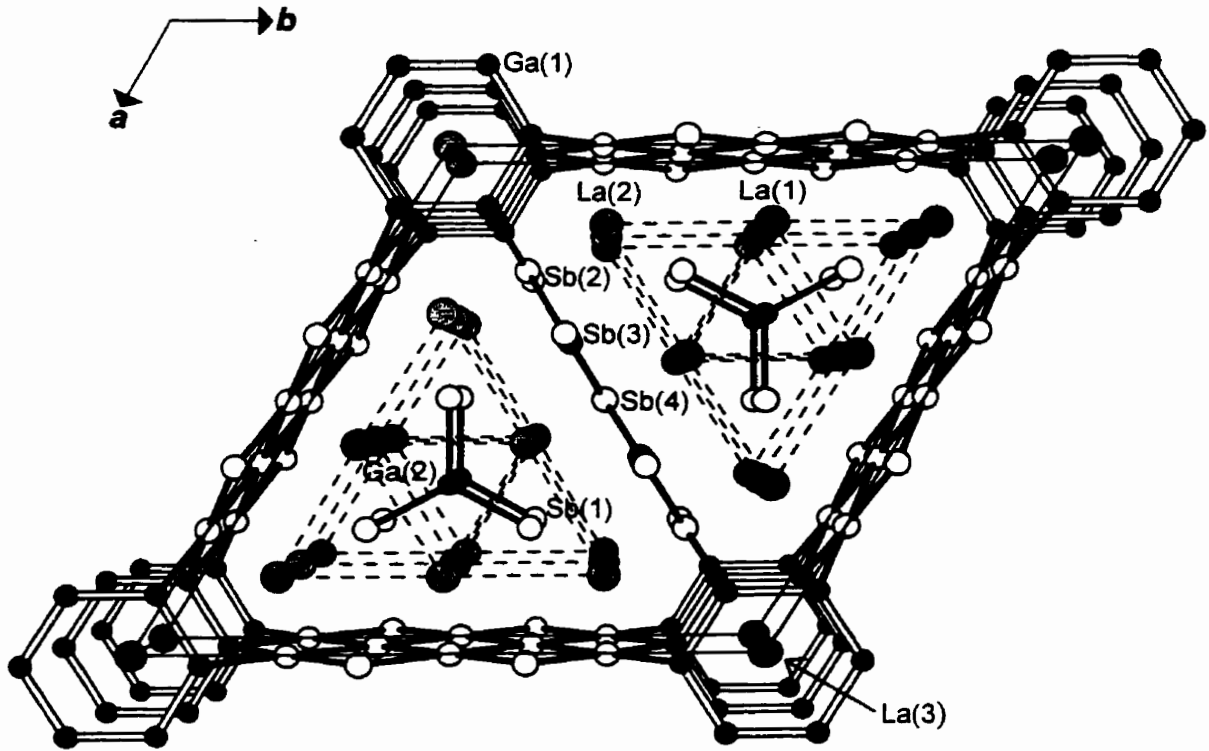
Figure 2-2. View of $La_{13}Ga_8Sb_{21}$ down the c axis showing the unit cell outline and the labelling scheme. The large lightly shaded circles are La atoms, the small solid circles are Ga atoms, and the medium open circles are Sb atoms. The dashed lines merely outline the assemblies of La_6 trigonal prisms.

Figure 2-3. View of $Pr_{12}Ga_4Sb_{23}$ down the a axis showing the unit cell outline and the labelling scheme. The large lightly shaded circles are Pr atoms, the small solid circles are Ga atoms, and the medium open circles are Sb atoms. The dashed lines merely outline the assemblies of Pr_6 trigonal prisms.
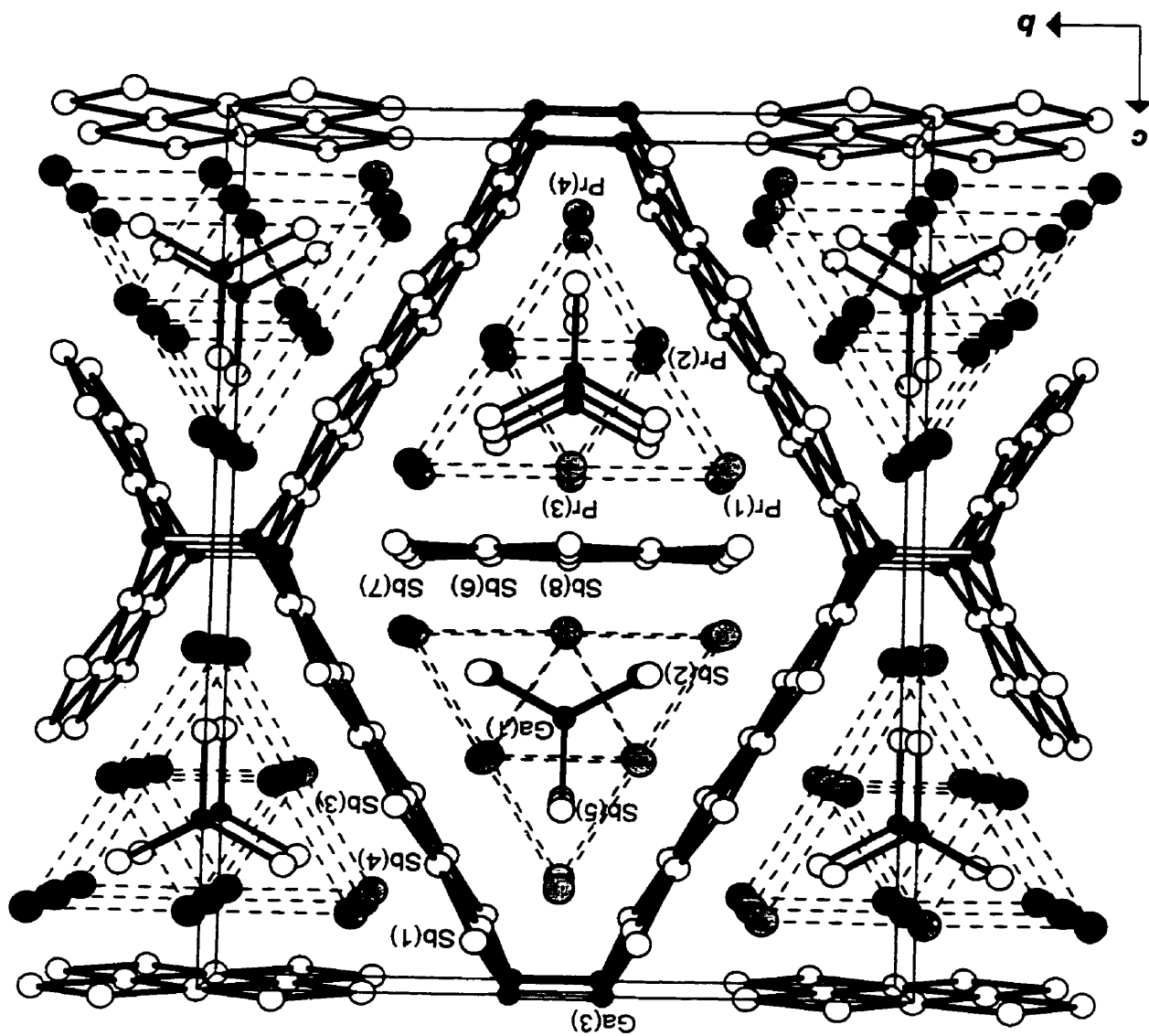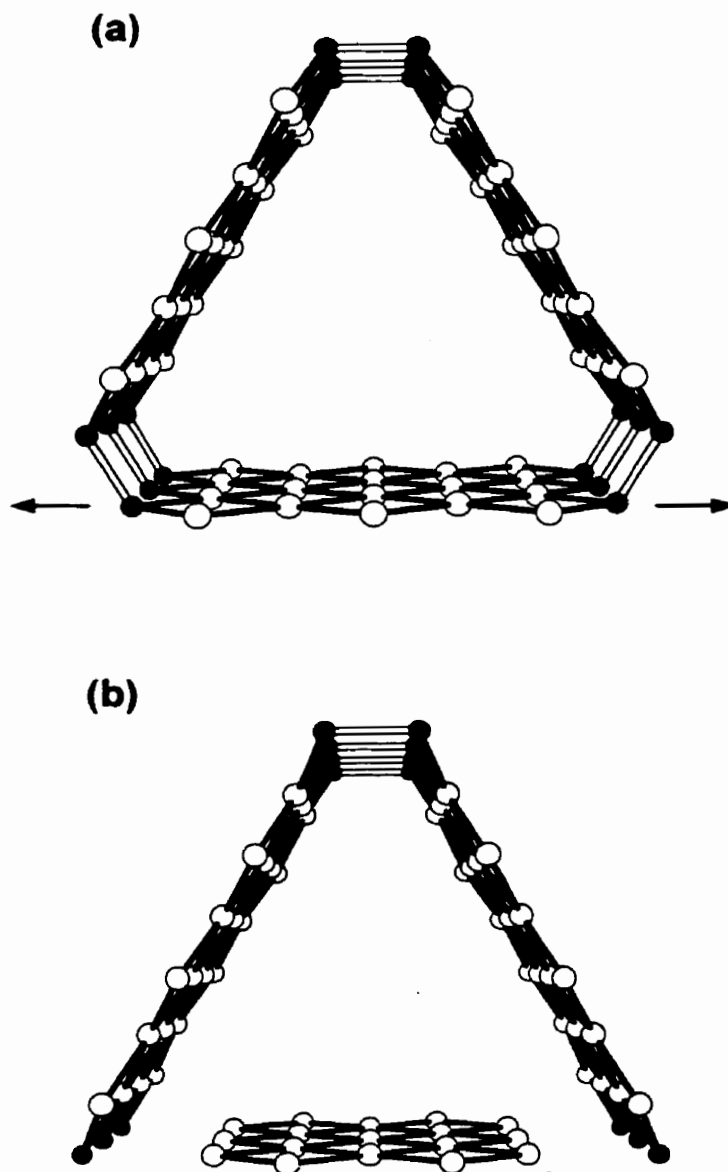
Figure 2-4. Comparison of the 21-atom channels in (a) $La_{13}Ga_8Sb_{21}$, composed of five-atom-wide Sb ribbons and (b) $Pr_{12}Ga_4Sb_{23}$, composed of two six-atom-wide Sb ribbons and one five-atom-wide Sb ribbon. These Sb ribbons are linked by Ga atoms.

(a) La$_{13}$Ga$_8$Sb$_{21}$
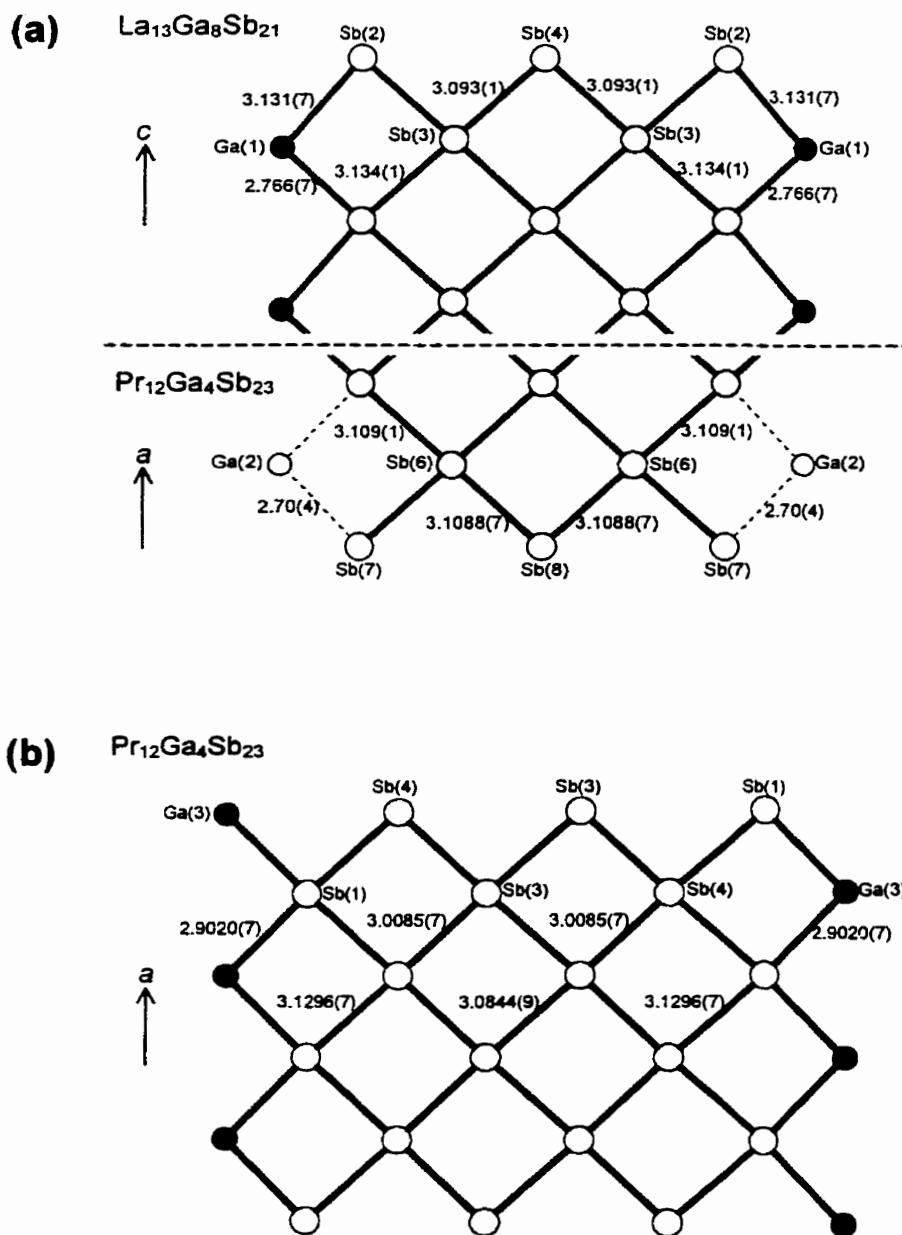
(b) Pr$_{12}$Ga$_4$Sb$_{23}$

Figure 2-5. Comparison of (a) the five-atom-wide Sb ribbons in La$_{13}$Ga$_8$Sb$_{21}$ and Pr$_{12}$Ga$_4$Sb$_{23}$, and (b) the six-atom-wide Sb ribbon in Pr$_{12}$Ga$_4$Sb$_{23}$, viewed perpendicular to their axes of infinite extension. The ribbons are bounded on two sides by Ga atoms, but in the case of the five-atom-wide Sb ribbon in Pr$_{12}$Ga$_4$Sb$_{23}$, the Ga(2) site is only occupied at 2.7(2)%. Bond lengths in Å are indicated.
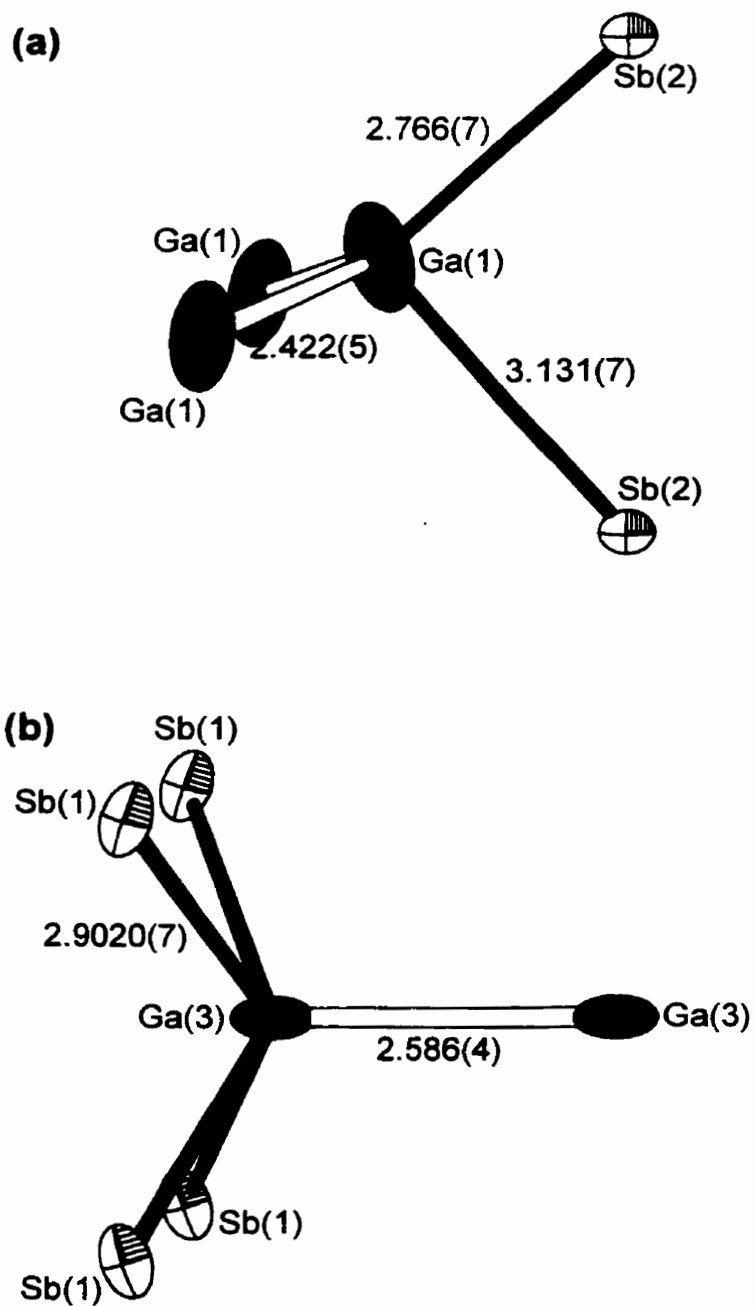
Figure 2-6. (a) Distorted tetrahedral coordination around Ga(1) in La$_{13}$Ga$_8$Sb$_{21}$. (b) Square pyramidal coordination around Ga(3) in Pr$_{12}$Ga$_4$Sb$_{23}$. Bond lengths in Å are indicated.

(a)

site	coordination environment		
central	La(1)	Pr(2)	Pr(3)
a–h	Sb	Sb	Sb
i–j	Ga (split)	Ga	Ga

(b)

site	coordination environment		
central	La(2)	Pr(1)	Pr(4)
a–g, j	Sb	Sb	Sb
h	Ga (split)	Sb (97.3%)	Ga
i	Ga (split)	Ga (2.7%)	Ga
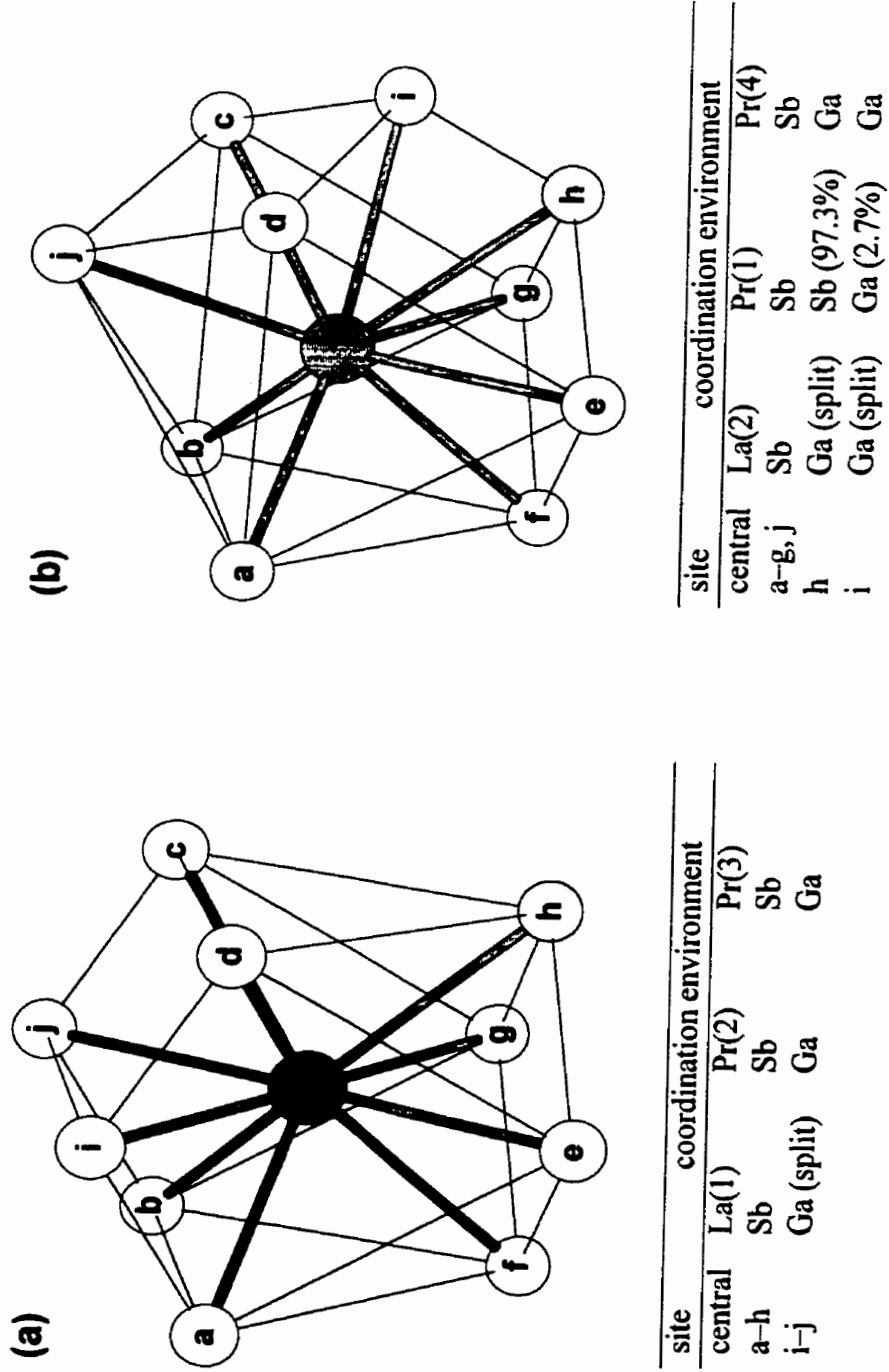
Figure 2-7. Coordination environments around La atoms in $La_{13}Ga_8Sb_{21}$ or Pr atoms in $Pr_{12}Ga_4Sb_{23}$. Sites **a–h** define a square antiprism, which is capped by additional atoms at sites **i** and **j** above (a) one square face or (b) one square and one triangular face.
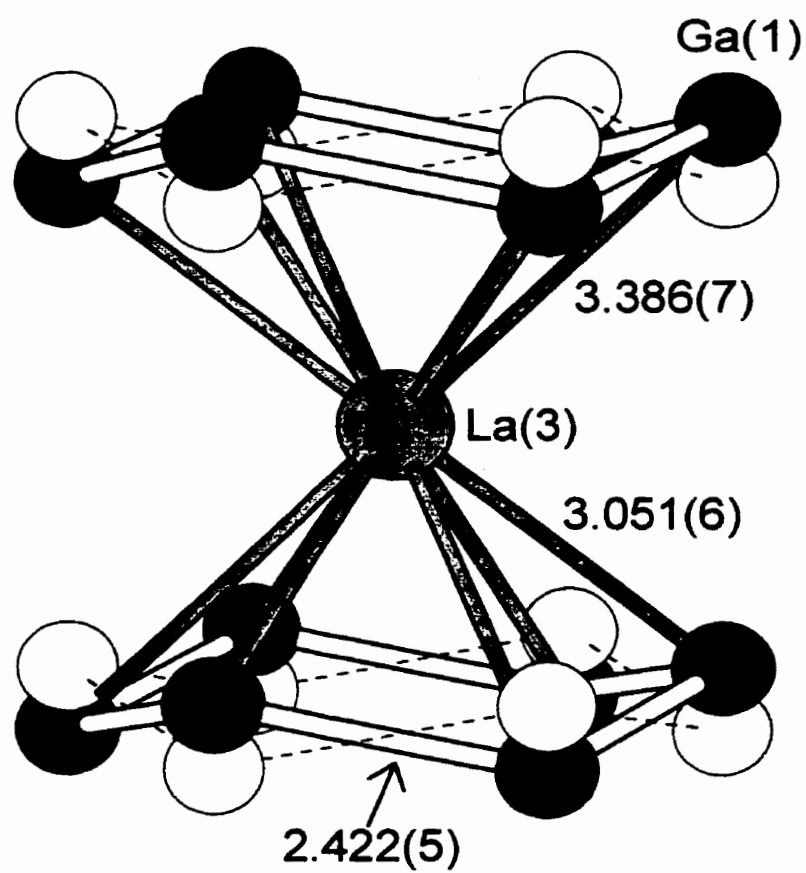
Figure 2-8. Coordination environment around La(3), sandwiched by two puckered Ga$_6$ rings, in La$_{13}$Ga$_8$Sb$_{21}$. The Ga(1) sites are approximately 50% occupied. Bond lengths in Å are indicated.

(a) $Cs_6SnAs_3O_{0.5}$

O

○ Cs

● Sn

○ As

(b) $Ba_{0.8}Hf_{12}As_{17.7}$

Ba

● Hf

○ As

(c) $La_{13}Ga_8Sb_{21}$

● La

● Ga

○ Sb
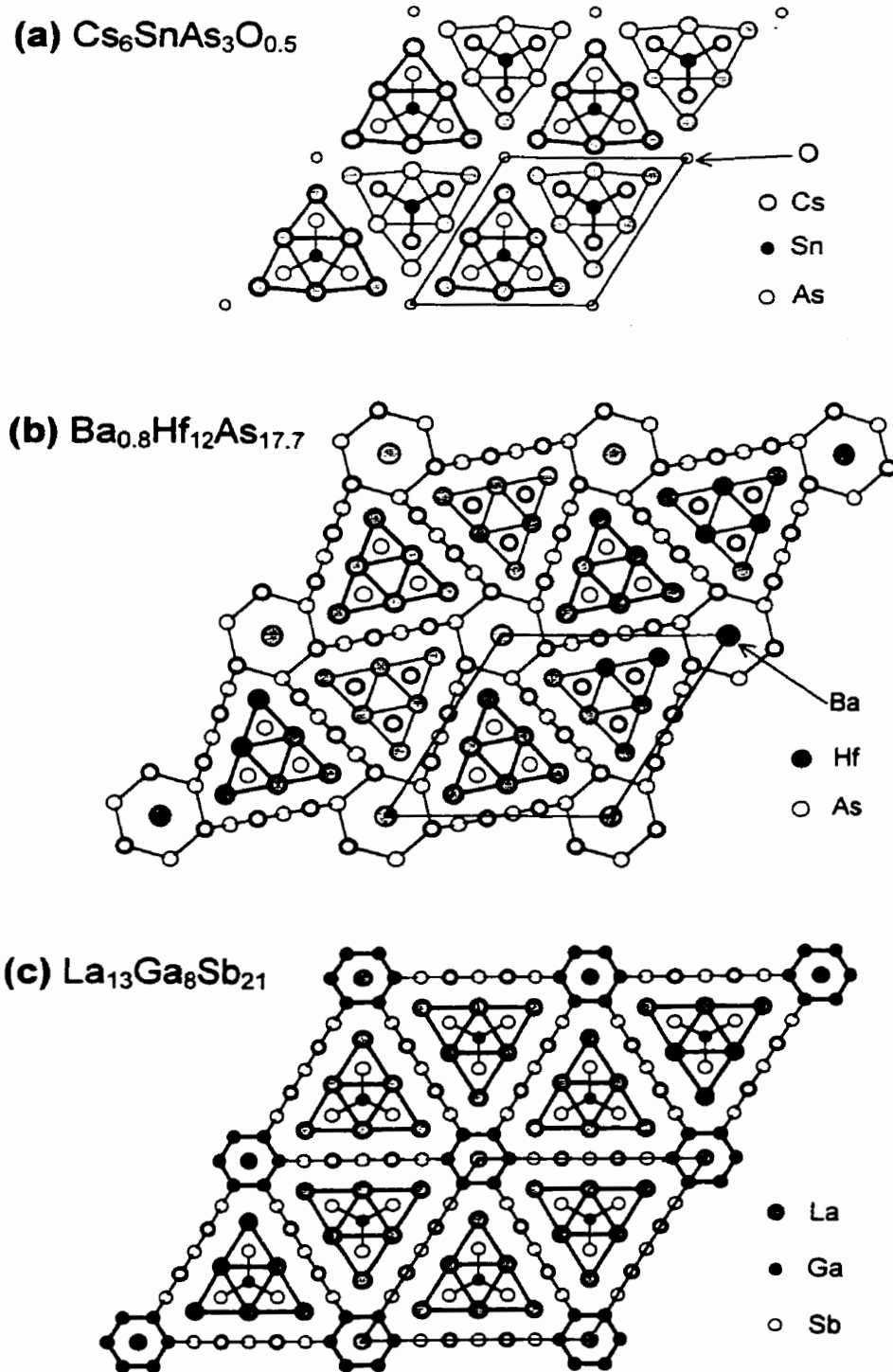
Figure 2-9. Comparison of the hexagonal structures of (a) $Cs_6SnAs_3O_{0.5}$, (b) $Ba_{0.8}Hf_{12}As_{17.7}$, and (c) $La_{13}Ga_8Sb_{21}$ shown in projection down the c axis. Circles with thicker rims are atoms residing in planes displaced by $c/2$.

(a) La$_6$MnSb$_{15}$

● La

● Mn

○ Sb

(b) Pr$_{12}$Ga$_4$Sb$_{23}$

● Pr

● Ga

○ Sb
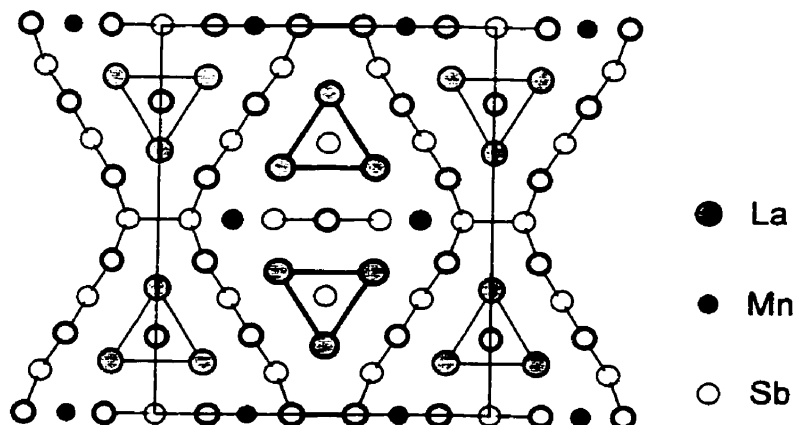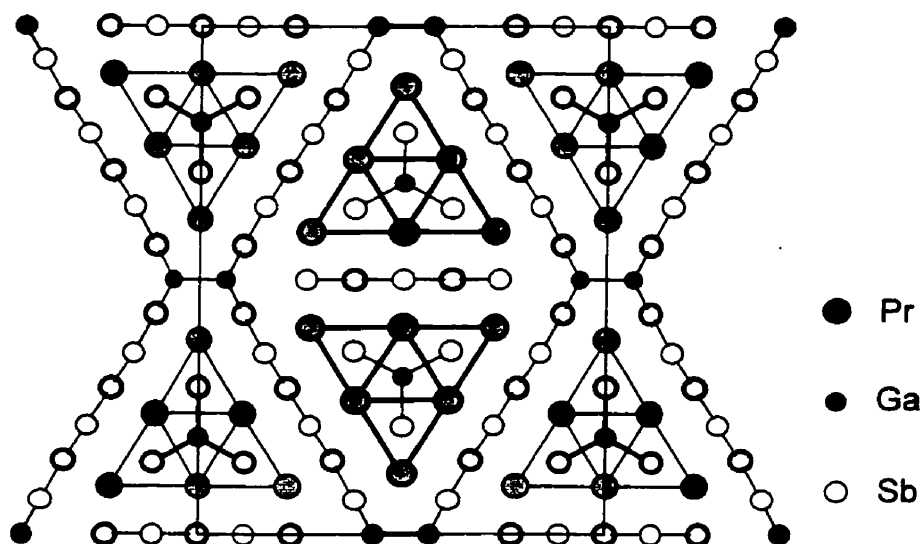
Figure 2-10. Comparison of the orthorhombic structures of (a) La$_6$MnSb$_{15}$ and (b) Pr$_{12}$Ga$_4$Sb$_{23}$ shown in projection down the shortest axis. Circles with thicker rims are atoms residing in planes displaced by ½ the short axis parameter.

References

(1)   *Chemistry, Structure, and Bonding of Zintl Phases and Ions*; Kauzlarich, S. M., Ed. VCH Publishers: New York, 1996.

(2)   For example, see the following. (a) $Na_2Ga_3Sb_3$: Cordier, G.; Ochmann, H.; Schäfer, H. *Mater. Res. Bull.* **1986**, *21*, 331. (b) Sr_3GaSb_3: Cordier, G.; Schäfer, H.; Stelter, M. *Z. Naturforsch. B: Chem. Sci.* **1987**, *42*, 1268. (c) $K_{20}Ga_6Sb_{12.66}$: Cordier, G.; Ochmann, H. *Z. Naturforsch. B: Chem. Sci.* **1990**, *45*, 277. (d) Cs_6GaSb_3: Blase, W.; Cordier, G.; Somer, M. *Z. Kristallogr.* **1992**, *199*, 277. (e) $Na_3Sr_3GaSb_4$: Somer, M.; Carrillo-Cabrera, W.; Nuß, J.; Peters, K.; von Schnering, H. G.; Cordier, G. *Z. Kristallogr.* **1996**, *211*, 479. (f) Eisenmann, B.; Cordier, G. In *Chemistry, Structure, and Bonding of Zintl Phases and Ions*; Kauzlarich, S. M., Ed. VCH Publishers: New York, 1996; p 61.

(3)   Papoian, G.; Hoffmann, R. *J. Solid State Chem.* **1998**, *139*, 8.

(4)   Ferguson, M. J.; Ellenwood, R. E.; Mar, A. *Inorg. Chem.* **1999**, *38*, 4503.

(5)   Ferguson, M. J.; Hushagen, R. W.; Mar, A. *Inorg. Chem.* **1996**, *35*, 4505.

(6)   Lam, R.; Mar, A. *Inorg. Chem.* **1998**, *37*, 5364.

(7)   *Filmscan* and *Jade 3.0*; Materials Data: Livermore, CA, 1996.

(8)   *POLSQ: Program for least-squares unit cell refinement*; Modified by D. Cahen and D. Keszler, Northwestern University, 1983.

(9)   Yvon, K.; Jeitschko, W.; Parthé, E. *J. Appl. Crystallogr.* **1977**, *10*, 73.

(10)   Sheldrick, G. M. *SHELXTL Version 5.1*; Bruker Analytical X-ray Systems: Madison, WI, 1997.

(11)   *International Tables for X-ray Crystallography*; Wilson, A. J. C., Ed. Kluwer: Dordrecht, The Netherlands, 1992; Vol. C.

(12)   Sologub, O.; Vybornov, M.; Rogl, P.; Hiebl, K.; Cordier, G.; Woll, P. *J. Solid State Chem.* **1996**, *122*, 266.

(13)   Brock, S. L.; Kauzlarich, S. M. *Comments Inorg. Chem.* **1995**, *17*, 213.

(14)   Gelato, L. M.; Parthé, E. *J. Appl. Crystallogr.* **1987**, *20*, 139.

(15)   Mills, A. M; Mar, A. *J. Am. Chem. Soc.* **2001**, *123*, 1151.

(16)   Donohue, J. *The Structures of the Elements*; John Wiley and Sons: New York, 1974.

(17)   Wang, R.; Steinfink, H. *Inorg. Chem.* **1967**, *6*, 1685.

(18)   Cordier, G.; Schäfer, H.; Woll, P. *Z. Naturforsch. B: Anorg. Chem. Org. Chem.* **1985**, *40*, 1097.

(19)   Straumanis, M. E.; Kim, C. D. *J. Appl. Phys.* **1965**, *36*, 3822.

(20)   Julien-Pouzol, M.; Jaulmes, S.; Guittard, M.; Alapini, F. *Acta Crystallogr. Sect. B: Struct. Crystallogr. Cryst. Chem.* **1979**, *35*, 2848.

(21)   Kimmel, G.; Dayan, D.; Zevin, L.; Pelleg, J. *Metall. Trans. A*; **1985**, *16*, 167.

(22)   Ling, R. G.; Belin, C. *Acta Crystallogr. Sect. B: Struct. Crystallogr. Cryst. Chem.* **1982**, *38*, 1101.

(23)   Brown, D. S.; Decken, A.; Cowley, A. H. *J. Am. Chem. Soc.* **1995**, *117*, 5421.

(24)   Bruzzone, G. *Boll. Sci. Fac. Chim. Ind. Bologna*; **1966**, *24*, 113.

(25)   Zheng, C.; Hoffmann, R. *Z. Naturforsch. B: Anorg. Chem. Org. Chem.* **1986**, *41*, 292.

(26)   Burdett, J. K.; Miller, G. J. *Chem. Mater.* **1990**, *2*, 12.

(27)   Häußermann, U.; Nesper, R. *J. Alloys Compd.* **1995**, *218*, 244.

(28)   Abdusalyamova, M. N.; Rahmatov, O. I.; Faslyeva, N. D.; Tchuiko, A. G. *J. Less-Common Met.* **1988**, *141*, L23.

(29)   Ball, A. R.; Gignoux, D.; Schmitt, D. *J. Magn. Magn. Mater.* **1993**, *119*, 96.

(30)   Dwight, A. E. *Rare Earths Mod. Sci. Technol.* **1980**, *2*, 39.

(31)   Iandelli, A. *Z. Anorg. Allg. Chem.* **1964**, *330*, 221.

(32)   Brylak, M.; Jeitschko, W. *Z. Naturforsch. B: Chem Sci.* **1994**, *49*, 747.

(33)   Wiberg, N.; Amelunxen, K.; Nöth, H.; Schwenk, H.; Kaim, W.; Klein, A.; Scheiring, T. *Angew. Chem. Int. Ed. Engl.* **1997**, *36*, 1213.

(34)   Li, X.-W.; Pennington, W. T.; Robinson, G. H. *J. Am. Chem. Soc.* **1995**, *117*, 7578.

(35)   (a) Power, P. P. *J. Chem. Soc. Dalton Trans.* **1998**, 2939. (b) Power, P. P. *Chem. Rev.* **1999**, *99*, 3463.

(36)   Ferguson, M. J.; Hushagen, R. W.; Mar, A. *J. Alloys Compd.* **1997**, *249*, 191.

(37)   Kutzelnigg, W. *Angew. Chem. Int. Ed. Engl.* **1984**, *23*, 272.

(38)   Gladyshevskii, E. I.; Grin, Yu. N. *Sov. Phys. Crystallogr. Trans. Kristallografiya*; **1982**, *26*, 683.

(39)   Parthé, E.; Chabot, B.; Hovestreydt, E. *Acta Cryst. Sect. B: Struct. Sci.* **1983**, *39*, 596.

(40)   Pivan, J.-Y.; Guérin, R.; Sergent, M. *J. Solid State Chem.* **1987**, *68*, 11.

(41)   Pivan, J.-Y.; Guérin, R.; Padiou, J.; Sergent, M. *J. Less-Common Met.* **1986**, *118*, 191.

(42)   Asbrand, M.; Eisenmann, B. *Z. Anorg. Allg. Chem.* **1994**, *620*, 1837.

Chapter 3

Electronic Structures and Properties of $RE_{12}Ga_4Sb_{23}$ (RE = La–Nd, Sm) and Superconducting $La_{13}Ga_8Sb_{21}$ [†]

Introduction

Intermetallic compounds M_xA_y or $M_xA_yB_z$ (M = alkali or alkaline-earth metal; A, B = main-group elements) containing a combination of highly electropositive and electronegative components tend to form structures with localized covalent bonding between the electronegative atoms, and closed-shell electronic configurations for all atoms.[1] As the electronegativity difference between components decreases, more unusual non-classical metalloid substructures featuring multicentre bonding become prevalent. For instance, many alkali metal gallide structures display networks of interconnected Ga clusters.[2] The delocalized bonding and non-classical geometries of these electron-deficient clusters can be explained through the application of Wade's rules.[3] Weak multicentre homoatomic bonding is also observed in the more electron-rich rare-earth antimonides. In these compounds, we find linear chains,[4] square ribbons,[5] and square nets[6] containing, to a first approximation, one-electron Sb–Sb bonds. Electron-counting schemes for these metalloid bonding networks have been detailed in a recent review.[7]

As part of our continuing investigation of the ternary rare-earth main-group antimonide systems, we have recently described the synthesis and characterization of $RE_{12}Ga_4Sb_{23}$ (RE = La–Nd, Sm) and $La_{13}Ga_8Sb_{21}$, the first examples of rare-earth gallium antimonides.[8] The related structures both contain extended Sb–Sb bonding networks and finite Ga–Ga bonded units: non-classical square ribbons of Sb atoms are linked by either Ga_2 pairs (in $RE_{12}Ga_4Sb_{23}$ (Figure 3-1)) or by unusual puckered Ga_6 rings (in $La_{13}Ga_8Sb_{21}$ (Figure 3-2)). Classical trigonal planar $GaSb_3$ units, typically found in $M_xGa_ySb_z$ Zintl compounds, are enclosed within the networks.[1]

The co-existence of (i) classical moieties that are strongly covalently bonded and finite (Ga_2 pairs, Ga_6 rings, $GaSb_3$ trigonal planes) with (ii) non-classical networks that are weakly bonded and extended (Sb ribbons), representing the bulk of the structure, implies an interesting electronic situation. Competition develops between localization of electrons in the isolated units and delocalization in the extended networks. Similar structural and electronic characteristics have been identified as prerequisites for the occurrence of superconductivity in several classes of compounds.[9] This paradigm has provided insight into why, for instance, certain rare-earth carbides and carbide halides, with structures consisting of discrete C_2 pairs within an extended metal–metal network of rare-earth atoms, are superconducting.[9a]

We report here the results of band structure calculations for $RE_{12}Ga_4Sb_{23}$ and $La_{13}Ga_8Sb_{21}$ that were performed in order to clarify the nature of the bonding in these compounds and to examine the applicability of the Zintl concept to these complicated structures. The calculations suggest metallic behaviour for both structures, and resistivity

measurements of the entire series of compounds confirm this prediction. In addition, $La_{13}Ga_8Sb_{21}$, undergoes a superconducting transition at 2.4 K.

Experimental Section

Band Structures. Tight-binding extended Hückel band structure calculations were performed on $La_{12}Ga_4Sb_{23}$ and $La_{13}Ga_8Sb_{21}$ using the EHMACC and YAeHMOP suites of programs.[10–12] (Although the crystal structure determination was on $Pr_{12}Ga_4Sb_{23}$, the La member of the $RE_{12}Ga_4Sb_{23}$ series was chosen for the band structure calculations to allow a better comparison with $La_{13}Ga_8Sb_{21}$. The atomic coordinates used for $La_{12}Ga_4Sb_{23}$ were calculated on the basis of positional parameters from the crystal structure of $Pr_{12}Ga_4Sb_{23}$ and refined cell parameters from the powder pattern of $La_{12}Ga_4Sb_{23}$.[8]) The atomic parameters used are listed in Table 3-1.[13–16]

Transport and Magnetic Measurements. $RE_{12}Ga_4Sb_{23}$ (RE = La–Nd, Sm) and $La_{13}Ga_8Sb_{21}$ were prepared as described previously. All transport measurements were made on crystals whose compositions were verified by energy-dispersive X-ray (EDX) analyses on a Hitachi S-2700 scanning electron microscope. Electrical resistivities of single crystals, typically 0.5–1.0 mm long and 0.05–0.2 mm wide, were measured with the current parallel to the needle axis (crystallographic a axis for $RE_{12}Ga_4Sb_{23}$ or c axis for $La_{13}Ga_8Sb_{21}$) by standard four-probe techniques on a Quantum Design PPMS system equipped with an AC-transport controller (Model 7100). A current of 0.1 mA and a frequency of 16 Hz were used. The superconducting transition temperature T_c of $La_{13}Ga_8Sb_{21}$ was determined as the point at which the resistivity is 90% that of the normal state.

For $La_{13}Ga_8Sb_{21}$, magnetic measurements were made on samples totalling ~ 10–20 mg of individually selected crystals, ground into powders. Magnetic data for $La_{13}Ga_8Sb_{21}$ powders were obtained with a Quantum Design 9T-PPMS DC-magnetometer/AC-susceptometer. AC magnetic susceptibility measurements between 2.0 and 3.2 K were made with a driving amplitude of 1 Oe and a frequency of 1000 Hz. Susceptibility values were corrected for contributions from the gelcap holder diamagnetism and the underlying sample diamagnetism (La, -20×10^{-6}; Ga -22×10^{-6}; Sb, -15×10^{-6} emu/mol).

Results and Discussion

Retrotheoretical Analysis. Detailed descriptions of the structures of orthorhombic $La_{12}Ga_4Sb_{23}$ (shown in Figure 3-1 down the a axis) and hexagonal $La_{13}Ga_8Sb_{21}$ (shown in Figure 3-2 down the c axis) have been presented previously.[8] The related structures are relatively complex, containing a variety of metalloid substructures. Both structures consist of four-prism columnar assemblies of Ga- or Sb-filled La_6 trigonal prisms residing in channels defined by extended networks of Ga and Sb atoms. By following a "retrotheoretical" analysis, as promoted by Papoian and Hoffmann, we will decompose the three-dimensional structures into more manageable lower-dimensional substructures (Figure 3-3).[17]

We assume, according to the Zintl concept, that the La atoms participate in predominantly ionic bonds by donating their valence electrons to the metalloid substructures.[18] Thus, if we begin by removing La^{3+} cations, we are left with the underlying metalloid frameworks, $[Ga_4Sb_{23}]^{36-}$ (in $La_{12}Ga_4Sb_{23}$) and $[Ga_8Sb_{21}]^{39-}$ (in

$La_{13}Ga_8Sb_{21}$). These can each be decomposed further into two non-interacting substructures: the Ga-linked Sb ribbons that outline the channels, and the isolated $GaSb_3$ trigonal planes that are contained within them (*ie*. $[(Ga_2Sb_{17})(GaSb_3)_2]^{36-}$ and $[(Ga_6Sb_{15})(GaSb_3)_2]^{39-}$). In $La_{12}Ga_4Sb_{23}$, the $[Ga_2Sb_{17}]$ substructure consists of an isolated $[Sb_5]$ ribbon embedded within a $[Ga_2Sb_{12}]$ framework, which in turn can be deconstructed (by breaking Ga–Ga bonds) into strongly kinked $[GaSb_6]$ sheets derived from an idealized square net (Figure 3-3a). In $La_{13}Ga_8Sb_{21}$, the $[Ga_6Sb_{15}]$ substructure can be deconstructed in two convenient ways: (i) by breaking Ga–Ga bonds to give isolated $[Ga_2Sb_5]$ ribbons, or (ii) by breaking Ga–Sb bonds to give Ga_6 rings and $[Sb_5]$ ribbons (Figure 3-3b).

Determining the distribution of the 36 electrons over the $[Ga_4Sb_{23}]$ substructure or the 39 electrons over the $[Ga_8Sb_{21}]$ substructure is more problematic, and indeed served as an impetus for the band structure calculations.[8] The Sb oxidation states can be assigned by adhering to the generally accepted, and recently summarized, conventions for classical and non-classical Sb networks.[7] However, the assignment of Ga oxidation states is more ambiguous, given the propensity of Ga to form electron-deficient compounds. Our approach is to assign, on the basis of well-established electron counting rules, initial charges to the metalloid substructures as we discuss each in turn. We then re-assemble them into the complete structures and re-adjust our assignments if necessary, following whatever insight we gain from the band structures.

[GaSb₃] Substructures. The simplest structural units found in both $La_{12}Ga_4Sb_{23}$ and $La_{13}Ga_8Sb_{21}$ are the $GaSb_3$ trigonal planes. Similar $GaSb_3$ trigonal planar units are commonly found in classical Zintl compounds, such as the alkali and alkaline-earth metal

gallium antimonides.[1] In these compounds, the large electronegativity difference between components supports the use of a Zintl analysis. Thus, for example, in Cs_6GaSb_3, the isolated $GaSb_3$ anions are assigned an overall charge of -6.[19] Within each $GaSb_3^{6-}$ anion, the assignment of oxidation states is straightforward. We first complete the octets of the more electronegative Sb atoms, and arrive at an oxidation state of -3 for each Sb atom. The central Ga atom, participating in three Ga–Sb bonds, is assigned an oxidation state of $+3$, and remains formally electron deficient.

In all of the alkali and alkaline-earth gallium antimonides, the $GaSb_3^{6-}$ anions are rigorously planar,[1] and the Ga–Sb bond lengths (*e.g.*, 2.608(5)–2.676(5) Å in Cs_6GaSb_3)[19] are somewhat shortened with respect to normal Ga–Sb single bonds (*e.g.*, 2.709(2)–2.752(5) Å in the isolated $GaSb_4^{9-}$ tetrahedra in $Na_3Sr_3GaSb_4$).[20] Partial double bond character has previously been suggested to explain these experimental observations.[21] Molecular orbital calculations performed for a planar $GaSb_3^{6-}$ anion confirm that π bonding does make a significant contribution (Mulliken overlap population (MOP) of 0.08 for Ga $4p_z$–Sb $5p_z$) to the strength of the Ga–Sb bonds (MOP of 0.75). By analogy with these classical Zintl anions, the planar geometry and shortened bond lengths (2.647(2)–2.666(2) Å) of the $GaSb_3$ units found in $La_{12}Ga_4Sb_{23}$ lead us to assign an overall charge of -6 to this substructure.[8]

Whereas the $GaSb_3$ units are planar in $La_{12}Ga_4Sb_{23}$, they are pyramidally distorted from the ideal planar geometry in $La_{13}Ga_8Sb_{21}$. The central Ga atoms are shifted slightly (~ 0.3 Å) above or below the plane of the Sb atoms (the Ga atoms are disordered over two close sites, each approximately 50% occupied), and the Sb–Ga–Sb angles are 118.81(4)°.[8] This pyramidalization is reminiscent of the well-known trigonal planar to

pyramidal distortion of GaX_3 species that accompanies the formation of Lewis acid-base adducts.[22] Our calculations reveal that the buildup of additional electron density at the central Ga atom is responsible for the distortion of the $GaSb_3$ units in $La_{13}Ga_8Sb_{21}$. As shown in Figure 3-4, the main effect of the slight pyramidalization is the stabilization of the antibonding π orbital ($2a_2''$ in planar and $2a_1$ in pyramidally distorted $GaSb_3$), the result of improved overlap between the s-p hybridized Ga and Sb orbitals. At the electron count proposed above for the $GaSb_3^{6-}$ anion of $La_{12}Ga_4Sb_{23}$, the lowest unoccupied molecular orbital (LUMO) is the antibonding π orbital. Upon addition of any electrons to the system, the distorted geometry becomes energetically favoured. Since the $GaSb_3$ units of $La_{13}Ga_8Sb_{21}$ are only slightly distorted from the ideal planar geometry and contain Ga–Sb bond lengths (2.620(2) Å) that are significantly shorter than typical single bonds,[8] we will assume, for simplicity in electron counting, that the reduction of the Ga centre occurs through the addition of one electron, i.e., $GaSb_3^{7-}$.

Although we have initially considered the $GaSb_3$ trigonal planar units as isolated anions, they are actually stacked along the short axis (~ 4 Å) of the structures of both $La_{12}Ga_4Sb_{23}$ and $La_{13}Ga_8Sb_{21}$. We performed band structure calculations on the one-dimensional array of $GaSb_3$ units in $La_{13}Ga_8Sb_{21}$ in order to examine the possibility that weak Ga–Ga bonding interactions are the driving force for the observed pyramidal distortion. The Ga–Sb antibonding π orbitals (mainly Ga p_z in character) of adjacent $GaSb_3$ trigonal planes have the correct symmetry to interact in a σ-type fashion along the stacking axis. If we assemble a one-dimensional stack of planar $GaSb_3^{6-}$ anions (1), the Ga–Sb antibonding π LUMO broadens into a band with Ga–Ga σ antibonding character at the centre of the Brillouin zone (Γ) and Ga–Ga σ bonding character at the edge (Z)

(Figure 3-5a). Adding one electron per $GaSb_3$ unit to the system leads to a half-filled band, making the one-dimensional stack prone to a Peierls distortion.[11]

1   **2**   **3**
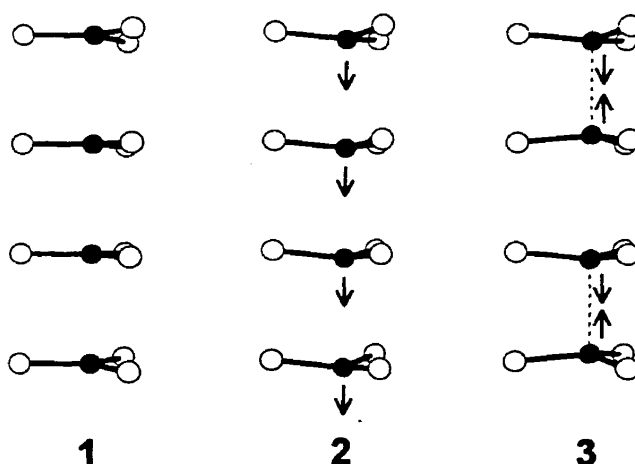
Two local stacking arrangements exist for the disordered $GaSb_3$ units in $La_{13}Ga_8Sb_{21}$: adjacent pyramidal $GaSb_3$ units may be either parallel, with an interunit Ga–Ga distance of 4.338(1) Å that is determined by the c parameter, or inverted with respect to one another, such that a shortened Ga–Ga distance of 3.763(1) Å results.[8] We examined both of the limiting one-dimensional arrangements (*i.e.*, all adjacent $GaSb_3$ units parallel -- a sliding distortion (**2**); or all adjacent $GaSb_3$ units inverted -- a pairing (Peierls) distortion (**3**)). The sliding distortion results in only a slight overall lowering of the energy of the Ga–Sb antibonding band. To prepare for the pairing distortion, the c parameter is doubled (and the c^* parameter is halved), so that the bands are "folded back," and the Bloch function midway between Γ and Z in Figure 3-5a would correspond to a degenerate pair at Z near –5 eV in Figure 3-5b. The effect of the pairing distortion (**3**) is dramatic: it removes the degeneracy, opening up an energy gap between two manifolds in which Ga–Ga bonding states are stabilized and Ga–Ga antibonding states are destabilized, as confirmed by inspection of the Ga–Ga crystal orbital overlap population (COOP) curve (Figure 3-5b). Based on our assignment of a –7 charge per

GaSb$_3$ unit, the pairing distortion is clearly preferred energetically. At this electron count, the interunit Ga–Ga bonding is maximized (MOP of 0.41), but the Ga–Sb bond strength is reduced (MOP of 0.66) since more Ga–Sb antibonding levels are populated (Figure 3-5b). The atomic charge determined for the central Ga atom decreases from +0.79 for [GaSb$_3$]$^{6-}$ to –0.04 upon addition of one electron per GaSb$_3$ unit to the system, while the average charge calculated for the Sb atoms remains relatively constant ($\sim$ –2.3).

Although these results support the possibility that individual one-dimensional [GaSb$_3$] stacks in La$_{13}$Ga$_8$Sb$_{21}$ undergo a pairing distortion, there was no evidence for superstructure from the crystal structure determination.[8] This is not surprising, considering that the stacks are far apart from each other (Figure 3-2). A random distribution of these stacks, while each individually ordered, would still give rise to an overall disorder in the structure.

Sb Ribbons. The most striking recurring theme in the structures of many Sb-rich ternary rare-earth antimonides is the occurrence of Sb networks that contain relatively long Sb–Sb bonds in the 3.0–3.2 Å range, longer than a single bond ($\sim$ 2.8 Å) but shorter than the van der Waals contact ($\sim$ 4.3 Å).[4-6] While square sheets of Sb atoms in this bonding range are encountered in numerous binary and ternary antimonides,[6] the structures of La$_{12}$Ga$_4$Sb$_{23}$ and La$_{13}$Ga$_8$Sb$_{21}$ point to a fecundity in bonding patterns that was previously unimaginable, but implied in the structures of α- and β-ZrSb$_2$,[23] and, more recently, La$_6$MnSb$_{15}$[5b] -- ribbons of varying widths can be excised from a square net.

As shown in Figure 3-6, La$_{12}$Ga$_4$Sb$_{23}$ and La$_{13}$Ga$_8$Sb$_{21}$ contain complex [Ga$_2$Sb$_{17}$] and [Ga$_6$Sb$_{15}$] substructures, respectively, that feature non-classical electron-rich

networks of Ga and Sb atoms. In both substructures, five- or six-atom-wide square Sb ribbons form the walls of large channels. These can be derived from a prototypical square sheet, for which a well-developed bonding theory exists.[7] According to a hypervalent bonding model, the weak Sb–Sb bonds within the square sheets are described as one-electron bonds, to a first approximation. Implicit in this model are the assumptions that little s-p mixing occurs, and that π bonding between Sb atoms is weak. Each Sb atom uses two p orbitals, each accommodating one electron, to form the in-plane bonds and the remaining p and s orbitals accommodate lone pairs to complete the Sb octets. Correspondingly, each Sb atom of a square sheet, and, by extension, an "inner" Sb atom within a ribbon, is assigned an oxidation state of −1. This model will serve as a basis for our description of the bonding in the actual $[Ga_2Sb_{17}]$ and $[Ga_6Sb_{15}]$ substructures.

$[Ga_2Sb_{17}]$ **Substructure in** $La_{12}Ga_4Sb_{23}$. In $La_{12}Ga_4Sb_{23}$, the channel walls are defined by one five-atom-wide Sb ribbon, and two eight-atom-wide sides composed of six-atom-wide Sb ribbons bordered by Ga atoms (Figure 3-6a). The eight-atom-wide sides are connected by Ga–Ga bonding, but the five-atom-wide Sb ribbon is isolated (the closest contact between this side and the others is ~ 4 Å). The anionic $[Ga_2Sb_{17}]$ network can, therefore, be dissected into two non-interacting substructures, the one-dimensional $[Sb_5]$ ribbon and the three-dimensional $[Ga_2Sb_{12}]$ network. These substructures in $La_{12}Ga_4Sb_{23}$ are even more complicated than those found in the closely related La_6MnSb_{15} structure: an $[Sb_3]$ ribbon and an $[Sb_{10}]$ network (referred to as an $[Sb_{20}]$ network in the original paper).[5b] A detailed band structure calculation was performed for La_6MnSb_{15}, and we follow a similar approach here.[17]

The [Sb₅] ribbon, containing 3.167(2) Å Sb–Sb bond distances,[8] may be considered as a segment excised from the two-dimensional Sb square sheet described above, and the oxidation states of the component Sb atoms assigned accordingly (4). The inner Sb atoms are assigned an oxidation state of –1, while the terminal Sb atoms, participating in only two one-electron bonds, require three lone pairs of electrons to complete their octets and are assigned an oxidation state of –2. Thus, we arrive at an overall charge of –7 for the [Sb₅] ribbon. The band structure and Sb–Sb COOP curve calculated for the $[Sb_5]^{7-}$ ribbon are shown in Figure 3-7. The calculations confirm our oxidation state assignments: the average charges determined for the inner and terminal Sb atoms are –1.00 and –2.00, respectively. At the proposed electron count, some Sb–Sb antibonding states have been filled (Figure 3-7b), and the overlap population determined for the Sb–Sb bonds is 0.20, within the range observed for the longer Sb–Sb contacts in Sb square sheets,[6a] and consistent with bond length correlations.[17]
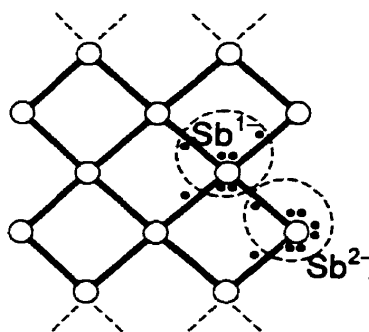
4

The [Ga₂Sb₁₂] substructure may be described as a stacking (along the b axis) of strongly kinked [GaSb₆] sheets, each derived from an idealized two-dimensional Sb square sheet (Figures 3-1, 3-3a, and 3-6a). The first step in this transformation is the substitution of Ga for Sb along every seventh diagonal of the sheet. As above, we can assign oxidation states to the atoms of this hypothetical structure: the substituted Ga

atoms, with two lone pairs, are assigned as Ga^{1-}, the neighbouring Sb atoms as Sb^{2-}, and the remaining Sb atoms as Sb^{1-}. The sheet is then folded along the Ga-substituted diagonal to produce a kinked sheet. In the related La_6MnSb_{15} structure, it was found that the kinking of an $[Sb_{10}]$ sheet, accompanied by *s-p* hybridization, produces relatively localized lone pairs at the corner Sb atoms.[17] Since lighter elements undergo *s-p* hybridization more readily than their heavier counterparts,[24] it is quite satisfying to find that kinking in the $[GaSb_6]$ sheet occurs along the Ga-substituted diagonals. As shown in Figure 3-8a, the localization of the lone pairs on the Ga atoms is reflected by the narrowness of the bands that involve contributions from the Ga p_y orbitals, which are perpendicular to the $[GaSb_6]$ sheet (note the Ga p_y projection accounting for the large spike near -7 eV in the DOS). When the kinked nets are stacked perpendicular to the *b* direction, the lone pairs on the Ga atoms of adjacent sheets are directed toward each other. Oxidation of the Ga atoms allows intersheet Ga–Ga bonding to occur (5); neighbouring $[GaSb_6]$ sheets are thus connected to complete the three-dimensional
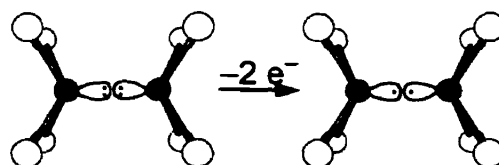
5

$[Ga_2Sb_{12}]$ network. In the DOS curve for the actual $[Ga_2Sb_{12}]$ substructure, the Ga p_y orbitals, now involved in Ga–Ga bonding, are dispersed over a wider energy range (Figure 3-8b). Since the observed 2.632(2) Ga–Ga distance is consistent with a single bond,[8] we assign an oxidation state of 0 to the Ga atoms, and an overall charge of -16 to the $[Ga_2Sb_{12}]$ substructure. The actual atomic charges determined for the Ga atoms (+0.05), adjacent Sb atoms (-1.66) and inner Sb atoms (-1.18) at this electron count are

in good agreement with our proposals. Inspection of the Ga–Ga COOP curve reveals that essentially all of the Ga–Ga bonding states are filled (Figure 3-9a). The overlap population of 0.77 determined for the Ga–Ga interactions is typical of a single bond. The COOP curves for the Ga–Sb and Sb–Sb interactions within the kinked square sheet are similar, but shifted in energy because of the differing electronegativities of the atoms involved (Figures 3-9b and c). Fewer Ga–Sb than Sb–Sb non-bonding and antibonding states are filled, and the overlap populations calculated for the 2.956(2) Å Ga–Sb (0.41) and 3.064(2)–3.187(2) Å Sb–Sb (0.14) interactions reflect this.[8] Both overlap populations are reduced with respect to those of full single bonds, supporting our description of these interactions as half-bonds.[9,17]

[Ga_6Sb_{15}] Substructure in $La_{13}Ga_8Sb_{21}$. In the [Ga_6Sb_{15}] substructure of $La_{13}Ga_8Sb_{21}$, three equivalent segments outline the large channels. Five-atom-wide Sb square ribbons are bordered by Ga atoms, forming seven-atom-wide channel walls (Figure 3-6b). In this case, strong Ga–Ga interactions link all of the walls, and unusual puckered Ga_6 rings are generated at the interface of six wall-sharing channels. The resulting three-dimensional [Ga_6Sb_{15}] network in $La_{13}Ga_8Sb_{21}$ can be analyzed by two approaches. We could proceed as before, considering Ga as a substituent in an otherwise all-Sb network. Here, we would propose that [Ga_6Sb_{15}] network is assembled by connecting three idealized isolated one-dimensional [Ga_2Sb_5] ribbons per unit cell, with Ga atoms at the terminal positions of each ribbon (Figure 3-3b). If we assume complete octets for all of the ribbon atoms, we arrive at the following oxidation state assignments: −3 for the terminal Ga atoms, −2 for the adjacent Sb atoms, and −1 for the inner Sb atoms (6). According to our model, the terminal Ga atoms, each participating in two one-

electron Ga–Sb bonds, have three lone pairs of electrons. When we bring the idealized ribbons together, each Ga atom must be oxidized by two electrons to form two Ga–Ga single bonds involving σ overlap of *s-p* hybrid orbitals, analogous to the process described earlier in Scheme 5. One lone pair of electrons remains at each Ga^{1-} atom of the resultant planar six-membered rings. Even this admittedly crude electron counting scheme leads to the implication that for π bonding to play a role in the Ga–Ga bonding within the rings, further oxidation of the Ga centres must take place.

6
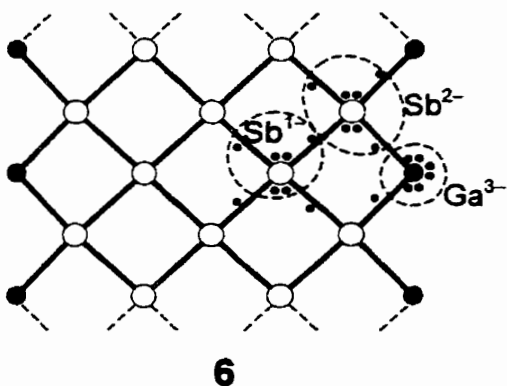
Since the electronic structure of planar six-membered rings is well known, we can shift our focus, in a second approach to understanding the $[Ga_6Sb_{15}]$ substructure, to the Ga_6 rings and consider what happens when they interact with $[Sb_5]$ ribbons. The molecular orbitals involving π overlap in an isolated planar Ga_6 ring are completely filled if we begin with the electron counting scheme above and assume that the lone pair of each Ga^{1-} atom resides in a p_z orbital (Figure 3-10a). When the Ga_6 rings are stacked in a one-dimensional array, these π-type molecular orbitals transform to a manifold of bands with little dispersion (because there is little interaction between the rings) and which are also completely filled. Now the $[Sb_5]^{7-}$ ribbons, whose band structure was examined earlier, are allowed to interact with the stack of Ga_6 rings. There are still some Sb–Sb

antibonding levels that are unoccupied and are lower in energy than the top of the Ga π

block, mostly Ga–Ga π antibonding in character (Figure 3-10b). We thus expect a

transfer of electrons to occur in which Ga atoms are further oxidized and Sb atoms are

further reduced, allowing Ga–Ga bonding to strengthen at the expense of a slight

weakening of the Sb–Sb bonds within the [Sb₅] ribbons.

7   **8**   **9**
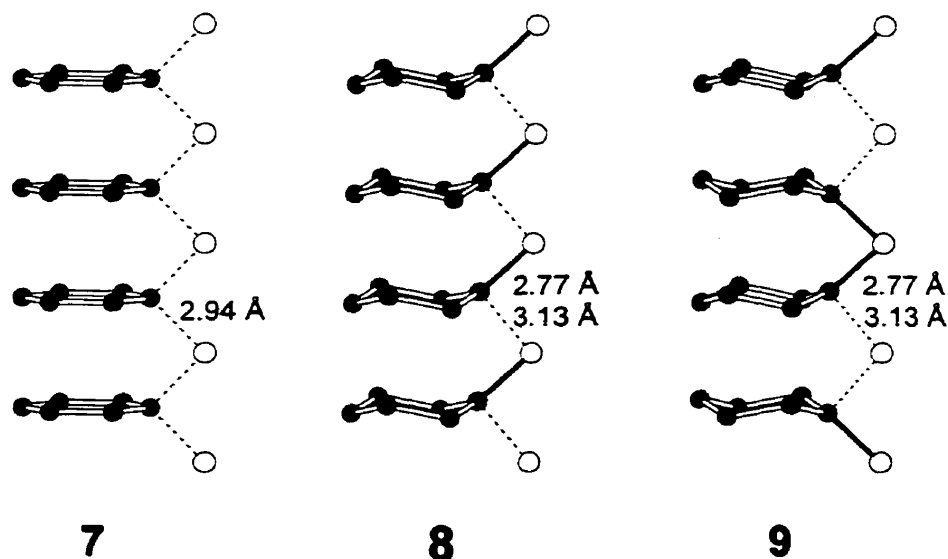
In the actual crystal structure, the ring Ga atoms are disordered over two sites.

The Ga₆ rings are assumed to be puckered into a chair conformation (Ga–Ga–Ga

115.9(3)°) to allow reasonable intraring Ga–Ga distances of 2.422(5) Å.[8] To probe the

origin of this puckering, we first examined a one-dimensional stack of planar Ga₆ rings

(7) that are surrounded by the immediately neighbouring Sb atoms, whose valence shells

were artificially completed, to give $[Ga_6Sb_6]^{24-}$ (only one of the spokes of surrounding Sb

atoms is shown in Scheme 7 for clarity). Although no evidence of long range ordering of

the puckered rings was detected in the crystal structure solution, two local orderings are

possible: adjacent rings may be parallel (8), with all inter-ring Ga–Ga distances being

4.338(9) Å, or inverted (9), with three short 3.843(8) Å inter-ring Ga–Ga contacts.[8] At

the proposed electron count, our one-dimensional calculations reveal that either of the two limiting puckered stacking arrangements is more stable (−856.7 and −852.6 eV/f.u. for the parallel and inverted arrangements, respectively) than the undistorted planar arrangement (−841.9 eV/f.u.). The main consequence of the ring puckering is that Ga–Ga and Ga–Sb σ-type orbitals involving s-p hybrids on each Ga atom are mixed in with Ga–Ga π-type orbitals. This mixing tends to strengthen half of the Ga–Sb bonds (2.766(7) Å) surrounding a Ga_6 ring.[8] For example, in the planar arrangement, the crystal orbital (at Γ) shown in **10** is Ga–Ga bonding but Ga–Sb antibonding; in the puckered arrangement, **11**, it becomes less Ga–Sb antibonding at the expense of slightly weakened Ga–Ga bonding. There is little difference in energies between the parallel and inverted puckered arrangements, largely because the inter-ring Ga–Ga interaction is essentially non-bonding (MOP ∼ 0). We consider only the (slightly) more stable parallel arrangement in our subsequent calculations.

10   **.11**
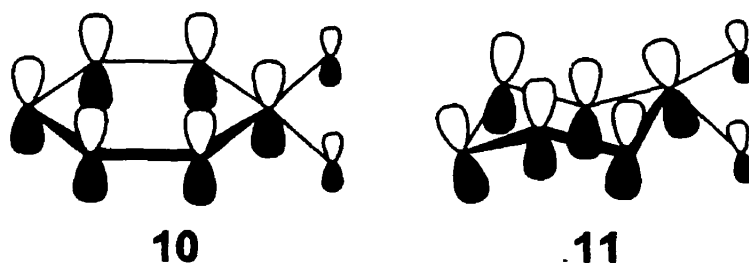
We are now in a position to examine the entire $[Ga_6Sb_{15}]$ substructure. From the first retrotheoretical approach ($[Ga_6Sb_{15}] \leftarrow 3\ [Ga_2Sb_5]$), we proposed oxidation states of −1 for Ga, −2 for adjacent Sb and −1 for inner Sb atoms, and we expected that Ga^{1-} atoms might have to be oxidized further, even after forming Ga–Ga bonds. From the second retrotheoretical approach ($[Ga_6Sb_{15}] \leftarrow [Ga_6] + 3\ [Sb_5]$), we saw that adjustments of Ga–Sb bonding interactions are necessary and that Sb–Sb bonds might have to weaken as

well. The DOS curve for $[Ga_6Sb_{15}]^{27-}$ and the COOP curves for the Ga–Ga, Ga–Sb, and Sb–Sb interactions are shown in Figure 3-11. The $[Sb_5]$ ribbon interacts significantly with the Ga π block, which can be roughly gauged by the broad energy range in which the Ga p_z contribution makes to the DOS (Figure 3-11a), as well as the extensive mixing of Ga–Ga, Ga–Sb, and Sb–Sb character in the states as seen in the COOP curves (Figures 3-11b–d). As anticipated from Figure 3-10b, this increased dispersion results in a transfer of electrons from Ga to the Sb ribbon atoms, which is reflected in the atomic charges determined for the $[Ga_6Sb_{15}]^{27-}$ substructure (–0.56 for the Ga atoms, –1.62 for the adjacent Sb atoms, and –1.54 for the inner Sb atoms). The large overlap population of 0.89 calculated for the Ga–Ga bonds within the six-membered ring is consistent with strengthened Ga–Ga bonding expected as a result of the depopulation of π^* bands. The reduction of the ribbon Sb atoms causes a substantial proportion of Sb–Sb antibonding levels to be filled so that the overlap population becomes essentially zero (0.002) for the Sb–Sb interactions; the weakening of Sb–Sb bonding has proceeded a little too far, but as we shall see later, this can be remedied when the rest of the $La_{13}Ga_8Sb_{21}$ structure is also considered. The long and short Ga–Sb interactions between the Ga_6 rings and Sb ribbons have overlap populations of 0.33 and 0.60, respectively, which substantiate their description as a 3-centre-2-electron bond with asymmetric distribution of electron density between the atoms.[8]

Assembling the Complete $La_{12}Ga_4Sb_{23}$ and $La_{13}Ga_8Sb_{21}$ Structures. At this stage, we are ready to re-assemble the composite $[Ga_4Sb_{23}]^{36-}$ and $[Ga_8Sb_{21}]^{39-}$ substructures of $La_{12}Ga_4Sb_{23}$ and $La_{13}Ga_8Sb_{21}$, respectively, from their component bonding networks. The overall charge (–36 or –39) is obtained assuming that the Zintl

concept applies; *i.e.*, the La atoms transfer their valence electrons entirely. We can compare this electron count to that obtained by summing up the contributions of the individual components that were analyzed separately.

For $La_{12}Ga_4Sb_{23}$, the process is relatively straightforward. We assigned charges of -6, -7 and -16 to the non-interacting $[GaSb_3]$, $[Sb_5]$, and $[Ga_2Sb_{12}]$ networks, respectively. At these electron counts, the Fermi levels for the substructures lie at -10.5, -7.6, and -5.4 eV, respectively. The total charge for the $[Ga_4Sb_{23}]$ substructure obtained by combining these networks is -35: $[Ga_2Sb_{12}]^{16-}[Sb_5]^{7-}[GaSb_3]^{6-}[GaSb_3]^{6-}$. This count is one electron less than that required by the Zintl concept, suggesting that one of the networks must be further reduced. The DOS curve for the composite $[Ga_4Sb_{23}]^{36-}$ substructure is shown in Figure 3-12a. Since the Fermi level for $[Ga_4Sb_{23}]^{36-}$ is calculated to be at -5.8 eV, the $[GaSb_3]$ trigonal planes and $[Sb_5]$ ribbons are likely candidates for reduction. The one extra electron per formula unit may be used for Ga–Ga bonding between $GaSb_3$ trigonal planes along a one-dimensional stack, just as they are in $La_{13}Ga_8Sb_{21}$. Although the crystal structure determination of $Pr_{12}Ga_4Sb_{23}$ shows that the $GaSb_3$ units are strictly planar, the elongation of the thermal ellipsoid along the c axis observed for the central Ga atom suggests that incipient interunit Ga–Ga bonds may be forming.[8] Alternatively, and perhaps more realistically, the $[Sb_5]$ ribbons may be reduced; the ability to act as an electron sink is often attributed to Sb square nets.[6b,9,17,25]

The re-assembly exercise for the composite $[Ga_8Sb_{21}]^{39-}$ substructure of $La_{13}Ga_8Sb_{21}$ is complicated by the disorder in the crystal structure.[8] At the -7 charge proposed for the one-dimensional $[GaSb_3]$ array, the most energetically favourable stacking arrangement (with a Fermi level of -6.2 eV) is that in which all adjacent $GaSb_3$

units are inverted with respect to one another. Our electronic structure calculations for the [Ga$_6$Sb$_{15}$] network indicate that the stacking arrangement of the Ga$_6$ rings makes little difference to the total energy. For simplicity, we assume that all neighbouring Ga$_6$ rings are parallel. At the –27 charge assigned to the [Ga$_6$Sb$_{15}$] network, the Fermi level for this arrangement lies at –3.4 eV. In our hypothetical ordered model for the composite [Ga$_8$Sb$_{21}$] substructure ($P\bar{3}$, $Z = 2$, $a = 17.657(2)$, $c = 8.676(2)$ Å), we double the c axis relative to the original crystal structure, and reduce the symmetry from hexagonal to trigonal. The total charge for the [Ga$_8$Sb$_{21}$] substructure obtained by combining these two networks is –41: [Ga$_6$Sb$_{15}$]$^{27-}$[GaSb$_3$]$^{7-}$[GaSb$_3$]$^{7-}$. This count is two electrons more than predicted by the Zintl analysis. The DOS curve for the ordered [Ga$_8$Sb$_{21}$]$^{39-}$ substructure is shown in Figure 3-13a, and the Fermi level is calculated to be at –4.0 eV. Since the Fermi level for the [GaSb$_3$] array lies well below –4.0 eV, it is the [Ga$_6$Sb$_{15}$] network that must be oxidized. The two electrons are removed from bands with Ga–Ga π bonding character and Sb–Sb antibonding character (Figures 3-11b and d). Accordingly, the oxidation of the [Ga$_6$Sb$_{15}$] network results in slightly weakened Ga–Ga bonding (MOP of 0.87) and strengthened Sb–Sb bonding (MOP of 0.05).

Inclusion of the La atoms in the band structure calculations does not drastically alter the overall picture. The DOS curves for the complete La$_{12}$Ga$_4$Sb$_{23}$ and La$_{13}$Ga$_8$Sb$_{21}$ structures, with the La contributions also indicated, are shown in Figures 3-12b and 3-13b, respectively. Although we have initially considered the La atoms as isolated La^{3+} cations, a substantial number of La states are populated. The La d-block states overlap with Ga and Sb states, resulting in electron transfer from the metalloid atoms to La and an attendant lowering of the Fermi levels to –8.5 eV for La$_{12}$Ga$_4$Sb$_{23}$ or to –7.8 eV for

$La_{13}Ga_8Sb_{21}$. The overlap populations calculated for the La–Ga and La–Sb interactions (0.07 and 0.23 for $La_{12}Ga_4Sb_{23}$; 0.11 and 0.22 for $La_{13}Ga_8Sb_{21}$, respectively) indicate significant covalency. Since the states that lie just below the Fermi levels in $[Ga_4Sb_{23}]^{36-}$ and $[Ga_8Sb_{21}]^{39-}$ are mainly Sb–Sb antibonding and Ga–Ga bonding in character, the reduction of the Fermi energies in the $La_{12}Ga_4Sb_{23}$ and $La_{13}Ga_8Sb_{21}$ band structures strengthens the Sb–Sb bonds of the channel-defining networks (MOP of 0.26 for $La_{12}Ga_4Sb_{23}$; MOP of 0.25 for $La_{13}Ga_8Sb_{21}$) and weakens the Ga–Ga bonds of the Ga_2 pairs (MOP of 0.67) or Ga_6 rings (MOP of 0.69), respectively. In each of the band structures, the Fermi level falls in a region of moderate DOS, crossing dispersive bands with contributions from La, Ga, and Sb. Metallic behaviour is thus predicted for $La_{12}Ga_4Sb_{23}$ (and by analogy $RE_{12}Ga_4Sb_{23}$) and $La_{13}Ga_8Sb_{21}$.

Transport and Magnetic Measurements. Resistivity measurements confirm that all $RE_{12}Ga_4Sb_{23}$ members, in the 2–300 K temperature range (Figure 3-14), and $La_{13}Ga_8Sb_{21}$, in the 2.4–300 K range (Figure 3-15), are metallic. The resistivity data for $RE_{12}Ga_4Sb_{23}$ are summarized in Table 3-2. Most members of the series (RE = La–Nd) have resistivities on the order of 10^{-4} Ω cm, but $Sm_{12}Ga_4Sb_{23}$, with a resistivity on the order of 10^{-2} Ω cm, is a much poorer conductor. All members generally exhibit a monotonic decrease in resistivity with temperature. The sharp decrease in slope below ~ 5 K observed for $Ce_{12}Ga_4Sb_{23}$ may be a consequence of a loss in spin-disorder scattering at low temperatures. Similar behaviour has been described for the antiferromagnetic Ce member of the $RE_6Ge_{5-x}Sb_{11+x}$ series of compounds.[26] We plan to make magnetic susceptibility measurements for $RE_{12}Ga_4Sb_{23}$ to investigate their

magnetic properties at low temperatures. For RE = Ce, these studies will help determine if the drop in resistivity arises from the presence of long-range magnetic ordering.

The high-temperature transport behaviour of $La_{13}Ga_8Sb_{21}$ ($\rho_{300\ K}$ = 1.26 × 10^{-4} Ω cm, $\rho_{300\ K}/\rho_{2.4\ K}$ = 1.94) resembles that observed for $La_{12}Ga_4Sb_{23}$, but at low temperatures, the resistivity drops abruptly to zero (Figure 3-15). This is assigned to a transition to a superconducting state with T_c = 2.4 K. Magnetic susceptibility measurements support this interpretation of the resistivity data: as shown in Figure 3-16, the onset of the characteristic diamagnetic response occurs below 2.5 K. However, the limiting diamagnetic susceptibility could not be reached because of instrumental constraints. The zero-field-cooled (ZFC) diamagnetic shielding and field-cooled Meissner effect curves measured with an applied field of 10 Oe are essentially superimposable in the temperature range examined. The temperature dependence of the AC magnetic susceptibility (χ'_{AC}) for three different applied field strengths under ZFC conditions is plotted in Figure 3-16. The superconducting transition broadens and shifts to slightly lower temperature with increasing field strength.

Conclusion. On the basis of our extended Hückel calculations (which are limited by their dependence on the availability of accurate atomic parameters), we are unable to provide a concrete explanation for the observation of superconductivity in $La_{13}Ga_8Sb_{21}$. However, we can speculate, in a very qualitative manner, on its origin. The $La_{13}Ga_8Sb_{21}$ structure consists of classical covalently-bonded $GaSb_3$ units enclosed in a non-classical network, composed of $[Sb_5]$ ribbons connected by Ga_6 rings, containing delocalized bonding. In the band structures of $La_{13}Ga_8Sb_{21}$, narrow quasi-molecular bands, derived from the stacked $GaSb_3$ units, and dispersive bands originating from the channel-defining

network, are present near the Fermi level. In this respect, the electronic situation is similar to that in the superconducting carbide halides, such as $Y_2Br_2C_2$, in which an extensive rare-earth metal–metal bonding network, the source of band broadening, encloses finite C_2 units that give rise to narrow bands.[9a] The co-existence of localized states and steep bands at the Fermi level has been proposed as a fingerprint in the search for superconductivity.[9] Unfortunately, this hypothesis does not explain why $La_{12}Ga_4Sb_{23}$, with crystal and electronic structures that are closely related to those of $La_{13}Ga_8Sb_{21}$, does not undergo a superconducting transition (down to 2 K). Nevertheless, the appearance of superconductivity in $La_{13}Ga_8Sb_{21}$, a compound at the "Zintl border" featuring classical and non-classical bonding networks, provides impetus for the continued exploration of systems with reduced electronegativity differences between the component atoms.

Table 3-1. Extended Hückel parameters.

Atom	Orbital	H_{ii} (eV)	ζ_{i1}	c_1	ζ_{i2}	c_2
Ga	$4s$	−14.58	1.77			
	$4p$	−6.75	1.55			
Sb	$5s$	−18.8	2.323			
	$5p$	−11.7	1.999			
La	$6s$	−6.5613	2.14			
	$6p$	−4.3769	2.08			
	$5d$	−7.5155	3.78	0.77651	1.381	0.45861

Table 3-2. Summary of resistivity data for $RE_{12}Ga_4Sb_{23}$.

Compound	$\rho_{300\,K}$ (mΩ cm)	$\rho_{300\,K}/\rho_{2\,K}$
$La_{12}Ga_4Sb_{23}$	0.157	1.34
$Ce_{12}Ga_4Sb_{23}$	0.225	1.46
$Pr_{12}Ga_4Sb_{23}$	0.177	1.47
$Nd_{12}Ga_4Sb_{23}$	0.143	2.83
$Sm_{12}Ga_4Sb_{23}$	16.0	1.10
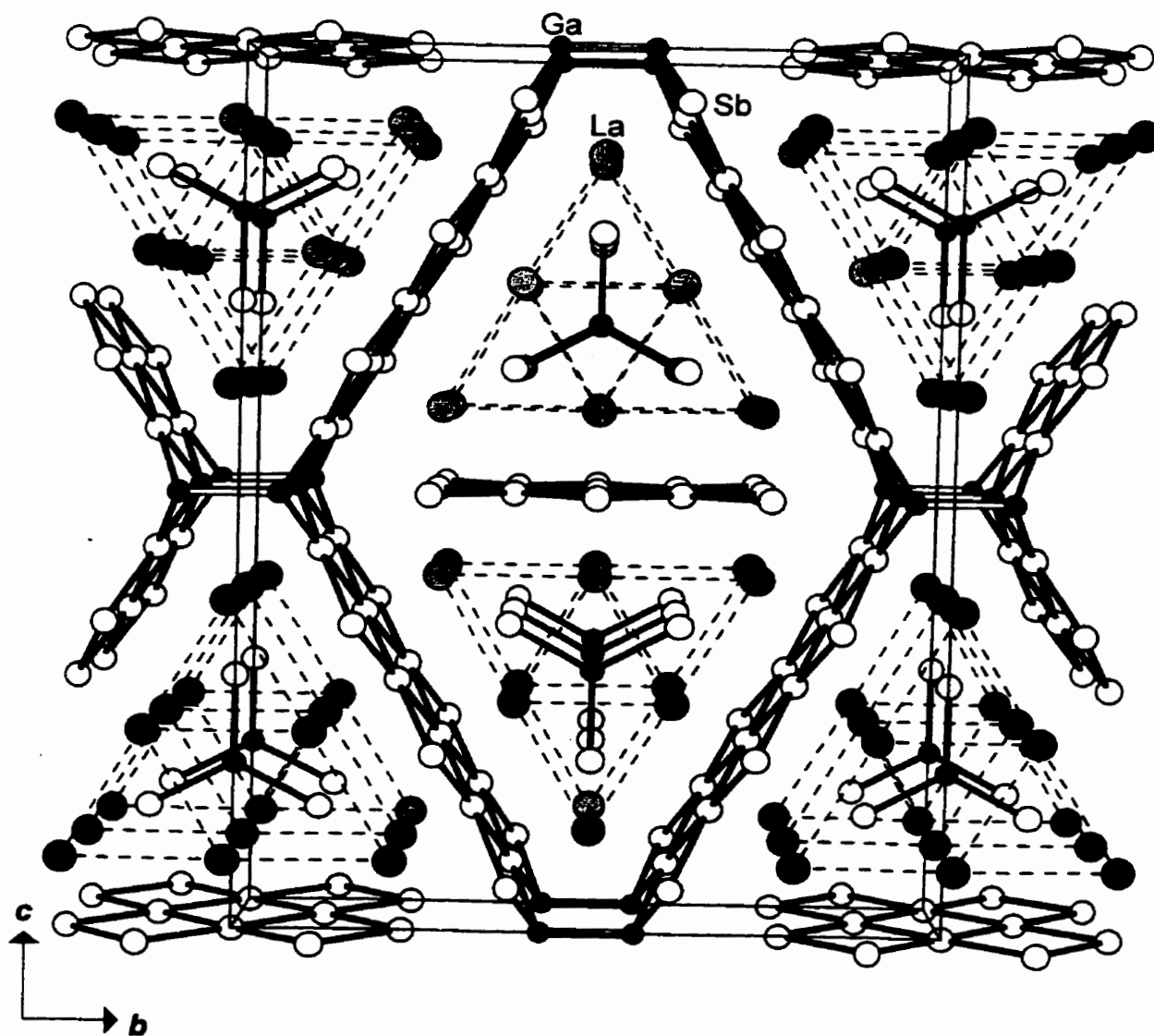
Figure 3-1. Structure of orthorhombic $La_{12}Ga_4Sb_{23}$ viewed down the a axis showing the unit cell outline. The large lightly shaded circles are La atoms, the small solid circles are Ga atoms, and the medium open circles are Sb atoms. The dashed lines merely outline the assemblies of La_6 trigonal prisms.
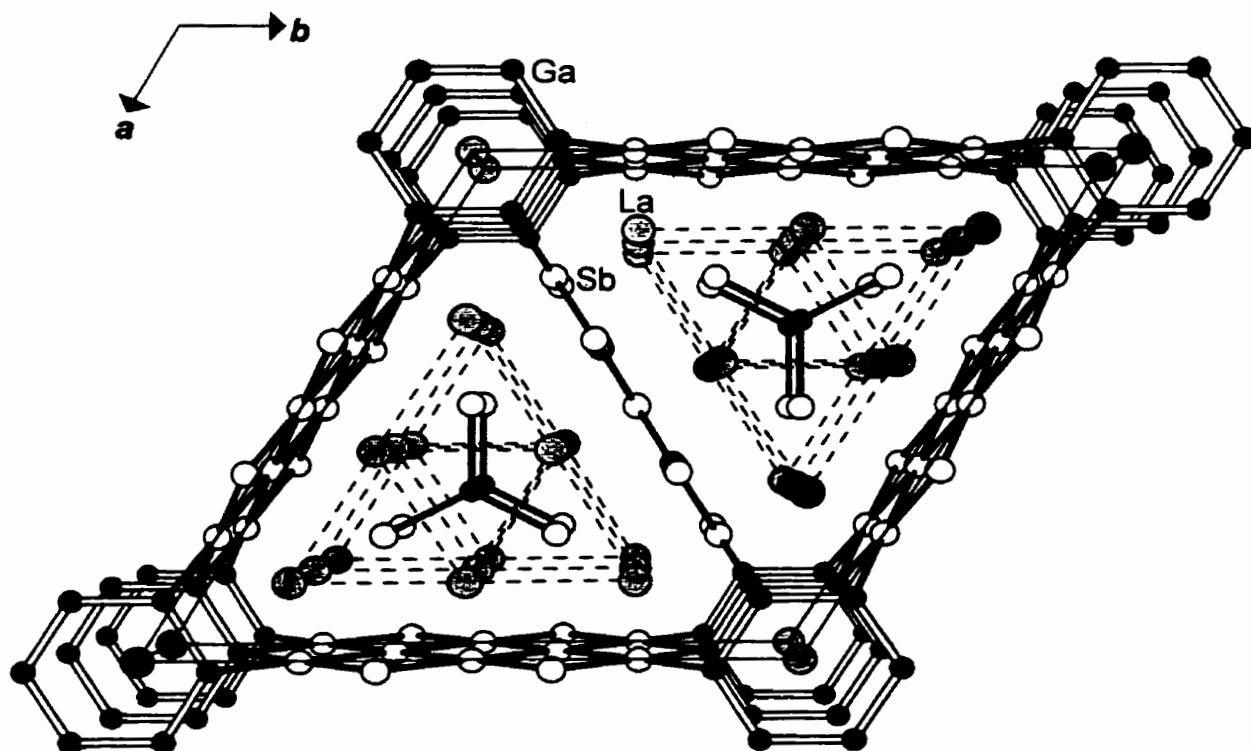
Figure 3-2. Structure of hexagonal La₁₃Ga₈Sb₂₁ viewed down the c axis showing the unit cell outline. The large lightly shaded circles are La atoms, the small solid circles are Ga atoms, and the medium open circles are Sb atoms. The dashed lines merely outline the assemblies of La₆ trigonal prisms.
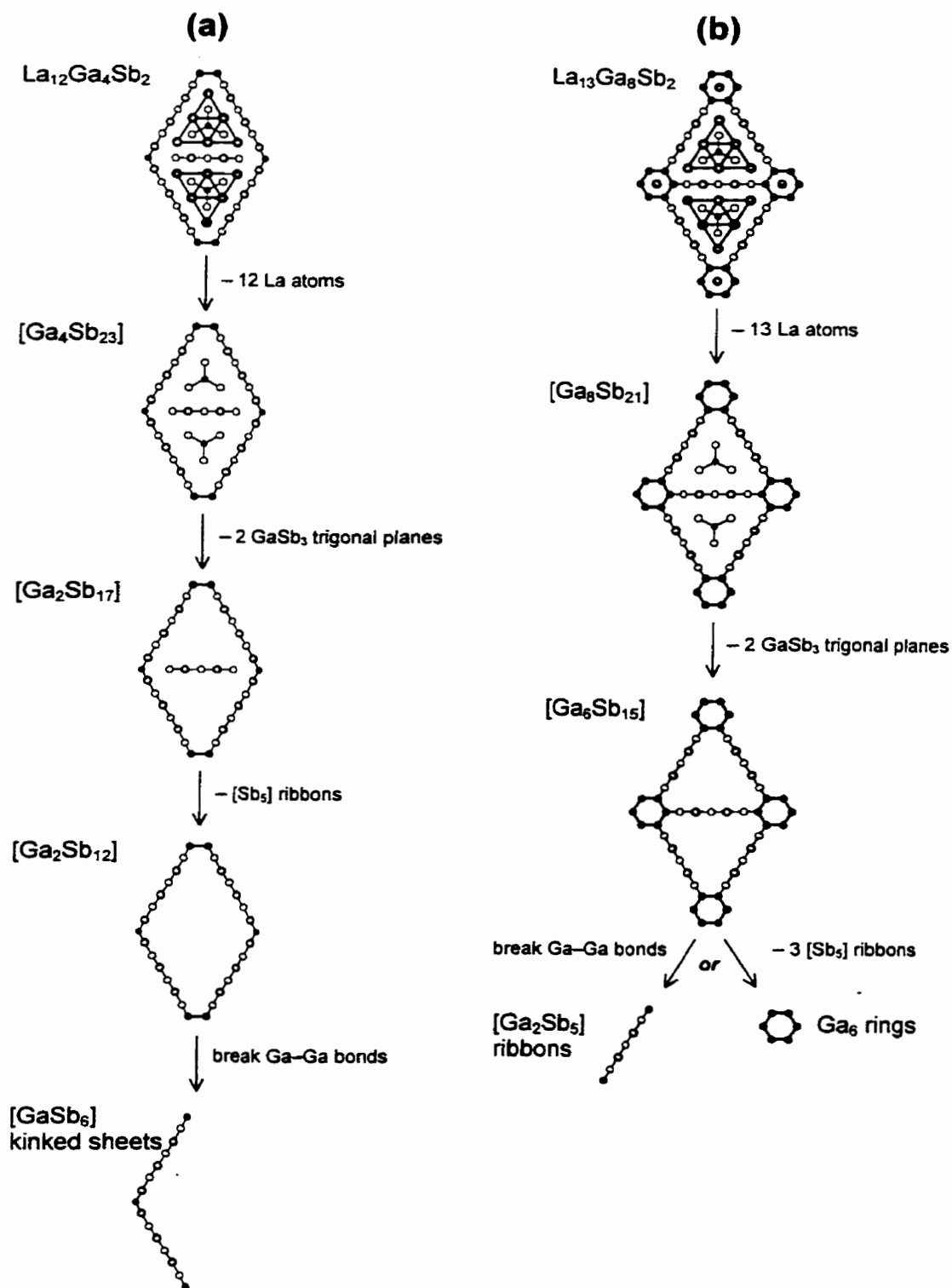
Figure 3-3. Retrotheoretical analysis of (a) La$_{12}$Ga$_4$Sb$_{23}$ and (b) La$_{13}$Ga$_8$Sb$_{21}$, in which the complex three-dimensional structures are decomposed into lower-dimensional substructures.
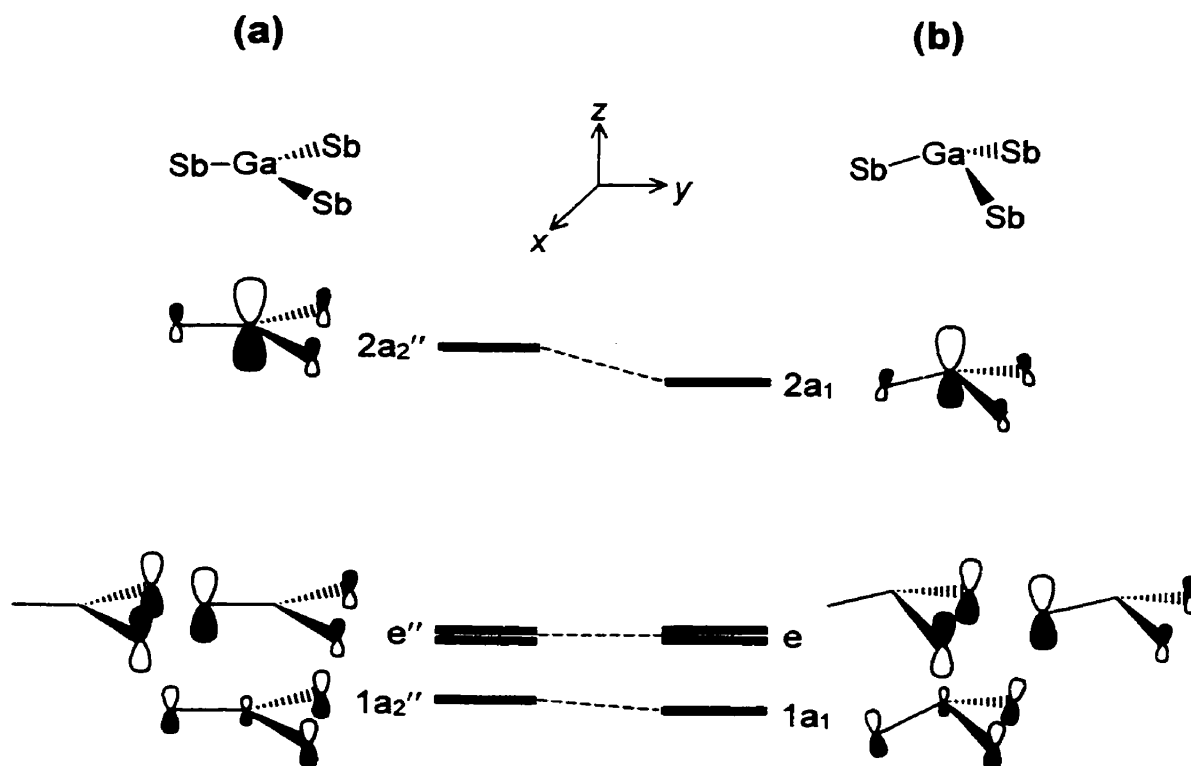
Figure 3-4. Molecular orbital (MO) schemes for the π systems of (a) planar GaSb$_3$ and (b) pyramidally distorted GaSb$_3$. The main consequence of a slight pyramidalization of the GaSb$_3$ unit is a stabilization of the antibonding π* MO.
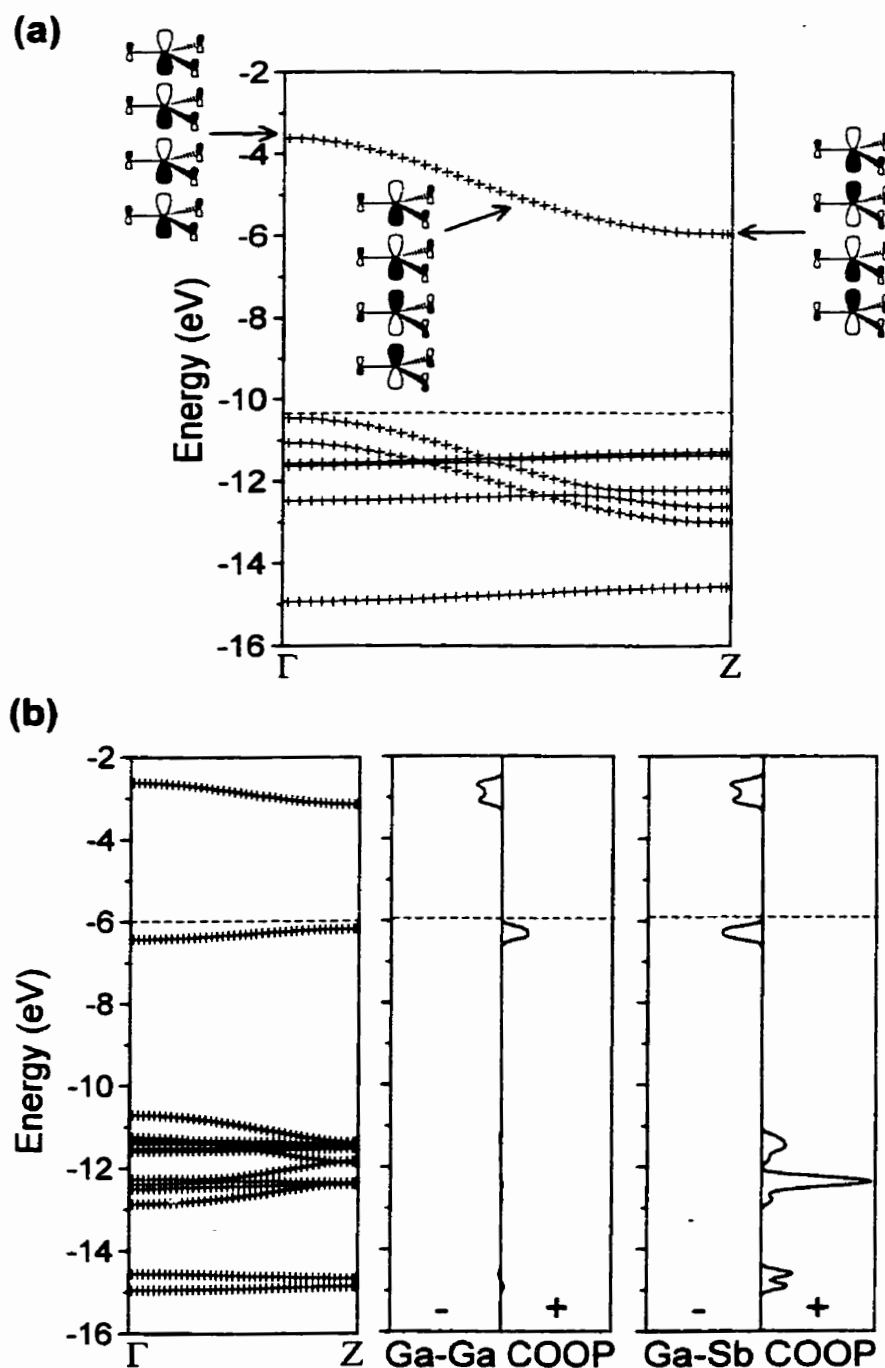
Figure 3-5. (a) Band structure for a one-dimensional stack of planar $GaSb_3^{6-}$ units (**1**), with the composition of crystal orbitals shown at different wave vectors in the lowest unoccupied band. (b) Band structure for a one-dimensional stack of paired pyramidal $GaSb_3^{7-}$ units (**3**), and the crystal orbital overlap population (COOP) curves for the interunit Ga–Ga and intraunit Ga–Sb interactions. The dashed horizontal lines in (a) and (b) represent the Fermi levels for the $[GaSb_3]^{6-}$ and $[GaSb_3]^{7-}$ substructures at the proposed electron counts.
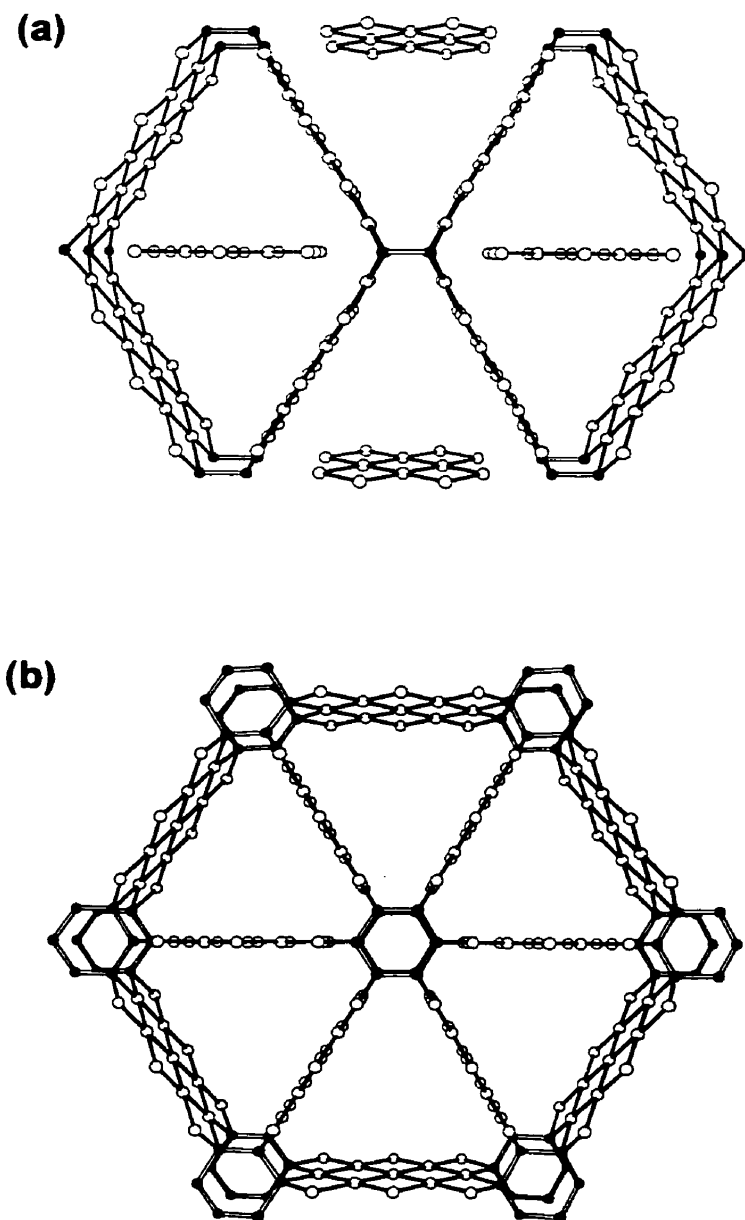
Figure 3-6. View of the channel-defining (a) [Ga₂Sb₁₇] network in La₁₂Ga₄Sb₂₃ and (b) [Ga₆Sb₁₅] network in La₁₃Ga₈Sb₂₁. In (a), six-atom-wide Sb ribbons are linked by Ga₂ pairs, resulting in a three-dimensional [Ga₂Sb₁₂] network, while one five-atom-wide ribbon [Sb₅] remains isolated. In (b), five-atom-wide Sb ribbons are linked by Ga₆ rings to complete the three-dimensional substructure.
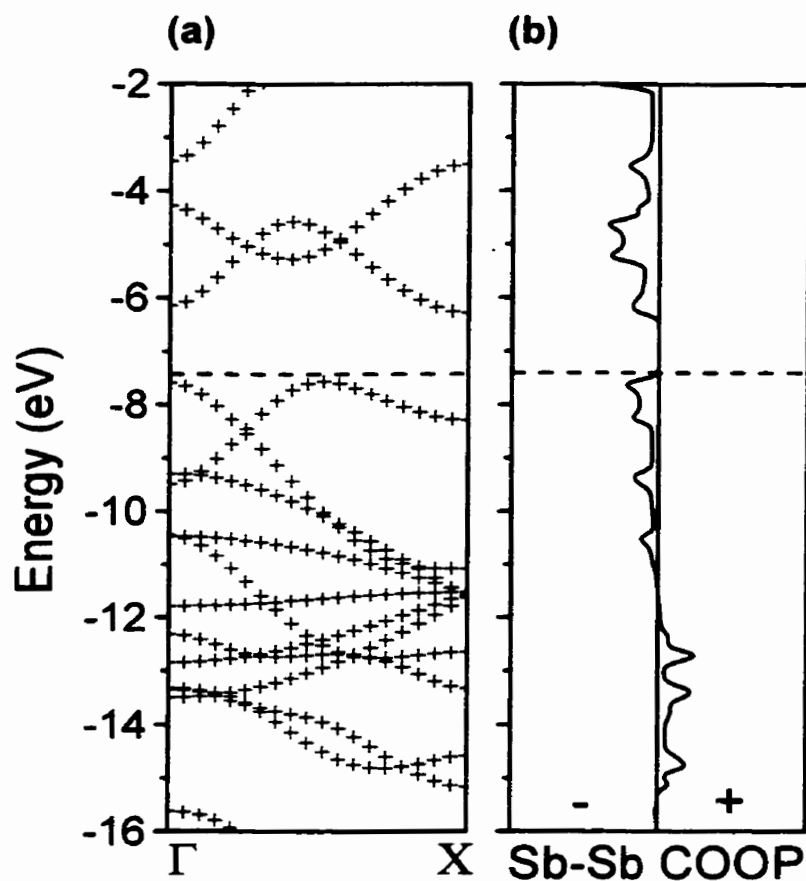
Figure 3-7. (a) Band structure and (b) Sb—Sb crystal orbital overlap population (COOP) curve for the one-dimensional $[Sb_5]^{7-}$ substructure of $La_{12}Ga_4Sb_{23}$. The dashed horizontal lines in (a) and (b) represent the Fermi level at the proposed electron count.
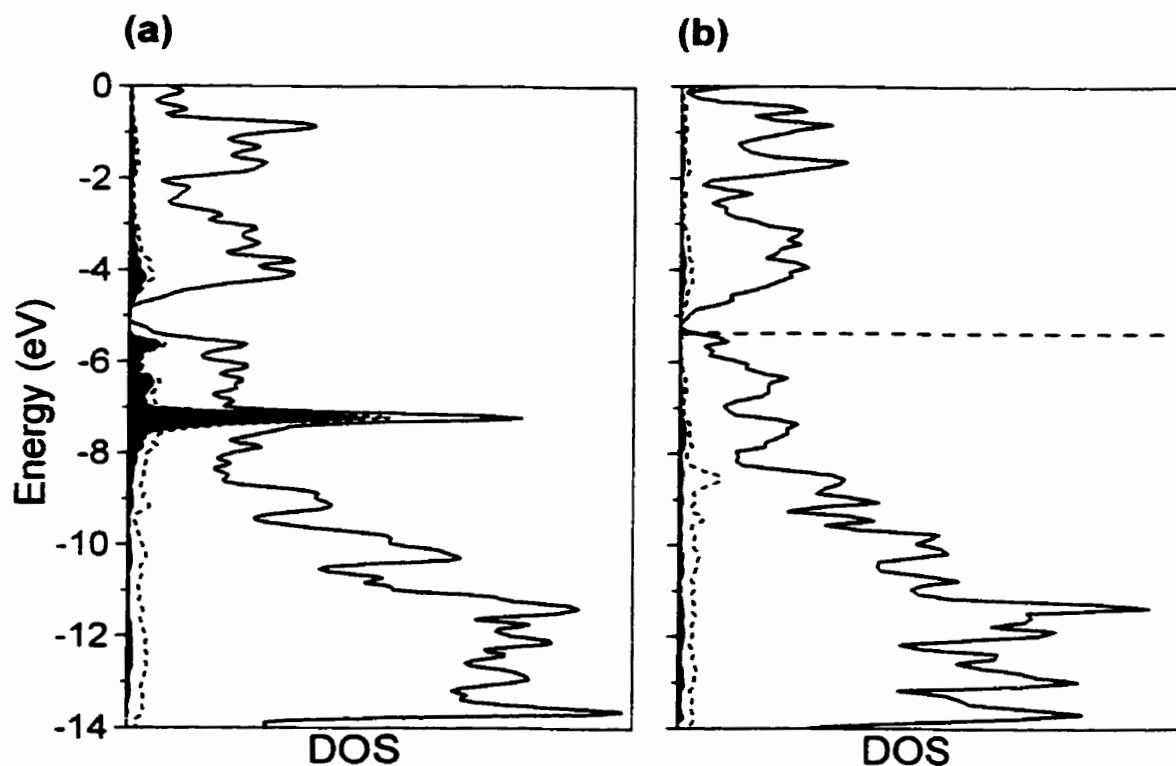
Figure 3-8. Density of states (DOS) for (a) the two-dimensional kinked $[Ga_2Sb_{12}]$ sheet and (b) the actual three-dimensional $[Ga_2Sb_{12}]^{16-}$ substructure of $La_{12}Ga_4Sb_{23}$ after Ga–Ga bonds are formed. The Ga projection is shown by the short dashed line, and the filled area of this curve represents the Ga p_y projection; what remains of the DOS is the Sb projection. Initially, the p_y orbitals participate in narrow (localized) bands. After Ga–Ga bond formation, the Ga p_y orbitals participate in more dispersive bonding and antibonding bands. The dashed horizontal line in (b) represents the Fermi level for $[Ga_2Sb_{12}]^{16-}$ at the proposed electron count.
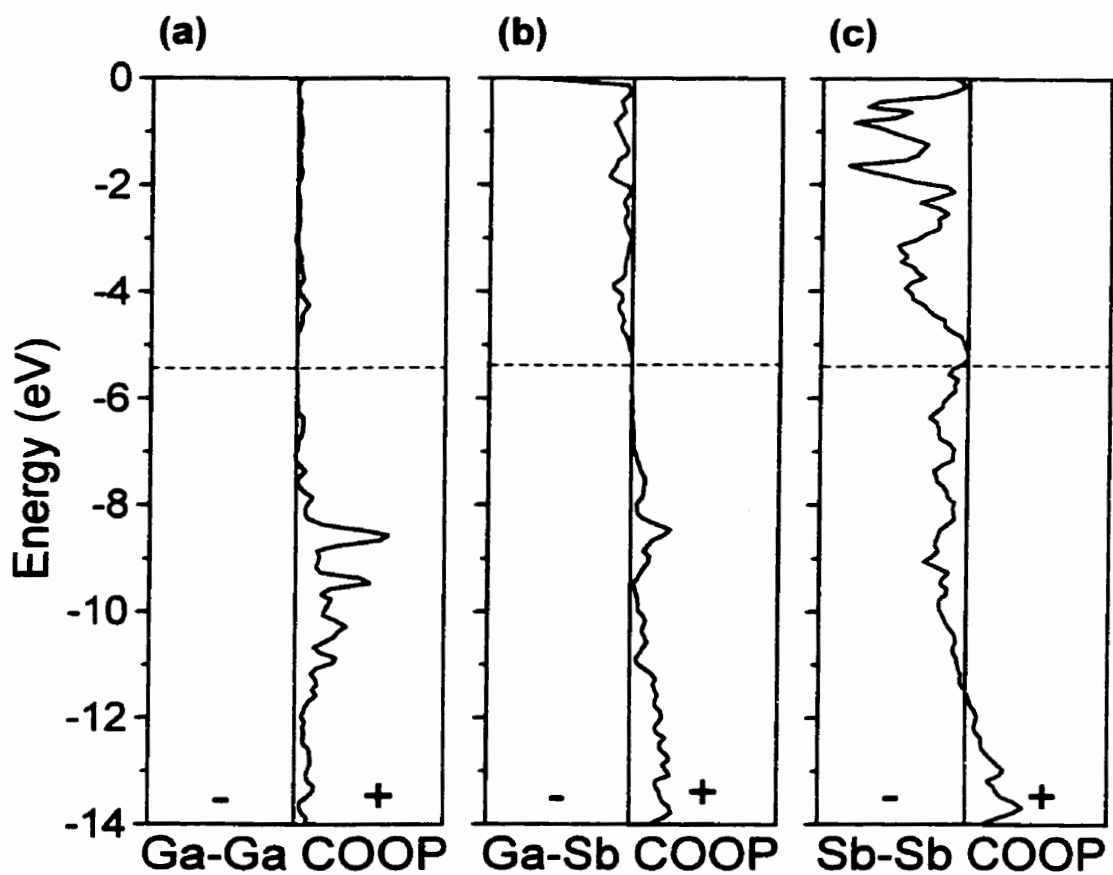
Figure 3-9. Crystal orbital overlap population (COOP) curves for the (a) Ga–Ga, (b) Ga–Sb, and (c) Sb–Sb interactions in the three-dimensional $[Ga_2Sb_{12}]^{16-}$ substructure of $La_{12}Ga_4Sb_{23}$. The dashed horizontal lines in (a)–(c) represent the Fermi level at the proposed electron count.
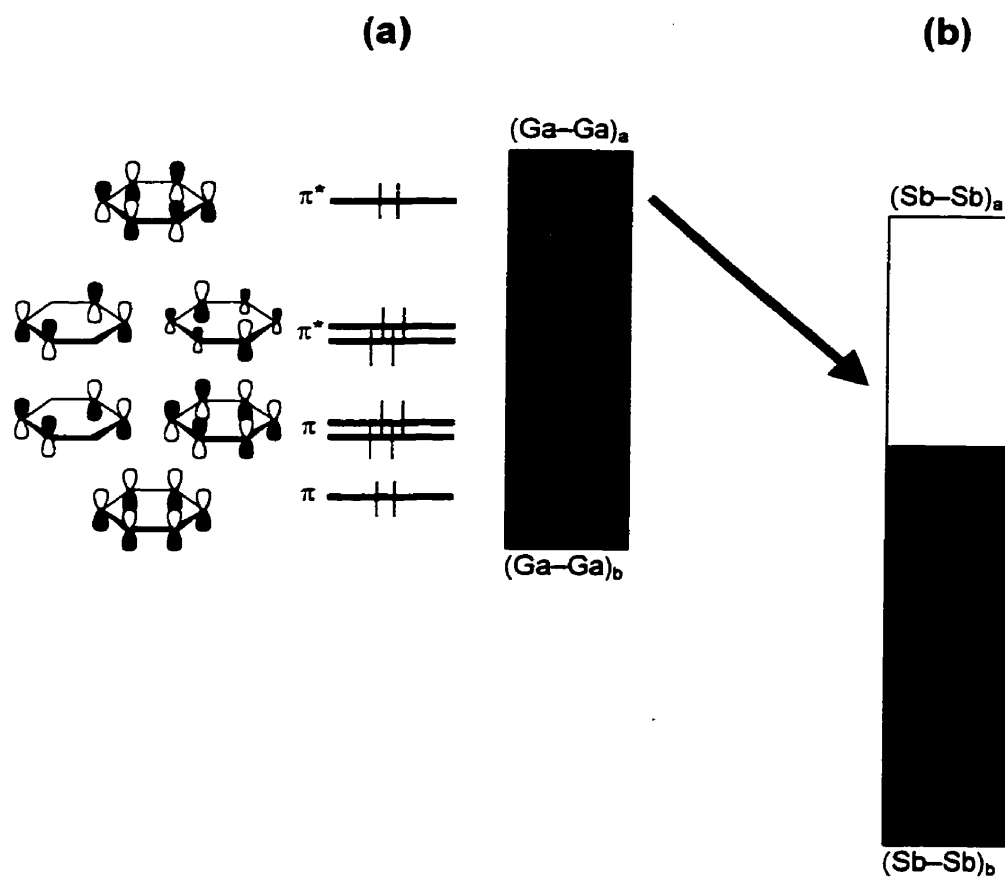
Figure 3-10. (a) When stacked into a one-dimensional array, the π MOs of a planar Ga₆ ring broaden into a block of states with Ga–Ga bonding character at low energy and Ga–Ga antibonding character at high energy. (b) Electrons from the top of the Ga–Ga π block are transferred to empty Sb–Sb antibonding levels available in the Sb block of an [Sb₅] ribbon.
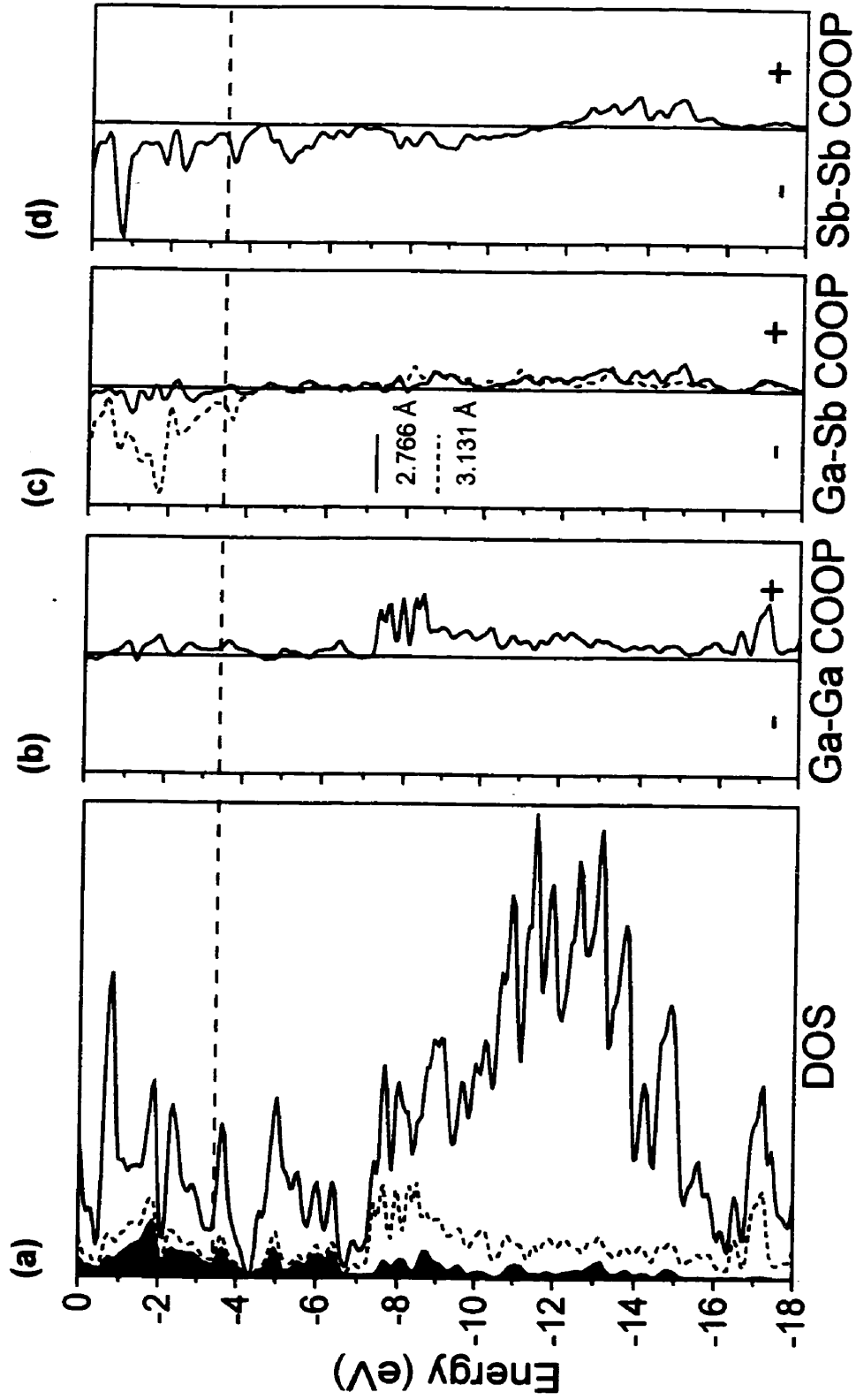
Figure 3-11. (a) Density of states (DOS) for the three-dimensional $[Ga_6Sb_{15}]^{27-}$ substructure of $La_{13}Ga_8Sb_{21}$. The Ga projection is shown by the short dashed line, and the filled area of this curve represents the Ga p_z projection; what remains of the DOS is the Sb projection. Crystal orbital overlap population (COOP) curves for the (b) Ga–Ga, (c) Ga–Sb, and (d) Sb–Sb interactions are also shown. The dashed horizontal lines in (a)–(d) represent the Fermi level at the proposed electron count.
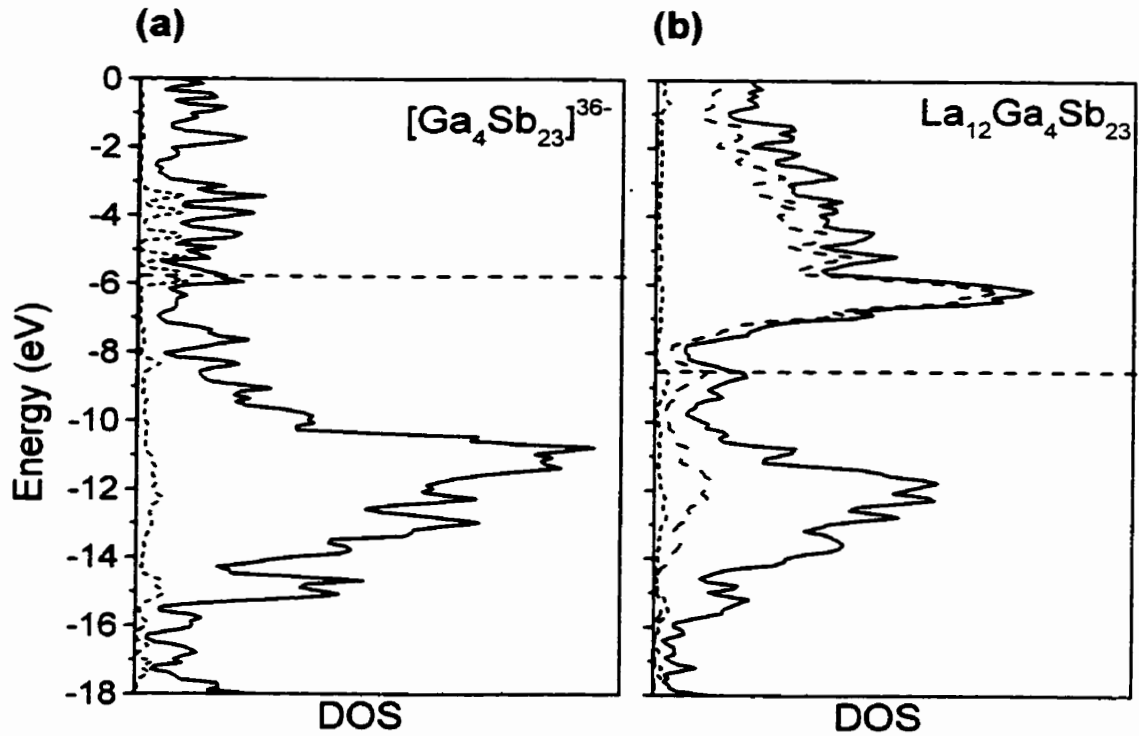
Figure 3-12. Density of states (DOS) for (a) the composite $[Ga_4Sb_{23}]^{36-}$ substructure and (b) the complete $La_{12}Ga_4Sb_{23}$ structure. The Ga projection is shown by the shorter-dashed line, and the La projection in (b) is shown by the longer-dashed line; what remains of the DOS is the Sb projection. The dashed horizontal lines in (a) and (b) indicate the Fermi levels.
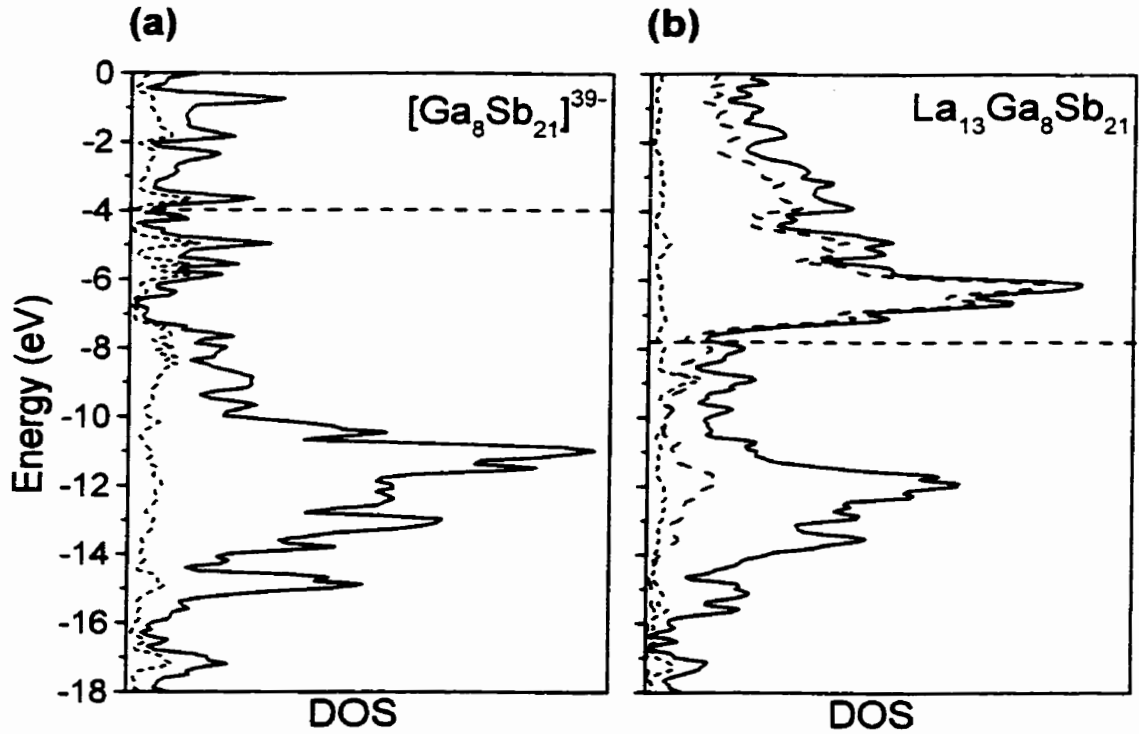
Figure 3-13. Density of states (DOS) for (a) the composite $[Ga_8Sb_{21}]^{39-}$ substructure and (b) the complete $La_{13}Ga_8Sb_{21}$ structure. The Ga projection is shown by the shorter-dashed line, and the La projection in (b) is shown by the longer-dashed line; what remains of the DOS is the Sb projection. The dashed horizontal lines in (a) and (b) indicate the Fermi levels.
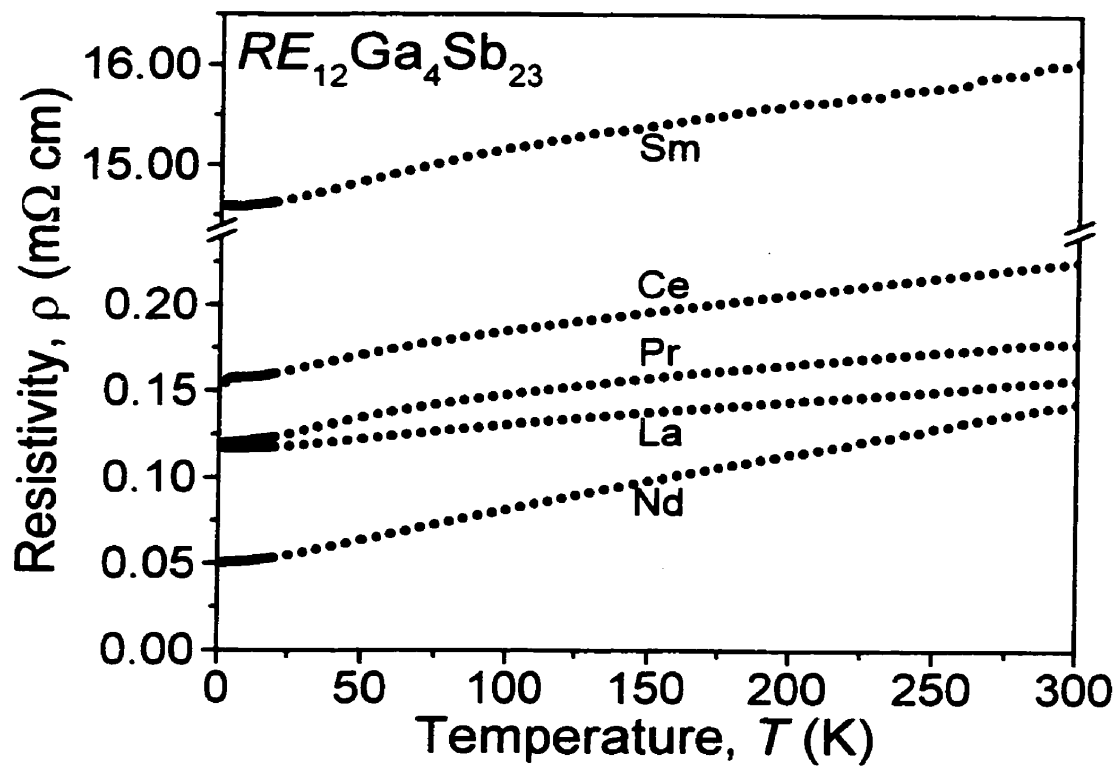
Figure 3-14. Temperature dependence of the resistivities of the $RE_{12}Ga_4Sb_{23}$ series.
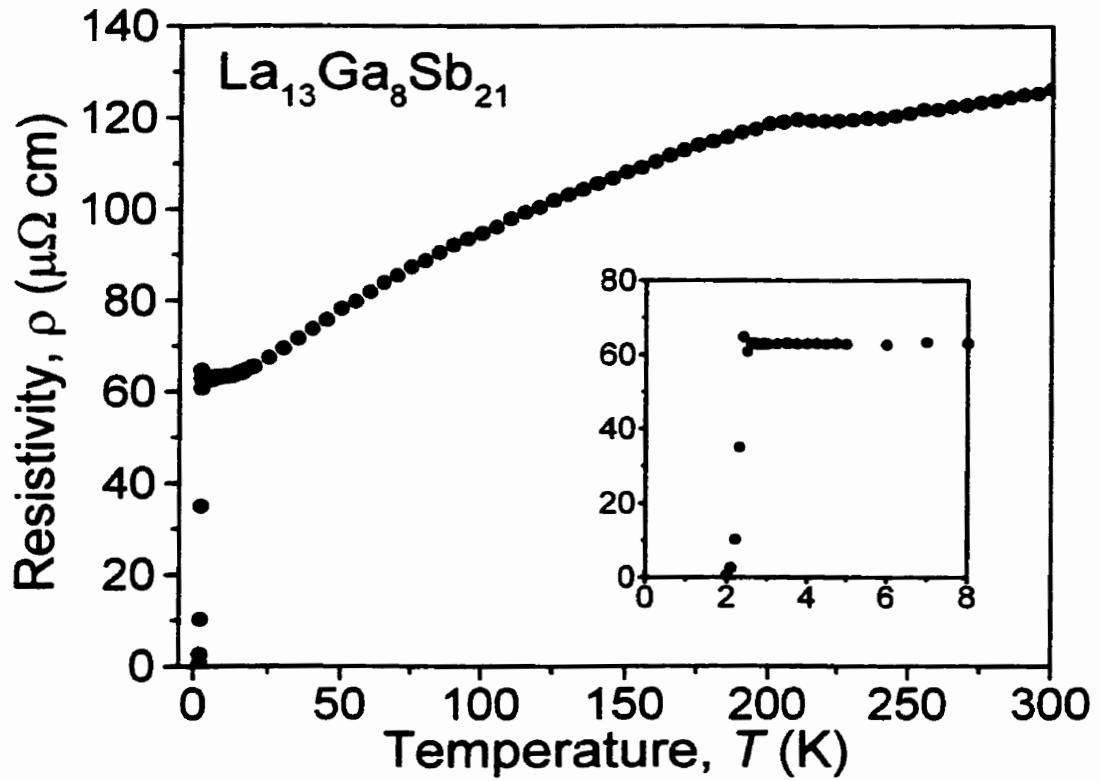
Figure 3-15. Temperature dependence of the resistivity of $La_{13}Ga_8Sb_{21}$. The inset gives an enlarged view showing the superconducting transition more clearly.
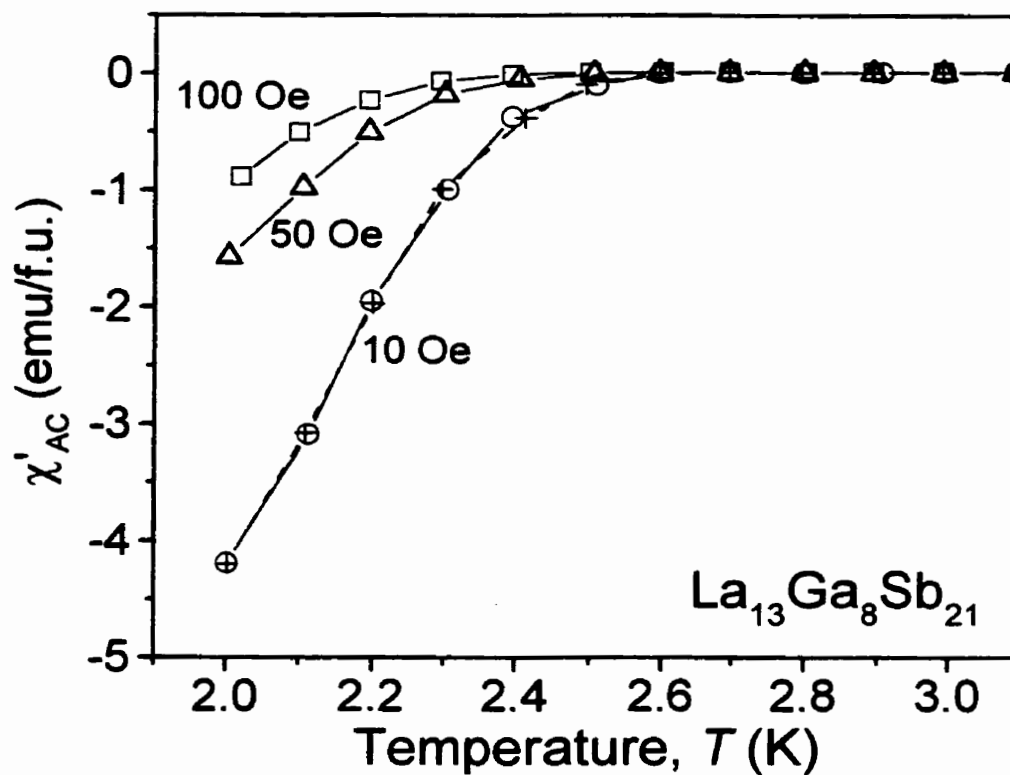
Figure 3-16. Temperature dependence of the zero-field-cooled AC magnetic susceptibility (χ'_{AC}) at three applied field strengths (O 10; Δ 50; □ 100 Oe), and of the field-cooled χ'_{AC} at 10 Oe (+) for La$_{13}$Ga$_8$Sb$_{21}$. The lines are drawn only for guidance.

References

(1) Eisenmann, B.; Cordier, G. In *Chemistry, Structure, and Bonding of Zintl Phases and Ions*; Kauzlarich, S. M., Ed. VCH Publishers: New York, 1996; p. 61.

(2) For example, see the following. (a) Li_3Ga_{14}: Stöhr, J.; Schäfer, H. *Rev. Chim. Minér.* **1982**, *19*, 122. (b) Na_7Ga_{13}: Frank-Cordier, U.; Cordier, G.; Schäfer, H. *Z. Naturforsch. B: Anorg. Chem. Org. Chem.* **1982**, *37*, 119. (c) KGa_3: Belin, C.; Ling, R. G. *C. R. Séances Acad. Sci. Ser. 2*; **1982**, *294*, 1083. (d) $RbGa_7$: Belin, C. *Acta Crystallogr. Sect. B: Struct. Crystallogr. Cryst. Chem.* **1981**, *37*, 2060.

(3) Wade, K. *Inorg. Chem. Radiochem.* **1976**, *18*, 1.

(4) For example, see the following. (a) RE_3MSb_5 (RE = La–Nd, Sm; M = Ti, Zr, Hf, Nb): Bolloré, G.; Ferguson, M. J.; Hushagen, R. W.; Mar, A. *Chem. Mater.* **1995**, *7*, 2229. (b) $Eu_{14}MnSb_{11}$: Rehr, A.; Kauzlarich, S. M. *J. Alloys Compd.* **1994**, *207/208*, 424.

(5) For example, see the following. (a) $RE_6Ge_{5-x}Sb_{11+x}$ (RE = La–Nd, Sm, Gd–Dy): Lam, R.; McDonald, R.; Mar, A. *Inorg. Chem.* **2001**, *40*, 952. (b) RE_6MSb_{15} (RE = La, Ce; M = Mn, Cu, Zn): Sologub, O.; Vybornov, M.; Rogl, P.; Hiebl, K.; Cordier, G.; Woll, P. *J. Solid State Chem.* **1996**, *122*, 266.

(6) For example, see the following. (a) $REIn_{0.8}Sb_2$ (RE = La–Nd): Ferguson, M. J.; Ellenwood, R. E.; Mar, A. *Inorg. Chem.* **1999**, *38*, 4503. (b) $RESn_{0.75}Sb_2$ (RE = La–Nd, Sm): Ferguson, M. J.; Hushagen, R. W.; Mar, A. *Inorg. Chem.* **1996**, *35*, 4505. (c) $RESb_2$ (RE = La–Nd, Sm): Wang, R.; Steinfink, H. *Inorg. Chem.* **1967**, *6*, 1685.

(7) Papoian, G. A.; Hoffmann, R. *Angew. Chem. Int. Ed.* **2000**, *39*, 2408.

(8) Mills, A. M.; Mar, A. *Inorg. Chem.* **2000**, *39*, 4599.

(9) For example, see the following. (a) Simon, A. *Angew. Chem. Int. Ed. Engl.* **1997**, *36*, 1788. (b) Köckerling, M.; Johrendt, D.; Finckh, E. W. *J. Am. Chem. Soc.* **1998**, *120*, 12297. (c) Fässler, T. F.; Kronseder, C. *Angew. Chem. Int. Ed. Engl.* **1997**, *36*, 2683.

(10) Whangbo, M.-H.; Hoffmann, R. *J. Am. Chem. Soc.* **1978**, *100*, 6093.

(11) Hoffmann, R. *Solids and Surfaces: A Chemist's View of Bonding in Extended Structures*; VCH Publishers: New York, 1988.

(12) Landrum, G. A. *YAeHMOP: Yet Another extended Hückel Molecular Orbital Package*; http://overlap.chem.cornell.edu:8080/yaehmop.html, 1995.

(13) Lulei, M.; Martin, J. D.; Hoistad, L.; Corbett, J. D. *J. Am. Chem. Soc.* **1997**, *119*, 513.

(14) Hinze, J.; Jaffé, H. H. *J. Phys. Chem.* **1963**, *67*, 1501.

(15) Canadell, E.; Eisenstein, O.; Rubio, J. *Organometallics*; **1984**, *3*, 759.

(16) Hughbanks, T.; Hoffmann, R.; Whangbo, M.-H.; Stewart, K. R.; Eisenstein, O.; Canadell, E. *J. Am. Chem. Soc.* **1982**, *104*, 3876.

(17) Papoian, G.; Hoffmann, R. *J. Solid State Chem.* **1998**, *139*, 8.

(18) *Chemistry, Structure, and Bonding of Zintl Phases and Ions*; Kauzlarich, S. M., Ed. VCH Publishers: New York, 1996.

(19) Blase, W.; Cordier, G.; Somer, M. *Z. Kristallogr.* **1992**, *199*, 277.

(20) Somer, M.; Carrillo-Cabrera, W.; Nuß, J.; Peters, K.; von Schnering, H. G.; Cordier, G. *Z. Kristallogr.* **1996**, *211*, 479.

(21) Cordier, G.; Ochmann, H. *Z. Naturforsch. B: Chem. Sci.* **1990**, *45*, 277.

(22) Albright, T. A.; Burdett, J. K.; Whangbo, M.-H. *Orbital Interactions in Chemistry*; John Wiley and Sons: New York, 1985.

(23) Garcia, E.; Corbett, J. D. *J. Solid State Chem.* **1988**, *73*, 452.

(24) Kutzelnigg, W. *Angew. Chem. Int. Ed. Engl.* **1984**, *23*, 272.

(25) Ferguson, M. J.; Hushagen, R. W.; Mar, A. *J. Alloys Compd.* **1997**, *249*, 191.

(26) Deakin, L.; Lam, R.; Mar, A. *Inorg. Chem.* **2001**, *40*, 960.

Chapter 4

Layered Rare-Earth Gallium Antimonides $REGaSb_2$ $(RE$ = La–Nd, Sm) [†]

Introduction

A large number of alkali and alkaline-earth metal gallium antimonides with a remarkable variety of structures have been characterized.[1] The bonding in these compounds can be successfully rationalized using the Zintl concept.[2] Accordingly, the more electropositive alkali or alkaline-earth metal donates its valence electrons to the more electronegative main-group elements, which then form bonds, homoatomic ones if necessary, to satisfy the octet rule. The resulting anionic substructures are manifested as discrete $GaSb_3$ trigonal planar or $GaSb_4$ tetrahedral units, or extended networks built up from these units. All exhibit strong covalent bonds between atoms with completed valence shells, as is characteristic of normal valence compounds.

Reduced electronegativity differences between the electropositive and electronegative components render the applicability of the Zintl concept on more questionable grounds. As one moves leftward in the periodic table , towards the group 13 and 14 elements, in choosing the electronegative (p-block) component, clusters and

---

[†] A version of this chapter has been published. Mills, A. M; Mar, A. *J. Am. Chem. Soc.* **2001**, *123*, 1151. Copyright 2001 American Chemical Society.

networks abound in the resulting structures.[2] But one can also move to the right in the periodic table in choosing the electropositive element, although such cases have not been examined as extensively. For many ternary rare-earth main-group element antimonides, the occurrence of non-classical bonding patterns requires that multicentre or partial bonding be invoked.[3] In our attempts to extend the diverse structural chemistry of the alkali or alkaline-earth metal gallium antimonides to rare-earth analogues, we have recently isolated the first examples of rare-earth gallium antimonides, $La_{13}Ga_8Sb_{21}$ and $RE_{12}Ga_4Sb_{23}$ (RE = La–Nd, Sm).[4] Both of these structures contain the characteristic trigonal planar $GaSb_3$ units of the alkali and alkaline-earth metal gallium antimonides, as well as more unusual Ga–Ga and Sb–Sb homoatomic bonding networks. One-dimensional square ribbons with intermediate Sb–Sb bonding are linked by either Ga_2 pairs (in $RE_{12}Ga_4Sb_{23}$) or six-membered Ga rings (in $La_{13}Ga_8Sb_{21}$). Here, we report the synthesis of a series of rare-earth gallium antimonides, $REGaSb_2$ (RE = La–Nd, Sm), that crystallize in one of two structure types, $SmGaSb_2$ (for RE = La, Sm) or $NdGaSb_2$ (for RE = Ce–Nd). In the $REGaSb_2$ structures, we find two-dimensional "Zintl layers" containing strong homoatomic Ga–Ga bonding in zigzag chains, in addition to strong Ga–Sb bonding. These alternate with Sb square sheets containing multicentre Sb–Sb bonding that are typical of binary and ternary rare-earth antimonides. The $REGaSb_2$ compounds are the newest members of a growing family of rare-earth main-group antimonides, $REM_{1-x}Sb_2$ (M = In, Sn), featuring strong M–M and M–Sb bonding in $^2_\infty[MSb]$ layers and intermediate Sb–Sb bonding in square nets.[5,6]

Experimental Section

Synthesis. Starting materials were powders of the rare-earth elements (99.9%, Alfa-Aesar), Sb powder (99.995%, Aldrich), and Ga granules (99.9999%, Alfa-Aesar). Reactions were carried out on a 0.4-g scale in evacuated fused-silica tubes (8-cm length; 10-mm i.d.). Elemental compositions were determined by energy-dispersive X-ray (EDX) analysis on a Hitachi S-2700 scanning electron microscope. X-ray powder patterns were collected on an Enraf-Nonius FR552 Guinier camera (Cu $K\alpha_1$ radiation; Si standard) and analyzed with the Filmscan and Jade 3.0 software packages.[7]

Attempts to grow single crystals of $La_{13}Ga_8Sb_{21}$ using a tin flux led to isolation of a new series of compounds of composition $LaGa_{1-x}Sn_xSb_2$. The Sn-rich end member of this series, $LaSn_{0.75}Sb_2$, has been described previously.[6] Although this reaction method yields large single crystals, some Sn is always incorporated into the product, and we were unable to synthesize the Ga-rich end member $LaGaSb_2$ by this route. Subsequent stoichiometric reactions at the composition $REGaSb_2$ (RE = La–Nd, Sm) led to the formation of products that were significantly contaminated with the $Pr_{12}Ga_4Sb_{23}$-type phases, except in the case of Sm. Single black plate-like crystals of $SmGaSb_2$ (Anal. (mol%): Sm 28.4(5), Ga 21.1(2), Sb 50.4(5)% (average of 4 analyses)) were obtained from a reaction of Sm, Ga, and Sb in the ratio 1:1:2 heated at 900 °C for 3 days, cooled to 500 °C over 4 days, then to 20 °C over 18 h. Use of an excess of Ga minimizes the formation of $Pr_{12}Ga_4Sb_{23}$-type impurities. Mixtures of the elements RE (RE = La–Nd), Ga, and Sb in the ratio 1:2:2, heated as before, resulted in powder products of $REGaSb_2$ that invariably contained unreacted Ga. The powder patterns of these products indicated that $LaGaSb_2$ also crystallizes in the orthorhombic $SmGaSb_2$-type phase. A more

symmetric tetragonal phase is adopted by RE = Ce–Nd. Grey rectangular plates of NdGaSb$_2$ (Anal. (mol%): Nd 24.8(3), Ga 27(1), Sb 48(1)% (average of 2 analyses)) were isolated from a reaction of Nd, Ga, and Sb in the ratio 1:2:2 heated at 800 °C for 3 days and then cooled to 20 °C over 18 h. The powder patterns of the REGaSb$_2$ phases, prepared at 900 °C as described above, were indexed, and the cell parameters refined with the use of the program POLSQ[8] are given in Table 4-1. The observed and calculated interplanar distances, as well as intensities determined using the program LAZY-PULVERIX,[9] are listed in Tables A-7 to A-11.

Structure Determination. Preliminary cell parameters for SmGaSb$_2$ and NdGaSb$_2$ were determined from Weissenberg photographs. Final cell parameters were determined from least-squares analysis of the setting angles of 24 reflections centred on an Enraf-Nonius CAD4 diffractometer in the range $20° \leq 2\theta(\text{Mo } K\alpha) \leq 50°$ for SmGaSb$_2$ and $20° \leq 2\theta(\text{Mo } K\alpha) \leq 42°$ for NdGaSb$_2$. Intensity data were collected at 22 °C with the θ–2θ scan technique in the range $4° \leq 2\theta(\text{Mo } K\alpha) \leq 70°$. Crystal data and further details of the data collections are given in Table 4-2. All calculations were carried out using the SHELXTL (Version 5.1) package.[10] Conventional atomic scattering factors and anomalous dispersion corrections were used.[11] Intensity data were reduced and averaged, and face-indexed numerical absorption corrections were applied in XPREP. Initial atomic positions were located by direct methods using XS, and refinements were performed by least-squares methods using XL.

Weissenberg photographs of SmGaSb$_2$ displayed Laue symmetry mmm and systematic extinctions (hkl: $h + k = 2n + 1$; $00l$, $l = 2n + 1$) consistent uniquely with the non-centrosymmetric orthorhombic space group $C222_1$. In particular, inspection of the

h0l reflections with $l = 2n + 1$ in the reciprocal space plots clearly confirmed the absence of a *c*-glide plane in SmGaSb$_2$ (out of 38 such data, 17 had $I > 3\sigma(I)$), ruling out the centrosymmetric space group *Cmcm*. The initial positions of the *RE* and Sb atoms in SmGaSb$_2$ (*C*222$_1$) were taken from those in the closely related structure of LaSn$_{0.75}$Sb$_2$ (*Cmcm*).[6] A first refinement revealed considerable electron density at a site located between [SmSb$_2$] layers. This site was assigned to Ga based on reasonable Ga–Sb(1) and Ga–Ga distances. The Ga atoms form chains running along the *c* axis that impart chirality to the SmGaSb$_2$ structure. In accordance with the calculated Flack parameter of 0.54(6),[11] the structure was refined as a racemic twin. Since substoichiometric occupation of the Sn site was observed in LaSn$_{0.75}$Sb$_2$, refinements were performed in which the occupancies of successive atoms were allowed to vary. These resulted in essentially 100% occupancy for all atoms, including Ga, giving the formula SmGaSb$_2$, consistent with the EDX analyses.

Reciprocal space plots of NdGaSb$_2$ revealed tetragonal Laue symmetry 4/*mmm* and systematic extinctions (*hkl*: $h + k + l = 2n + 1$; *hk*0: $h = 2n + 1$; *hhl*: $2h + l = 4n + 1$, 2 or 3) consistent uniquely with the space group *I*4$_1$/*amd*. Initial positions for the Nd and Sb atoms were found by direct methods. An initial refinement revealed additional electron density between [NdSb$_2$] layers that was assigned as Ga by analogy with SmGaSb$_2$. In this case, however, the mirror plane at 0, *y*, *z* generates two sets of Ga zigzag chains, resulting in close Ga–Ga contacts (1.43 and 2.17 Å). The Ga site must, therefore, have a maximum occupancy of 50% (only one set of Ga chains may be present). The possibility that the disorder in the Ga position is a consequence of improper choice of space group was considered; however, the disordered Ga chains

reappeared when the structure was solved in the non-centrosymmetric orthorhombic space group $I2_12_12_1$. As above, refinements allowing the occupancies of successive atoms to vary freely resulted in essentially half occupancy for the Ga site and full occupancy for all other atoms. The final formula, $NdGaSb_2$ (with $Z = 8$), is consistent with EDX analyses.

In both cases, the final refinement led to a featureless electron density map ($\Delta\rho_{max}$ = 3.32, $\Delta\rho_{min}$ = −3.52 e Å^{-3} for $SmGaSb_2$; $\Delta\rho_{max}$ = 3.22, $\Delta\rho_{min}$ = −1.95 e Å^{-3} for $NdGaSb_2$) and to reasonable displacement parameters for all atoms, except Ga. The components of the Ga thermal ellipsoids in the plane of the Ga chains are somewhat large in both structures. This behaviour may represent the tendency of the atoms inserted between the [$RESb_2$] layers to disorder over several sites, as has been observed in $LaSn_{0.75}Sb_2$.[6] The atomic positions of $SmGaSb_2$ and $NdGaSb_2$ were standardized with the program STRUCTURE TIDY.[13] Final values of the positional and displacement parameters are given in Table 4-3, and interatomic distances are listed in Table 4-4. Anisotropic displacement parameters are listed in Table A-12.

Band Structure. A tight-binding extended Hückel band structure calculation was performed on the anionic [$GaSb_2$]$^{3-}$ substructure of $SmGaSb_2$ using the EHMACC suite of programs.[14,15] The atomic parameters used are listed in Table 4-5.[16-18] Properties were extracted from the band structure using 108 k points in the irreducible portion of the Brillouin zone.

Results and Discussion

Structures. The structures of $SmGaSb_2$ (Figure 4-1) and $NdGaSb_2$ (Figure 4-2) are closely related. Both are composed of two-dimensional anionic layers of composition $\frac{2}{\infty}[GaSb]$ and $\frac{2}{\infty}[Sb]$ separated by RE atoms. Different stacking arrangements of these layers generate the two structure types. We will first describe the features common to both structure types, and then consider the relationship between them.

The $\frac{2}{\infty}[GaSb]$ layers are "Zintl layers" containing strong covalent bonding. Each Ga atom is coordinated by two Sb(1) atoms and two other Ga atoms ($SmGaSb_2$, Ga–Sb(1) 2.7606(12) Å, Ga–Ga 2.539(2) Å; $NdGaSb_2$, Ga–Sb(1) 2.7485(17) Å, Ga–Ga 2.605(3) Å) in a distorted tetrahedral fashion (Figure 4-3a). The Ga atoms that are viewed as the ligands in a given $Ga(Ga_2Sb_2)$ tetrahedron serve as centres of adjacent coordination polyhedra so as to form infinite one-dimensional zigzag Ga chains. Parallel Ga chains are then joined by Ga–Sb bonding to complete the $\frac{2}{\infty}[GaSb]$ layer. In the case of $NdGaSb_2$, the zigzag Ga chains are disordered over two possible configurations, as shown in Figure 4-4. Ga-centred tetrahedra are the basic building blocks of many alkali and alkaline-earth metal gallium antimonide Zintl phases, and the Ga–Sb bond distances in these phases are similar to those above (for example, the chains of corner-sharing $GaSb_4$ tetrahedra in Sr_3GaSb_3 contain Ga–Sb distances of 2.642–2.798 Å[2b]). The $\frac{2}{\infty}[GaSb]$ layer contains Ga–Ga bonding, which, while unusual for alkali and alkaline-earth metal gallium antimonides, appears to be a recurring feature in rare-earth metal gallium antimonides. Only one antimonide Zintl phase, $Na_2Ga_3Sb_3$, features a Ga–Ga bond (2.541(3) Å).[2a] However, the zigzag Ga chains in $SmGaSb_2$ and $NdGaSb_2$ resemble, but differ in conformation from, the *cis-trans* Ge chains formed by a similar

connectivity of $Ge(Ge_2As_2)$ tetrahedra found in the three-dimensional anionic substructure of $BaGe_2As_2$.[19] Isolated Ga zigzag chains with Ga–Ga bond distances (2.623(1) Å) comparable to those in $SmGaSb_2$ and $NdGaSb_2$ are contained in the binary gallide Li_2Ga.[20]

Within the $^2_\infty[Sb]$ layers of $SmGaSb_2$ and $NdGaSb_2$, each Sb atom is bonded to four other Sb atoms ($SmGaSb_2$, Sb(2)–Sb(2) 3.0549(2) Å; $NdGaSb_2$, Sb(2)–Sb(3) 3.0749(2) Å), forming a flat square sheet. (Even though $SmGaSb_2$ is orthorhombic, the Sb(2)–Sb(2)–Sb(2) angles are close to 90° (89.692(9)–90.307(9)°) as a result of the a and c parameters being nearly the same.) These Sb–Sb distances are long compared to the intralayer Sb–Sb bond length (2.908 Å) but shorter than the weakly bonding interlayer distance (3.355 Å) in elemental Sb.[21] Rather, they are typical of the Sb–Sb distances occurring in the Sb square sheets of $SmSb_2$ (3.03(2)–3.09(2) Å)[22] or $REM_{1-x}Sb_2$ (3.097(2) Å for M = Zn;[23] 3.119(3)–3.142(3) Å for M = In;[5] 3.0952(3) Å for M = Sn[6]). In these binary and ternary rare-earth antimonides, extension of the Zintl concept to account for partial bond order leads to the interpretation of such intermediate Sb–Sb bonds as one-electron or half-bonds, to a first approximation.[3,5,6]

The RE atoms, located between the $^2_\infty[GaSb]$ and $^2_\infty[Sb]$ layers, centre square antiprism-based polyhedra, as is typical in structures containing Sb square sheets and ribbons (Figure 4-3b).[4-6,22,23] Each RE atom is coordinated by eight Sb atoms: four Sb(1) atoms from the $^2_\infty[GaSb]$ layer define one square face, and four Sb(2) (in $SmGaSb_2$), or two Sb(2) and two Sb(3) (in $NdGaSb_2$), atoms from the $^2_\infty[Sb]$ net define the second square face ($SmGaSb_2$, Sm–Sb 3.2169(3)–3.2754(6) Å; $NdGaSb_2$, Nd–Sb 3.2431(4)–3.2986(6) Å). Two Ga atoms then cap the larger Sb(1) square face ($SmGaSb_2$, Sm–Ga

3.3155(7) Å; NdGaSb$_2$, Nd–Ga 3.3549(10) Å). Similar Ga-capped Sb antiprisms surrounding *RE* atoms are found in La$_{13}$Ga$_8$Sb$_{21}$ and *RE*$_{12}$Ga$_4$Sb$_{23}$. The *RE*–Sb and *RE*–Ga distances in Sm$_{12}$Ga$_4$Sb$_{23}$ (Sm–Sb 3.174(2)–3.304(2), Sm–Ga 3.232(2)–3.353(2) Å) or Nd$_{12}$Ga$_4$Sb$_{23}$ (Nd–Sb 3.211(1)–3.341(1), Nd–Ga 3.270(1)–3.393(1) Å) are comparable to those above.[24]

The portrayal of the SmGaSb$_2$ and NdGaSb$_2$ structures in Figures 4-1 and 4-2, respectively, emphasizes the covalent layered networks $_\infty^2[\text{GaSb}]$ and $_\infty^2[\text{Sb}]$ between which *RE* atoms are inserted. But it is equally valid to consider the structures as stacked slabs of composition $_\infty^2[RE\text{Sb}_2]$ between which zigzag Ga chains are to be inserted. Within such $_\infty^2[RE\text{Sb}_2]$ slabs, the *RE* atoms are positioned above and below the $_\infty^2[\text{Sb}]$ square sheet such that no two *RE* atoms share the same square face. Sandwiching these are the Sb(1) atoms arranged in nearly square (SmGaSb$_2$) or square (NdGaSb$_2$) nets that are half as dense as the $_\infty^2[\text{Sb}]$ sheet and whose dimensions are defined by the cell parameters in the plane of the nets. The stacking of the $_\infty^2[RE\text{Sb}_2]$ slabs determines the orientation in which the inserted zigzag Ga chains run, since each Ga atom must be bonded to two Sb(1) atoms, one in the $_\infty^2[RE\text{Sb}_2]$ slab above and one in the slab below. As shown in Figures 4-1 and 4-2, all of the zigzag Ga chains in SmGaSb$_2$ are parallel and run along the *c* direction, whereas the zigzag Ga chains in NdGaSb$_2$ are mutually perpendicular and alternately run along the *a* or *b* direction. In SmGaSb$_2$, the $_\infty^2[RE\text{Sb}_2]$ slabs are mutually displaced by ½$\vec{a}$ as they are stacked along the *b* axis, so that two such slabs are needed before the sequence is repeated. In NdGaSb$_2$, the $_\infty^2[RE\text{Sb}_2]$ slabs are mutually displaced alternately by ½$\vec{a}$ *and* ½$\vec{b}$ as they are stacked along the *c* axis, so

that four such slabs are needed before the sequence is repeated. This difference in the stacking sequence of the $_\infty^2[RESb_2]$ slabs causes the stacking axis (c) in NdGaSb$_2$ to be doubled with respect to the stacking axis (b) in SmGaSb$_2$.

Structural Relationships. This viewpoint of describing the stacking sequence of $_\infty^2[RESb_2]$ slabs followed by insertion of "guest" atoms is helpful in illuminating the structural relationships not only between SmGaSb$_2$ and NdGaSb$_2$, but also with many other structures. Indeed, SmGaSb$_2$ and NdGaSb$_2$ can be considered as stacking variants of ternary rare-earth antimonides $REM_{1-x}Sb_2$ with structures consisting of $_\infty^2[RESb_2]$ slabs separated by layers of M atoms. As shown in Figure 4-5, these ternary antimonides can also be derived from a simpler "host" structure.

Many binary rare-earth compounds REX_2 (X = S, Se, Te; P, As, Sb; Si, Ge) adopt the ZrSiS-type structure (Figure 4-5a), or distortions thereof, in which the non-metal X occupies the Si and S sites.[25,26] In this structure, $_\infty^2[Zr(SiS)]$ slabs are stacked directly on top of each other along c without any displacement along a or b, and are held together by S–S bonds. This stacking arrangement generates a tetrahedral site that is occupied by Zn atoms in the structure of LaZn$_{0.52}$Sb$_2$, which consists of $_\infty^2[LaSb_2]$ slabs stacked in the same way as the $_\infty^2[Zr(SiS)]$ slabs in ZrSiS.[23] LaZn$_{0.52}$Sb$_2$ belongs to a large family of ternary rare-earth antimonides $REM_{1-x}Sb_2$ where the inserted M atoms can be not only Zn, but also many other transition or post-transition metals (M = Mn–Cu, Pd–Cd, Au).[23,27] This filled structure is known, among other labels, as the HfCuSi$_2$-type.[28]

The binary rare-earth antimonide YbSb$_2$, containing divalent Yb, adopts the ZrSi$_2$-type structure (Figure 4-5b).[29,30] The $_\infty^2[ZrSi_2]$ slabs, which are held by Si–Si

bonds, are displaced by $\frac{1}{2}\vec{a}$ as they are stacked along b, in exactly the same sequence as the $_\infty^2[SmSb_2]$ slabs in $SmGaSb_2$. A reduction in symmetry occurs as the Ga chains are inserted into the $ZrSi_2$-type structure ($Cmcm$) to form the $SmGaSb_2$ structure ($C222_1$). Finally, $NdGaSb_2$ represents a new stacking variant whose arrangement of $_\infty^2[NdSb_2]$ slabs has no counterpart in a simpler binary rare-earth structure, but does occur in the $_\infty^2[(Zr_{0.75}Al_{0.25})(Al_{0.38}Si_{0.62})_2]$ slabs found in the $Zr_3Al_4Si_5$-type structure (Figure 4-5c).[31] Insertion of the Ga chains into the $Zr_3Al_4Si_5$-type structure to form the $NdGaSb_2$ structure does not alter the space group ($I4_1/amd$) in this case because of the occurrence of disorder in the Ga chains (see above). With each $_\infty^2[RESb_2]$ slab being approximately 10 Å thick, the length of the stacking axis reflects the stacking sequence repeat for $LaZn_{0.52}Sb_2$ (~ 10 Å), $SmGaSb_2$ (~ 20 Å), and $NdGaSb_2$ (~ 40 Å).

Comparison of $REGaSb_2$ to other representative members ($LaZn_{0.52}Sb_2$, $LaIn_{0.8}Sb_2$, and $LaSn_{0.75}Sb_2$) of this emerging class of ternary rare-earth antimonides $REM_{1-x}Sb_2$ illustrates the influence of valence electron count and size of the inserted M atoms on the structure adopted. As shown in Figure 4-6, the nature of the inserted M atoms determines not only the extent of possible M–M bonding, but also the directionality and strength of M–Sb bonding, and hence ultimately the stacking arrangement. In $LaZn_{0.52}Sb_2$ (Figure 4-6a), the inserted Zn atoms form a perfectly square M net possibly containing weak Zn–Zn bonding.[23] (While d^{10}–d^{10} interactions may be questionable for Zn, they may be more plausible for Cd in the isostructural $LaCd_{0.7}Sb_2$.[27d,32]) The preference of Zn for a tetrahedral coordination dictates that the $_\infty^2[LaSb_2]$ slabs be stacked directly on top of each other. Replacement of Zn by a more electron-rich main-group

element, such as Ga, In, or Sn, is accompanied by distortion of the perfectly square M net to form main-group element chains. In $LaIn_{0.8}Sb_2$ (Figure 4-6b), the square M net distorts to form parallel zigzag chains containing strong In–In bonding.[5] Each In atom is coordinated by three Sb atoms and two other In atoms in a distorted square pyramidal fashion. In $REGaSb_2$ (Figure 4-6c), the distortion of the square M net is so severe that this description is no longer useful and the transition to M chains is fairly progressed. Each Ga atom is now coordinated by only two Sb atoms and two other Ga atoms in a tetrahedral fashion. Also consistent with the smaller size of Ga vs. In, the Ga–Ga zigzag chains (~ 2.5 Å) are coplanar, whereas the In–In zigzag chains (~ 3.0 Å) are slightly canted with respect to the planes of the surrounding Sb sheets. Finally, in $LaSn_{0.75}Sb_2$, the even more electron-rich Sn atoms are inserted into partially occupied sites closely spaced in a nearly linear arrangement.[6] On a local level, a plausible interpretation is that each Sn atom is bonded strongly to two surrounding Sb atoms, or weakly to four Sb atoms, or somewhere in between, depending on the site occupied.

The formation of parallel chains in $LaIn_{0.8}Sb_2$, $REGaSb_2$, and $LaSn_{0.75}Sb_2$ requires a shifting of the Sb atoms above and below the M nets. In order to fulfill the M–Sb bonding requirements consistent with the preferred local coordination of M, adjacent $_{\infty}^{2}[RE\,Sb_2]$ slabs must be displaced by half a unit cell length perpendicular to the chain direction (Figure 4-6) The stacking sequence of the $_{\infty}^{2}[RE\,Sb_2]$ layers is identical in orthorhombic $SmGaSb_2$ and $LaSn_{0.75}Sb_2$ (Figure 4-5b) (and these compounds would be isostructural were it not for the different arrangement of the inserted M atoms). In monoclinic $LaIn_{0.8}Sb_2$, the adjacent slabs are shifted by slightly less than half a unit cell length with respect to one another, but the stacking arrangement is otherwise similar.

Another consequence of the chain formation is to render inequivalent the lattice parameters in the plane of the M layers (with the exception of $NdGaSb_2$) as the symmetry is reduced from tetragonal ($LaZn_{0.52}Sb_2$) to orthorhombic ($SmGaSb_2$, $LaSn_{0.75}Sb_2$) to monoclinic ($LaIn_{0.8}Sb_2$). In $LaIn_{0.8}Sb_2$ ($a = 4.521(3)$, $b = 4.331(3)$ Å) and $LaSn_{0.75}Sb_2$ ($a = 4.2435(5)$, $c = 4.5053(6)$ Å), the difference between these parameters is relatively large. In these structures, there is only one energetically favourable way of placing the M chains over the $^2_\infty[LaSb_2]$ layers, and no stacking variants are observed. In $SmGaSb_2$ ($a = 4.3087(5)$, $c = 4.3319(4)$ Å) the difference between the cell parameters in the plane of the Ga chains is small, and in tetragonal $NdGaSb_2$ ($a = b = 4.3486(3)$ Å) it is non-existent. Once one layer of Ga chains has been placed over the $^2_\infty[RESb_2]$ slab, there is little difference in energy between having the Ga chains in the next layer run parallel or perpendicular to those in the first. As discussed above, the $SmGaSb_2$ structure results if the Ga chains are always parallel, while in the $NdGaSb_2$ structure, the zigzag Ga chains alternate in direction. Why no intermediate stacking variants have been observed is not clear. Nor can we explain why certain rare-earth elements prefer either the $SmGaSb_2$ structure (La, Sm) or the $NdGaSb_2$ structure (Ce, Pr, Nd), crystallizing exclusively in one structure type.

Bonding. We can now attempt to apply the Zintl concept to $REGaSb_2$. If we assume that the RE atoms, attaining a +3 oxidation state, participate in predominantly ionic bonds by donating their valence electrons to the anionic substructure, then we arrive at the formulation $RE^{3+}[(GaSb)(Sb)]^{3-}$. The assignment of oxidation states in the $^2_\infty[GaSb]$ layer, which contains normal Ga–Sb and Ga–Ga single bonds, is straightforward. Since Sb is more electronegative than Ga, we first satisfy the Sb octets,

neglecting any Ga–Sb bonding, and arrive at an oxidation state of –3 for the isolated

Sb(1) atoms. Each Ga atom participates in two Ga–Ga bonds, and is therefore assigned

an oxidation state of +1. On the basis of these oxidation state assignments, we can

describe the layer as $_\infty^2[GaSb]^{2-}$, isoelectronic to the $_\infty^2[GeAs]^{1-}$ anionic substructure of

the Zintl phase $BaGe_2As_2$ in which Ge, rather than Ga, chains occur.[19] In order to

maintain charge balance, the remaining Sb atoms of the $_\infty^2[Sb]$ square net must have an

oxidation state of –1, consistent with each Sb atom participating in four half-bonds. The

concept of intermediate one-electron Sb–Sb bonds has been used to successfully

rationalize the bonding in a variety of compounds, and has now gained acceptance.[3–6,33]

To a first approximation, then, the Zintl concept leads to a bonding model for

$REGaSb_2$ in which the anionic substructure is composed of well-separated and non-

interacting layers, $_\infty^2[GaSb]^{2-}$ and $_\infty^2[Sb]^{1-}$. To test the validity of this proposed bonding

model, the band structure of the anionic $[GaSb_2]^{3-}$ substructure of the simpler $SmGaSb_2$

structure was calculated. As expected, the band structure of $[GaSb_2]^{3-}$ is simply a

superposition of the band structures of each layer (Figure 4-7). In the density of states

(DOS) curve for the $_\infty^2[GaSb]^{2-}$ layer (Figure 4-7a), the lower energy states originate

largely from the more electronegative Sb, and the higher energy states, located just below

a band gap near –7.5 eV, originate mainly from Ga. However, there is substantial mixing

of the Ga and Sb states, indicative of the strong covalent character of the Ga–Sb bonding.

If the octets of all atoms in the $_\infty^2[GaSb]^{2-}$ layer are completed, as required by the

oxidation state assignment proposed above, then, at this electron count, all states up to the

band gap are filled, in agreement with our description of this two-dimensional layer as a

"Zintl layer." The DOS curve for the Sb square net (Figure 4-7b) shows a continuous

distribution of energy levels, with no band gap between bonding and antibonding states. At the electron count required to produce a $^2_\infty[Sb]^{1-}$ layer, the Fermi level lies at -10.7 eV. However, when the $^2_\infty[GaSb]^{2-}$ and $^2_\infty[Sb]^{1-}$ layers are stacked to form the three-dimensional $[GaSb_2]^{3-}$ framework, the Sb square net acts as an electron sink, accepting electrons from the $^2_\infty[GaSb]$ layer into Sb–Sb antibonding levels. The position of the Fermi level is now equalized to -8.7 eV in the composite $[GaSb_2]^{3-}$ substructure (Figure 4-7c). The Fermi level falls in a region of moderate DOS, and metallic behaviour is predicted for SmGaSb$_2$ (and by analogy REGaSb$_2$).

The nature of bonding in the $[GaSb_2]^{3-}$ framework can be clarified by closer inspection of the crystal orbital overlap population (COOP) curves for the Ga–Ga, Ga–Sb and Sb–Sb interactions, shown in Figure 4-8. Even though the lowering of the Fermi level in the $^2_\infty[GaSb]$ layer weakens Ga–Ga bonding slightly (Figure 4-8a), the Ga–Sb bonding is strengthened slightly as antibonding levels are depopulated (Figure 4-8b). With these bonding levels largely filled, bonding within the $^2_\infty[GaSb]$ layer remains strong and covalent, as indicated by the Mulliken overlap populations determined for the Ga–Ga (0.58) and Ga–Sb (0.56) interactions. In the $^2_\infty[Sb]$ layer, the raising of the Fermi level causes some levels that are only weakly Sb–Sb antibonding to be occupied (Figure 4-8c). The overlap population for the Sb–Sb bonds is 0.35, approximately half of what is normally seen for full single bonds and consistent with bond length correlations.[34] The band structure thus validates the Zintl picture of these bonds as roughly half-bonds, and confirms the role of such Sb square nets as electron sinks permitting some degree of electron acceptance which weakens the Sb–Sb bonds only slightly.[6,34]

When Ga is replaced by In, the substoichiometric point phase, $LaIn_{0.8}Sb_2$, in which the In zigzag chains of the $\frac{2}{\infty}[In_{0.8}Sb]$ layer are randomly segmented by vacancies, results. The main differences between the $[GaSb_2]^{3-}$ and the $[In_{0.8}Sb_2]^{3-}$ band structures occur in the $\frac{2}{\infty}[MSb]$ layer contributions.[35] The energy states with a significant contribution from the less electronegative In are, in general, higher in energy than the corresponding Ga states, while the $\frac{2}{\infty}[Sb]$ net contribution to the band structure is relatively unaffected by changes in the $\frac{2}{\infty}[MSb]$ layer. Accordingly, the Fermi level is at a higher energy in $[In_{0.8}Sb_2]^{3-}$ (–6.8 eV) than in $[GaSb_2]^{3-}$ (–8.7 eV). Even at a substoichiometric In site occupation, more Sb–Sb antibonding levels are filled in $[In_{0.8}Sb_2]^{3-}$ than in $[GaSb_2]^{3-}$. Assuming a rigid band model, addition of any electrons to $[In_{0.8}Sb_2]^{3-}$ to give a stoichiometric $[InSb_2]^{3-}$ structure would cause a dramatic weakening of the Sb–Sb bonding, but only a slight increase in In–In bonding. Vacancies are thus an inherent feature needed to stabilize the $[In_{0.8}Sb_2]^{3-}$ structure.[5] In contrast, in $[GaSb_2]^{3-}$, full occupation of the Ga sites maximizes the Ga–Ga bond strength, and the simultaneous weakening of the Sb–Sb bonding in the square net is less important.

The presence of unoccupied Ga–Ga bonding levels just above the Fermi level of $[GaSb_2]^{3-}$ suggests that at least partial substitution of Ga with an element having more valence electrons should be possible. When Ga is replaced by the obvious candidate, Ge, new ternary compounds, $RE_6Ge_{5-x}Sb_{11+x}$, with a different structure type are formed.[36] However, doping Sn for Ga is possible (which is not surprising, since the structures of $SmGaSb_2$ and $LaSn_{0.75}Sb_2$ are so similar). Preliminary experiments indicate the existence of a solid solution $LaGa_{1-x}Sn_xSb_2$ in a range that extends to at least $x \approx 0.6$. A single crystal structure determined for one member, $LaGa_{0.9}Sn_{0.1}Sb_2$, shows that small amounts

of Sn can be substituted for Ga without any distortion of the $SmGaSb_2$-type structure.[37] Further study of this system could provide some insight into the driving force responsible for the distortion from zigzag Ga to linear Sn chains, and the reason for substoichiometric occupation of the Sn site in $LaSn_{0.75}Sb_2$.

In conclusion, the RE–Ga–Sb system is a rich one that augments a growing family of ternary rare-earth main-group element antimonides characterized by extensive homoatomic bonding of the main-group elements. The structure of $REGaSb_2$ shares many common features with $La_{13}Ga_8Sb_{21}$ and $RE_{12}Ga_4Sb_{23}$, such as the presence of strong Ga–Ga bonds and ribbons or square nets of more weakly bonded Sb atoms.[4] However, whereas the Zintl concept has been successful here in accounting for the electronic structure of $REGaSb_2$, as confirmed by the band structure calculations, it has difficulties in rationalizing the structures of $La_{13}Ga_8Sb_{21}$ and $RE_{12}Ga_4Sb_{23}$. It is precisely in these regions of muddy applicability (intermediate electronegativity differences) where new or unusual modes of bonding are likely to be found; the challenge is for us to discover and understand them.

Table 4-1. Cell parameters for ternary REGaSb$_2$ compounds.

Compound	Structure type	a (Å)	b (Å)	c (Å)	V (Å^3)
LaGaSb$_2$	SmGaSb$_2$-type	4.382(3)	22.775(13)	4.474(3)	446.5(4)
CeGaSb$_2$	NdGaSb$_2$-type	4.3708(16)	4.3708(16)	45.07(2)	860.9(6)
PrGaSb$_2$	NdGaSb$_2$-type	4.3599(16)	4.3599(16)	44.81(2)	851.8(5)
NdGaSb$_2$	NdGaSb$_2$-type	4.3427(15)	4.3427(15)	44.545(19)	840.1(5)
SmGaSb$_2$	SmGaSb$_2$-type	4.304(3)	22.121(13)	4.320(3)	411.3(3)

Table 4-2. Crystallographic data for SmGaSb$_2$ and NdGaSb$_2$.

Formula	SmGaSb$_2$	NdGaSb$_2$
Formula mass (amu)	463.57	457.46
Space group	D_2^5–$C222_1$ (No. 20)	D_{4h}^{19}–$I4_1/amd$ (No. 141)
a (Å)	4.3087(5) [a]	4.3486(3) [b]
b (Å)	22.093(4) [a]	4.3486(3) [b]
c (Å)	4.3319(4) [a]	44.579(8) [b]
V (Å^3)	412.36(10)	843.0(2)
Z	4	8
T (°C)	22	22
Diffractometer	Enraf-Nonius CAD4	Enraf-Nonius CAD4
ρ_{calc} (g cm^{-3})	7.467	7.209
Crystal dimensions (mm)	Rectangular plate, 0.16 × 0.12 × 0.01	Rectangular plate, 0.11 × 0.08 × 0.01
Radiation	Graphite-monochromated Mo $K\alpha$, $\lambda = 0.71073$ Å	Graphite-monochromated Mo $K\alpha$, $\lambda = 0.71073$ Å
μ(Mo $K\alpha$) (cm^{-1})	332.1	308.8
Transmission factors [c]	0.076–0.654	0.132–0.964
Scan type	θ–2θ	θ–2θ
Scan speed (deg. min^{-1})	1.67	1.67
Scan range (deg.)	0.70 + 0.344 tan θ	0.60 + 0.344 tanθ
2θ limits	4° ≤ 2θ(Mo $K\alpha$) ≤ 70°	4° ≤ 2θ(Mo $K\alpha$) ≤ 70°
Data collected	$-6 \leq h \leq 6, -35 \leq k \leq 35, -6 \leq l \leq 6$	$-7 \leq h \leq 7, -7 \leq k \leq 7, -71 \leq l \leq 71$
No. of data collected	3582	6770
No. of unique data, including $F_o^2 < 0$	907 ($R_{int} = 0.076$)	560 ($R_{int} = 0.103$)
No. of unique data, with $F_o^2 > 2\sigma(F_o^2)$	848	440
No. of variables [d]	23	19
Flack parameter [e]	0.54(6)	——
$R(F)$ for $F_o^2 > 2\sigma(F_o^2)$ [f]	0.029	0.034
$R_w(F_o^2)$ [g]	0.074	0.073

Table 4-2. Crystallographic data for $SmGaSb_2$ and $NdGaSb_2$ (continued).

Goodness of fit [h]	1.06	1.10
$\Delta\rho_{max}, \Delta\rho_{min}$ (e Å^{-3})	3.3, –3.5	3.2, –1.9

[a] Obtained from a refinement constrained so that $\alpha = \beta = \gamma = 90°$.

[b] Obtained from a refinement constrained so that $a = b$ and $\alpha = \beta = \gamma = 90°$.

[c] An empirical face-indexed Gaussian-type absorption correction was applied, with the use of programs in the SHELXTL package (Sheldrick, G. M. *SHELXTL Version 5.1*; Bruker Analytical X-ray Systems: Madison, WI, 1997).

[d] Including an extinction coefficient.

[e] Flack, H. D. *Acta Crystallogr. Sect. A: Found. Crystallogr.* **1983**, *39*, 876.

[f] $R(F) = \sum \left\| F_o \right| - \left| F_c \right\| / \sum |F_o|$.

[g] $R_w(F_o^2) = \left[\sum \left[w(F_o^2 - F_c^2)^2 \right] / \sum wF_o^4 \right]^{1/2}$; $w^{-1} = \left[\sigma^2(F_o^2) + (aP)^2 + bP \right]$ where $P = \left[\max(F_o^2, 0) + 2F_c^2 \right] / 3$. For $SmGaSb_2$, $a = 0.0308$, $b = 7.8140$; for $NdGaSb_2$, $a = 0.0229$, $b = 30.9047$.

[h] $GooF = \left[\sum \left[w(F_o^2 - F_c^2)^2 \right] / (n - p) \right]^{1/2}$ where n is the number of reflections and p is the total number of parameters refined.

Table 4-3. Positional and equivalent isotropic displacement parameters for SmGaSb$_2$ and NdGaSb$_2$.

Atom	Wyckoff position	Occupancy	x	y	z	U_{eq} (Å^2) [a]
			SmGaSb$_2$			
Sm	4b	1	0	0.138632(18)	1/4	0.00760(12)
Ga	4a	1	0.1538(4)	0	0	0.0232(3)
Sb(1)	4b	1	0	0.40698(3)	1/4	0.00881(13)
Sb(2)	4b	1	0	0.75016(2)	1/4	0.00795(13)
			NdGaSb$_2$			
Nd	8e	1	0	1/4	0.069357(14)	0.00908(16)
Ga	16f	0.5	0.1649(7)	0	0	0.0345(7)
Sb(1)	8e	1	0	1/4	0.203764(18)	0.01077(18)
Sb(2)	4b	1	0	1/4	3/8	0.0100(2)
Sb(3)	4a	1	0	3/4	1/8	0.0096(2)

[a] U_{eq} is defined as one-third of the trace of the orthogonalized U_{ij} tensor.

Table 4-4. Selected interatomic distances (Å) in SmGaSb$_2$ and NdGaSb$_2$.

SmGaSb$_2$		NdGaSb$_2$	
Sm–Sb(1)	3.2169(3) (×4)	Nd–Sb(1)	3.2431(4) (×4)
Sm–Sb(2)	3.2730(6) (×2)	Nd–Sb(2)	3.2986(6) (×2)
Sm–Sb(2)	3.2754(6) (×2)	Nd–Sb(3)	3.2986(6) (×2)
Sm–Ga	3.3155(7) (×2)	Nd–Ga	3.3549(10) (×2)
Ga–Ga	2.539(2) (×2)	Ga–Ga	2.605(3) (×2)
Ga–Sb(1)	2.7606(12) (×2)	Ga–Sb(1)	2.7485(17) (×2)
Sb(2)–Sb(2)	3.0549(2) (×4)	Sb(2)–Sb(3)	3.0749(2) (×4)

Table 4-5. Extended Hückel parameters.

Atom	Orbital	H_{ii} (eV)	ζ_{i1}
Ga	$4s$	−14.58	1.77
	$4p$	−6.75	1.55
Sb	$5s$	−18.8	2.323
	$5p$	−11.7	1.999
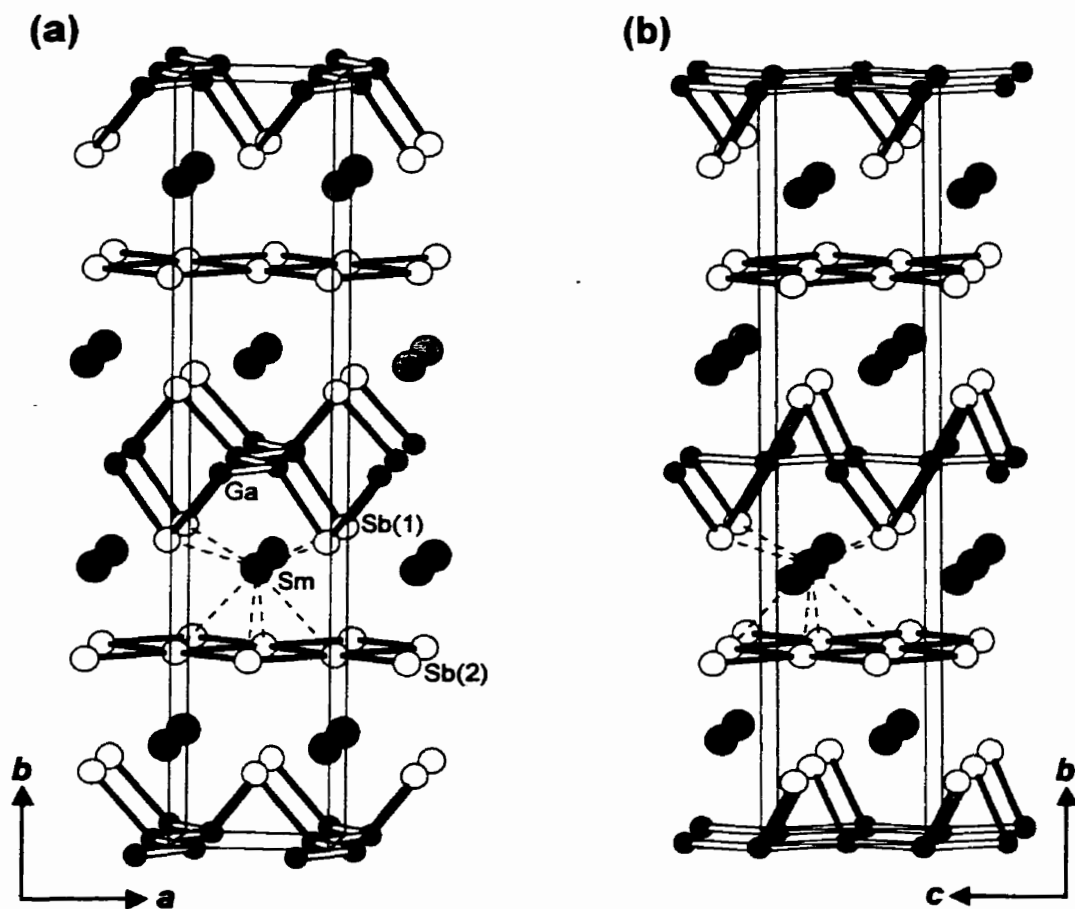
Figure 4-1. Views of SmGaSb$_2$ (a) down the c axis and (b) down the a axis showing the unit cell outline and the labelling scheme. The large lightly shaded circles are Sm atoms, the small solid circles are Ga atoms, and the medium open circles are Sb atoms.
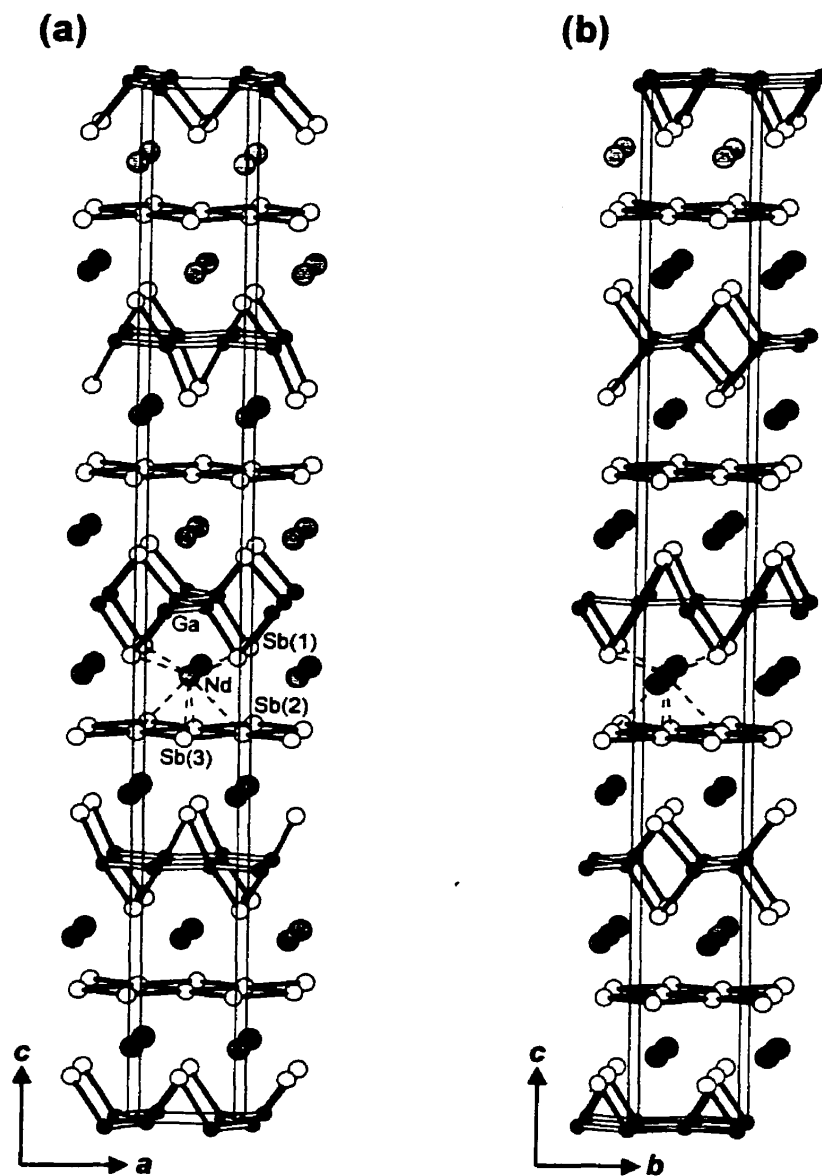
Figure 4-2. Views of $NdGaSb_2$ (a) down the b axis and (b) down the a axis showing the unit cell outline and the labelling scheme. The large lightly shaded circles are Nd atoms, the small solid circles are Ga atoms, and the medium open circles are Sb atoms.
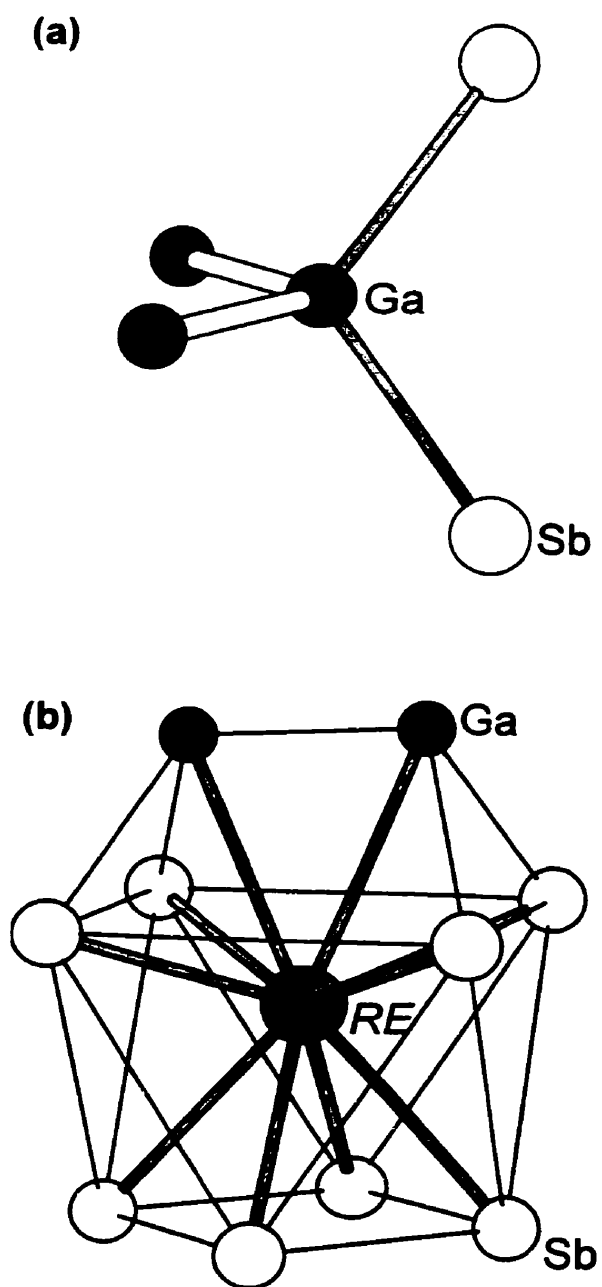
Figure 4-3. (a) Distorted tetrahedral coordination around Ga in SmGaSb$_2$ and NdGaSb$_2$.
(b) Coordination environment around *RE* atoms in SmGaSb$_2$ and NdGaSb$_2$.
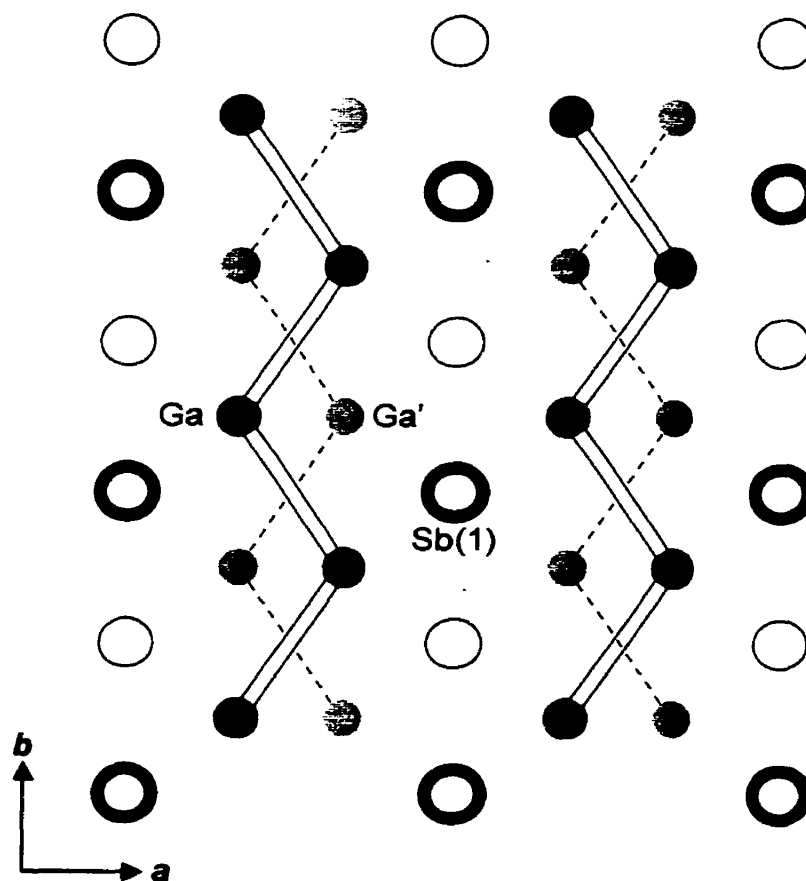
Figure 4-4. View down the c axis of a $_\infty^2[\text{GaSb}]$ layer in NdGaSb_2 showing the disorder of the zigzag Ga chains, associated with a 50% occupancy of the Ga site. Sb atoms with thick rims reside on planes displaced perpendicular to the plane of the page relative to those with thin rims.
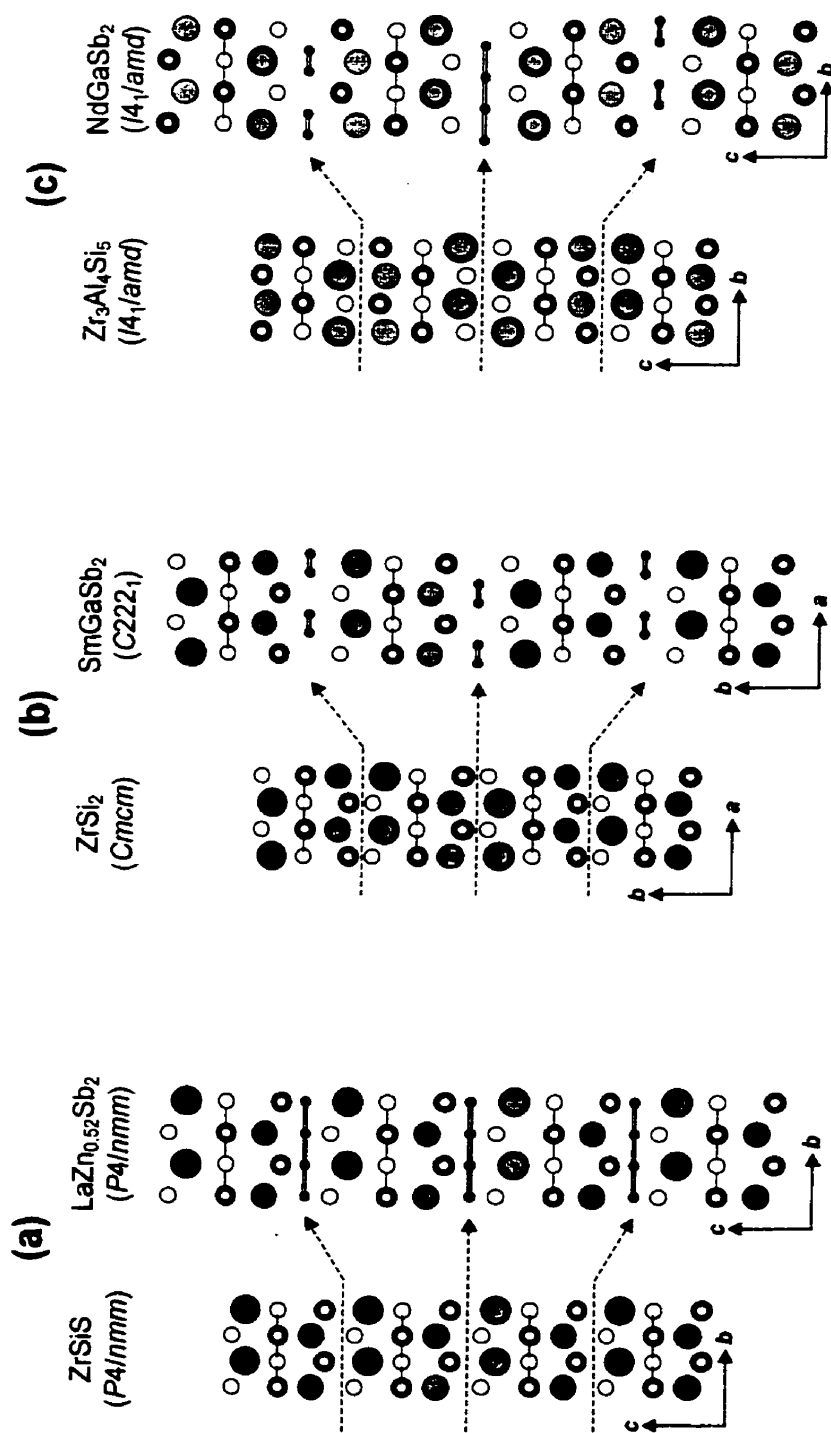
Figure 4-5. Comparison of the stacking sequence of $^2_\infty[RE\text{Sb}_2]$ slabs in ternary rare-earth antimonides $RE M_{1-x}\text{Sb}_2$ and their relationship to simpler host structures into which M atoms are inserted. (a) AAAA stacking sequence (10 Å repeat) of slabs in ZrSiS-type and $\text{LaZn}_{0.52}\text{Sb}_2$ structures. (b) ABAB stacking sequence (20 Å repeat) of slabs in ZrSi_2-type and SmGaSb_2 structures. (c) ABCD stacking sequence (40 Å repeat) of slabs in $\text{Zr}_3\text{Al}_4\text{Si}_5$-type and NdGaSb_2 structures. The large lightly shaded circles are the electropositive atoms (RE, Zr, Al), the small solid circles are the M atoms (Zn, Ga), and the medium open circles are the other atoms X (Al, Si, Sb, S). Atoms with thick rims reside on planes displaced by half a unit cell parameter perpendicular to the plane of the page relative to those with thin rims. The inserted M atoms lie between these planes.

(a) $LaZn_{0.52}Sb_2$ **(b)** $LaIn_{0.8}Sb_2$ **(c)** $REGaSb_2$ **(d)** $LaSn_{0.75}Sb_2$
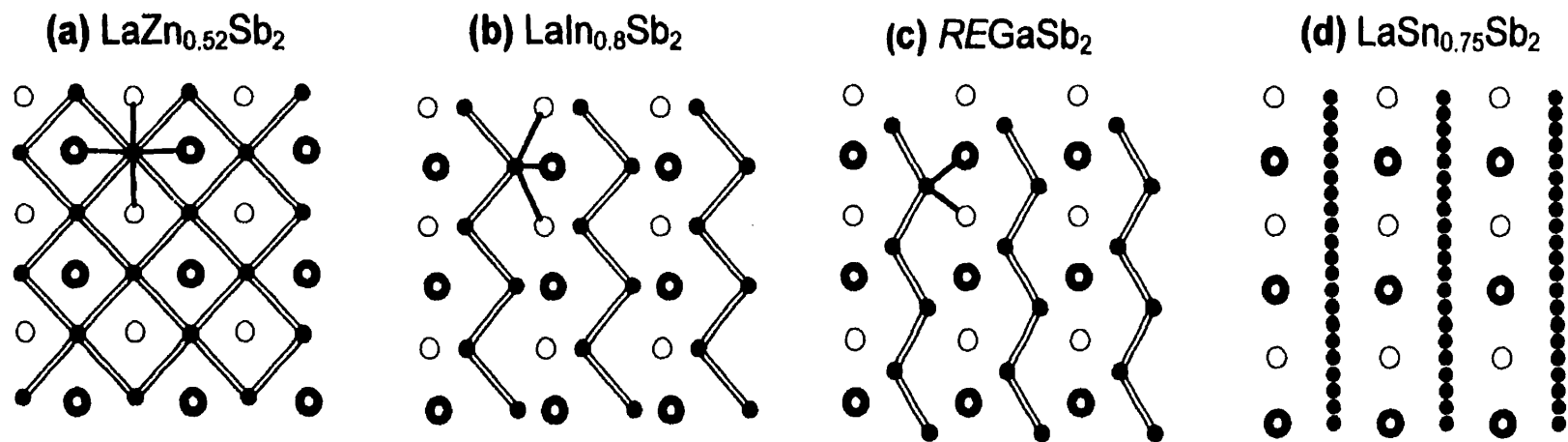
Figure 4-6. Comparison of the $^2_\infty[MSb]$ layers in (a) $LaZn_{0.52}Sb_2$, (b) $LaIn_{0.8}Sb_2$, (c) $REGaSb_2$, and (d) $LaSn_{0.75}Sb_2$ shown in projection down the stacking direction. The small solid circles are the M atoms (Zn, In, Ga, Sn) and the open circles are the Sb atoms. Sb atoms with thick rims reside on planes displaced perpendicular to the plane of the page relative to those with thin rims. The inserted M atoms lie between these planes. The ideal square Zn net in $LaZn_{0.52}Sb_2$ is distorted to form zigzag Ga or In chains in $LaIn_{0.8}Sb_2$ and $REGaSb_2$, and disordered linear Sn chains in $LaSn_{0.75}Sb_2$. Note also the shifting of the plane of Sb atoms with thick rims as this distortion occurs.

(a) $^2_\infty[GaSb]^{2-}$ **(b)** $^2_\infty[Sb]^{1-}$ **(c)** $[GaSb_2]^{3-}$
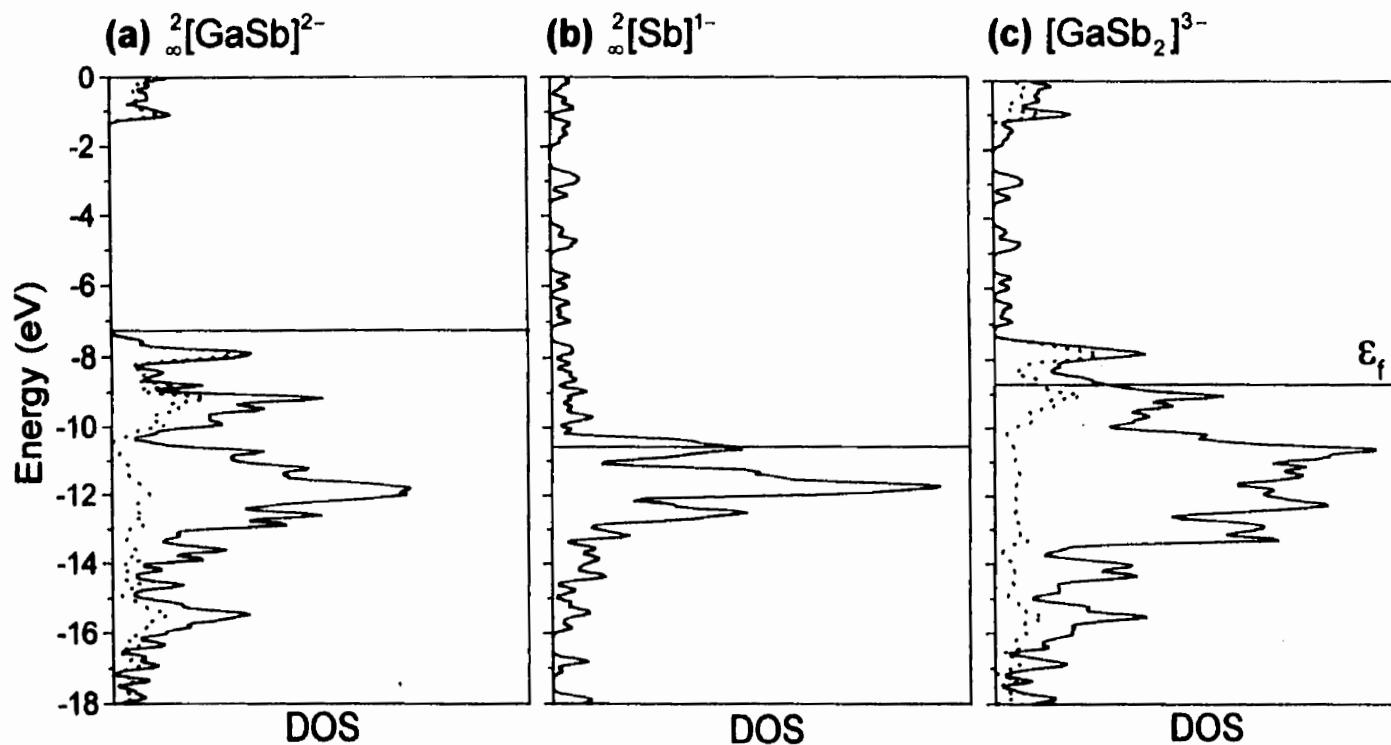
Figure 4-7. Density of states (DOS) for (a) $^2_\infty[GaSb]^{2-}$ layer, (b) $^2_\infty[Sb]^{1-}$ square net, and (c) the composite $[GaSb_2]^{3-}$ substructure of SmGaSb$_2$. The Ga projection is shown by the dotted line; what remains of the total DOS is the Sb projection. The Fermi level at -8.7 eV is shown by the horizontal line in (c).
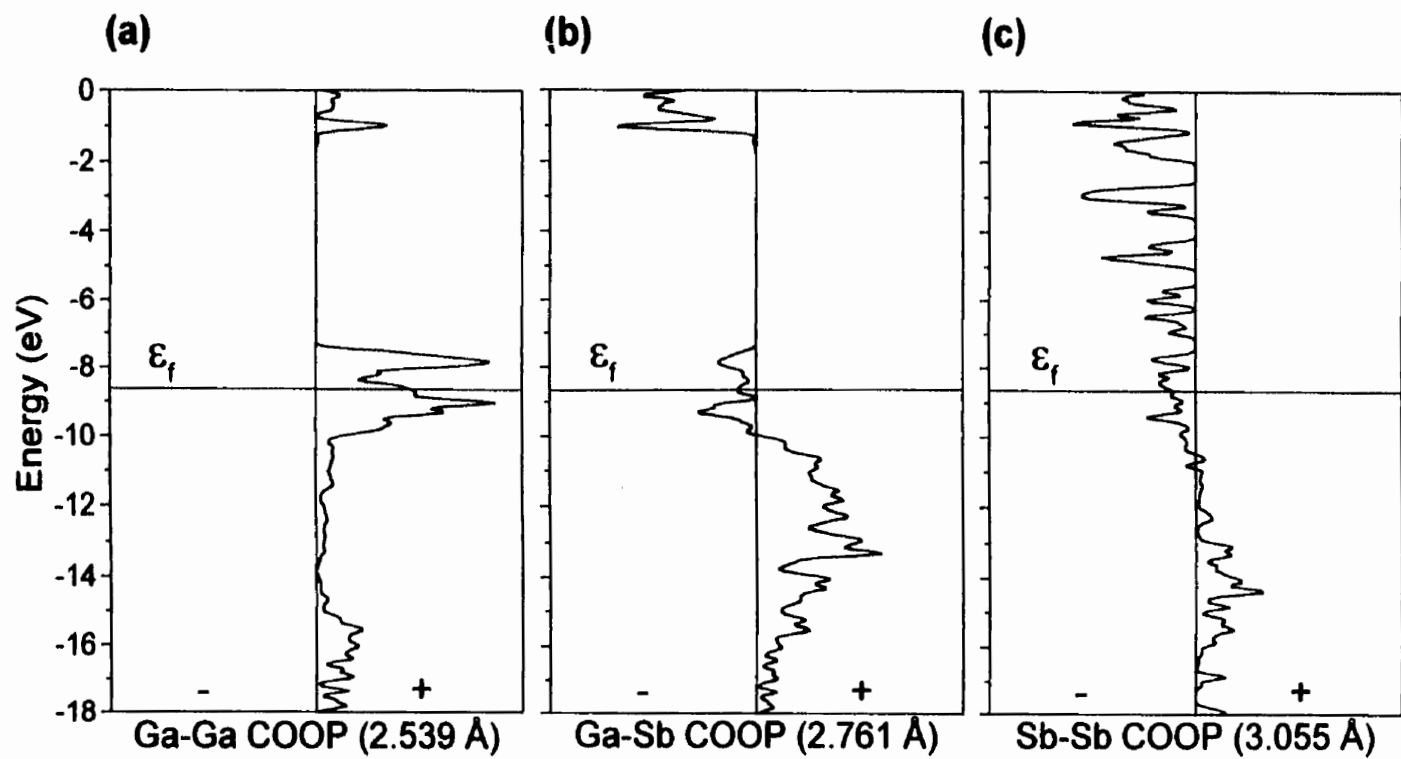
Figure 4-8. Crystal orbital overlap population (COOP) curves for (a) Ga–Ga (2.539(2) Å), (b) Ga–Sb (2.7606(12) Å), and (c) Sb–Sb (3.0549(2) Å) interactions in the $[GaSb_2]^{3-}$ substructure of $SmGaSb_2$.

References

(1) For example, see the following. (a) $Na_2Ga_3Sb_3$: Cordier, G.; Ochmann, H.; Schäfer, H. *Mater. Res. Bull.* **1986**, *21*, 331. (b) Sr_3GaSb_3: Cordier, G.; Schäfer, H.; Stelter, M. *Z. Naturforsch. B: Chem. Sci.* **1987**, *42*, 1268. (c) $K_{20}Ga_6Sb_{12.66}$: Cordier, G.; Ochmann, H. *Z. Naturforsch. B: Chem. Sci.* **1990**, *45*, 277. (d) Cs_6GaSb_3: Blase, W.; Cordier, G.; Somer, M. *Z. Kristallogr.* **1992**, *199*, 277. (e) $Na_3Sr_3GaSb_4$: Somer, M.; Carrillo-Cabrera, W.; Nuß, J.; Peters, K.; von Schnering, H. G.; Cordier, G. *Z. Kristallogr.* **1996**, *211*, 479. (f) Eisenmann, B.; Cordier, G. In *Chemistry, Structure, and Bonding of Zintl Phases and Ions*; Kauzlarich, S. M., Ed. VCH Publishers: New York, 1996; p 61.

(2) (a) *Chemistry, Structure, and Bonding of Zintl Phases and Ions*; Kauzlarich, S. M., Ed. VCH Publishers: New York, 1996. (b) Corbett, J. D. *Angew. Chem. Int. Ed.* **2000**, *39*, 670.

(3) Papoian, G. A.; Hoffmann, R. *Angew. Chem. Int. Ed.* **2000**, *39*, 2408.

(4) Mills, A. M.; Mar, A. *Inorg. Chem.* **2000**, *39*, 4599.

(5) Ferguson, M. J.; Ellenwood, R. E.; Mar, A. *Inorg. Chem.* **1999**, *38*, 4503.

(6) Ferguson, M. J.; Hushagen, R. W.; Mar, A. *Inorg. Chem.* **1996**, *35*, 4505.

(7) *Filmscan* and *Jade 3.0*; Materials Data: Livermore, CA, 1996.

(8) *POLSQ: Program for least-squares unit cell refinement*; Modified by D. Cahen and D. Keszler, Northwestern University, 1983.

(9) Yvon, K.; Jeitschko, W.; Parthé, E. *J. Appl. Crystallogr.* **1977**, *10*, 73.

(10) Sheldrick, G. M. *SHELXTL Version 5.1*; Bruker Analytical X-ray Systems: Madison, WI, 1997.

(11) *International Tables for X-ray Crystallography*; Wilson, A. J. C., Ed. Kluwer: Dordrecht, The Netherlands, 1992; Vol. C.

(12) Flack, H. D. *Acta Crystallogr. Sect. A: Found. Crystallogr.* **1983**, *39*, 876.

(13) Gelato, L. M.; Parthé, E. *J. Appl. Crystallogr.* **1987**, *20*, 139.

(14) Whangbo, M.-H.; Hoffmann, R. *J. Am. Chem. Soc.* **1978**, *100*, 6093.

(15) Hoffmann, R. *Solids and Surfaces: A Chemist's View of Bonding in Extended Structures*; VCH Publishers: New York, 1988.

(16)   Hinze, J.; Jaffé, H. H. *J. Phys. Chem.* **1963**, *67*, 1501.

(17)   Canadell, E.; Eisenstein, O.; Rubio, J. *Organometallics*; **1984**, *3*, 759.

(18)   Hughbanks, T.; Hoffmann, R.; Whangbo, M.-H.; Stewart, K. R.; Eisenstein, O.; Canadell, E. *J. Am. Chem. Soc.* **1982**, *104*, 3876.

(19)   Eisenmann, B.; Schäfer, H. *Z. Naturforsch. B: Anorg. Chem. Org. Chem.* **1981**, *36*, 415.

(20)   Müller, W.; Stöhr, J. *Z. Naturforsch. B: Anorg. Chem. Org. Chem.* **1977**, *32*, 631.

(21)   Donohue, J. *The Structures of the Elements*; John Wiley and Sons: New York, 1974.

(22)   Wang, R.; Steinfink, H. *Inorg. Chem.* **1967**, *6*, 1685.

(23)   Cordier, G.; Schäfer, H.; Woll, P. *Z. Naturforsch. B: Anorg. Chem. Org. Chem.* **1985**, *40*, 1097.

(24)   The RE–Sb and RE–Ga bond lengths in $Sm_{12}Ga_4Sb_{23}$ and $Nd_{12}Ga_4Sb_{23}$ were calculated based on positional parameters from the crystal structure of $Pr_{12}Ga_4Sb_{23}$ and refined cell parameters from the powder patterns of $Sm_{12}Ga_4Sb_{23}$ and $Nd_{12}Ga_4Sb_{23}$, respectively.[4]

(25)   Böttcher, P.; Doert, Th.; Arnold, H.; Tamazyan, R. *Z. Kristallogr.* **2000**, *215*, 246.

(26)   Klein Haneveld, A. J.; Jellinek, F. *Recl. Trav. Chim. Pays-Bas*, **1964**, *83*, 776.

(27)   (a) Leithe-Jasper, A.; Rogl, P. *J. Alloys Compd.* **1994**, *203*, 133. (b) Sologub, O.; Hiebl, K.; Rogl, P.; Noël, H.; Bodak, O. *J. Alloys Compd.* **1994**, *210*, 153. (c) Sologub, O.; Noël, H.; Leithe-Jasper, A.; Rogl, P.; Bodak, O. I. *J. Solid State Chem.* **1995**, *115*, 441. (d) Sologub, O.; Hiebl, K.; Rogl, P.; Bodak, O. *J. Alloys Compd.* **1995**, *227*, 40. (e) Brylak, M.; Möller, M. H.; Jeitschko, W. *J. Solid State Chem.* **1995**, *115*, 305. (f) Wollesen, P.; Jeitschko, W.; Brylak, M.; Dietrich, L. *J. Alloys Compd.* **1996**, *245*, L5.

(28)   Andrukhiv, L. S.; Lysenko, L. O.; Yarmolyuk, Ya. P.; Hladyshevsky, E. I. *Dopov. Akad. Nauk Ukr. RSR, Ser. A: Fiz.-Mat. Tekh. Nauk*; **1975**, 645.

(29)   Wang, R.; Bodnar, R.; Steinfink, H. *Inorg. Chem.* **1966**, *5*, 1468.

(30)   Cotter, P. G.; Kohn, J. A.; Potter, R. A. *J. Am. Ceram. Soc.* **1956**, *39*, 11.

(31)   Schubert, K.; Frank, K.; Gohle, R.; Maldonado, A.; Meissner, H. G.; Raman, A.; Rossteutscher, W. *Naturwissenschaften*; **1963**, *50*, 41.

(32)   (a) Pyykkö, P. *Chem. Rev.* **1997**, *97*, 597. (b) Mehrotra, P. K.; Hoffmann, R. *Inorg. Chem.* **1978**, *17*, 2187.

(33)   Brylak, M.; Jeitschko, W. *Z. Naturforsch. B: Chem. Sci.* **1994**, *49*, 747.

(34)   Papoian, G.; Hoffmann, R. *J. Solid State Chem.* **1998**, *139*, 8.

(35)   Mills, A. M.; Mar, A. Unpublished calculations.

(36)   Lam, R.; McDonald, R.; Mar, A. *Inorg. Chem.* **2001**, *40*, 952.

(37)   Mills, A. M.; Mar, A. Unpublished results.

Chapter 5

Structures of the Ternary Iron Germanium Pnictides $FeGe_{1-x}Pn_x$ (Pn = P, As, Sb) [†]

Introduction

As part of a general search for new ternary pnictides with useful physical properties, an investigation of the pseudo-binary FeGe–FePn (Pn = P, As, Sb) systems was undertaken. The parent binaries FeGe and FePn were chosen in part because they display a variety of interesting magnetic behaviours. We reasoned that the structures, and hence properties, of any ternary phases formed would be influenced by factors such as relative atomic sizes, electronegativities, and valence electron concentrations that are easily manipulated in these systems through, for instance, the elaboration of solid solutions $FeGe_{1-x}Pn_x$.

Of the three known polymorphs of iron monogermanide FeGe,[1] there exists a hexagonal one, which adopts the relatively rare CoSn-type crystal structure[2,3] and which exhibits a double-cone antiferromagnetic magnetic structure.[4-6] Substitutional studies involving FeGe are sparse, with only the CoSn-type compound Fe_2GaGe[7] and the CoSn-related solid solutions $Fe_{33}Ge_{29+x}X_{6-x}$ (X = Si, P)[8] having been reported to date. Since the

---

CoSn-type structure is related to many other intermetallic structures, including those of important permanent magnet materials such as $SmCo_5$ and Sm_2Co_{17},[9,10] further studies seem warranted.

The iron monopnictides FePn also display a range of magnetic behaviours, from helical ferromagnetism in FeP and FeAs,[11,12] which adopt the MnP-type structure,[13,14] to antiferromagnetism in FeSb,[15] which adopts the NiAs-type structure.[16] Numerous studies involving substitution of the transition metal M_xFe$_{1-x}Pn$ (M = Ti, V, Cr, Mn, Co, Ni; Pn = P, As, Sb) have been carried out in order to modify the properties of the parent binary FePn as well as to effect transitions between the MnP- and NiAs-type structures by changing the electron count.[17-28] In contrast, surprisingly few studies have explored the effects of anion substitution,[29-33] even though it has been demonstrated that structures and magnetic properties will also be influenced by partial substitution of Pn with other metalloids, causing changes in the number of unpaired metal electrons and the metal–metal bond lengths.[34,35]

Structural studies on the CoGe$_{1-x}Pn_x$ systems were carried out earlier;[36] extended studies into the FeGe$_{1-x}Pn_x$ (Pn = P, As, Sb) systems are now reported herein. The antimonide system is particularly rich, encompassing new intermetallic compounds whose structures were determined at x = 0.20 (FeGe$_{0.80}$Sb$_{0.20}$ or Fe$_3$Ge$_{2.4}$Sb$_{0.6}$) and x = 0.33 (FeGe$_{0.67}$Sb$_{0.33}$ or Fe$_3$Ge$_2$Sb). The formation of these compounds provides insight into the importance of Sb–Sb bonding to the stability of these "stuffed" CoSn-type structures.

Experimental Section

Synthesis. Starting materials were the elemental powders: Fe (99.9%, Cerac), Ge (99.999%, Cerac), P (99.995%, Cerac), As (99.99%, Alfa-Aesar), Sb (99.995%, Aldrich). Reactions were carried out on a 0.250-g scale in evacuated fused-silica tubes (8 cm-length; 10-mm i.d.). Elemental compositions were determined by energy-dispersive X-ray (EDX) analysis on a Hitachi S-2700 scanning electron microscope. X-ray powder patterns were collected on an Enraf-Nonius FR552 Guinier camera (Cu $K\alpha_1$ radiation; Si standard) and analyzed with the Filmscan and Jade 3.0 software packages.[37]

Mixtures of reactants with loading stoichiometry $FeGe_{1-x}Pn_x$ ($0 \leq x \leq 1$ in increments of 0.1; $Pn = $ P, As, Sb) were heated at 700 °C for 4 days and then quenched to room temperature. Solid solutions with the MnP-type structure form over wide regions of homogeneity for the phosphide $FeGe_{1-x}P_x$ ($0.4 \leq x \leq 1.0$) and arsenide $FeGe_{1-x}As_x$ ($0.3 \leq x \leq 1.0$) systems. A structure determination of a single crystal of $FeGe_{0.15}P_{0.85}$, grown in a tin flux, confirms the MnP-type structure showing complete disordering of Ge and P in the unique anion site.[38] In contrast, solid solutions of the NiAs-type structure form for the antimonide system $FeGe_{1-x}Sb_x$ ($0.4 \leq x \leq 1.0$). No evidence for superstructures was observed in the course of indexing the powder patterns of the three solid solutions above. The cell parameters refined with the use of the program POLSQ[39] are given in Tables 5-1 and 5-2.

Analysis of the reactions at the Ge-rich end of the $FeGe_{1-x}Sb_x$ ($0 \leq x \leq 0.4$) series indicated the presence of phases whose powder patterns resemble that of hexagonal FeGe. These were eventually identified as members of a family of CoSn-related structures containing stuffed Sb_2 pairs. Reactions carried out at various temperatures

between 600 and 900 °C showed the persistence of these compounds, and the refined cell parameters for the products obtained at 700 °C are listed in Table 5-2. Single crystals of an intermediate member $FeGe_{0.80}Sb_{0.20}$ and the limiting member $FeGe_{0.67}Sb_{0.33}$ were grown in separate reactions. Reaction of Fe, Ge, and Sb in the ratio 1:0.8:0.2 at 800 °C for 5 days, followed by cooling to 500 °C over 4 days and to 20 °C over 12 h, results in hexagonal prismatic crystals of $FeGe_{0.80}Sb_{0.20}$ (Anal. (mol%): Fe 49(1), Ge 40(1), Sb 11.0(3)% (average of 2 analyses)). Similarly, reaction of Fe, Ge, and Sb in the ratio 1:0.6:0.4 at 700 °C for 4 days followed by cooling to 20 °C over 12 h results in hexagonal prismatic crystals of $FeGe_{0.67}Sb_{0.33}$ (Anal. (mol%): Fe 50(1), Ge 34.2(7), Sb 15.6(3)% (average of 4 analyses)). Powder diffraction data for $FeGe_{0.80}Sb_{0.20}$ and $FeGe_{0.67}Sb_{0.33}$ (observed and calculated interplanar distances, as well as intensities determined using the program LAZY-PULVERIX[40]) are listed in Tables A-13 and A-14.

Structure Determination. Preliminary cell parameters for $FeGe_{0.80}Sb_{0.20}$ and $FeGe_{0.67}Sb_{0.33}$ were determined from Weissenberg photographs, which revealed Laue symmetry 6/*mmm* in both cases. The presence of six-fold rotational symmetry in upper-level photographs rules out trigonal space groups. Final cell parameters were determined from least-squares analysis of the setting angles of 24 reflections centred on an Enraf-Nonius CAD4 diffractometer in the range $20° \leq 2\theta(Mo\ K\alpha) \leq 39°$ for $FeGe_{0.80}Sb_{0.20}$ and $27° \leq 2\theta(Mo\ K\alpha) \leq 57°$ for $FeGe_{0.67}Sb_{0.33}$. Intensity data were collected at 22 °C with the $\theta–2\theta$ scan technique in the range $5° \leq 2\theta(Mo\ K\alpha) \leq 60°$ for $FeGe_{0.80}Sb_{0.20}$ and $5° \leq 2\theta(Mo\ K\alpha) \leq 70°$ for $FeGe_{0.67}Sb_{0.33}$. Crystal data and further details of the data collections are given in Table 5-3. All calculations were carried out using the SHELXTL (Version 5.1) package.[41] Conventional atomic scattering factors and anomalous

dispersion corrections were used.[42] Intensity data were reduced and averaged, and face-indexed Gaussian-type absorption corrections were applied in XPREP. Initial atomic positions were located by direct methods using XS, and refinements were performed by least-squares methods using XL.

The determination of space groups deserves some discussion. Careful inspection of the $hh\overline{2h}l$ reflections with $l = 2n + 1$ in the reciprocal space plots clearly reveals the presence of a c-glide plane in $FeGe_{0.80}Sb_{0.20}$ (out of 300 such data, only 2 had $I > 3\sigma(I)$) and the absence of a c-glide plane in $FeGe_{0.67}Sb_{0.33}$ (out of 420 such data, 119 had $I > 3\sigma(I)$). Thus, $P6_3/mmc$ was chosen for $FeGe_{0.80}Sb_{0.20}$ and $P6/mmm$ was chosen for $FeGe_{0.67}Sb_{0.33}$. The choice of $P6/mmm$ for $FeGe_{0.67}Sb_{0.33}$ is supported by its isotypy with $CoGe_{0.67}Sb_{0.33}$[36] and its relation to the structure of the parent binary FeGe (CoSn-type),[1] both of which also crystallize in $P6/mmm$. Attempted solution of the structure of $FeGe_{0.80}Sb_{0.20}$ in $P6/mmm$ was unsuccessful. Moreover, the excellent match between the observed and calculated powder patterns for $FeGe_{0.80}Sb_{0.20}$ eliminates any possibility that the difference in space group is an artifact of twinning problems in the single crystal.

The structure determination of $FeGe_{0.67}Sb_{0.33}$ was the more straightforward one. With the assumption that $FeGe_{0.67}Sb_{0.33}$ is isostructural to $CoGe_{0.67}Sb_{0.33}$,[36] the initial atomic positions were chosen from the latter, and refinement proceeded smoothly. Since the Sb(1) site in $CoGe_{0.67}Sb_{0.33}$ was found to deviate slightly from full occupancy, refinements allowing the occupancies of successive atoms in $FeGe_{0.67}Sb_{0.33}$ to vary were conducted. These resulted in essentially 100% occupancy for all atoms except Sb(1) and Sb(2), which show only slight deviations from full occupancies at 95.1(6) and 97.4(8)%, respectively. The resulting formula can be written as "$Fe_3Ge_2Sb_{0.96}$" (with $Z = 6$), close

to the ideal formula of "Fe_3Ge_2Sb" and in excellent agreement with the elemental analysis. For simplicity, and for ease of comparison to the parent binary FeGe, we use the formula "$FeGe_{0.67}Sb_{0.33}$" interchangeably with "Fe_3Ge_2Sb."

The initial positions of all atoms in $FeGe_{0.80}Sb_{0.20}$, except Ge(2) and Ge(3), were found by direct methods, and atomic assignments were made in analogy to $FeGe_{0.67}Sb_{0.33}$ and FeGe. A first refinement revealed considerable electron density at the sites 0, 0, 0 and $\frac{1}{3}$, $\frac{2}{3}$, ~ 0, located at the centres of iron hexagons, 0.52 Å from Sb(2) and 0.60 Å from Sb(1), respectively. These positions were assigned to Ge atoms on the basis of reasonable Fe–Ge bond lengths and the assumption that this structure represents a member of a series $FeGe_{1-x}Sb_x$ in which Sb_2 pairs have partially replaced the Ge(1) atoms of FeGe. The proximity of the positions of Ge(2) and Ge(3) to those of Sb(1) and Sb(2), respectively, requires that these sites be partially occupied. The Ge(2)/Sb(1) and Ge(3)/Sb(2) displacement parameters were constrained to be identical in order to obviate the high correlation between the positional and displacement parameters of these closely-spaced sites. Refinements allowing the occupancies of successive atoms to vary freely resulted in essentially full occupancy for Fe(1), Fe(2), and Ge(1), but considerably less than 100% for the other atoms. In the final refinement, the Fe(1), Fe(2), and Ge(1) occupancies were fixed at 100%, while those for the remaining atoms converged to 29.0(9)% for Ge(2), 49(1)% for Ge(3), 59.4(9)% for Sb(1), and 22.2(6)% for Sb(2). The resulting formula can be written as "$Fe_3Ge_{2.36}Sb_{0.54}$" (with $Z = 6$), in excellent agreement with the elemental analysis and the nominal loaded composition of "$Fe_3Ge_{2.4}Sb_{0.6}$." Again, in order to emphasize structural relations, we refer to this compound interchangeably as "$FeGe_{0.80}Sb_{0.20}$" or "$Fe_3Ge_{2.4}Sb_{0.6}$."

The final refinements for $FeGe_{0.67}Sb_{0.33}$ and $FeGe_{0.80}Sb_{0.20}$ lead to reasonable values for the anisotropic displacement parameters and to featureless difference electron density maps ($\Delta\rho_{max} = 1.82$, $\Delta\rho_{min} = -2.16$ e Å^{-3} for $FeGe_{0.67}Sb_{0.33}$; $\Delta\rho_{max} = 2.65$, $\Delta\rho_{min} = -1.14$ e Å^{-3} for $FeGe_{0.80}Sb_{0.20}$). (Some of the thermal ellipsoids are elongated along the c direction, consistent with what is observed in the related structure of CoSn and explicable by the unusual coordination of atoms within large hexagonal channels.[2]) The atomic positions were standardized with the program STRUCTURE TIDY.[43] Final values of the positional and displacement parameters are given in Table 5-4, and interatomic distances are listed in Table 5-5. Anisotropic displacement parameters for $FeGe_{0.67}Sb_{0.33}$ and $FeGe_{0.80}Sb_{0.20}$ are listed in Table A-15.

Results and Discussion

Solid Solution Ranges. Ternary solid solutions form for all three pnictide systems $FeGe_{1-x}Pn_x$ ($Pn = $ P, As, Sb), with the phosphide and arsenide systems displaying similar behaviour and the antimonide system being unique. In the ranges $0.4 \leq x \leq 1.0$ for $FeGe_{1-x}P_x$ and $0.3 \leq x \leq 1.0$ for $FeGe_{1-x}As_x$, single-phase products are obtained whose powder patterns are consistent with the MnP-type structure. Extrapolating from the single-crystal structure of a representative member, $FeGe_{0.15}P_{0.85}$,[38] we presume that Ge and Pn are completely disordered over the anion site for all regions of solid solubility. Figures 5-1 and 5-2 show plots of the orthorhombic cell parameters derived from the powder patterns for $FeGe_{1-x}P_x$ and $FeGe_{1-x}As_x$, respectively, as a function of x. Starting from the pnicogen-rich end, $FePn$ ($Pn = $ P, As) ($x = 1.0$), substitution of Pn with Ge through decreasing x causes the cell volume to expand in $FeGe_{1-x}P_x$ but to remain

relatively constant in $FeGe_{1-x}As_x$. These trends are consistent with Ge being larger than P, but similar in size to As. The cell expansion is isotropic on decreasing x in $FeGe_{1-x}P_x$, as seen in the increases in a, b, and c (Figure 5-1), with relative expansions of ~ 2% each to account for the 6% increase in cell volume on going from FeP to $FeGe_{0.6}P_{0.4}$. In contrast, the apparent constancy in the cell volume on decreasing x in $FeGe_{1-x}As_x$ results from the near cancellation of the relative contraction of 1.8% in b with the relative expansions of 1.1% in a and 0.6% in c on going from FeAs to $FeGe_{0.7}As_{0.3}$ (Figure 5-2). In the MnP structure, which adopts an orthorhombic distortion of the more symmetric hexagonal NiAs structure, the metal atoms are shifted to form two close metal–metal contacts in the bc plane in addition to the two contacts in the ac plane that are remnants of the metal–metal bonding network in the NiAs structure.[13,44] The anions are also shifted to form metalloid–metalloid contacts in the ab plane. These distortions result in zigzag chains of metal atoms along the a direction, and similar chains of metal and of metalloid atoms along the b direction. The interpretation of the trend in cell parameters in $FeGe_{1-x}As_x$, then, is that as Ge atoms replace As atoms, there is a slight strengthening of the metalloid–metalloid bonding along the b direction, accompanied by a weakening of the Fe–Fe bonding in the zigzag chains along the a direction.

In the Ge-rich end of the $FeGe_{1-x}P_x$ $(0 < x < 0.4)$ and $FeGe_{1-x}As_x$ $(0 < x < 0.3)$ systems, products form whose powder patterns are very complicated and do not appear to match either those of the known binary iron germanides or pnictides, or of a hexagonal $Fe_{33}Ge_{29+x}P_{6-x}$ phase identified recently.[8] Attempts to index these patterns by trial and error were unsuccessful, and it is possible that these are not single-phase products or are of low symmetry. At $x = 0$, the hexagonal FeGe phase is obtained.

In the antimonide system $FeGe_{1-x}Sb_x$, two major regimes are found, as depicted in Figure 5-3. In the Ge-rich region, $0 \le x \le 0.4$, a series of ternary compounds which adopt superstructures related to the CoSn-type, to be described in more detail later, forms. In the Sb-rich region, $0.4 \le x \le 1.0$, ternary solid solutions with the NiAs-type structure form, which may be regarded as resulting from partial substitution of Ge for Sb in the parent binary FeSb ($x = 1.0$). However, the NiAs-type phase is formed along with significant amounts of $FeSb_2$. This is not unexpected given that at 700 °C in the binary Fe–Sb system $FeSb_2$ coexists with $Fe_{1+x}Sb$ (a non-stoichiometric metal-rich phase with extra Fe atoms entering vacant sites in the ideal NiAs-type structure, leading towards the Ni_2In-type structure).[45] The compositions of the ternary phases in this region, therefore, cannot be directly related to the loading composition. Nevertheless, general trends in the cell parameters (Figure 5-3) are readily understood, with a, c, and V contracting as smaller Ge atoms replace Sb atoms in FeSb with decreasing x, and reaching a plateau at x $\approx$ 0.5. The formula $FeGe_{0.5}Sb_{0.5}$ thus corresponds approximately to the limiting composition for the NiAs-type phase. At $x = 0.4$, a miscibility gap occurs, and a new phase appears which is more closely related to the CoSn-type binary FeGe.

Structures of $FeGe_{0.80}Sb_{0.20}$ and $FeGe_{0.67}Sb_{0.33}$. A series of structures is elaborated in the region $0 \le x \le 0.4$ of the $FeGe_{1-x}Sb_x$ system, with FeGe at one extreme, $FeGe_{0.67}Sb_{0.33}$ at the other extreme, and $FeGe_{0.80}Sb_{0.20}$ as a representative intermediate structure. All three can be decomposed into a common framework of composition Fe_3Ge_2 comprising 3636 (kagomé) nets of Fe atoms and 6^3 honeycomb nets of Ge atoms, as shown in Figure 5-4. When stacked in an alternating fashion along the c direction (Figure 5-4a), the overlapping Fe and Ge nets leave open channels along 0, 0, z and

$\frac{1}{3}$, $\frac{2}{3}$, z. These channels can be occupied by single Ge atoms at the centre of hexagons in the plane of the 3636 Fe nets (sites marked by $\times$ or $+$ in Figure 5-4c), or by Sb_2 pairs whose centre of mass lies at the centre of hexagons in the plane of the 6^3 Ge nets (sites marked by $\square$, $\triangle$, $\lozenge$, or $\triangledown$ in Figures 5-4b and d). The differing occupancy of these sites distinguishes the three structures of FeGe, $FeGe_{0.80}Sb_{0.20}$, and $FeGe_{0.67}Sb_{0.33}$ from each other, as listed in Table 5-6 and shown in Figure 5-5.

In FeGe, all the planar hexagonal sites within the 3636 Fe nets ($\times$, $+$) are completely occupied by the Ge(1) atoms (Figure 5-5a). (These sites are really equivalent in FeGe, whose smaller unit cell can be transformed to those of $FeGe_{0.80}Sb_{0.20}$ and $FeGe_{0.67}Sb_{0.33}$ via $\vec{a} = 2\vec{a}' + \vec{b}'$, $\vec{b} = -\vec{a}' + \vec{b}'$, and $\vec{c} = 2\vec{c}'$.) At the other extreme, in $FeGe_{0.67}Sb_{0.33}$, the 0, 0, z sites in one 6^3 Ge net ($\triangle$) and the $\frac{1}{3}$, $\frac{2}{3}$, z sites in the other 6^3 Ge net ($\lozenge$) are essentially completely occupied by Sb_2 pairs in an ordered fashion (Figure 5-5c). The ordering of these Sb_2 pairs within the two kinds of Ge nets gives rise to the superstructure and the larger unit cell (with 6 times the volume of the FeGe unit cell) observed in $FeGe_{0.67}Sb_{0.33}$. It is also possible to regard the $FeGe_{0.67}Sb_{0.33}$ structure (Figure 5-5c) as resulting from Sb atoms replacing the Ge(1) atoms in FeGe (Figure 5-5a), followed by a shift of these atoms above and below the Fe nets. This point of view reinforces the compositional similarity of FeGe (Fe_3Ge_2 framework + Ge atoms = Fe_3Ge_3) and $FeGe_{0.67}Sb_{0.33}$ (Fe_3Ge_2 framework + shifted Sb atoms = Fe_3Ge_2Sb). However, we prefer the description of an Sb_2 *pair* because bonding considerations suggest that this is an inseparable entity and because it facilitates the description of the intermediate structures between FeGe and $FeGe_{0.67}Sb_{0.33}$. In $FeGe_{0.80}Sb_{0.20}$, all possible sites within the Fe nets are occupied by Ge atoms, and all possible sites within the Ge

nets are occupied by Sb_2 pairs, but at the partial occupancies shown in Figure 5-5b. Both single Ge atoms and Sb_2 pairs fill the channels of the Fe_3Ge_2 framework in a disordered manner in this structure. Although the partial occupancy of Sb(1) and Sb(2) can also imply the presence of *single* Sb atoms on a local scale, we favour an interpretation in which the insertion of Sb_2 *pairs* gradually excludes the presence of Ge(2) or Ge(3) atoms directly above and below in the sandwiching Fe nets. Continuing this process of insertion of Sb_2 pairs concomitant with removal of Ge atoms leads ultimately to the limiting structure of $FeGe_{0.67}Sb_{0.33}$.

The insertion of Sb_2 pairs into the 0, 0, z and $\frac{1}{3}$, $\frac{2}{3}$, z channels introduces distortions in the Fe and Ge nets, as can be discerned by examining the distances listed in Table 5-6. Within the 3636 nets, each Fe atom is bonded to four neighbouring Fe atoms in the same plane. In FeGe, the Fe nets are perfectly flat and undistorted, with all Fe–Fe distances equal at 2.5013(2) Å.[1] With increasing Sb content, the Fe–Fe bonds lengthen to 2.525(2)–2.547(1) Å in $FeGe_{0.80}Sb_{0.20}$ and further to 2.5963(8)–2.598(2) Å in $FeGe_{0.67}Sb_{0.33}$, and the Fe nets become ruffled. Within the 6^3 nets that alternate in stacking with the Fe nets, each Ge atom is bonded to three neighbouring Ge atoms in the same plane. In FeGe, the Ge nets are again flat and undistorted, with all Ge–Ge distances equal at 2.8883(2) Å.[1] Insertion of Sb_2 pairs has a dramatic effect in distorting these Ge nets to form short and long Ge(1)–Ge(1) interactions of 2.792(2) and 2.917(3)–3.086(3) Å, respectively, in $FeGe_{0.80}Sb_{0.20}$. Finally, at the extreme of $FeGe_{0.67}Sb_{0.33}$, the Ge nets have distorted to become two types: the Ge(1) net which segregates into isolated 6-membered rings (intraring 2.827(1) *vs.* inter-ring 3.334(4) Å distances), and the Ge(2) net which segregates into pairs (short 2.732(3) *vs.* long 3.128(3) Å distances). These two

nets are also distinguishable because the Ge(1) net contains the Sb(1) pairs, occupying the $\frac{1}{3}$, $\frac{2}{3}$, z sites which are twice as dense as the 0, 0, z sites, while the Ge(2) net contains the Sb(2) pairs.

Although these structures have been represented by a stacking of layers, it is important to realize that bonding extends between the layers as well, in the c direction. Each Fe atom in the 3636 net is bonded to four Ge atoms at 2.474(1)–2.495(1) Å in $FeGe_{0.80}Sb_{0.20}$ and 2.471(1)–2.520(1) Å in $FeGe_{0.67}Sb_{0.33}$ in the adjacent Ge nets above and below. These distances are reasonable, when compared to the 2.4892(3) Å Fe–Ge(2) bonds found in FeGe.[1] Alternatively, the Ge atoms in the 6^3 nets can be regarded as being coordinated in a trigonal prismatic fashion to six Fe atoms. The Sb–Sb distances in the Sb_2 pairs of $FeGe_{0.80}Sb_{0.20}$ (2.801(1)–2.845(6) Å) and $FeGe_{0.67}Sb_{0.33}$ (2.835(2)–2.895(2) Å) imply strong bonding interactions, equivalent to a single bond such as found in elemental α-Sb (2.908 Å)[46] or in the Sb_2 pairs of $FeSb_2$ (2.887(1) Å).[47] Each filling atom (Sb or Ge) is additionally coordinated to a hexagon of Fe atoms at Fe–Sb distances of 2.585(2)–2.611(2) Å in $FeGe_{0.80}Sb_{0.20}$ and 2.6322(3)–2.654(2) Å in $FeGe_{0.67}Sb_{0.33}$, or at shorter Fe–Ge distances of 2.524(2)–2.556(2) Å in $FeGe_{0.80}Sb_{0.20}$. These bond lengths are similar to those found in other compounds (e.g., Fe–Sb distances of 2.68 Å in FeSb[16] and 2.5762(6)–2.616(1) Å in $FeSb_2$;[47] Fe–Ge(1) distance of 2.5013(2) Å in FeGe[1]).

The trends in the cell parameters shown in Figure 5-3 in the Ge-rich end of $FeGe_{1-x}Sb_x$ are now understandable. Starting from FeGe ($x = 0$) and increasing x, the effect of replacing larger Sb atoms for Ge atoms produces an overall increase in cell volume. However, this volume increase occurs mainly because insertion of Sb_2 pairs spreads apart the nets along a, to permit reasonable Fe–Sb bonds to form. Note that the c

axis actually contracts on increasing x, implying strengthened bonding along this direction, consistent with the crystal structures.

MnP- and NiAs-Type Phases in FeGe$_{1-x}$Pn$_x$. The binary transition metal monopnictides commonly adopt the hexagonal NiAs-type structure or its orthorhombic MnP- or NiP-type derivatives,[13,48] and many workers have classified these structural differences on the basis of simple criteria such as atomic sizes, electronegativities, and valence electron counts.[19,44,49–54] These schemes also succeed when extended to mixed-metal solid solutions $M_{1-x}M'_xPn$. However, it is not obvious if they can be applied equally well to mixed-anion systems, since partial substitution of a pnicogen with another metalloid introduces more profound effects (changes in average anion size, electronegativity, average number of electrons in metalloid valence p orbitals) than can be realized in mixed-metal systems, where the d-electron count is primarily changed. Moreover, in the systems under consideration, we would not expect complete substitution of Ge for Pn while retaining a MnP- or NiAs-type structure because FeGe adopts a different structure.

Although several kinds of structural maps have been developed that separate the binary pnictides into the MnP- and NiAs-type domains,[49,50,53,54] the simplest is the Mooser-Pearson plot, which uses the average principal quantum number of the valence shell $\bar{n}$ and the difference in electronegativities of cation and anion $\Delta\chi$ as coordinates.[53,54] With higher $\bar{n}$ and lower $\Delta\chi$, homoatomic directional bonding becomes less important, so it is not surprising that FeSb ($\bar{n} = 4.5$, $\Delta\chi = 0.1$) adopts the more symmetric NiAs-type structure while FeP ($\bar{n} = 3.5$, $\Delta\chi = 0.4$) and FeAs ($\bar{n} = 4$, $\Delta\chi = 0.3$) adopt the distorted MnP-type structure. Ge substitution for P increases $\bar{n}$ and

reduces $\Delta\chi$ in FeP, and Ge substitution for As only reduces $\Delta\chi$ in FeAs. Neither of these changes is sufficient to draw these systems out of the region of the MnP-type structure, as observed experimentally. On the other hand, Ge substitution for Sb mainly reduces $\bar{n}$ in FeSb, with the expectation that, at some point, a new phase may form which features directional bonding. However, the structure formed is *not* the predicted MnP-type, but rather a CoSn-related-type for $FeGe_{1-x}Sb_x$ $(0 \leq x \leq 0.4)$. Calculation of the electron localization function for CoSn has indicated that bonding within the 6^3 Sn layers is directional and covalent,[55] and we assume that this holds as well for $FeGe_{0.80}Sb_{0.20}$ and $FeGe_{0.67}Sb_{0.33}$.

For transition metal monophosphides and less reliably for the monoarsenides, a valence electron count below 11 favours the NiAs-type and from 11 to 14, the MnP-type structure.[19,44] Accordingly, all members of $FeGe_{1-x}P_x$ $(0.4 \leq x \leq 1.0)$ and $FeGe_{1-x}As_x$ $(0.3 \leq x \leq 1.0)$, having electron counts from 12.3 to 13, fall within the MnP-type region. Band structure calculations have substantiated this empirical relationship by showing that occupation of metal–metal bonding levels favours the MnP-type structure in this range of electron counts.[44]

CoSn-Related Phases in $FeGe_{1-x}Sb_x$. FeGe is the only germanide to adopt the hexagonal CoSn-type structure which is encountered almost exclusively in binary compounds of the first-row transition metals and the heavier group 13 and 14 elements (In, Tl, Sn, Pb).[56] The hexagonal FeGe phase is formed only within a narrow temperature range (630–740 °C), transforming to cubic and monoclinic polymorphs at lower and higher temperatures, respectively.[1] Since the compounds $FeGe_{0.80}Sb_{0.20}$ and $FeGe_{0.67}Sb_{0.33}$ could be synthesized over a wider temperature range (at least 600–900 °C),

the substitution of Sb for Ge appears to promote the stabilization of the CoSn-type structure. Because the Sb atoms are presumably too large to fill the hexagonal planar sites within the 3636 Fe net left vacant when the filling Ge atoms leave, they instead form pairs that reside in the hexagonal channels. This suggests that it may be feasible to insert other large atoms such as Sn, and experiments are underway to verify this.

Unlike most intermetallic compounds which are characterized by closest packing and dense arrangements of atoms, the CoSn-type structure is unusual in featuring large voids at the centres of hexagons in the 6^3 metalloid nets which can be potentially filled by guest atoms.[2,55] Thus, inserting large electropositive atoms (R) into such vacant sites in FeGe results in the family of compounds $R\text{Fe}_6\text{Ge}_6$ (R = Li, Mg, Sc, Y, Pr, Nd, Sm, Gd–Lu, U, Ti, Zr, Hf, Nb, Mn).[57–63] The Ge atoms previously in the plane of the 3636 Fe net are displaced above and below so as to form Ge_2 pairs, analogous to the Sb_2 pairs in $\text{FeGe}_{0.67}\text{Sb}_{0.33}$. Indeed, the compound LiFe_6Ge_6 would be isostructural to $\text{FeGe}_{0.67}\text{Sb}_{0.33}$ were it not for the inserted Li atom: $\text{LiFe}_6\text{Ge}_6 \equiv \square\text{Fe}_6(\text{Ge}_4\text{Sb}_2)$.[57] There also exists a Mg-filled member, MgFe_6Ge_6, but with a different ordering of Ge_2 pairs.[58] We may assume, following the Zintl concept,[64,65] that the electropositive atom R donates its valence electrons to the FeGe network (i.e., $\text{Mg}^{2+}[\text{Fe}_6\text{Ge}_6]^{2-}$) to produce an equivalent effect to that achieved by substitution of an element with more valence electrons (such as Sb) for the filling Ge atoms in FeGe. The ordering of the Ge_2 or Sb_2 pairs may still depend on subtle size effects, but it is clear that electronic factors are probably relevant in the pairing of atoms in these compounds. Sb_2 pairs are normally found in Zintl compounds where electron counting rules, based on full electron transfer from the electropositive component to each Sb atom which attains an octet, can account well for the bonding.[66,67]

That these pairs persist in an intermetallic structure such as the CoSn-type indicates the importance of Sb–Sb bonding, which must make a significant contribution towards the stability of these compounds. Since the system $FeSn_{1-x}Sb_x$ ($0 \le x \le 0.2$) was reported to adopt the undistorted CoSn-type structure, it should be re-examined in light of this proposal.[68] Furthermore, the relationship of $FeGe_{0.67}Sb_{0.33}$ to $LiFe_6Ge_6$ suggests that a variety of electropositive atoms R can also be inserted into a $FeGe_{0.67}Sb_{0.33}$ host, and preliminary experiments towards this aim confirm this. Finally, given the range of magnetic properties exhibited by both FeGe and their filled RFe_6Ge_6 derivatives, we anticipate equally interesting behaviour for $FeGe_{1-x}Pn_x$.

Table 5-1. Cell parameters for MnP-type products obtained in $FeGe_{1-x}Pn_x$ ($Pn = $ P, As) reactions.

Loading composition	a (Å)	b (Å)	c (Å)	V (Å^3)
$FeGe_{1-x}P_x$				
$FeGe_{0.6}P_{0.4}$	5.310(2)	3.169(1)	5.915(2)	99.55(4)
$FeGe_{0.5}P_{0.5}$	5.302(3)	3.178(2)	5.918(3)	99.72(7)
$FeGe_{0.4}P_{0.6}$	5.300(2)	3.169(1)	5.913(2)	99.32(4)
$FeGe_{0.3}P_{0.7}$	5.272(3)	3.163(1)	5.886(3)	98.15(6)
$FeGe_{0.2}P_{0.8}$	5.250(3)	3.138(2)	5.853(3)	96.43(8)
$FeGe_{0.1}P_{0.9}$	5.211(2)	3.116(1)	5.812(2)	94.36(5)
FeP	5.191(3)	3.108(2)	5.794(3)	93.46(6)
$FeGe_{1-x}As_x$				
$FeGe_{0.7}As_{0.3}$	5.497(3)	3.311(2)	6.065(4)	110.38(8)
$FeGe_{0.6}As_{0.4}$	5.509(3)	3.318(2)	6.076(3)	111.07(7)
$FeGe_{0.5}As_{0.5}$	5.494(2)	3.316(2)	6.065(3)	110.48(6)
$FeGe_{0.4}As_{0.6}$	5.495(2)	3.321(2)	6.060(2)	110.60(6)
$FeGe_{0.3}As_{0.7}$	5.480(3)	3.329(2)	6.049(4)	110.35(9)
$FeGe_{0.2}As_{0.8}$	5.468(3)	3.344(2)	6.040(3)	110.45(8)
$FeGe_{0.1}As_{0.9}$	5.449(2)	3.351(2)	6.032(3)	110.15(6)
FeAs	5.436(2)	3.370(2)	6.028(3)	110.43(7)

Table 5-2. Cell parameters for products obtained in $FeGe_{1-x}Sb_x$ reactions.

Loading composition	Structure type of product	a (Å)	c (Å)	V (Å^3)
FeGe [a]	CoSn	8.664(2)	8.118(4)	527.9(3)
$FeGe_{0.9}Sb_{0.1}$	stuffed CoSn	8.786(2)	8.012(3)	535.4(3)
$FeGe_{0.8}Sb_{0.2}$	stuffed CoSn	8.888(2)	7.973(3)	545.5(3)
$FeGe_{0.7}Sb_{0.3}$	stuffed CoSn	8.948(2)	7.939(3)	550.5(3)
$FeGe_{0.6}Sb_{0.4}$	stuffed CoSn	9.009(3)	7.919(3)	556.7(3)
	NiAs	4.004(2)	5.027(3)	69.81(6)
$FeGe_{0.5}Sb_{0.5}$	NiAs	3.9993(6)	5.034(1)	69.73(2)
$FeGe_{0.4}Sb_{0.6}$	NiAs	3.996(2)	5.052(3)	69.86(6)
$FeGe_{0.3}Sb_{0.7}$	NiAs	4.025(2)	5.090(3)	71.42(7)
$FeGe_{0.2}Sb_{0.8}$	NiAs	4.043(1)	5.116(3)	72.41(4)
$FeGe_{0.1}Sb_{0.9}$	NiAs	4.0555(9)	5.129(1)	73.06(3)
FeSb	NiAs	4.076(1)	5.135(2)	73.87(4)

[a] The smaller unit cell of FeGe has been transformed to match the larger unit cells of the superstructures adopted by $FeGe_{0.80}Sb_{0.20}$ or $FeGe_{0.67}Sb_{0.33}$ ($a = \sqrt{3}\,a'$, $c = 2c'$, and $V = 6V'$).

Table 5-3. Crystallographic data for $FeGe_{0.80}Sb_{0.20}$ and $FeGe_{0.67}Sb_{0.33}$.

Formula	$Fe_3Ge_{2.4}Sb_{0.6}$ ($FeGe_{0.80}Sb_{0.20}$)	Fe_3Ge_2Sb ($FeGe_{0.67}Sb_{0.33}$)
Formula mass (amu)	405.10	429.41
Space group	D_{6h}^4–$P6_3/mmc$ (No. 194)	D_{6h}^1–$P6/mmm$ (No. 191)
a (Å)	8.7958(18) [a]	8.9885(5) [a]
c (Å)	8.0040(18) [a]	7.9043(6) [a]
V (Å^3)	536.3(2)	553.05(6)
Z	6	6
T (°C)	22	22
Diffractometer	Enraf-Nonius CAD4	Enraf-Nonius CAD4
ρ_{calc} (g cm^{-3})	7.526	7.736
Crystal dimensions (mm)	Hexagonal prism, 0.20 × 0.07 × 0.06	Hexagonal prism, 0.13 × 0.04 × 0.04
Radiation	Graphite-monochromated Mo $K\alpha$, $\lambda = 0.71073$ Å	Graphite-monochromated Mo $K\alpha$, $\lambda = 0.71073$ Å
μ(Mo $K\alpha$) (cm^{-1})	351.9	342.5
Transmission factors [b]	0.054–0.227	0.095–0.364
Scan type	θ–2θ	θ–2θ
Scan speed (deg. min^{-1})	1.67	1.67
Scan range (deg.)	$0.80 + 0.344 \tan\theta$	$0.80 + 0.344 \tan\theta$
2θ limits	$5° \leq 2\theta$(Mo $K\alpha$) $\leq 60°$	$5° \leq 2\theta$(Mo $K\alpha$) $\leq 70°$
Data collected	$-12 \leq h \leq 12$, $-12 \leq k \leq 12$, $-11 \leq l \leq 11$	$-14 \leq h \leq 14$, $-14 \leq k \leq 14$, $-12 \leq l \leq 12$
No. of data collected	5938	9738
No. of unique data, including $F_o^2 < 0$	331 ($R_{int} = 0.162$)	539 ($R_{int} = 0.190$)
No. of unique data, with $F_o^2 > 2\sigma(F_o^2)$	200	390
No. of variables [c]	29	28
$R(F)$ for $F_o^2 > 2\sigma(F_o^2)$ [d]	0.041	0.037
$R_w(F_o^2)$ [e]	0.120	0.080
Goodness of fit [f]	1.13	1.12
$\Delta\rho_{max}$, $\Delta\rho_{min}$ (e Å^{-3})	1.8, −2.2	2.7, −1.1

Table 5-3. Crystallographic data for $FeGe_{0.80}Sb_{0.20}$ and $FeGe_{0.67}Sb_{0.33}$ (continued).

[a] Obtained from a refinement constrained so that $\alpha = \beta = 90°$ and $\gamma = 120°$.

[b] An empirical face-indexed Gaussian-type absorption correction was applied, with the use of programs in the SHELXTL package (Sheldrick, G. M. *SHELXTL Version 5.1*; Bruker Analytical X-ray Systems: Madison, WI, 1997).

[c] Including an extinction coefficient.

[d] $R(F) = \sum \left\| F_o \right| - \left| F_c \right\| / \sum \left| F_o \right|$.

[e] $R_w(F_o^2) = \left[\sum \left[w(F_o^2 - F_c^2)^2 \right] / \sum w F_o^4 \right]^{1/2}$; $w^{-1} = \left[\sigma^2(F_o^2) + (aP)^2 + bP \right]$ where $P = \left[\max(F_o^2, 0) + 2F_c^2 \right] / 3$. For $FeGe_{0.80}Sb_{0.20}$, $a = 0.0400$, $b = 7.1719$; for $FeGe_{0.67}Sb_{0.33}$, $a = 0.0187$, $b = 1.3813$.

[f] $GooF = \left[\sum \left[w(F_o^2 - F_c^2)^2 \right] / (n - p) \right]^{1/2}$ where n is the number of reflections and p is the total number of parameters refined.

Table 5-4. Positional and equivalent isotropic displacement parameters for $FeGe_{0.80}Sb_{0.20}$ and $FeGe_{0.67}Sb_{0.33}$.

Atom	Wyckoff position	Occupancy	x	y	z	U_{eq} (Å^2) ^{a}
			$Fe_3Ge_{2.4}Sb_{0.6}$ ($FeGe_{0.80}Sb_{0.20}$)			
Fe(1)	12k	1	0.16563(13)	0.3312(3)	0.00506(14)	0.0091(5)
Fe(2)	6g	1	1/2	0	0	0.0087(6)
Ge(1)	12j	1	0.33972(17)	0.01113(13)	1/4	0.0111(5)
Ge(2)	4f	0.290(9)	1/3	2/3	0.5032(14)	0.0099(7)
Ge(3)	2a	0.49(1)	0	0	0	0.0057(17)
Sb(1)	4f	0.594(9)	1/3	2/3	0.0723(4)	0.0099(7)
Sb(2)	4e	0.222(6)	0	0	0.0750(7)	0.0057(17)
			Fe_3Ge_2Sb ($FeGe_{0.67}Sb_{0.33}$)			
Fe(1)	12o	1	0.16690(10)	0.3338(2)	0.24422(11)	0.0060(2)
Fe(2)	6i	1	1/2	0	0.26089(19)	0.0073(3)
Ge(1)	6k	1	0.31452(12)	0	1/2	0.0071(2)
Ge(2)	6j	1	0.34802(14)	0	0	0.0080(3)
Sb(1)	4h	0.951(6)	1/3	2/3	0.31686(12)	0.0067(2)
Sb(2)	2e	0.974(8)	0	0	0.17931(17)	0.0064(3)

^{a} U_{eq} is defined as one-third of the trace of the orthogonalized U_{ij} tensor.

Table 5-5. Selected interatomic distances (Å) in $FeGe_{0.80}Sb_{0.20}$ and $FeGe_{0.67}Sb_{0.33}$.

$FeGe_{0.80}Sb_{0.20}$			
Fe(1)–Ge(1)	2.4741(12) (×2)	Fe(2)–Ge(1)	2.4777(9) (×4)
Fe(1)–Ge(1)	2.4949(12) (×2)	Fe(2)–Ge(2)	2.5393(5) (×2)
Fe(1)–Ge(3)	2.524(2)	Fe(2)–Sb(1)	2.6042(9) (×2)
Fe(1)–Fe(1)	2.525(2) (×2)	Ge(1)–Ge(1)	2.792(2)
Fe(1)–Fe(2)	2.5474(11) (×2)	Ge(1)–Ge(1)	2.917(3)
Fe(1)–Ge(2)	2.556(2)	Sb(1)–Sb(1)	2.845(6)
Fe(1)–Sb(2)	2.585(2)	Sb(2)–Sb(2)	2.801(12)
Fe(1)–Sb(2)	2.603(2)		

$FeGe_{0.67}Sb_{0.33}$			
Fe(1)–Ge(1)	2.4714(8) (×2)	Fe(2)–Ge(2)	2.4735(14) (×2)
Fe(1)–Ge(2)	2.4870(8) (×2)	Fe(2)–Ge(1)	2.5203(13) (×2)
Fe(1)–Fe(2)	2.5963(8) (×2)	Fe(2)–Sb(1)	2.6322(3) (×2)
Fe(1)–Fe(1)	2.5984(16) (×2)	Ge(1)–Ge(1)	2.8270(11) (×2)
Fe(1)–Sb(2)	2.6486(16)	Ge(2)–Ge(2)	2.732(3)
Fe(1)–Sb(1)	2.6539(16)	Sb(1)–Sb(1)	2.895(2)
		Sb(2)–Sb(2)	2.835(3)

Table 5-6. Site occupations (in 3636 Fe and 6^3 Ge nets) and homoatomic bond distances (Å) in $FeGe_{0.80}Sb_{0.20}$ and $FeGe_{0.67}Sb_{0.33}$.

	FeGe	$FeGe_{0.80}Sb_{0.20}$ ($Fe_3Ge_{2.4}Sb_{0.6}$)	$FeGe_{0.67}Sb_{0.33}$ (Fe_3Ge_2Sb)
Sites along 0, 0, z [a]			
In Ge net (▢)	‾‾‾‾	Sb$_2$ pairs	‾‾‾‾
In Fe net (×)	Ge	Ge	‾‾‾‾
In Ge net (△)	‾‾‾‾	Sb$_2$ pairs	Sb$_2$ pairs
Sites along $\frac{1}{3}$, $\frac{2}{3}$, z [a]			
In Ge net (◊)	‾‾‾‾	Sb$_2$ pairs	Sb$_2$ pairs
In Fe net (+)	Ge	Ge	‾‾‾‾
In Ge net (▽)	‾‾‾‾	Sb$_2$ pairs	‾‾‾‾
d(Fe–Fe)	2.5013(2)	2.525(2)–2.547(1)	2.5963(8)–2.598(2)
d(Ge–Ge)	2.8883(2)	2.792(2)–3.086(3)	2.732(3)–3.334(4)
d(Sb–Sb)	‾‾‾‾	2.801(1)–2.845(6)	2.835(3)–2.895(2)

[a] Symbols representing these sites are defined in Figure 5-4.
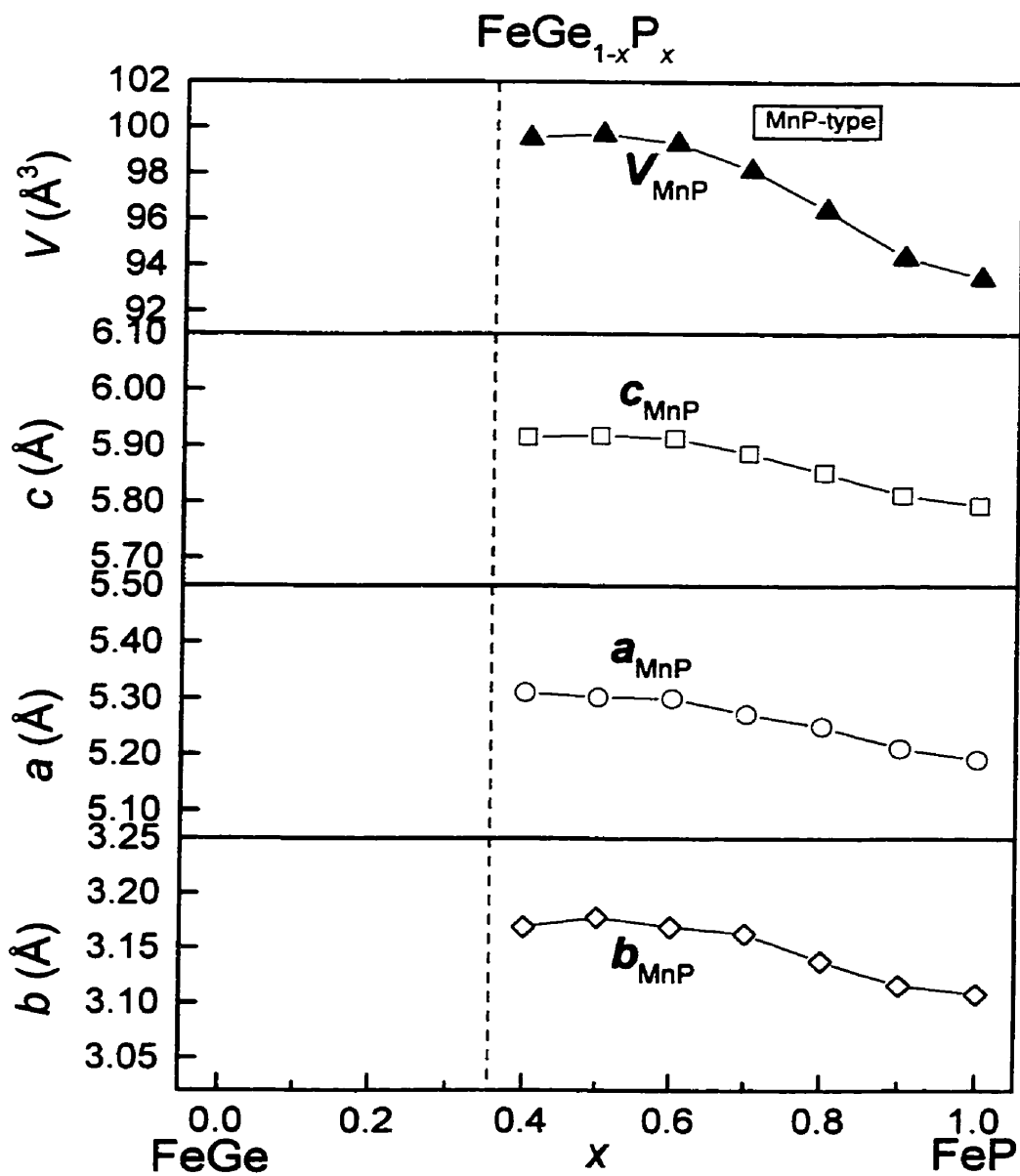
Figure 5-1. Plot of the orthorhombic cell parameters for $FeGe_{1-x}P_x$. Ternary solid solutions of the MnP-type structure form for $0.4 \leq x \leq 1.0$.
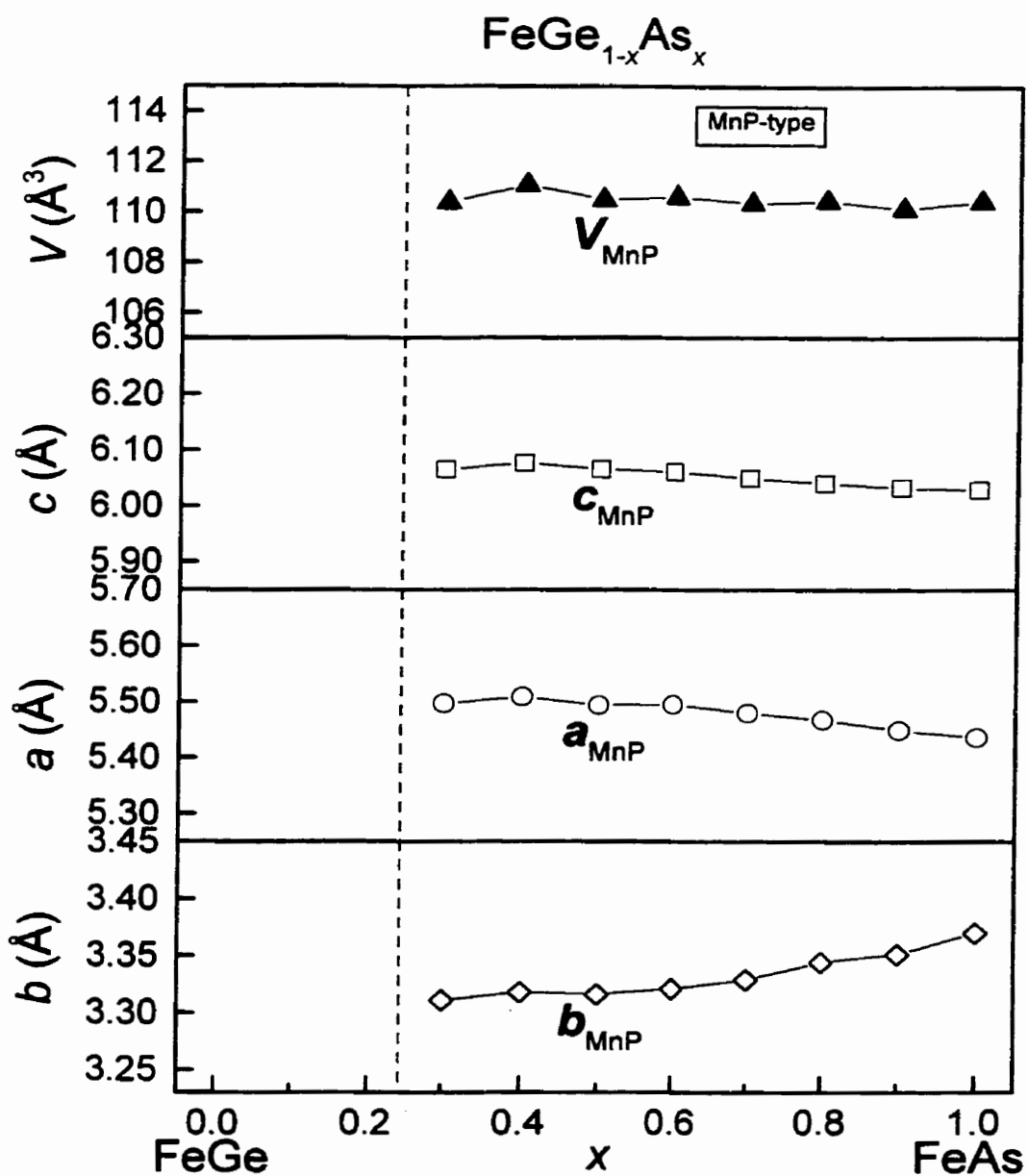
Figure 5-2. Plot of the orthorhombic cell parameters for $FeGe_{1-x}As_x$. Ternary solid solutions of the MnP-type structure form for $0.3 \leq x \leq 1.0$.
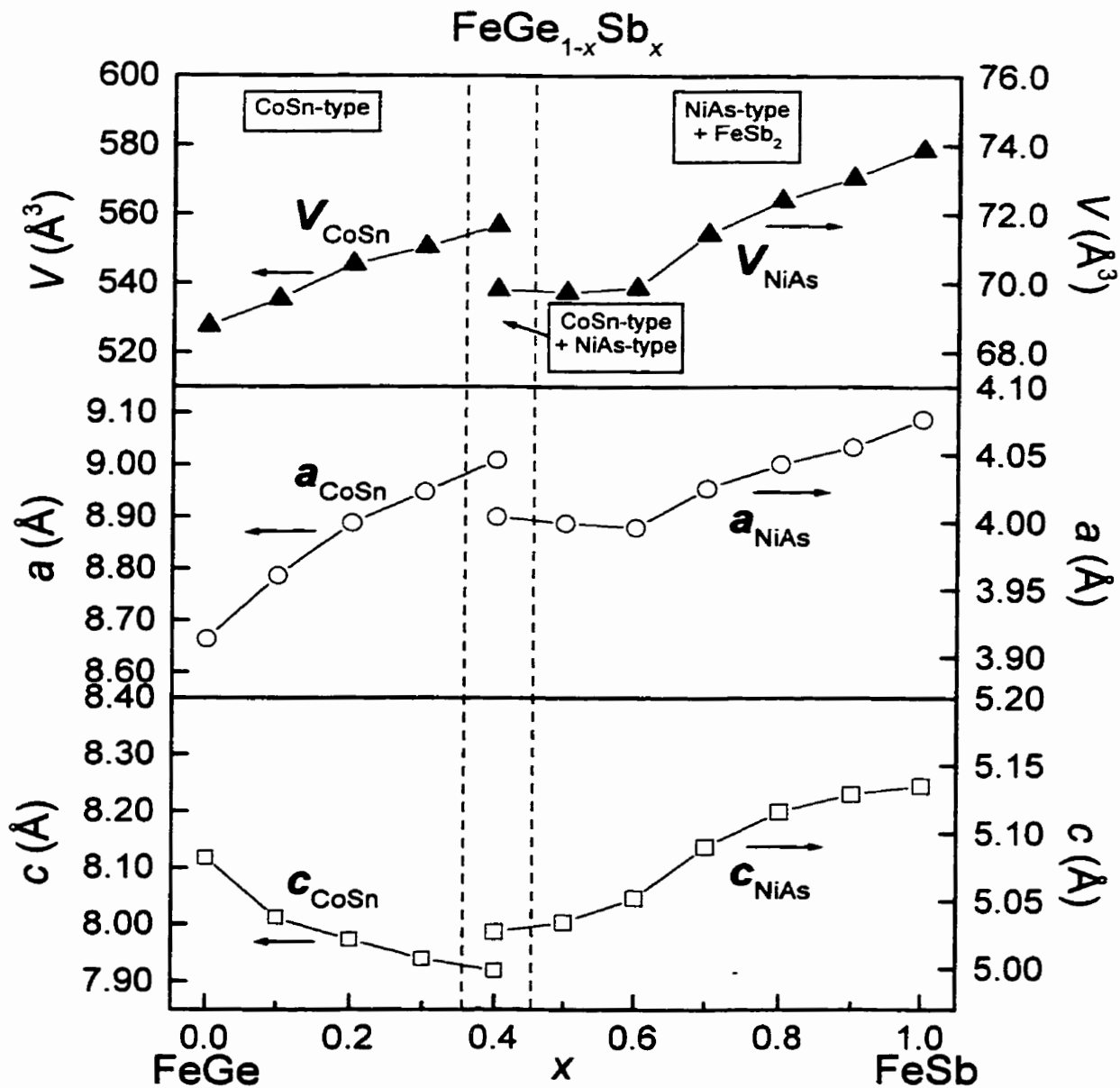
Figure 5-3. Plot of the hexagonal cell parameters for CoSn-related-type structures ($0 \leq x \leq 0.4$) and NiAs-type structures ($0.4 \leq x \leq 1.0$) in $FeGe_{1-x}Sb_x$. The cell parameters for FeGe ($x = 0$) have been transformed to correspond to those of the ternary $FeGe_{1-x}Sb_x$ ($x \leq 0.4$) superstructures.

(a) Stacking of Ge and Fe nets

a ——————— Ge ———————	
α ———●——— Fe ———————	
a' ——————— Ge ———┃———	
α ———●——— Fe ———————	
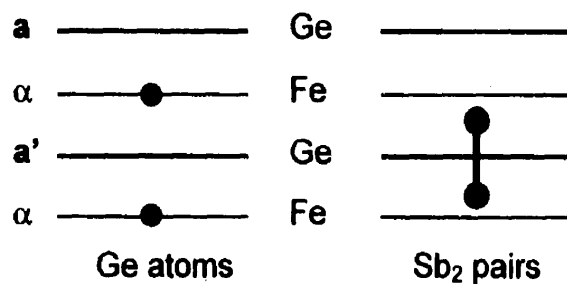
Ge atoms   Sb₂ pairs
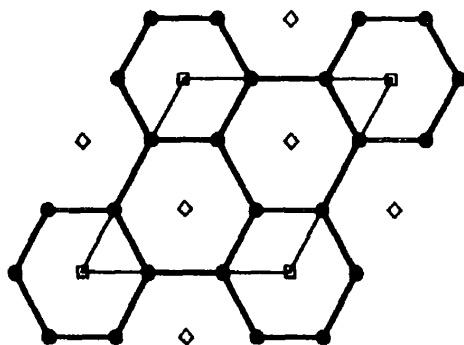
(b) 6^3 **Ge net [a]**   **(c)** 3636 (kagomé) Fe net [α]   **(d)** 6^3 Ge net [a']
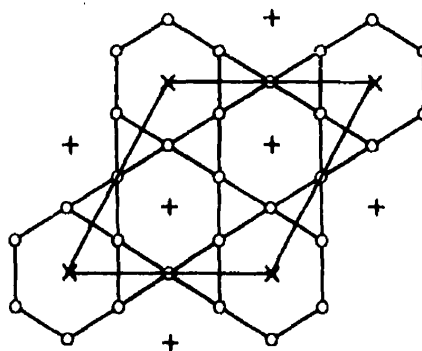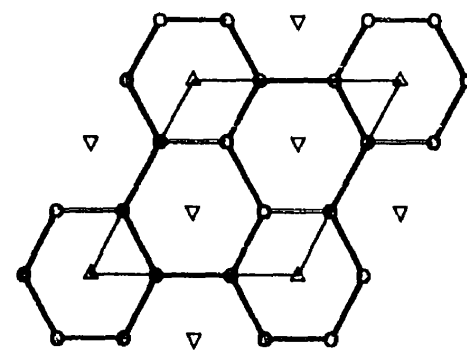
Figure 5-4. (a) Stacking of 3636 (kagomé) Fe nets and 6^3 Ge nets in an $a\alpha a'\alpha$ fashion leads to open channels along $0, 0, z$ and $\frac{1}{3}, \frac{2}{3}, z$ that can be filled by Ge atoms in the Fe net, or Sb_2 *pairs* skewering the Ge net. Potential sites within these nets viewed down the c direction are shown in (b), (c), and (d), and are occupied as listed in Table 5-6 to result in the structures of FeGe, $FeGe_{0.80}Sb_{0.20}$, and $FeGe_{0.67}Sb_{0.33}$ (Figure 5-5).
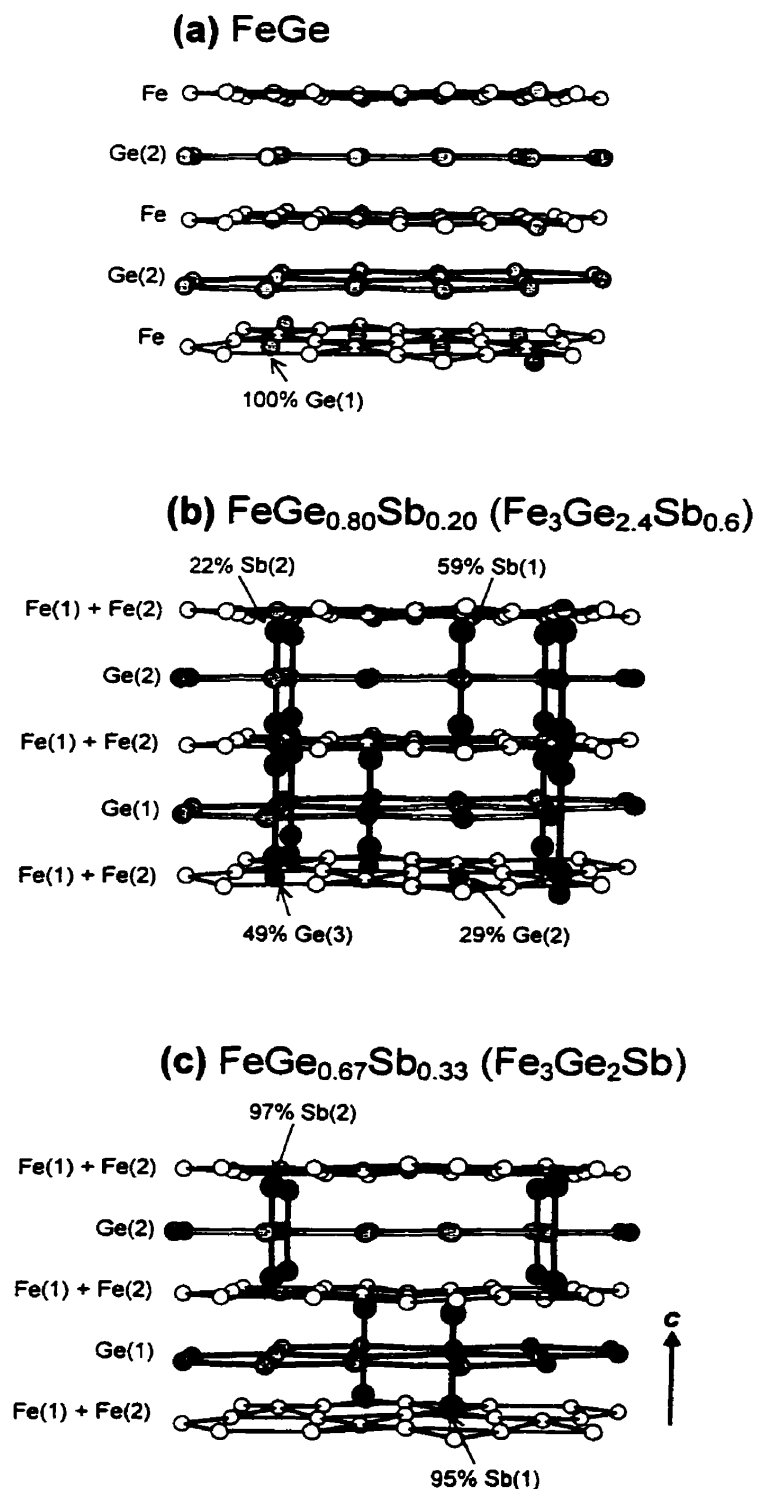
Figure 5-5. Comparison of the structures of (a) FeGe, (b) $FeGe_{0.80}Sb_{0.20}$, and (c) $FeGe_{0.67}Sb_{0.33}$, viewed perpendicular to the c direction. Small open circles are Fe, medium lightly shaded circles are Ge, and large solid circles are Sb. Partial occupancies of the filling Ge atoms and Sb_2 pairs are indicated.

References

(1)   Richardson, M. *Acta Chem. Scand.* **1967**, *21*, 2305.

(2)   Larsson, A. K.; Haeberlein, M.; Lidin, S.; Schwarz, U. *J. Alloys Compd.* **1996**, *240*, 79.

(3)   Nial, O. *Z. Anorg. Allg. Chem.* **1938**, *238*, 287.

(4)   Bernhard, J.; Lebech, B.; Beckman, O. *J. Phys. F: Met. Phys.* **1988**, *18*, 539.

(5)   Bernhard, J.; Lebech, B.; Beckman, O. *J. Phys. F: Met. Phys.* **1984**, *14*, 2379.

(6)   Forsyth, J. B.; Wilkinson, C.; Gardner, P. *J. Phys. F: Met.* Phys. **1978**, *8*, 2195.

(7)   Schubert, K.; Balk, M.; Bhan, S.; Breimer, H.; Esslinger, P.; Stolz, E. *Naturwissenschaften*; **1959**, *46*, 647.

(8)   Berger, R.; Tergenius, L.-E.; Gandour, A. M.; Häggström, L.; Nordblad, P. Private communication.

(9)   Buschow, K. H. J.; van der Goot, A. S. *J. Less-Common Met.* **1968**, *14*, 323.

(10)   Nesbitt, E. A.; Wernick, J. H. *Rare Earth Permanent Magnets*; Academic Press: New York, 1973.

(11)   Felcher, G. P.; Smith, F. A.; Bellavance, D.; Wold, A. *Phys. Rev. B: Solid State*; **1971**, *3*, 3046.

(12)   Selte, K.; Kjekshus, A.; Andresen, A. F. *Acta Chem. Scand.* **1972**, *26*, 3101.

(13)   Rundqvist, S. *Acta Chem. Scand.* **1962**, *16*, 287.

(14)   Selte, K.; Kjekshus, A. *Acta Chem. Scand.* **1969**, *23*, 2047.

(15)   Picone, P. J.; Clark, P. E. *J. Magn. Magn. Mater.* **1981**, *25*, 140.

(16)   Kumar, R.; Harchand, K. S.; Vishwamittar; Chandra, K.; Jernberg, P.; Ericsson, T.; Wäppling, R. *Phys. Rev. B: Condens. Matter*; **1985**, *32*, 69.

(17)   Skolozdra, R. V.; Mel'nik, G. A.; Aksel'rud, L. G. *Crystallogr. Rep. Transl. Kristallografiya*; **1998**, *43*, 380.

(18)   Selte, K.; Kjekshus, A.; Oftedal, T. A. *Acta Chem. Scand. Ser. A*; **1974**, *28*, 803.

(19)   Fjellvåg, H.; Kjekshus, A. *Acta Chem. Scand. Ser. A*; **1986**, *40*, 8.

(20) Selte, K.; Fjellvåg, H.; Kjekshus, A.; Andresen, A. F. *Acta Chem. Scand. Ser. A*; **1979**, *33*, 727.

(21) Hellner, E.; Heger, G.; Mullen, D.; Treutmann, W. *Mater. Res. Bull.* **1975**, *10*, 91.

(22) Fjellvåg, H.; Kjekshus, A.; Andresen, A. F. *Acta Chem. Scand. Ser. A*; **1984**, *38*, 711.

(23) Fjellvåg, H.; Kjekshus, A.; Andresen, A. F.; Zieba, A. *J. Magn. Magn. Mater.* **1988**, *73*, 318.

(24) Seshu Bai, V.; Rama Rao, K. V. S. *J. Phys. F: Met. Phys.* **1983**, *13*, 695.

(25) Selte, K.; Birkeland, L.; Kjekshus, A. *Acta Chem. Scand. Ser. A*; **1978**, *32*, 731.

(26) Selte, K.; Kjekshus, A.; Aaby, S.; Andresen, A. F. *Acta Chem. Scand. Ser. A*; **1975**, *29*, 810.

(27) Andreassen Delphin, I. L.; Selte, K.; Kjekshus, A.; Andresen, A. F. *Acta Chem. Scand. Ser. A*; **1978**, *32*, 179.

(28) Gal'perina, T. N.; Zelenin, L. P.; Fedorova, T. A.; Sidorenko, F. A.; Gel'd, P. V. *Phys. Met. Metallogr. (Engl. Transl.)*; **1977**, *43*, 183.

(29) Moze, O.; Greaves, C.; Bouree-Vigneron, F.; Cockayne, B.; MacEwan, W. R.; Smith, N. A.; Harris, I. R. *Solid State Commun.* **1993**, *87*, 151.

(30) Smith, N. A.; Hill, P. J.; Devlin, E.; Forsyth, H.; Harris, I. R.; Cockayne, B.; MacEwan, W. R. *J. Alloys Compd.* **1992**, *179*, 111.

(31) Vasilev, E. A.; Virchenko, V. A. *Phys. Status Solidi A*; **1982**, *70*, K141.

(32) Selte, K.; Kjekshus, A.; Oftedal, T. A.; Andresen, A. F. *Acta Chem. Scand. Ser. A*; **1974**, *28*, 957.

(33) Rais, A.; Terzieff, P.; Yousif, A. A.; Gismelseed, A. M. *Mater. Lett.* **1998**, *33*, 261.

(34) Harris, I. R.; Smith, N. A.; Devlin, E.; Cockayne, B.; MacEwan, W. R.; Longworth, G. *J. Less-Common Met.* **1989**, *146*, 103.

(35) Fjellvåg, H.; Kjekshus, A. *Acta Chem. Scand.* **1997**, *51*, 910.

(36) Mills, A. M.; Lam, R.; Mar, A. *Can. J. Chem.* **1998**, *76*, 1588.

(37)   *Filmscan* and *Jade 3.0*; Materials Data: Livermore, CA, 1996.

(38)   Mills, A. M.; Mar, A. Unpublished results.

(39)   *POLSQ: Program for least-squares unit cell refinement*; Modified by D. Cahen
          and D. Keszler, Northwestern University, 1983.

(40)   Yvon, K.; Jeitschko, W.; Parthé, E. *J. Appl. Crystallogr.* **1977**, *10*, 73.

(41)   Sheldrick, G. M. *SHELXTL Version 5.1*; Bruker Analytical X-ray Systems:
          Madison, WI, 1997.

(42)   *International Tables for X-ray Crystallography*; Wilson, A. J. C., Ed. Kluwer:
          Dordrecht, The Netherlands, 1992; Vol. C.

(43)   Gelato, L. M.; Parthé, E. *J. Appl. Crystallogr.* **1987**, *20*, 139.

(44)   Tremel, W.; Hoffmann, R.; Silvestre, J. *J. Am. Chem. Soc.* **1986**, *108*, 5174.

(45)   Richter, K. W.; Ipser, H. *J. Alloys Compd.* **1997**, *247*, 247.

(46)   Donohue, J. *The Structures of the Elements*; John Wiley and Sons: New York,
          1974.

(47)   Holseth, H.; Kjekshus, A. *Acta Chem. Scand.* **1969**, *23*, 3043.

(48)   Larsson, E. *Ark. Kemi*; **1964**, *23*, 335.

(49)   Phillips, J. C. *Phys. Rev. B: Condens. Matter*; **1988**, *37*, 2483.

(50)   Pettifor, D. G.; Podloucky, R. *Phys. Rev. Lett.* **1984**, *53*, 1080.

(51)   Franzen, H. F.; Haas, C.; Jellinek, F. *Phys. Rev. B: Solid State*; **1974**, *10*, 1248.

(52)   Selte, K.; Kjekshus, A. *Acta Chem. Scand.* **1973**, *27*, 3195.

(53)   Pearson, W. B. *The Crystal Chemistry and Physics of Metals and Alloys*; John
          Wiley and Sons: New York, 1972.

(54)   Mooser, E.; Pearson, W. B. *Acta Crystallogr.* **1959**, *12*, 1015.

(55)   Simak, S. I.; Häußermann, U.; Abrikosov, I. A.; Eriksson, O.; Wills, J. M.; Lidin,
          S.; Johansson, B. *Phys. Rev. Lett.* **1997**, *79*, 1333.

(56)   Villars, P. *Pearson's Handbook, Desk Edition: Crystallographic Data for
          Intermetallic Phases*; ASM International: Materials Park, OH, 1997.

(57)   Welk, E.; Schuster, H.-U. *Z. Anorg. Allg. Chem.* **1976**, *424*, 193.

(58)   Buchholz, W.; Schuster, H.-U. *Z. Naturforsch. B: Anorg. Chem. Org. Chem.* **1978.** *33*, 877.

(59)   Venturini, G.; Welter, R.; Malaman, B. *J. Alloys Compd.* **1992**, *185*, 99.

(60)   Mruz, O. Ya.; Starodub, P. K.; Bodak, O. I. *Dopov. Akad. Nauk Ukr. RSR Ser. B: Geol. Khim. Biol. Nauki*; **1984**, 44.

(61)   Gonçalves, A. P.; Waerenborgh, J. C.; Bonfait, G.; Amaro, A.; Godinho, M. M.; Almeida, M.; Spirlet, J. C. *J. Alloys Compd.* **1994**, *204*, 59.

(62)   Olenych, R. R.; Aksel'rud, L. G.; Yarmolyuk, Ya. P. *Dopov. Akad. Nauk Ukr. RSR Ser. A: Fiz.-Mat. Tekh. Nauki*; **1981**, *43*, 84.

(63)   Malaman, B.; Roques, B.; Courtois, A.; Protas, J. *Acta Crystallogr. Sect. B: Struct. Crystallogr. Cryst. Chem.* **1976**, *32*, 1352.

(64)   *Chemistry, Structure, and Bonding of Zintl Phases and Ions*; Kauzlarich, S. M., Ed. VCH Publishers: New York, 1996.

(65)   Hoistad, L. M. *Inorg. Chem.* **1995**, *34*, 2711.

(66)   Müller, W. *Z. Naturforsch. B: Anorg. Chem. Org. Chem.* **1977**, *32*, 357.

(67)   Wang, R.; Steinfink, H. *Inorg. Chem.* **1967**, *6*, 1685.

(68)   Pavlyuk, V. V.; Bodak, O. I.; Slowinska, A.; Kevorkov, D. G.; Dmytriv, G. S. *Pol. J. Chem.* **1997**, *71*, 11.

Chapter 6

Structures of the Quaternary Iron Germanium Antimonides $R_{1-x}(R,Fe)_6Ge_4(Ge,Sb)_2$ (*R* = Ti, Cr, Mn), Filled Derivatives of $FeGe_{1-x}Sb_x$ [†]

Introduction

Our recent investigation of the pseudo-binary FeGe–FeSb system led to the characterization of a new series of intermetallic compounds, $FeGe_{1-x}Sb_x$ ($0 \le x \le 0.33$),[1] in which Sb_2 pairs gradually replace the isolated Ge atoms of CoSn-type FeGe.[2] Unlike most intermetallic compounds which typically display dense packing of atoms, the compounds $FeGe_{1-x}Sb_x$ feature unusually large hexagonal bipyramidal holes.[3] In FeGe, these vacant sites can be filled by a variety of electropositive guest atoms (*R*), giving the family of compounds RFe_6Ge_6 (*R* = Li, Mg, Sc, Y, Pr, Nd, Sm, Gd–Lu, U, Ti, Zr, Hf, Nb, Mn).[4] Variations in the arrangement of the inserted *R* atoms lead to several different hexagonal structure types[4] and complex superstructures of lower symmetry.[4c,5] Since the structures of RFe_6Ge_6 are closely related to the $CaCu_5$-type structure adopted by the commercial permanent magnet $SmCo_5$,[6] the magnetic behaviour of these compounds has been the focus of considerable attention. The insertion of magnetic transition and rare-

---

earth metal guests, in particular, allows the manipulation of the properties of the antiferromagnetic FeGe host.[4c,5,7] Given the extensive interstitial chemistry that FeGe undergoes, we had anticipated similar behaviour for an intermetallic $FeGe_{1-x}Sb_x$ host structure. Here we report the synthesis of the first members of a series of analogous compounds, $R_{1-x}(R,Fe)_6Ge_4(Ge,Sb)_2$, resulting from the filling of these sites in $FeGe_{1-x}Sb_x$: in $Ti_{0.5}Fe_6Ge_5Sb$, $Cr_{0.8}Fe_{5.3}Ge_{5.2}Sb_{0.8}$, and $Mn_{1.8}Fe_{4.6}Ge_{4.9}Sb_{1.1}$, early transition metals are inserted into the vacant sites, and, in the case of $R = Cr$ and Mn, are partially substituted for the Fe atoms of the host structure.

Experimental Section

Synthesis. Starting materials were the elemental powders: Ti (99.98%, Cerac), V (99.5%, Cerac), Cr (99.95%, Cerac), Mn (99.95%, Cerac), Fe (99.9%, Cerac), Ge (99.999%, Cerac), Sb (99.995%, Aldrich). Reactions were carried out on a 0.250-g scale in evacuated fused-silica tubes (8-cm length; 10-mm i.d.). Elemental compositions were determined by energy-dispersive X-ray (EDX) analysis on a Hitachi S-2700 scanning electron microscope. X-ray powder patterns were collected on an Enraf-Nonius FR552 Guinier camera (Cu $K\alpha_1$ radiation; Si standard).

Following the synthesis of Fe_3Ge_2Sb,[1] we reasoned that vacant sites present in this structure could be filled by electropositive metals R. In order to verify our hypothesis, reactions at the composition $RFe_6Ge_4Sb_2$ ($R = $ Ti–Mn), corresponding to full occupation of the vacant sites, were carried out. Stoichiometric mixtures of the elements were heated at 850 °C for 4–5 days, slowly cooled to 500 °C over 4 days, then cooled to 20 °C over 12 h. For $R = $ Ti, Cr, and Mn, the resulting products contained the title

compounds $R_{1-x}(R,Fe)_6Ge_4(Ge,Sb)_2$, isolated as grey hexagonal prisms, as well as numerous impurity phases, including $FeGe_{1-x}Sb_x$, $R(R,Fe)_6Ge_6$, and quaternary NiAs-type compounds. EDX analyses of several crystals in each system revealed considerable phase width in the $R_{1-x}(R,Fe)_6Ge_4(Ge,Sb)_2$ products: variable substoichiometric occupation of the vacant sites by R, partial substitution of R atoms for the Fe atoms of the Fe_3Ge_2 framework, and partial substitution of Ge for the channel-filling Sb atoms were all observed. Three crystals with varying compositions were selected for structure determination: $Ti_{0.5}Fe_6Ge_5Sb$ (Anal. (mol%): Ti 4.6(2), Fe 48.4(7), Ge 38.0(4), Sb 9.0(4)% (average of 3 analyses)), $Cr_{0.8}Fe_{5.3}Ge_{5.2}Sb_{0.8}$ (Anal. (mol%): Cr 7.1(3), Fe 43.7(6), Ge 41(1), Sb 8(1)% (average of 3 analyses)), and $Mn_{1.8}Fe_{4.6}Ge_{4.9}Sb_{1.1}$ (Anal. (mol%): Mn 14(2), Fe 37(3), Ge 39(2), Sb 9(2)% (average of 3 analyses)). In the case of R = V, however, the only quaternary products formed crystallized in the NiAs-type structure. The absence of an analogous "$V_{1-x}(V,Fe)_6Ge_4(Ge,Sb)_2$" phase is not unexpected given that $V(V,Fe)_6Ge_6$ is not known.

Structure Determination. Pre-screening of the crystals of $R_{1-x}(R,Fe)_6Ge_4(Ge,Sb)_2$ was essential owing to their similarity in colour and habit to $FeGe_{1-x}Sb_x$ and $R(R,Fe)_6Ge_6$. Preliminary cell parameters were obtained from Weissenberg photographs. Long-exposure photographs show weak but observable intensities for reflections with odd l, indicating the presence of superstructure along c. Final cell parameters for $Ti_{0.5}Fe_6Ge_5Sb$ and $Cr_{0.8}Fe_{5.3}Ge_{5.2}Sb_{0.8}$ were determined from least-squares analysis of the setting angles of 1528 reflections in the range $7° \le 2\theta(Mo$ $K\alpha) \le 52°$, or 989 reflections in the range $7° \le 2\theta(Mo\ K\alpha) \le 62°$, respectively, centred on a Bruker P4/RA/SMART–1000 CCD system. Final cell parameters for

$Mn_{1.8}Fe_{4.6}Ge_{4.9}Sb_{1.1}$ were determined from least-squares analysis of the setting angles of 24 reflections in the range $20° \leq 2\theta(Mo\ K\alpha) \leq 42°$ centred on an Enraf-Nonius CAD4 diffractometer. Intensity data were collected at 22 °C, using a combination of ϕ rotations (0.3°) and ω scans (0.3°) in the range $6° \leq 2\theta(Mo\ K\alpha) \leq 52°$ for $Ti_{0.5}Fe_6Ge_5Sb$, and $6° \leq 2\theta(Mo\ K\alpha) \leq 64°$ for $Cr_{0.8}Fe_{5.3}Ge_{5.2}Sb_{0.8}$, or with the $\theta-2\theta$ scan technique in the range $6° \leq 2\theta(Mo\ K\alpha) \leq 70°$ for $Mn_{1.8}Fe_{4.6}Ge_{4.9}Sb_{1.1}$. Crystal data and further details of the data collections are given in Table 6-1. All calculations were carried out using the SHELXTL (Version 5.1) package.[8] Conventional atomic scattering factors and anomalous dispersion corrections were used.[9] Intensity data were reduced and averaged, and face-indexed absorption corrections were applied in XPREP. Initial atomic positions were located by direct methods using XS, and refinements were performed by least-squares methods using XL.

Weissenberg photographs of $Ti_{0.5}Fe_6Ge_5Sb$, $Cr_{0.8}Fe_{5.3}Ge_{5.2}Sb_{0.8}$, and $Mn_{1.8}Fe_{4.6}Ge_{4.9}Sb_{1.1}$ revealed hexagonal Laue symmetry $6/mmm$ and no systematic extinctions. On the basis of intensity statistics and the successful structure solution, the centrosymmetric space group $P6/mmm$ was chosen. Since an intermediate member of the $FeGe_{1-x}Sb_x$ series, $FeGe_{0.8}Sb_{0.2}$, was found to crystallize in the space group $P6_3/mmc$, the $hh\overline{2h}l$ reflections with $l = 2n + 1$, whose absence would be diagnostic of a c-glide, were carefully inspected in the reciprocal space plots. Although these superstructure reflections are inherently weak, they were clearly present in each data set (out of 297, 337, and 408 such reflections in $Ti_{0.5}Fe_6Ge_5Sb$, $Cr_{0.8}Fe_{5.3}Ge_{5.2}Sb_{0.8}$, and $Mn_{1.8}Fe_{4.6}Ge_{4.9}Sb_{1.1}$, respectively, 142, 34, and 42 had $I > 3\sigma(I)$), ruling out the alternative space group $P6_3/mmc$. The choice of $P6/mmm$ is supported by the fact that

FeGe, Fe_3Ge_2Sb, and the three hexagonal structure types adopted by $R(R,Fe)_6Ge_6$ (YCo_6Ge_6, $HfFe_6Ge_6$, and $LiFe_6Ge_6$) all crystallize in this space group.

On the basis of similar powder patterns, cell parameters, and space group, the structures of $R_{1-x}(R,Fe)_6Ge_4(Ge,Sb)_2$ were assumed to be filled derivatives of the host structure Fe_3Ge_2Sb (Co_3Ge_2Sb-type),[1] isostructural to $LiFe_6Ge_6$.[4a] The initial atomic positions of $M(1)$, $M(2)$, $Ge(1)$, $Ge(2)$, $X(1)$, and $X(2)$ were chosen from Fe_3Ge_2Sb. In $Ti_{0.5}Fe_6Ge_5Sb$, the $M(1)$ and $M(2)$ sites are completely filled by Fe. However, for $Cr_{0.8}Fe_{5.3}Ge_{5.2}Sb_{0.8}$ and $Mn_{1.8}Fe_{4.6}Ge_{4.9}Sb_{1.1}$, EDX analyses indicated the partial substitution of Cr or Mn atoms for Fe, and the distribution of R and Fe over the $M(1)$ and $M(2)$ sites was fixed as calculated from these results. EDX analyses also revealed the partial substitution of Ge for Sb in the channel-filling $X(1)$ and $X(2)$ dumbbell sites in all three structures. Each of these sites was restrained to be fully occupied (with a standard deviation of 0.1%), and the total amount of Sb distributed over the two sites was additionally restrained to the value obtained from the EDX analysis of each crystal (with a standard deviation of 10%). A first refinement revealed considerable electron density at the sites $\frac{1}{3}$, $\frac{2}{3}$, 0 ($R(1)$) and 0, 0, $\frac{1}{2}$ ($R(2)$) at the centres of Ge hexagons, which were assigned to Ti, Cr, or Mn atoms. The sum of the partial occupancies of both R sites was restrained to agree with the EDX analyses (with a standard deviation of 10%). Because strong correlation between occupancy and displacement parameters introduced difficulties in modelling these partially occupied sites, the R sites were refined isotropically. For $Ti_{0.5}Fe_6Ge_5Sb$ and $Cr_{0.8}Fe_{5.3}Ge_{5.2}Sb_{0.8}$, refinement of the $R(1)$ and $R(2)$ displacement parameters proceeded satisfactorily only if they were constrained to be identical.

In the case of $Cr_{0.8}Fe_{5.3}Ge_{5.2}Sb_{0.8}$, additional electron density was present at the sites 0, 0, $\sim \frac{1}{4}$ and $\frac{1}{3}$, $\frac{2}{3}$, $\sim \frac{1}{4}$, located approximately 2 Å from $X(1)$ and $X(2)$, respectively, within channels extending along the c direction. These positions were assigned to Ge atoms on the basis of reasonable bond lengths and by analogy with the structure of $FeGe_{0.8}Sb_{0.2}$ in which isolated Ge atoms, as well as Sb_2 pairs, are found.[1] The proximity of the positions of Ge(3) and Ge(4) to those of $X(1)$ and $X(2)$, respectively, precludes these sites from being simultaneously occupied. The occupancies of the Ge and X sites along each channel were thus refined with the restraint that their sum be 100% (with a standard deviation of 0.1%). The Ge(3)/$X(1)$ and Ge(4)/$X(2)$ displacement parameters were constrained to be identical, given the significant correlation in the refinement parameters of these closely spaced sites.

In the final refinements, the occupancies of the $R(1)$, $R(2)$, $X(1)$, and $X(2)$ (and Ge(3), Ge(4) in $Cr_{0.8}Fe_{5.3}Ge_{5.2}Sb_{0.8}$) sites converged to the values indicated in Table 6-2. The resulting formulae $Ti_{0.5}Fe_6Ge_5Sb$, $Cr_{0.8}Fe_{5.3}Ge_{5.2}Sb_{0.8}$, and $Mn_{1.8}Fe_{4.6}Ge_{4.9}Sb_{1.1}$ are in excellent agreement with the EDX analyses. Featureless electron density maps ($\Delta\rho_{max} =$ 3.50, $\Delta\rho_{min} = -1.94$ e Å^{-3} for $Ti_{0.5}Fe_6Ge_5Sb$; $\Delta\rho_{max} = 2.10$, $\Delta\rho_{min} = -1.75$ e Å^{-3} for $Cr_{0.8}Fe_{5.3}Ge_{5.2}Sb_{0.8}$; $\Delta\rho_{max} = 3.00$, $\Delta\rho_{min} = -1.82$ e Å^{-3} for $Mn_{1.8}Fe_{4.6}Ge_{4.9}Sb_{1.1}$), and reasonable isotropic (R sites) and anisotropic (all other sites) displacement parameters were obtained for all three compounds. However, the thermal ellipsoids for the channel-filling $X(1)$ and $X(2)$ (and Ge(3), Ge(4) in $Cr_{0.8}Fe_{5.3}Ge_{5.2}Sb_{0.8}$) sites are somewhat elongated along the c direction. This behaviour is typical of the channel-filling atoms in the related structures of Fe_3Ge_2Sb, $FeGe_{0.8}Sb_{0.2}$,[1] and $CoSn$,[3b] and is likely a result of the unusual coordination of these atoms. In $R_{1-x}(R,Fe)_6Ge_4(Ge,Sb)_2$, the elongated X site

displacement parameters may also indicate that a range of X–X bond distances is possible, as a consequence of the disorder at the X sites. The atomic positions of $Ti_{0.5}Fe_6Ge_5Sb$, $Cr_{0.8}Fe_{5.3}Ge_{5.2}Sb_{0.8}$, and $Mn_{1.8}Fe_{4.6}Ge_{4.9}Sb_{1.1}$ were standardized with the program STRUCTURE TIDY.[10] Final values of the positional and displacement parameters are given in Table 6-2, and interatomic distances are listed in Table 6-3. Anisotropic displacement parameters are listed in Table A-16.

Results and Discussion

Structures. A view of the structure of $R_{1-x}(R,Fe)_6Ge_4(Ge,Sb)_2$ perpendicular to the c direction is presented in Figure 6-1. Together with $FeGe$,[2] $FeGe_{1-x}Sb_x$,[1] and $R(R,Fe)_6Ge_6$,[4] the new compounds $Ti_{0.5}Fe_6Ge_5Sb$, $Cr_{0.8}Fe_{5.3}Ge_{5.2}Sb_{0.8}$, and $Mn_{1.8}Fe_{4.6}Ge_{4.9}Sb_{1.1}$ all share a common framework of composition M_3Ge_2 built up from M and Ge atom nets stacked alternately along the c axis, as shown in Figure 6-2. At $z \approx$ ¼ and ¾, $M(1)$ and $M(2)$ atoms form a 3636 (kagomé) net (α). In $Ti_{0.5}Fe_6Ge_5Sb$, the M sites are completely occupied by Fe atoms; however, in $Cr_{0.8}Fe_{5.3}Ge_{5.2}Sb_{0.8}$ and $Mn_{1.8}Fe_{4.6}Ge_{4.9}Sb_{1.1}$, the smaller transition metal atoms partially replace the Fe atoms of the framework, resulting in M site occupancies of 11% Cr, 89% Fe, and 23% Mn, 77% Fe, respectively. At $z = $ ½, Ge(1) atoms form a distorted 6^3 net containing isolated six-membered Ge rings (**a'**). At $z = 0$, Ge(2) atoms form a similar 6^3 net containing Ge_2 pairs (**a**). When stacked in the sequence aαa'α, the M and Ge nets overlap in such a way as to leave hexagonal channels along 0, 0, z and $\frac{1}{3}$, $\frac{2}{3}$, z (Figure 6-2a). Transition metal atoms (Ti, Cr, or Mn) occupy the sites $R(1)$ and $R(2)$ located at the centres of hexagons in the plane of the Ge nets (Figures 6-2b and d). Ge and Sb atoms are disordered over the X_2

dumbbell sites $X(1)$ and $X(2)$ that skewer the hexagons of the Ge nets (Figures 6-2b and d). In $Cr_{0.8}Fe_{5.3}Ge_{5.2}Sb_{0.8}$, additional sites, Ge(3) and Ge(4), centre hexagons in the plane of the Fe nets (Figure 6-2c). The channel-filling R, X, and Ge sites are occupied as listed in Table 6-4.

In all three structures, the R sites are only partially occupied (Table 6-4), but there is a marked preference for the $R(1)$ site, especially in the case of the largest transition metal, Ti. When the two possible R sites -- $R(1)$ at the centre of a hexagon composed of three Ge_2 pairs (Figure 6-2b), and $R(2)$ at the centre of an isolated Ge_6 ring (Figure 6-2d) -- are compared, the reason for this preference becomes obvious. In each of the sites, the R atom is bonded to six Ge atoms in the same plane. However, the $R(1)$–Ge(2) distances ($Ti_{0.5}Fe_6Ge_5Sb$, 2.8982(9) Å; $Cr_{0.8}Fe_{5.3}Ge_{5.2}Sb_{0.8}$, 2.9059(8) Å; $Mn_{1.8}Fe_{4.6}Ge_{4.9}Sb_{1.1}$, 2.9194(9) Å) correspond more closely to ideal R–Ge distances (cf., Ti–Ge distance of 2.91 Å in $TiFe_6Ge_6$,[4f] or the Mn–Ge distance of 2.93 Å in $Mn_2Fe_5Ge_6$[4g]), while the corresponding $R(2)$–Ge(1) separations ($Ti_{0.5}Fe_6Ge_5Sb$, 2.808(2) Å; $Cr_{0.8}Fe_{5.3}Ge_{5.2}Sb_{0.8}$, 2.831(1) Å; $Mn_{1.8}Fe_{4.6}Ge_{4.9}Sb_{1.1}$, 2.818(2) Å) are significantly shorter.

Each R atom is additionally bonded to two atoms in X sites above and below the plane of the Ge net, along the hexagonal channels. The $X(1)$ and $X(2)$ sites are disordered, containing Ge and Sb atoms at the occupancies listed in Table 6-4. Again, we find more favourable bonding distances for $R(1)$–X. The $R(1)$–$X(1)$ distances ($Ti_{0.5}Fe_6Ge_5Sb$, 2.665(2) Å; $Cr_{0.8}Fe_{5.3}Ge_{5.2}Sb_{0.8}$, 2.618(3) Å; $Mn_{1.8}Fe_{4.6}Ge_{4.9}Sb_{1.1}$, 2.614(2) Å) are somewhat shorter than the corresponding distances in $TiFe_6Ge_6$ (2.74 Å)[4f] or $Mn_2Fe_5Ge_6$ (2.72 Å),[4g] but are still longer than the $R(2)$–$X(2)$ distances ($Ti_{0.5}Fe_6Ge_5Sb$, 2.553(2) Å; $Cr_{0.8}Fe_{5.3}Ge_{5.2}Sb_{0.8}$, 2.592(5) Å; $Mn_{1.8}Fe_{4.6}Ge_{4.9}Sb_{1.1}$,

2.561(2) Å). Both sets of bonding distances are reasonable for R–Ge bonds when compared to those found in Ti_6Ge_5 (2.50(1)–2.95(2) Å),[11] CrGe (2.55–2.64 Å),[12] or $Mn_{11}Ge_8$ (2.442(2)–2.8902(7) Å),[13] but are shorter than most R–Sb bonding distances. Unusually short R–Ge distances along the hexagonal channels are commonly encountered in RFe_6Ge_6 compounds when R is a larger rare-earth metal, so it is possible that a similar situation exists here.[4c,d] Nonetheless, such short R–Sb distances are not unprecedented; R–Sb distances in the 2.4–2.5 Å range occur in the Ni_2In-type compounds $Ti_{1+x}Sb$, $Cr_{1+x}Sb$ and $Mn_{1+x}Sb$.[14] Since the R sites are only partially occupied, it seems probable that the majority of the vacancies are located near Sb, rather than Ge atoms, and, in fact, there is a noticeable correlation between the occupancy of the R site and the proportion of Ge at the X site along each channel.

In $Cr_{0.8}Fe_{5.3}Ge_{5.2}Sb_{0.8}$, the Ge(3) and Ge(4) sites in the plane of the 3636 M net (Figure 6-2c) are located approximately 2 Å from Cr(1) and Cr(2), respectively, along the direction of the hexagonal channels (Figure 6-1). This distance is unreasonably short for Cr–Ge bonds and precludes the Ge and Cr sites from being simultaneously occupied. In other words, a vacancy must always occur at the R site next to Ge(3) or Ge(4) in the same channel. The Ge(3) and Ge(4) sites are also very close ($\sim$ 0.5–0.6 Å) to $X(1)$ and $X(2)$ in these channels (Figure 6-1), which means that on a local level either the Ge site or the X site is filled, but not both simultaneously. Along the 0, 0, z channel, the Ge(4) and $X(2)$ sites are 15(2) and 86(3)% occupied, respectively. Likewise, along the $\frac{1}{3}$, $\frac{2}{3}$, z channel, the respective occupancies of the Ge(3) and $X(1)$ sites are 33.8(6) and 66(2)%.

The Ge and Sb atoms that occupy the $X(1)$ and $X(2)$ sites are arranged in X_2 pairs that may represent Ge_2, Sb_2, or GeSb dumbbells, depending on the local occupancy of the

sites. Accordingly, the X–X distances in these pairs are also dependent on the distribution of Ge and Sb over the sites. Within each structure, the longer $X(2)$–$X(2)$ distances ($Ti_{0.5}Fe_6Ge_5Sb$, 2.872(4) Å; $Cr_{0.8}Fe_{5.3}Ge_{5.2}Sb_{0.8}$, 2.84(1) Å; $Mn_{1.8}Fe_{4.6}Ge_{4.9}Sb_{1.1}$, 2.844(5) Å) are associated with a higher proportion of Sb in the dumbbell site (64(2)%, 54(2)%, and 79(2)%, respectively), consistent with a local environment of mostly GeSb and Sb_2 pairs. These distances are similar to those observed in the Sb_2 dumbbells of Fe_3Ge_2Sb (2.835(3)–2.895(2) Å) or $FeGe_{0.8}Sb_{0.2}$ (2.80(1)–2.845(6) Å),[1] and imply strong Sb–Sb or weaker Ge–Sb bonding interactions. Conversely, the shorter $X(1)$–$X(1)$ distances ($Ti_{0.5}Fe_6Ge_5Sb$, 2.649(3) Å; $Cr_{0.8}Fe_{5.3}Ge_{5.2}Sb_{0.8}$, 2.788(5) Å; $Mn_{1.8}Fe_{4.6}Ge_{4.9}Sb_{1.1}$, 2.738(5) Å) reflect a lower proportion of Sb in the dumbbell site (40(2)%, 36(2)%, and 47(2)%, respectively). In the case of $Ti_{0.5}Fe_6Ge_5Sb$, the hypothetical $X(1)_2$ local environment consists of a significant proportion of Ge_2 pairs, and the observed $X(1)$–$X(1)$ distance is only slightly longer than the 2.56 Å distance in the Ge_2 pairs of $TiFe_6Ge_6$.[4f] Of course, it is important to realize that the thermal parameters of both the $X(1)$ and $X(2)$ sites are elongated along the dumbbell bonding axes. The observed $X(1)$–$X(1)$ and $X(2)$–$X(2)$ separations may be considered as average distances; the true bonding distances of the Ge_2, GeSb, or Sb_2 pairs present may be somewhat shortened or lengthened with respect to these values.

The size and nature of the atoms or atom pairs that fill the open channels of the M_3Ge_2 framework inevitably influence the bonding within the framework. As shown in Figure 6-2c, each M atom of the 3636 nets is bonded to four other M atoms in the same plane (M–M: $Ti_{0.5}Fe_6Ge_5Sb$, 2.5304(9)–2.605(2) Å; $Cr_{0.8}Fe_{5.3}Ge_{5.2}Sb_{0.8}$, 2.5462(9)–2.575(2) Å; $Mn_{1.8}Fe_{4.6}Ge_{4.9}Sb_{1.1}$, 2.557(1)–2.608(2) Å). Comparison of these M–M

distances to the corresponding separations in $TiFe_6Ge_6$ (2.52 Å)[4f] or $Mn_2Fe_5Ge_6$ (2.54 Å)[4g] reveals that the substitution of larger Sb atoms for Ge in the Ge_2 dumbbells of $R(R,Fe)_6Ge_6$ causes a slight expansion of the metal atom nets. This expansion is presumably necessary to maintain $M–X$ distances ($Ti_{0.5}Fe_6Ge_5Sb$, 2.602(2)–2.655(2) Å; $Cr_{0.8}Fe_{5.3}Ge_{5.2}Sb_{0.8}$, 2.615(2)–2.635(2) Å; $Mn_{1.8}Fe_{4.6}Ge_{4.9}Sb_{1.1}$, 2.621(2)–2.661(2) Å) that are suitable for M–Ge or M–Sb bonds. In $Cr_{0.8}Fe_{5.3}Ge_{5.2}Sb_{0.8}$, the isolated Ge atoms are bonded to M atoms at shorter distances of 2.535(2)–2.576(2) Å. Each metal atom in the 3636 nets of all three structures is additionally bonded to four Ge atoms in the adjacent Ge nets above and below at similar M–Ge distances ($Ti_{0.5}Fe_6Ge_5Sb$, 2.475(2)–2.516(2) Å; $Cr_{0.8}Fe_{5.3}Ge_{5.2}Sb_{0.8}$, 2.4830(9)–2.518(1) Å; $Mn_{1.8}Fe_{4.6}Ge_{4.9}Sb_{1.1}$, 2.477(1)–2.526(2) Å).

Two types of distorted 6^3 Ge nets (Figures 6-2b and d) alternate in stacking with the M nets. The Ge(1) atoms cluster into isolated six-membered rings (intraring/inter-ring Ge(1)–Ge(1): $Ti_{0.5}Fe_6Ge_5Sb$, 2.808(2)/3.230(5) Å; $Cr_{0.8}Fe_{5.3}Ge_{5.2}Sb_{0.8}$, 2.831(1)/3.188(3) Å; $Mn_{1.8}Fe_{4.6}Ge_{4.9}Sb_{1.1}$, 2.818(2)/3.274(4) Å). In the Ge(2) net, the Ge atoms segregate into pairs (short/long Ge(2)–Ge(2): $Ti_{0.5}Fe_6Ge_5Sb$, 2.742(4)/3.052(4) Å; $Cr_{0.8}Fe_{5.3}Ge_{5.2}Sb_{0.8}$, 2.769(3)/3.041(3) Å; $Mn_{1.8}Fe_{4.6}Ge_{4.9}Sb_{1.1}$, 2.762(3)/3.074(3) Å). Similar Ge–Ge distances are observed in the compound $FeGe_{0.8}Sb_{0.2}$ (2.792(2)–3.086(3) Å) which adopts a similar structure containing only one type of 6^3 Ge net.[1] Although a direct comparison between these distances is not possible, calculation of the average separations in $R_{1-x}(R,Fe)_6Ge_4(Ge,Sb)_2$ (2.949(2)–2.970(2) Å) and $FeGe_{0.8}Sb_{0.2}$ (2.932(2) Å) indicates that the insertion of R atoms into sites in the Ge nets leads to an expansion of these nets.

Structural Relationships. The existence of $R\text{Fe}_6\text{Ge}_6$,[4] which are filled derivatives of FeGe,[2] led us to postulate that analogous $R\text{Fe}_6\text{Ge}_4\text{Sb}_2$ derivatives of $\text{Fe}_3\text{Ge}_2\text{Sb}$[1] could be synthesized. However, the resulting compounds $R_{1-x}(R,\text{Fe})_6\text{Ge}_4(\text{Ge},\text{Sb})_2$ are more accurately described as filled variants of intermediate members of the solid solution $\text{FeGe}_{1-x}\text{Sb}_x$ (or the hypothetical compounds $(R,\text{Fe})\text{Ge}_{1-x}\text{Sb}_x$). A series of CoSn-related structures is elaborated in the $\text{FeGe}_{1-x}\text{Sb}_x$ ($0 \leq x \leq 0.33$) system, with FeGe (CoSn-type) at one extreme and $\text{Fe}_3\text{Ge}_2\text{Sb}$ ($\text{Co}_3\text{Ge}_2\text{Sb}$-type) at the other.[1] In these compounds, a framework of composition Fe_3Ge_2 is retained, while the channel-filling Ge atoms of FeGe are gradually replaced by Sb. In FeGe, the planar hexagonal sites within the 3636 Fe nets are completely occupied by isolated Ge atoms. As Sb atoms are substituted for the isolated Ge atoms, these shift above and below the plane of the Fe nets to form Sb_2 pairs that skewer the 6^3 Ge nets. At the Sb-rich extreme of the series, the channels of $\text{Fe}_3\text{Ge}_2\text{Sb}$ are completely filled by Sb_2 dumbbells. In intermediate members, such as $\text{FeGe}_{0.8}\text{Sb}_{0.2}$, both isolated Ge atoms and Sb_2 dumbbells fill the framework channels in a disordered manner (Figure 6-3a).

Vacant sites in the planes of the 6^3 Ge nets are present in all of the $\text{FeGe}_{1-x}\text{Sb}_x$ structures. The new quaternary compounds, $\text{Ti}_{0.5}\text{Fe}_6\text{Ge}_5\text{Sb}$, $\text{Cr}_{0.8}\text{Fe}_{5.3}\text{Ge}_{5.2}\text{Sb}_{0.8}$, and $\text{Mn}_{1.8}\text{Fe}_{4.6}\text{Ge}_{4.9}\text{Sb}_{1.1}$, may be considered as filled derivatives of $\text{FeGe}_{0.83}\text{Sb}_{0.17}$, $(\text{Cr}_{0.11}\text{Fe}_{0.89})\text{Ge}_{0.87}\text{Sb}_{0.13}$, and $(\text{Mn}_{0.23}\text{Fe}_{0.77})\text{Ge}_{0.82}\text{Sb}_{0.18}$, respectively (Figures 6-3a and b). With the insertion of guest R atoms into ~ 40–50% of the vacancies in $\text{FeGe}_{1-x}\text{Sb}_x$, all of the formerly isolated Ge atoms pair into Ge_2 or GeSb dumbbells in $\text{Ti}_{0.5}\text{Fe}_6\text{Ge}_5\text{Sb}$ and $\text{Mn}_{1.8}\text{Fe}_{4.6}\text{Ge}_{4.9}\text{Sb}_{1.1}$. If we rewrite the formulae of $\text{Ti}_{0.5}\text{Fe}_6\text{Ge}_5\text{Sb}$ and $\text{Mn}_{1.8}\text{Fe}_{4.6}\text{Ge}_{4.9}\text{Sb}_{1.1}$ as $\text{Ti}_{0.5}\text{Fe}_6\text{Ge}_4(\text{GeSb})$ and $\text{Mn}_{0.4}(\text{Mn}_{1.4}\text{Fe}_{4.6})\text{Ge}_4(\text{Ge}_{0.9}\text{Sb}_{1.1})$, it

becomes apparent that the R site occupancies and the proportion of Ge in the dumbbell sites are effectively related according to $R_{1-x}(R,Fe)_6Ge_4(Ge_{2-2x}Sb_{2x})$. In $Cr_{0.8}Fe_{5.3}Ge_{5.2}Sb_{0.8}$, or $Cr_{0.1}(Cr_{0.7}Fe_{5.3})Ge_4(Ge_{0.6})(Ge_{0.6}Sb_{0.8})$, Cr atoms occupy only ~ 15% of the available R sites, and an appreciable number of the channel-filling Ge atoms remain unpaired. Although we would expect, based on the relationship proposed above, that the proportion of Ge atoms in the dumbbell sites would be equal to the occupancy of the R sites, with the remainder of the Ge atoms left unpaired, (*ie.*, $R_{1-x}(R,Fe)_6Ge_4Ge_y(Ge_{2-2x}Sb_{2x-y}))$, the proportion of Ge atoms in dumbbell sites is considerably higher than expected. As explained in further detail below, problems in the structure solution may account for this discrepancy.

That the insertion of electropositive R atoms is necessary for the formation of Ge_2 or GeSb dumbbells implies that a combination of size effects and electronic factors may be responsible. If size effects are dominant, a model for the local ordering along the channels of $R_{1-x}(R,Fe)_6Ge_4(Ge,Sb)_2$ can be envisioned (Figure 6-4). The channel-filling Sb atoms of $(R,Fe)Ge_{1-x}Sb_x$, too large to fill the hexagonal planar sites in the 3636 M net, occupy dumbbell sites in the hexagonal channels. Because the $R-X$ distances observed in these compounds are unusually short for R–Sb bonds, as discussed earlier, the sites adjacent to the Sb_2 pairs remain vacant when R guest atoms are introduced into the structure. Instead, the R atoms are inserted near channel-filling Ge atoms. As a result, the isolated Ge atoms of the $(R,Fe)Ge_{1-x}Sb_x$ host are displaced from the plane of the M net, forming pairs, to achieve reasonable R–Ge bond distances. However, if the neighbouring R site is vacant, the channel-filling Ge atom remains unpaired. According to this model, the R sites next to Sb and isolated Ge atoms are empty, while the sites next

to Ge dumbbell atoms are always filled. In $Ti_{0.5}Fe_6Ge_5Sb$, $Cr_{0.8}Fe_{5.3}Ge_{5.2}Sb_{0.8}$, and

$Mn_{1.8}Fe_{4.6}Ge_{4.9}Sb_{1.1}$ the correlation between the R site occupancies and the proportion of

Ge in the dumbbell sites along each channel is not perfect; some Ge atoms have no

neighbouring R atom. However, this failure may be a result of problems in modelling

disorder and partial occupancies in the crystal structure determinations. If the structures

are solved with the restriction that the amount of Ge in the X site be equal to twice the

occupancy of the R site, reasonable solutions, with slightly higher agreement factors, are

obtained.

Electronic factors may also be important in the formation of Ge-containing

dumbbells. Although it greatly oversimplifies the situation, we may use the Zintl concept

to explain the relationship between $R_{1-x}(R,Fe)_6Ge_4(Ge,Sb)_2$ and $FeGe_{1-x}Sb_x$.[15] The

electropositive R atoms inserted into $FeGe_{1-x}Sb_x$ donate valence electrons to the

$FeGe_{1-x}Sb_x$ host, causing the pairing of channel-filling Ge atoms, the same effect as that

achieved by substitution of a metalloid with more valence electrons, Sb, for Ge. Were it

not for the inserted R atoms, the filled derivatives of $FeGe_{1-x}Sb_x$ (ie., $Ti_{0.5}Fe_6Ge_5Sb$ and

$Mn_{1.8}Fe_{4.6}Ge_{4.9}Sb_{1.1}$) would be isostructural to Fe_3Ge_2Sb (or $Fe_6Ge_4Sb_2$).[1] In

$Cr_{0.8}Fe_{5.3}Ge_{5.2}Sb_{0.8}$, fewer Cr atoms occupy the R sites, and the number of valence

electrons donated to the $(Cr_{0.11}Fe_{0.89})Ge_{0.87}Sb_{0.13}$ network is not enough to pair all of the

Ge atoms. In support of this electron-transfer hypothesis, recent neutron diffraction and

^{57}Fe Mössbauer studies have demonstrated that both the ordered magnetic moment and

the hyperfine field on the Fe atoms of RFe_6Ge_6 (R = Sc, Ti, Zr, Hf, Nb) are higher than in

the parent compound FeGe and increase with the R valency.[16]

As shown in Figures 6-3b and c, the $R_{1-x}(R,Fe)_6Ge_4(Ge,Sb)_2$ compounds may alternatively be considered as substitutional derivatives of the transition metal-filled germanides $R(R,Fe)_6Ge_6$.[4] Although no Cr-filled germanides, $Cr(Cr,Fe)_6Ge_6$, have been reported, the parent compounds of $Ti_{0.5}Fe_6Ge_5Sb$ and $Mn_{1.8}Fe_{4.6}Ge_{4.9}Sb_{1.1}$ do exist. Both $TiFe_6Ge_6$[4f] and $Mn_2Fe_5Ge_6$[4g] adopt the $HfFe_6Ge_6$ structure type. (Although $Mn_4Fe_3Ge_6$ was the first compound with this structure type to be reported,[4g] Pearson's Handbook describes the structure as the $MgFe_6Ge_6$ type,[4b,17] and most of the literature refers to it as the $HfFe_6Ge_6$ type.[4f] We accept the $HfFe_6Ge_6$ designation since it is currently in wide use.) The $HfFe_6Ge_6$ structure is based on an undistorted Fe_3Ge_2 framework composed of perfectly symmetric 6^3 Ge nets and 3636 Fe nets. Hf atoms and Ge_2 pairs fill the channels of the framework according to a simple ordering scheme: the channel sites in the Ge(1) nets at $z = 0$ are completely filled by Ge_2 pairs, while those in the Ge(2) nets at $z = \frac{1}{2}$ are filled by Hf atoms. Thus, the structure can be described in terms of dumbbell-containing and R-containing slabs stacked alternately along the c direction (Figure 6-3c).

The $HfFe_6Ge_6$-type parent compounds, $TiFe_6Ge_6$[4f] and $Mn_2Fe_5Ge_6$,[4g] can be transformed into $Ti_{0.5}Fe_6Ge_5Sb$ and $Mn_{1.8}Fe_{4.6}Ge_{4.9}Sb_{1.1}$ by substitution of larger Sb atoms for Ge atoms in the dumbbell sites, followed by removal of some of the channel-filling R atoms (Figures 6-3-b and c). If the $HfFe_6Ge_6$-type structure were retained, the substitution of Sb for Ge would spread apart the Ge(1) nets, while the removal of R atoms would shrink the Ge(2) net, leading to structural instability. The $LiFe_6Ge_6$ structure type adopted by $Ti_{0.5}Fe_6Ge_5Sb$ and $Mn_{1.8}Fe_{4.6}Ge_{4.9}Sb_{1.1}$ offers a more favourable arrangement: both R atoms and X_2 dumbbells occupy the channel sites of each Ge net (Figure 6-3b).[4a]

Of the large family of $R(R,Fe)_6Ge_6$ compounds (R = Li, Mg, Sc, Y, Pr, Nd, Sm, Gd–Lu, U, Ti, Zr, Hf, Nb, Mn),[4] only one, the member with the smallest inserted R atoms $LiFe_6Ge_6$ crystallizes in this relatively rare structure.[4a] In general, the transition metal- and smaller rare-earth-filled members adopt the $HfFe_6Ge_6$-type structure,[4c,f,g] while the larger rare-earth-filled members adopt structures with more complex R/Ge_2 ordering schemes that are often unresolved, resulting in the disordered average structure YCo_6Ge_6.[4c–e] Since $R(R,Fe)_6Ge_6$ compounds form for such a large range of R atoms, an equally extensive family of $R_{1-x}(R,Fe)_6Ge_4(Ge,Sb)_2$ compounds may also exist. Preliminary experiments confirm that the series of $R_{1-x}(R,Fe)_6Ge_4(Ge,Sb)_2$ compounds can be extended to include at least R = Gd and Yb,[18] suggesting that a larger family of compounds with a rich structural chemistry remains to be explored.

Table 6-1. Crystallographic data for $Ti_{0.5}Fe_6Ge_5Sb$, $Cr_{0.8}Fe_{5.3}Ge_{5.2}Sb_{0.8}$, and $Mn_{1.8}Fe_{4.6}Ge_{4.9}Sb_{1.1}$.

Formula	$Ti_{0.49(1)}Fe_6Ge_{5.04(3)}Sb_{0.96(4)}$	$Cr_{0.81(1)}Fe_{5.34}Ge_{5.17(4)}Sb_{0.84(3)}$	$Mn_{1.78(2)}Fe_{4.62}Ge_{4.85(2)}Sb_{1.15(2)}$
Formula mass (amu)	841.30	817.92	847.89
Space group	D_{6h}^1–$P6/mmm$ (No. 191)	D_{6h}^1–$P6/mmm$ (No. 191)	D_{6h}^1–$P6/mmm$ (No. 191)
a (Å)	8.8452(11)^a	8.8504(12)^a	8.9099(13)^a
c (Å)	7.9785(9)^a	8.0246(10)^a	7.9665(9)^a
V (Å^3)	540.59(11)	544.35(12)	547.70(13)
Z	3	3	3
T (°C)	22	22	22
Diffractometer	Bruker P4/RA/SMART–1000 CCD	Bruker P4/RA/SMART–1000 CCD	Enraf-Nonius CAD4
ρ_{calc} (g cm^{-3})	7.753	7.485	7.712
Crystal dimensions (mm)	Hexagonal prism, 0.10 × 0.04 × 0.04	Hexagonal prism, 0.10 × 0.05 × 0.05	Hexagonal prism, 0.09 × 0.04 × 0.04
Radiation	Graphite-monochromated Mo $K\alpha$, λ = 0.71073 Å	Graphite-monochromated Mo $K\alpha$, λ = 0.71073 Å	Graphite-monochromated Mo $K\alpha$, λ = 0.71073 Å
μ(Mo $K\alpha$) (cm^{-1})	362.95	355.15	355.52
Transmission factors ^{b}	0.167–0.326	0.160–0.314	0.142–0.331
Scan type	Mixture of ϕ rotations (0.3°) and ω scans (0.3°)	Mixture of ϕ rotations (0.3°) and ω scans (0.3°)	θ–2θ
Scan speed (deg. min.$^{-1}$)	——	——	1.67
Scan range (deg.)	——	——	0.80 + 0.344 tanθ

Table 6-1. Crystallographic data for Ti$_{0.5}$Fe$_6$Ge$_5$Sb, Cr$_{0.8}$Fe$_{5.3}$Ge$_{5.2}$Sb$_{0.8}$, and Mn$_{1.8}$Fe$_{4.6}$Ge$_{4.9}$Sb$_{1.1}$ (continued).

2θ limits	$6° \le 2\theta(\text{Mo } K\alpha) \le 52°$	$6° \le 2\theta(\text{Mo } K\alpha) \le 64°$	$6° \le 2\theta(\text{Mo } K\alpha) \le 70°$
Data collected	$-10 \le h \le 11, -11 \le k \le 10,$ $-9 \le l \le 9$	$-13 \le h \le 13, -13 \le k \le 13,$ $-12 \le l \le 3$	$-14 \le h \le 14, -14 \le k \le 14,$ $-12 \le l \le 12$
No. of data collected	3327	4481	9588
No. of unique data, including $F_0^2 < 0$	261 ($R_{\text{int}} = 0.038$)	423 ($R_{\text{int}} = 0.047$)	533 ($R_{\text{int}} = 0.188$)
No. of unique data, with $F_0^2 > 2\sigma(F_0^2)$	216	242	321
No. of variables ^{c}	33 (4 restraints)	36 (4 restraints)	34 (4 restraints)
$R(F)$ for $F_0^2 > 2\sigma(F_0^2)$ ^{d}	0.029	0.032	0.045
$R_{\text{w}}(F_0^2)$ ^{e}	0.055	0.087	0.100
Goodness of fit ^{f}	1.17	1.08	1.10
$\Delta\rho_{\text{min}}, \Delta\rho_{\text{max}}$ (e Å^{-3})	3.5, −1.9	2.1, −1.7	3.0, −1.8

^{a} Obtained from a refinement constrained so that $a = b$, $\alpha = \beta = 90°$, and $\gamma = 120°$.

^{b} An empirical face-indexed Gaussian-type absorption correction was applied, with the use of the programs in the SHELXTL package (Sheldrick, G. M. *SHELXTL Version 5.1*; Bruker Analytical X-ray Systems: Madison, WI, 1997).

^{c} Including an extinction coefficient.

^{d} $R(F) = \sum ||F_\text{o}| - |F_\text{c}|| / \sum |F_\text{o}|$.

^{e} $R_{\text{w}}(F_0^2) = \left[\sum \left[w(F_0^2 - F_c^2)^2 \right] / \sum w F_\text{o}^4 \right]^{1/2}$; $w^{-1} = \left[\sigma^2(F_\text{o}^2) + (aP)^2 + bP \right]$ where $P = \left[\max(F_\text{o}^2, 0) + 2F_c^2 \right] / 3$. For Ti$_{0.5}Fe_6Ge_5$Sb, $a = 0.0059$, $b = 17.8509$; for Cr$_{0.8}$Fe$_{5.3}$Ge$_{5.2}$Sb$_{0.8}$, $a = 0.0395$, $b = 0.1933$; for Mn$_{1.8}$Fe$_{4.6}$Ge$_{4.9}$Sb$_{1.1}$, $a = 0.0354$, $b = 0.0000$.

Table 6-1. Crystallographic data for $Ti_{0.5}Fe_6Ge_5Sb$, $Cr_{0.8}Fe_{5.3}Ge_{5.2}Sb_{0.8}$, and $Mn_{1.8}Fe_{4.6}Ge_{4.9}Sb_{1.1}$ (continued).

f $GooF = \left[\left[\sum \left[w(F_o^2 - F_c^2)^2 \right] / (n - p) \right]^{1/2} \right]$ where n is the number of reflections and p is the total number of parameters refined.

Table 6-2. Positional and equivalent isotropic displacement parameters for $Ti_{0.5}Fe_6Ge_5Sb$, $Cr_{0.8}Fe_{5.3}Ge_{5.2}Sb_{0.8}$, and $Mn_{1.8}Fe_{4.6}Ge_{4.9}Sb_{1.1}$.

Atom	Wyckoff position	Occupancy	x	y	z	U_{iso} or U_{eq} $(Å^2)$ [a]
			$Ti_{0.5}Fe_6Ge_5Sb$			
Ti(1)	2c	0.72(2)	1/3	2/3	0	0.005(2)
Ti(2)	1b	0.03(2)	0	0	1/2	0.005(2)
M(1) [b]	12o	1	0.17001(12)	0.3400(2)	0.24469(15)	0.0074(4)
M(2) [b]	6i	1	1/2	0	0.2582(2)	0.0079(6)
Ge(1)	6k	1	0.3174(2)	0	1/2	0.0077(4)
Ge(2)	6j	1	0.3450(2)	0	0	0.0073(4)
X(1) [c]	4h	1.00(2)	1/3	2/3	0.3340(2)	0.0123(6)
X(2) [d]	2e	1.00(3)	0	0	0.1800(3)	0.0067(6)
			$Cr_{0.8}Fe_{5.3}Ge_{5.2}Sb_{0.8}$			
Cr(1)	2c	0.14(1)	1/3	2/3	0	0.021(5)
Cr(2)	1b	0.16(2)	0	0	1/2	0.021(5)
M(1) [b]	12o	1	0.16800(11)	0.3360(2)	0.24626(13)	0.0069(3)
M(2) [b]	6i	1	1/2	0	0.25712(16)	0.0074(4)
Ge(1)	6k	1	0.31992(15)	0	1/2	0.0087(3)
Ge(2)	6j	1	0.34356(16)	0	0	0.0084(3)
Ge(3)	4h	0.338(6)	1/3	2/3	0.2477(9)	0.0107(7)
Ge(4)	2e	0.15(2)	0	0	0.241(5)	0.0078(9)
X(1) [c]	4h	0.66(2)	1/3	2/3	0.3263(3)	0.0107(7)
X(2) [d]	2e	0.86(3)	0	0	0.1769(7)	0.0078(9)
			$Mn_{1.8}Fe_{4.6}Ge_{4.9}Sb_{1.1}$			
Mn(1)	2c	0.52(2)	1/3	2/3	0	0.018(3)
Mn(2)	1b	0.15(3)	0	0	1/2	0.032(18)
M(1) [b]	12o	1	0.16896(12)	0.3379(2)	0.2451(2)	0.0082(3)
M(2) [b]	6i	1	1/2	0	0.2585(2)	0.0077(5)
Ge(1)	6k	1	0.31627(18)	0	1/2	0.0074(3)
Ge(2)	6j	1	0.34499(19)	0	0	0.0093(3)

Table 6-2. Positional and equivalent isotropic displacement parameters for $Ti_{0.5}Fe_6Ge_5Sb$, $Cr_{0.8}Fe_{5.3}Ge_{5.2}Sb_{0.8}$, and $Mn_{1.8}Fe_{4.6}Ge_{4.9}Sb_{1.1}$ (continued).

$X(1)$ [c]	$4h$	1.00(2)	1/3	2/3	0.3281(3)	0.0120(4)
$X(2)$ [d]	$2e$	1.00(3)	0	0	0.1785(3)	0.0079(5)

[a] Sites $R(1)$ and $R(2)$ were refined isotropically, and the given value is U_{iso}. All other sites were refined anisotropically, and the given value is U_{eq}, defined as one-third of the trace of the orthogonalized U_{ij} tensor.

[b] Sites $M(1)$ and $M(2)$ contain 100% Fe in $Ti_{0.5}Fe_6Ge_5Sb$; 11% Cr, 89% Fe in $Cr_{0.8}Fe_{5.3}Ge_{5.2}Sb_{0.8}$; and 23% Mn, 77% Fe in $Mn_{1.8}Fe_{4.6}Ge_{4.9}Sb_{1.1}$. These ratios were fixed at compositions determined by EDX analysis.

[c] Site $X(1)$ contains 60(2)% Ge, 40(2)% Sb in $Ti_{0.5}Fe_6Ge_5Sb$; 30(2)% Ge, 36(2)% Sb (and 34% vacancies) in $Cr_{0.8}Fe_{5.3}Ge_{5.2}Sb_{0.8}$; 53(2)% Ge, 47(2)% Sb in $Mn_{1.8}Fe_{4.6}Ge_{4.9}Sb_{1.1}$.

[d] Site $X(2)$ contains 36(2)% Ge, 64(2)% Sb in $Ti_{0.5}Fe_6Ge_5Sb$; 32(3)% Ge, 54(2)% Sb (and 14% vacancies) in $Cr_{0.8}Fe_{5.3}Ge_{5.2}Sb_{0.8}$; 21(2)% Ge, 79(2)% Sb in $Mn_{1.8}Fe_{4.6}Ge_{4.9}Sb_{1.1}$.

Table 6-3. Selected interatomic distances (Å) in $Ti_{0.5}Fe_6Ge_5Sb$, $Cr_{0.8}Fe_{5.3}Ge_{5.2}Sb_{0.8}$, and $Mn_{1.8}Fe_{4.6}Ge_{4.9}Sb_{1.1}$.

	$Ti_{0.5}Fe_6Ge_5Sb$	$Cr_{0.8}Fe_{5.3}Ge_{5.2}Sb_{0.8}$	$Mn_{1.8}Fe_{4.6}Ge_{4.9}Sb_{1.1}$
$R(1)$—Ge(2) (×6)	2.8982(9)	2.9059(8)	2.9194(9)
$R(1)$—X(1) [a] (×2)	2.6649(17)	2.618(3)	2.614(2)
$R(2)$—Ge(1) (×6)	2.8076(19)	2.8314(14)	2.8179(17)
$R(2)$—X(2) [b] (×2)	2.553(2)	2.592(5)	2.561(2)
$M(1)$—M(1) [c] (×2)	2.6047(18)	2.5753(17)	2.608(2)
$M(1)$—M(2) [c] (×2)	2.5304(9)	2.5462(9)	2.5567(10)
$M(1)$—Ge(1) [c] (×2)	2.4799(11)	2.4830(9)	2.4770(14)
$M(1)$—Ge(2) [c] (×2)	2.4781(11)	2.4940(9)	2.4857(14)
$M(1)$—Ge(3) [c,d]	——	2.5345(17)	——
$M(1)$—Ge(4) [c,d]	——	2.5756(19)	——
$M(1)$—X(1) [a,c]	2.6016(18)	2.6146(18)	2.621(2)
$M(1)$—X(2) [b,c]	2.6554(18)	2.635(2)	2.661(2)
$M(2)$—Ge(1) [c] (×2)	2.5160(19)	2.5177(13)	2.5264(19)
$M(2)$—Ge(2) [c] (×2)	2.4745(18)	2.4848(14)	2.4793(19)
$M(2)$—Ge(3) [c,d] (×2)	——	2.5560(4)	——
$M(2)$—X(1) [a,c] (×2)	2.6240(6)	2.6145(7)	2.6313(8)
Ge(1)—Ge(1) (×2)	2.8076(19)	2.8314(14)	2.8179(17)
Ge(2)—Ge(2)	2.742(4)	2.769(3)	2.762(3)
X(1)—X(1) [a]	2.649(3)	2.788(5)	2.738(5)
X(2)—X(2) [b]	2.872(4)	2.840(11) ·	2.844(5)

[a] Site X(1) contains 60(2)% Ge, 40(2)% Sb in $Ti_{0.5}Fe_6Ge_5Sb$; 30(2)% Ge, 36(2)% Sb (and 34% vacancies) in $Cr_{0.8}Fe_{5.3}Ge_{5.2}Sb_{0.8}$; 53(2)% Ge, 47(2)% Sb in $Mn_{1.8}Fe_{4.6}Ge_{4.9}Sb_{1.1}$.

[b] Site X(2) contains 36(2)% Ge, 64(2)% Sb in $Ti_{0.5}Fe_6Ge_5Sb$; 32(3)% Ge, 54(2)% Sb (and 14% vacancies) in $Cr_{0.8}Fe_{5.3}Ge_{5.2}Sb_{0.8}$; 21(2)% Ge, 79(2)% Sb in $Mn_{1.8}Fe_{4.6}Ge_{4.9}Sb_{1.1}$.

[c] Sites $M(1)$ and $M(2)$ contain 100% Fe in $Ti_{0.5}Fe_6Ge_5Sb$; 11% Cr, 89% Fe in $Cr_{0.8}Fe_{5.3}Ge_{5.2}Sb_{0.8}$; and 23% Mn, 77% Fe in $Mn_{1.8}Fe_{4.6}Ge_{4.9}Sb_{1.1}$. These ratios were fixed at values determined by EDX analysis.

Table 6-3. Selected interatomic distances (Å) in $Ti_{0.5}Fe_6Ge_5Sb$, $Cr_{0.8}Fe_{5.3}Ge_{5.2}Sb_{0.8}$, and
  · $Mn_{1.8}Fe_{4.6}Ge_{4.9}Sb_{1.1}$ (continued).

[d] Sites Ge(3) and Ge(4) are only occupied in $Cr_{0.8}Fe_{5.3}Ge_{5.2}Sb_{0.8}$.

Table 6-4. Site occupations (in 3636 M and 6^3 Ge nets) [a] and bond distances (Å) in $Ti_{0.5}Fe_6Ge_5Sb$, $Cr_{0.8}Fe_{5.3}Ge_{5.2}Sb_{0.8}$, and $Mn_{1.8}Fe_{4.6}Ge_{4.9}Sb_{1.1}$.

		$Ti_{0.5}Fe_6Ge_5Sb$	$Cr_{0.8}Fe_{5.3}Ge_{5.2}Sb_{0.8}$	$Mn_{1.8}Fe_{4.6}Ge_{4.9}Sb_{1.1}$
Sites along $0, 0, z$				
In Ge(2) net ($z = 0$):	$X(2)$	36(2)% Ge, 64(2)% Sb	32(3)% Ge, 54(2)% Sb (and 14% vacancies)	21(2)% Ge, 79(2)% Sb
In M net ($z = \frac{1}{4}, \frac{3}{4}$):	Ge(4) [b]	—	15(2)% Ge	—
In Ge(1) net ($z = \frac{1}{2}$):	$R(2)$	3(2)% Ti	16(2)% Cr	15(3)% Mn
Sites along $\frac{1}{3}, \frac{2}{3}, z$				
In Ge(2) net ($z = 0$):	$R(1)$	72(2)% Ti	14(1)% Cr	52(2)% Mn
In M net ($z = \frac{1}{4}, \frac{3}{4}$):	Ge(3) [b]	—	33.8(6)% Ge	—
In Ge(1) net ($z = \frac{1}{2}$):	$X(1)$	60(2)% Ge, 40(2)% Sb	30(2)% Ge, 36(2)%Sb (and 34% vacancies)	53(2)% Ge, 47(2)% Sb
$d(M–M)$		2.5304(9)–2.6047(18)	2.5462(9)–2.5753(17)	2.5567(10)–2.608(2)
$d(Ge–Ge)$		2.742(4)–3.230(5)	2.769(3)–3.188(3)	2.762(3)–3.274(4)
$d(X–X)$		2.649(3)–2.872(4)	2.788(5)–2.840(11)	2.738(5)–2.844(5)

[a] M nets contain 100% Fe in $Ti_{0.5}Fe_6Ge_5Sb$; 11% Cr, 89% Fe in $Cr_{0.8}Fe_{5.3}Ge_{5.2}Sb_{0.8}$; and 23% Mn, 77% Fe in $Mn_{1.8}Fe_{4.6}Ge_{4.9}Sb_{1.1}$.

[b] Sites Ge(3) and Ge(4) are only occupied in $Cr_{0.8}Fe_{5.3}Ge_{5.2}Sb_{0.8}$.
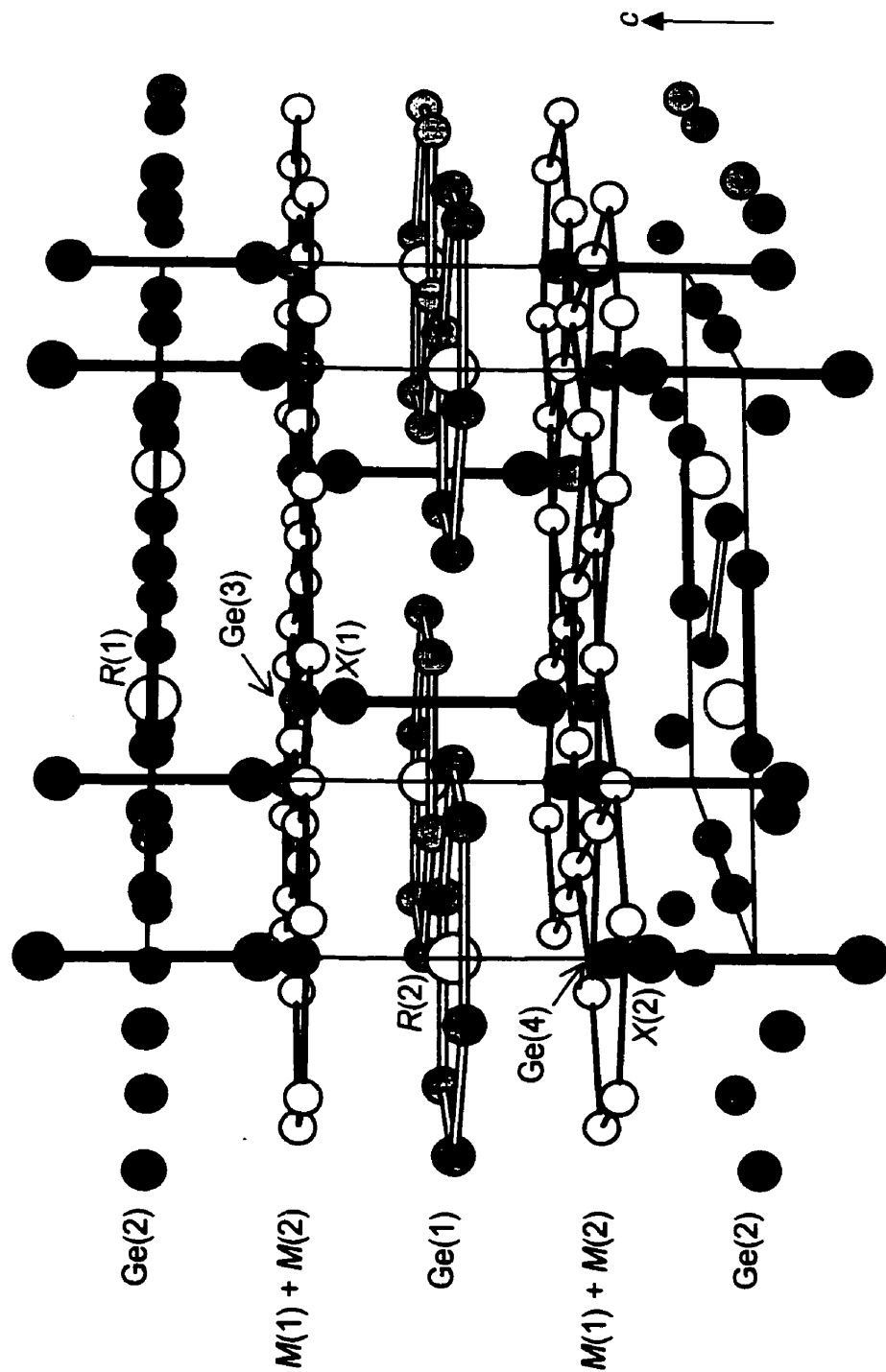
Figure 6-1. View of $R_{1-x}(R,Fe)_6Ge_4(Ge,Sb)_2$ perpendicular to the c direction showing the unit cell outline and labelling scheme. The large open circles are R atoms, the small open circles are M sites (occupied by Fe and R atoms), the medium lightly shaded circles are Ge atoms, and the large solid circles are X sites (occupied by Ge and Sb atoms). Sites Ge(3) and Ge(4) are only occupied for R = Cr.

(a) Stacking of Ge and M nets

Ge

M

Ge

M

a

α

a'

α

Ge atoms

R atoms + X_2 pairs

(b) 6³ Ge(2) net [a] (z = 0)

X(2)

R(1)

(c) 3636 (kagomé) M net [α] (z ≈ ¼, ¾)

Ge(3)

Ge(4)

(d) 6³ Ge(1) net [a'] (z = ½)

R(2)

X(1)
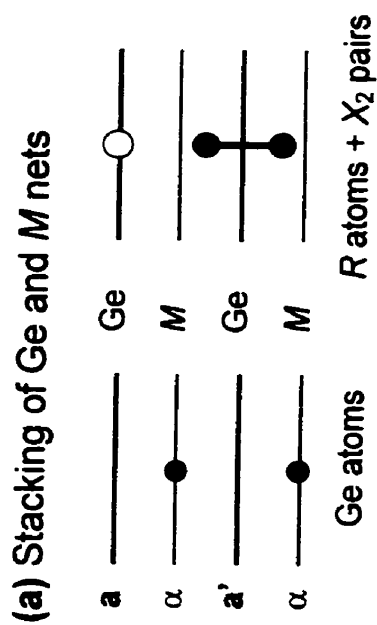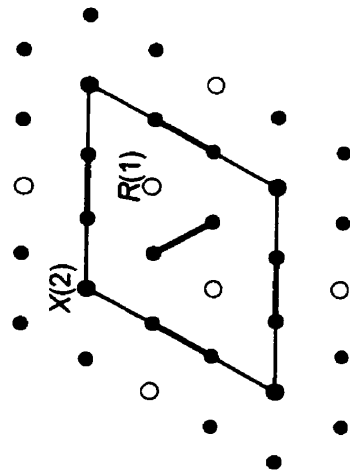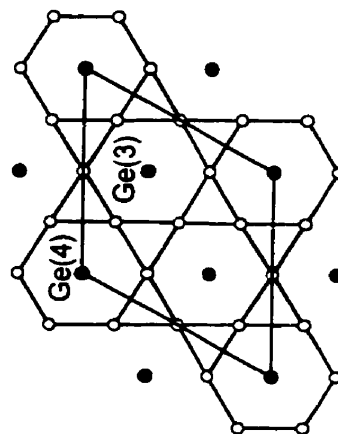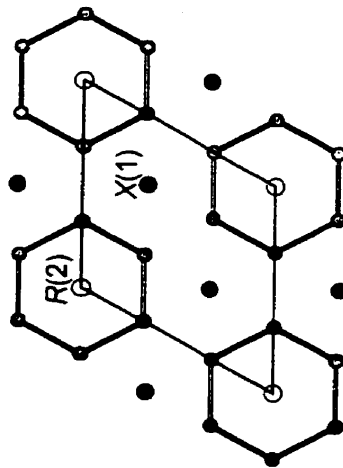
Figure 6-2. (a) Stacking of 3636 (kagomé) M nets and 6^3 Ge nets in an $a\alpha a'\alpha$ fashion leads to open channels along $0, 0, z$ and $\frac{1}{3}, \frac{2}{3}, z$ that can be filled by Ge atoms in the M net, R atoms in the Ge net, or X_2 pairs skewering the Ge net. The location of these sites within the nets (viewed down the c direction) is shown in (b), (c), and (d). The sites are occupied as listed in Table 6-4 to result in the structures of $Ti_{0.5}Fe_6Ge_5Sb$, $Cr_{0.8}Fe_{5.3}Ge_{5.2}Sb_{0.8}$, and $Mn_{1.8}Fe_{4.6}Ge_{4.9}Sb_{1.1}$.

(a) $FeGe_{0.8}Sb_{0.2}$

22% Sb   59% Sb

Ge

Fe

Ge

Fe

49% Ge   29% Ge

$+ R \rightarrow$

(b) $Ti_{0.5}Fe_6Ge_5Sb$

36% Ge, 64% Sb   72% Ti

$+ Sb$
$- Ge, R$

3% Ti   60% Ge, 40% Sb

(c) $TiFe_6Ge_6$

100% Ge

100% Ti
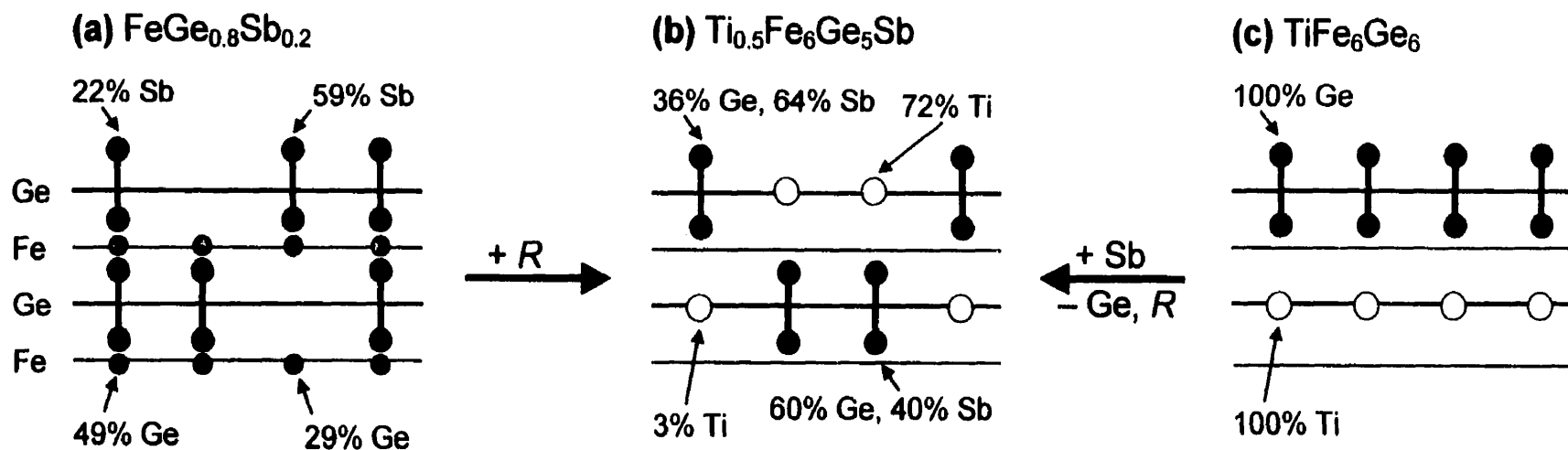
Figure 6-3. Comparison of the channel-filling R atom/X_2 pair orderings in the structures of (a) $FeGe_{0.8}Sb_{0.2}$, (b) $Ti_{0.5}Fe_6Ge_5Sb$, and (c) $TiFe_6Ge_6$, as projected onto the (010) plane of the larger $Ti_{0.5}Fe_6Ge_5Sb$ cell. In $FeGe_{0.8}Sb_{0.2}$, isolated Ge atoms and Sb_2 dumbbells fill the framework channels in a disordered manner. The insertion of R atoms into $FeGe_{0.8}Sb_{0.2}$ effects the pairing of isolated Ge atoms, resulting in the $Ti_{0.5}Fe_6Ge_5Sb$ structure. Alternatively, $TiFe_6Ge_6$ can be transformed into $Ti_{0.5}Fe_6Ge_5Sb$ by partial substitution of Sb atoms for Ge in the dumbbell sites, followed by removal of some R atoms.
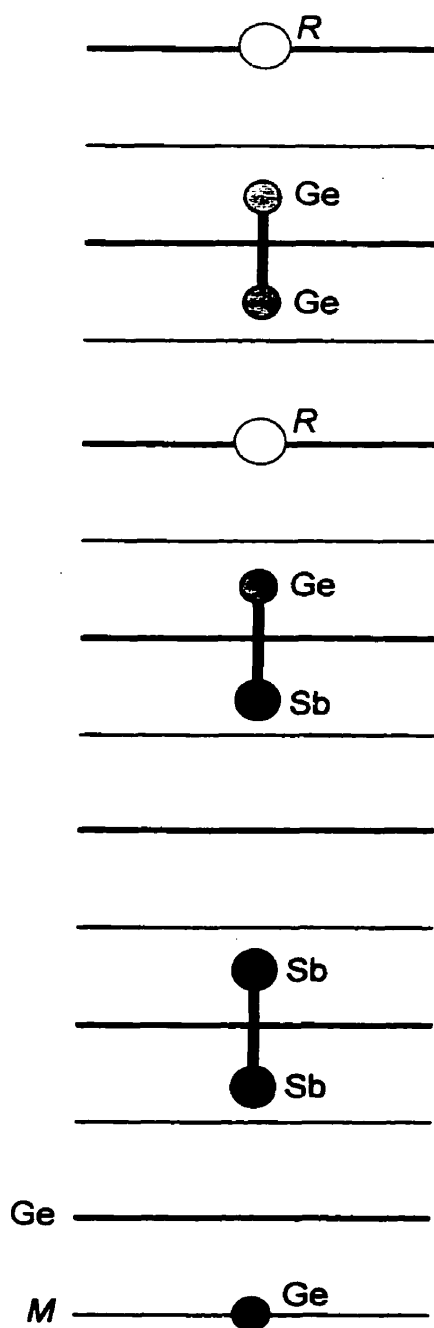
Figure 6-4. Possible local ordering model for the channel-filling R, Ge, and Sb atoms of $R_{1-x}(R,Fe)_6Ge_4(Ge,Sb)_2$. The R sites next to Sb dumbbell atoms and isolated Ge atoms are empty, while the sites next to Ge dumbbell atoms are always filled.

References

(1)   Mills, A. M., Mar, A. *J. Alloys Compd.* **2000**, *298*, 82.

(2)   Richardson, M. *Acta Chem. Scand.* **1967**, *21*, 2305.

(3)   (a) Simak, S. I.; Häußermann, U.; Abrikosov, I. A.; Eriksson, O.; Wills, J. M.; Lidin, S.; Johansson, B. *Phys. Rev. Lett.* **1997**, *79*, 1333. (b) Larsson, A. K.; Haeberlein, M.; Lidin, S.; Schwartz, U. *J. Alloys Compd.* **1996**, *240*, 79.

(4)   (a) Welk, E.; Schuster, H.-U. *Z. Anorg. Allg. Chem.* **1976**, *424*, 193. (b) Buchholz, W.; Schuster, H.-U. *Z. Naturforsch. B: Anorg. Chem. Org. Chem.* **1978**, *33*, 877. (c) Venturini, G.; Welter, R.; Malaman, B. *J. Alloys Compd.* **1992**, *185*, 99. (d) Mruz, O. Ya.; Starodub, P. K.; Bodak, O. I. *Dopov. Akad. Nauk Ukr. RSR Ser. B: Geol. Khim. Biol. Nauki*; **1984**, 44. (e) Gonçalves, A. P.; Waerenborgh, J. C.; Bonfait, G.; Amaro, A.; Godinho, M. M.; Almeida, M.; Spirlet, J. C. *J. Alloys Compd.* **1994**, *204*, 59. (f) Olenych, R. R.; Aksel'rud, L. G.; Yarmolyuk, Ya. P. *Dopov. Akad. Nauk Ukr. RSR Ser. A: Fiz.-Mat. Tekh. Nauki*; **1981**, *43*, 84. (g) Malaman, B.; Roques, B.; Courtois, A.; Protas, J. *Acta Crystallogr. Sect. B: Struct. Crystallogr. Cryst. Chem.* **1976**, *32*, 1352.

(5)   For example, see the following. (a) Zaharko, O.; Schobinger-Papamantellos, P.; Rodríguez-Carvajal, J.; Buschow, K. H. J. *J. Alloys Compd.* **1999**, *288*, 50. (b) Zaharko, O.; Schobinger-Papamantellos, P.; Ritter, C.; Rodríguez-Carvajal, J.; Buschow, K. H. J. *J. Magn. Magn. Mater.* **1998**, *187*, 293. (c) Schobinger-Papamantellos, P.; Oleksyn, O.; Rodríguez-Carvajal, J.; André, G.; Brück, E.; Buschow, K. H. J. *J. Magn. Magn. Mater.* **1998**, *182*, 96. (d) Schobinger-Papamantellos, P.; Buschow, K. H. J.; de Boer, F. R.; Ritter, C.; Isnard, O.; Fauth, F. *J. Alloys Compd.* **1998**, *267*, 59. (e) Oleksyn, O.; Schobinger-Papamantellos, P.; Rodríguez-Carvajal, J.; Brück, E.; Buschow, K. H. J. *J. Alloys Compd.* **1997**, *257*, 36.

(6)   Nesbitt, E. A.; Wernick, J. H. *Rare Earth Permanent Magnets*; Academic Press: New York, 1973.

(7)   For example, see the following. (a) Hori, T.; Tuchiya, Y.; Funahashi, S.; Akimitsu, M.; Shimojo, Y.; Shiraishi, H.; Nakagawa, Y. *J. Magn. Magn. Mater.* **1998**, *177–181*, 1425. (b) Ryan, D. H.; Cadogan, J. M. *J. Appl. Phys.* **1996**, *79*, 6004. (c) Wang, Y. B.; Wiarda, D.; Ryan, D. H.; Cadogan, J. M. *IEEE Trans. Magn.* **1994**, *30*, 4951. (d) Hori, T.; Shiraishi, H.; Kato, H.; Kido, G.; Nakagawa, Y. *J. Magn. Magn. Mater.* **1992**, *104–107*, 2043.

(8)   Sheldrick, G. M. *SHELXTL Version 5.1*; Bruker Analytical X-ray Systems: Madison, WI, 1997.

(9) *International Tables for X-ray Crystallography*; Wilson, A. J. C., Ed. Kluwer: Dordrecht, The Netherlands, 1992; Vol. C.

(10) Gelato, L. M.; Parthé, E. *J. Appl. Crystallogr.* **1987**, *20*, 139.

(11) Spinat, P.; Fruchart, R.; Herpin, P. *Bull. Soc. Fr. Minéral. Cristallogr.* **1970**, *93*, 23.

(12) Kolenda, M.; Leciejewicz, J.; Szytula, A. *Phys. Status Solidi B*; **1973**, *57*, K107.

(13) Ohba, T.; Watanabe, N.; Komura, Y. *Acta Crystallogr. Sect. B: Struct. Sci.* **1984**, *40*, 351.

(14) Kjekshus, A.; Walseth, K. P. *Acta Chem. Scand.* **1969**, *23*, 2621.

(15) *Chemistry, Structure, and Bonding of Zintl Phases and Ions*; Kauzlarich, S. M., Ed. VCH Publishers: New York, 1996.

(16) Mazet, T.; Isnard, O.; Malaman, B. *Solid State Commun.* **2000**, *114*, 91.

(17) Villars, P. *Pearson's Handbook, Desk Edition: Crystallographic Data for Intermetallic Phases*; ASM International: Materials Park, OH, 1997.

(18) Mills, A.; Anderson, E. J.; Mar, A. Unpublished results.

Chapter 7

Conclusion

Structure, Bonding, and Properties of New Intermetallic Antimonides

Several new intermetallic antimonides, involving either a rare-earth or a transition metal, a main-group element (A = Ga, Ge), and Sb, have been synthesized during this research. These compounds expand our knowledge of the chemistry of the heavier main-group elements. Prior to this research, the metal–A–Sb systems included mainly ternary compounds of the electropositive alkali and alkaline-earth metals and disordered variants of binary transition metal antimonides.[1] $La_{13}Ga_8Sb_{21}$, $RE_{12}Ga_4Sb_{23}$ (RE = La–Nd, Sm),[2] and REGaSb$_2$ (RE = La–Nd, Sm)[3] represent the first examples of rare-earth gallium antimonides. $FeGe_{1-x}Sb_x$ ($0 \leq x \leq 0.33$)[4] and $R_{1-x}(R,Fe)_6Ge_4(Ge,Sb)_2$ (R = Ti, Cr, Mn)[5] add to the small family of well-defined transition metal germanium antimonides that was previously limited to ZrGeSb[6] and Co_3Ge_2Sb.[7]

Homoatomic Bonding Patterns. The structures of the new antimonides confirm our initial prediction that, with reduced electronegativity differences between the metal and metalloid components, more unusual modes of bonding would be encountered. All are relatively complex, featuring extensive Sb–Sb and A–A homoatomic bonding networks that test the limits of current bonding theories. The predominance of homoatomic bonding in the metalloid substructures of these compounds is remarkable,

given that most alkali and alkaline-earth metal main-group element antimonides are characterized by mainly heteroatomic A–Sb interactions.[8]

These new antimonides reveal that Sb shows unusual versatility in its homoatomic bonding, from strong single bonds in classical Sb_2 pairs to weak half-bonds in non-classical square nets and ribbons. In the rare-earth gallium antimonides, we find two-dimensional square nets in REGaSb$_2$ (Figure 7-1a) and one-dimensional Sb ribbons in La$_{13}$Ga$_8$Sb$_{21}$ and RE_{12}Ga$_4$Sb$_{23}$ (Figures 7-1b and c) containing relatively long Sb–Sb bonds ($\sim$ 3.0–3.2 Å).[2,3] While square sheets of Sb atoms are encountered in numerous binary and ternary antimonides, including the rare-earth main-group element antimonides REIn$_{0.8}$Sb$_2$ (RE = La–Nd)[9] and RESn$_{0.78}$Sb$_2$ (RE = La–Nd, Sm),[10] the occurrence of Sb ribbons suggests a rich structural chemistry that is yet to be elucidated. Ribbons of varying widths, excised from a two-dimensional sheet, can be assembled into elaborate frameworks. The three- and four-atom-wide Sb ribbons first observed in α- and β-ZrSb$_2$[11] are used as walls in the pseudo-hexagonal channels of the recently identified compounds RE_6MSb$_{15}$ (RE = La, Ce; M = Mn, Cu, Zn)[12] and RE_6Ge$_{5-x}$Sb$_{11+x}$ (RE = La–Nd, Sm, Gd–Dy).[13] Here, in La$_{13}$Ga$_8$Sb$_{21}$ and RE_{12}Ga$_4$Sb$_{23}$, hexagonal or pseudo-hexagonal channels, respectively, are constructed from five- and six-atom-wide Sb ribbons. One can envision that even wider ribbons are possible. The few known examples of ribbon-containing antimonides are potentially members of a larger family of compounds containing complex non-classical Sb substructures.

Discrete Sb_2 pairs (Figure 7-2a) containing classical covalent bonds in the range $\sim$ 2.8–2.9 Å occur in the ternary and quaternary iron germanium antimonides FeGe$_{1-x}$Sb$_x$[4] and $R_{1-x}(R,$Fe$)_6$Ge$_4$(Ge,Sb)$_2$.[5] Similar Sb_2 dumbbells are found in many binary and

ternary transition metal antimonides, including $FeSb_2$.[14] In the Sb substructure of $FeSb_2$, the Sb_2 pairs (Sb–Sb 2.887(1) Å) are stacked in a ladder arrangement at an interpair distance of 3.197(1) Å that indicates a weaker bonding interaction. Self-isolated pairs, such as those found in $FeGe_{1-x}Sb_x$ and $R(R,Fe)_6Ge_4(Ge,Sb)_2$, are more typically found in Zintl compounds, for example $K_2Ba_3Sb_4$.[15]

The new intermetallic antimonides also feature homoatomic A–A bonding networks. Classical Ga substructures characterized by strong Ga–Ga bonding (~ 2.4–2.6 Å) are encountered in the rare-earth gallium antimonides: finite Ga_2 pairs and puckered Ga_6 rings link Sb ribbons in $RE_{12}Ga_4Sb_3$ and $La_{13}Ga_8Sb_{21}$, respectively,[2] and one-dimensional zigzag Ga chains occur in the $_\infty^2[GaSb]$ layers of $REGaSb_2$ (Figure 7-3).[3] Isolated Ga_2 pairs and zigzag Ga chains are observed in the substructures of the Zintl compound $Na_2Ga_3Sb_3$[16] and the binary gallide Li_2Ga,[17] respectively, but the isolated Ga_6 rings are more unusual. Although two-dimensional layers of interconnected puckered rings are found in Li_2Ga_3,[17] the Ga substructure of $La_{13}Ga_8Sb_{21}$ contains the first example of a discrete Ga_6 ring.

In $FeGe_{1-x}Sb_x$ and $R_{1-x}(R,Fe)_6Ge_4(Ge,Sb)_2$, the Ge substructures consist of two-dimensional non-classical honeycomb (6^3) nets (Figure 7-2b).[4,5] The Ge–Ge bonding interactions within these sheets (~ 2.7–3.3 Å) are considerably longer than full single bonds (~ 2.4–2.5 Å), suggesting a range of fractional bond orders. Because of its ability to accommodate different strengths of Ge–Ge interactions, the honeycomb net is a recurring structural feature in many binary germanides: for example, in the AlB_2-type rare-earth germanides $REGe_{2-x}$ (RE = Y, Nd, Sm, Gd–Lu), 6^3 Ge nets (segmented by

vacancies) contain strong classical bonds,[18] while in the CoSn-type germanide FeGe, weaker non-classical interactions occur within the nets.[19]

Electron Counting. Although the Zintl concept works well in describing the bonding of the alkali and alkaline-earth main-group element antimonides,[8] the assumption of complete electron transfer from the metal component to the metalloid substructure breaks down as the electronegativity difference between components is reduced. The rationalization of the bonding in the new rare-earth gallium antimonides and transition metal germanium antimonides studied is further complicated by the presence of non-classical networks in the metalloid substructures. While well-established electron counting rules exist for classical and non-classical Sb networks,[20] the distribution of electrons over the homoatomic $A-A$ substructures, for which such rules have not yet been developed, is more challenging.

For the rare-earth gallium antimonides, in which the electronegativity difference between the rare-earth metal and metalloid components is relatively pronounced, the Zintl electron transfer concept serves as a good starting point. Electronic structure calculations confirm that the Zintl description of bonding in the classical $^2_\infty[GaSb]$ layer and the non-classical square Sb net of $RE GaSb_2$ is a good first approximation.[3] For the more complex $La_{13}Ga_8Sb_{21}$ and $RE_{12}Ga_4Sb_{23}$ structures, application of the Zintl concept is not as straightforward.[21] In both cases, the assignment of oxidation states in the metalloid substructure, following a "retrotheoretical" band structure analysis, leads to an overall charge that is inconsistent with that calculated based on a complete transfer of electrons from the RE atoms. This failure can be resolved by allowing for the possibility that the electron count of the non-classical Sb networks may deviate from the ideal.

Because the states near the Fermi levels of the Sb network band structures are mainly non-bonding in character, the square nets and ribbons of Sb atoms are able to tolerate some degree of oxidation or reduction without significant distortion.

Since the electronegativities of Fe, Ge, and Sb are very similar, the Zintl approach is inappropriate for $FeGe_{1-x}Sb_x$. Although the electron count per Sb_2 pair can be assigned by analogy with dumbbell-containing Zintl phases, the presence of Fe–Fe and intermediate Ge–Ge interactions makes the distribution of the remaining valence electrons in the overall structure extremely difficult. However, the Zintl electron transfer concept is useful in describing the relationship between the $FeGe_{1-x}Sb_x$ series of compounds and their filled derivatives $R_{1-x}(R,Fe)_6Ge_4(Ge,Sb)_2$.[5] Upon insertion, the electropositive early transition metals R donate valence electrons to the $FeGe_{1-x}Sb_x$ host, causing the pairing of channel-filling Ge atoms. The result of this Zintl-type electron transfer is equivalent to the Sb_2 dumbbell formation that occurs as the valence electron concentration of $FeGe_{1-x}Sb_x$ is increased through the substitution of Sb for Ge.[4]

Physical Properties and Future Directions. The classical alkali and alkaline-earth metal Zintl compounds, with structures that can be rationalized in terms of metal cations and covalently-bonded metalloid subnetworks, should, by definition, exhibit diamagnetic and semiconducting behaviour.[8] In the rare-earth gallium antimonides and the iron germanium antimonides, the presence of metal centres with unpaired f or d electrons and metalloid substructures containing weak multicentre bonding lead to the possibility of magnetic ordering and metallic conductivity. Furthermore, the low-dimensional nature of the new antimonide structures should engender anisotropic physical properties.

Electronic structure calculations suggest metallic behaviour for $RE\mathrm{GaSb_2}$, $RE_{12}\mathrm{Ga_4Sb_{23}}$, and $\mathrm{La_{13}Ga_8Sb_{21}}$. Even without including the rare-earth metals (for which the extended Hückel parameters are less reliable) in the calculations, bands originating from the metalloid substructure cross the Fermi level.[3,21] The bonding interactions within the non-classical Sb networks are sufficiently weak that no gap exists between the valence and conduction band. While the resistivities of $RE\mathrm{GaSb_2}$ have not yet been measured, resistivity measurements for the complete $RE_{12}\mathrm{Ga_4Sb_{23}}$ series confirm that all are metallic.[21] $\mathrm{La_{13}Ga_8Sb_{21}}$ exhibits metallic behaviour at high temperatures, but is superconducting at low temperatures, as corroborated by the observation of the Meissner effect in magnetic studies.[21] The co-existence of discrete classical structural units and an extended non-classical Sb network in the structure of $\mathrm{La_{13}Ga_8Sb_{21}}$ may play a role in the appearance of superconductivity.

The magnetic properties of $RE\mathrm{GaSb_2}$ and $RE_{12}\mathrm{Ga_4Sb_{23}}$ should also be investigated. In both structures, extended Sb networks segregate low-dimensional assemblies of rare-earth atoms, either two-dimensional layers, in $RE\mathrm{GaSb_2}$, or one-dimensional columnar stackings, in $RE_{12}\mathrm{Ga_4Sb_{23}}$. The intralayer or intracolumn $RE{-}RE$ distances are significantly shorter than the interlayer or intercolumn distances, suggesting that these compounds may potentially display low-dimensional magnetism. The results of resistivity measurements for the $RE_{12}\mathrm{Ga_4Sb_{23}}$ series already hint at possible low-temperature magnetic ordering.[21]

Since the crystal structures of $\mathrm{FeGe_{1-x}Sb_x}$ and $R_{1-x}(R,\mathrm{Fe})_6\mathrm{Ge_4(Ge,Sb)_2}$ are closely related to those of the permanent magnet materials $\mathrm{Sm_2Fe_{17}N_x}$ and $\mathrm{SmCo_5}$,[22] these compounds are expected to possess interesting magnetic properties. Non-magnetic Ge

nets separate two-dimensional Fe layers in $FeGe_{1-x}Sb_x$. In the parent compound FeGe, this arrangement leads to ferromagnetic coupling within the Fe nets and antiferromagnetic interactions between adjacent nets.[23] The substitution of Sb for Ge provides a means of controlling the inter and intranet Fe–Fe distances and coupling interactions. The insertion of transition metal atoms, particularly Cr and Mn, into $FeGe_{1-x}Sb_x$ may give rise to more complex magnetic behaviour in $R_{1-x}(R,Fe)_6Ge_4(Ge,Sb)_2$. However, before these magnetic studies can be carried out, phase pure material must be synthesized. Since there are numerous impurity phases in these systems, this task will be a major hurdle to overcome.

Further studies of the physical properties of the new intermetallic compounds are essential to complete our understanding of these materials. The crystal structure determinations and electronic structure calculations presented here provide a basis for the development of structure-property relationships. We have discovered some recurring homoatomic bonding patterns: pairs, rings, and chains containing strong covalent bonding; ribbons and nets containing weaker delocalized bonding that is tunable to some extent. We have also tested the limits of the established bonding theories for intermetallic compounds. By correlating these results with transport and magnetic phenomena, we may gain insight into the design of materials with specific properties. Of course, in order to reach this goal, a more extensive library of compounds and properties will have to be established.

(a) $^2_\infty[\text{Sb}]$

(b) $^1_\infty[\text{Sb}_6]$

(c) $^1_\infty[\text{Sb}_5]$
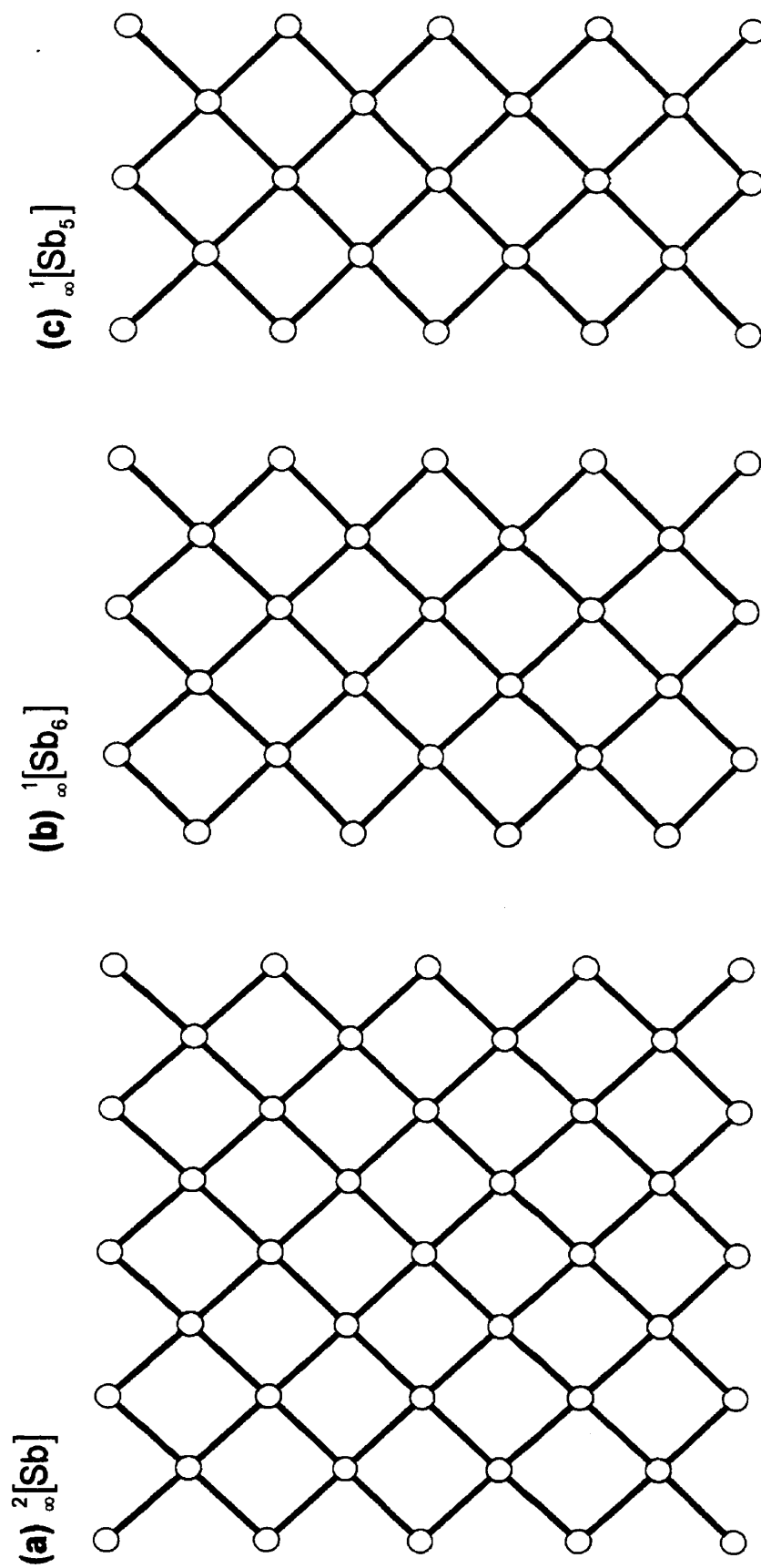
Figure 7-1. Non-classical Sb networks found in rare-earth gallium antimonides: (a) two-dimensional $^2_\infty[\text{Sb}]$ net in $RE\text{GaSb}_2$, (b) one-dimensional six-atom-wide $^1_\infty[\text{Sb}_6]$ ribbon in $RE_{12}\text{Ga}_4\text{Sb}_{23}$, and (c) one-dimensional five-atom-wide $^1_\infty[\text{Sb}_5]$ ribbon in $\text{La}_{13}\text{Ga}_8\text{Sb}_{21}$ and $RE_{12}\text{Ga}_4\text{Sb}_{23}$.
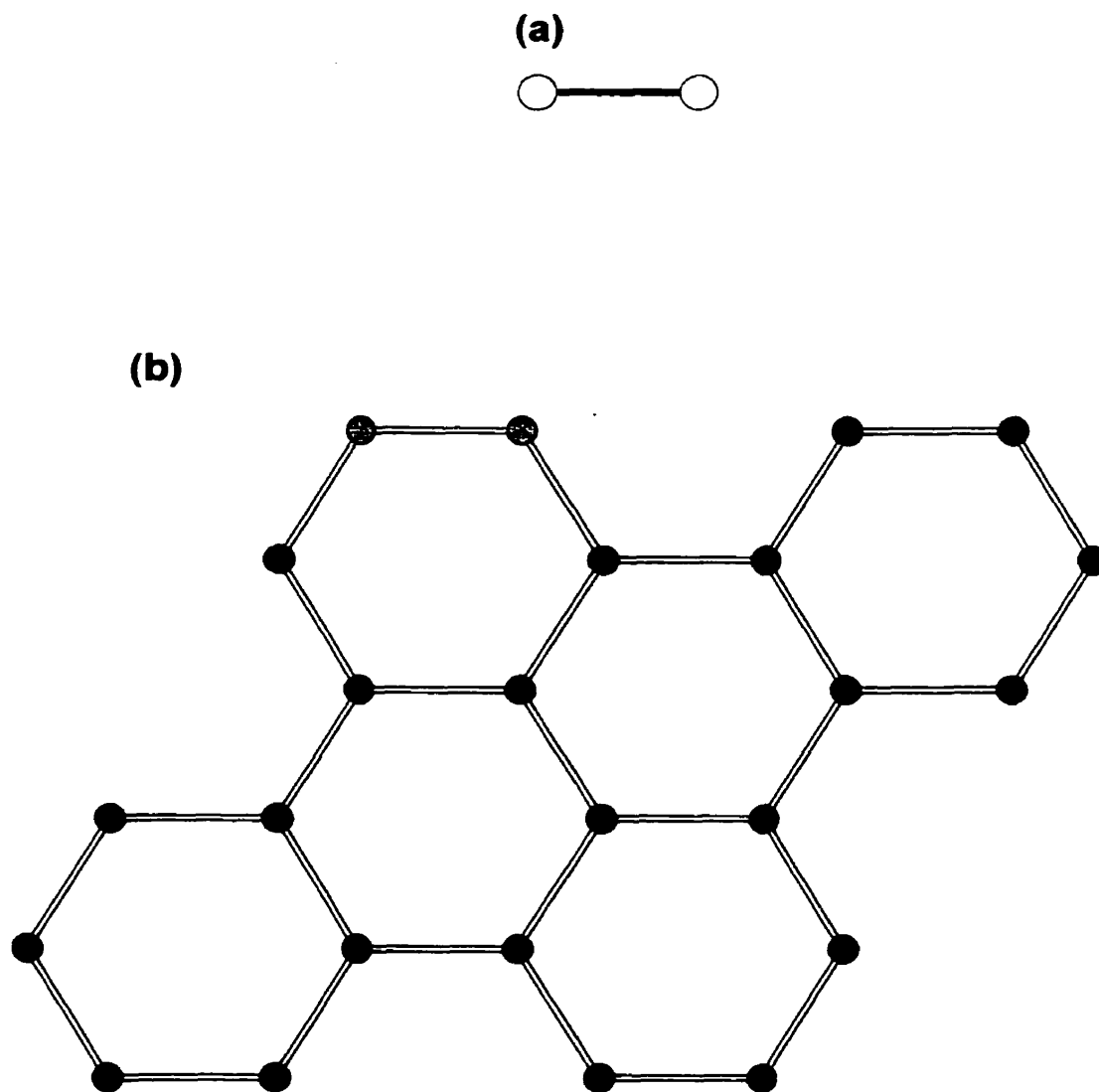
Figure 7-2. Homoatomic bonding networks found in $FeGe_{1-x}Sb_x$ and $R_{1-x}(R,Fe)_6Ge_4(Ge,Sb)_2$: (a) discrete Sb_2 dumbbell and (b) two-dimensional $^2_\infty[Ge]$ net.
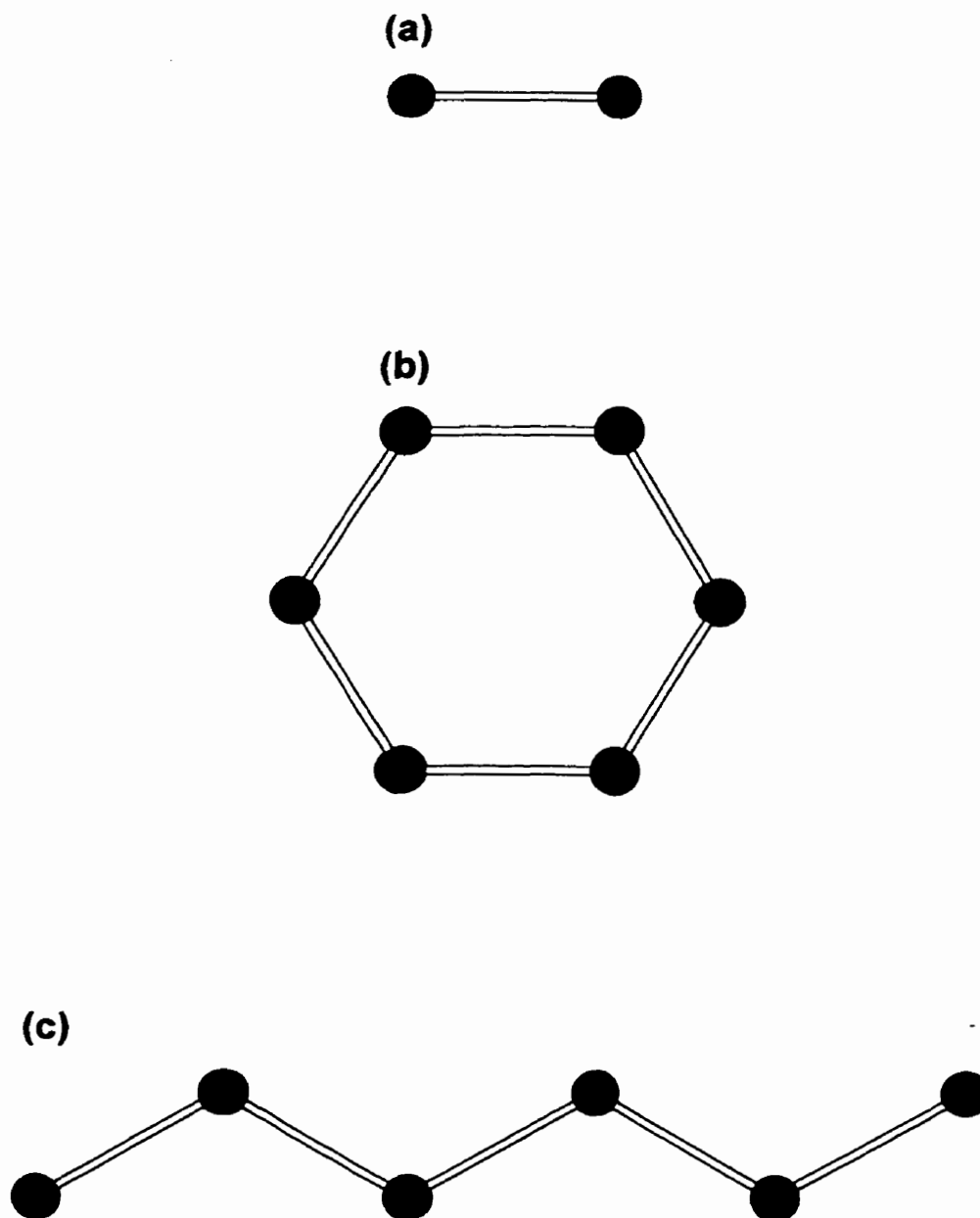
Figure 7-3. Classical Ga networks found in rare-earth gallium antimonides: (a) discrete Ga_2 pair in $RE_{12}Ga_4Sb_{23}$, (b) discrete Ga_6 ring in $La_{13}Ga_8Sb_{21}$, and (c) one-dimensional zigzag $^1_\infty[Ga]$ chain in $REGaSb_2$.

References

(1)   Villars, P. *Pearson's Handbook, Desk Edition: Crystallographic Data for Intermetallic Phases*; ASM International: Materials Park, OH, 1997.

(2)   Mills, A. M.; Mar, A. *Inorg. Chem.* **2000**, *39*, 4599.

(3)   Mills, A. M; Mar, A. *J. Am. Chem. Soc.* **2001**, *123*, 1151.

(4)   Mills, A. M.; Mar, A. *J. Alloys Compd.* **2000**, *298*, 82.

(5)   Mills, A. M.; Anderson, E. J.; Mar, A. *J. Alloys Compd.* In press.

(6)   Lam, R.; Mar, A. *J. Solid State Chem.* **1997**, *134*, 388.

(7)   Mills, A. M.; Lam, R.; Mar, A. *Can. J. Chem.* **1998**, *76*, 1588.

(8)   *Chemistry, Structure, and Bonding of Zintl Phases and Ions*; Kauzlarich, S. M., Ed. VCH Publishers: New York, 1996.

(9)   Ferguson, M. J.; Ellenwood, R. E.; Mar, A. *Inorg. Chem.* **1999**, *38*, 4503.

(10)   Ferguson, M. J.; Hushagen, R. W.; Mar, A. *Inorg. Chem.* **1996**, *35*, 4505.

(11)   Garcia, E.; Corbett, J. D. *J. Solid State Chem.* **1988**, *73*, 452.

(12)   Sologub, O.; Vybornov, M.; Rogl, P.; Hiebl, K.; Cordier, G.; Woll, P. *J. Solid State Chem.* **1996**, *122*, 266.

(13)   Lam, R.; McDonald, R.; Mar, A. *Inorg. Chem.* **2001**, *40*, 952.

(14)   Holseth, H.; Kjekshus, A. *Acta Chem. Scand.* **1969**, *23*, 3043.

(15)   Eisenmann, B.; Gieck, C.; Rößler, U. *Z. Anorg. Allg. Chem.* **1999**, *625*, 1331.

(16)   Cordier, G.; Ochmann, H.; Schäfer, H. *Mater. Res. Bull.* **1986**, *21*, 331.

(17)   Müller, W.; Stöhr, J. *Z. Naturforsch. B: Anorg. Chem. Org. Chem.* **1977**, *32*, 631.

(18)   Venturini, G.; Ijjaali, I.; Malaman, B. *J. Alloys Compd.* **1999**, *284*, 262.

(19)   Richardson, M. *Acta Chem. Scand.* **1967**, *21*, 2305.

(20)   Papoian, G. A.; Hoffmann, R. *Angew. Chem. Int. Ed.* **2000**, *39*, 2408.

(21)   Mills, A. M.; Deakin, L.; Mar, A. *Chem. Mater.* In press.

(22)   (a) Buschow, K. H. J.; van der Goot, A. S. *J. Less-Common Met.* **1968**, *14*, 323. (b) Nesbitt, E. A.; Wernick, J. H. *Rare Earth Permanent Magnets*; Academic Press: New York, 1973.

(23)   (a) Bernhard, J.; Lebech, B.; Beckman, O. *J. Phys. F: Met. Phys.* **1988**, *18*, 539. (b) Bernhard, J.; Lebech, B.; Beckman, O. *J. Phys. F: Met. Phys.* **1984**, *14*, 2379. (c) Forsyth, J. B.; Wilkinson, C.; Gardner, P. *J. Phys. F: Met.* Phys. **1978**, *8*, 2195.

Appendix

Table A-1. X-ray powder diffraction data for $La_{12}Ga_4Sb_{23}$.[a]

hkl	d_{obs} (Å)	d_{calc} (Å)	I/I_0 [b]	hkl	d_{obs} (Å)	d_{calc} (Å)	I/I_0 [b]
0 1 1	——	15.912	6	0 5 11	2.076	2.077	14
1 0 3	——	3.909	5	0 10 0	1.976	1.975	6
0 5 3	3.625	3.614	16	0 0 14	1.917	1.919	6
1 3 2	3.512	3.501	8	0 9 7	1.904	1.905	9
0 0 8	3.367	3.358	9	1 8 7	1.872	1.873	12
0 5 5	3.190	3.182	15	2 5 3	1.862	1.862	5
1 1 6	3.072	3.080	6	1 9 6	1.793	1.794	9
1 4 3	3.072	3.065	42	2 5 5	1.793	1.794	6
0 6 4	2.961	2.956	5	1 1 14	1.749	1.748	5
1 0 7	2.883	2.876	67	2 8 0	1.630	1.631	10
1 5 2	2.861	2.856	16	2 4 10	1.597	1.598	20
1 4 5	2.792	2.788	9	2 5 11	1.501	1.501	11
1 5 4	2.686	2.680	100	1 9 12	1.473	1.474	5
1 1 8	2.638	2.633	13	2 0 14	1.437	1.438	5
1 6 3	2.523	2.518	5	2 9 7	1.431	1.432	8
0 8 0	2.472	2.469	16	1 4 17	1.420	1.422	25
1 0 9	2.465	2.460	6	1 13 4	1.401	1.402	18
1 5 6	2.451	2.447	6	1 9 14	1.369	1.371	16
0 4 10	2.361	2.360	29	3 0 7	1.354	1.355	9
0 9 1	2.187	2.187	5	3 5 4	1.332	1.333	16
2 0 0	2.174	2.172	39	0 13 11	1.289	1.290	6

[a] The orthorhombic cell parameters refined from the powder pattern, obtained on a Guinier camera at room temperature, are: $a = 4.344(2)$, $b = 19.750(7)$, $c = 26.860(11)$ Å, and $V = 2305(1)$ Å^3.

[b] The intensities were calculated based on positional parameters from the crystal structure of $Pr_{12}Ga_4Sb_{23}$ with the use of the program LAZY-PULVERIX (Yvon, K.; Jeitschko, W.; Parthé, E. *J. Appl. Crystallogr.* **1977**, *10*, 73).

Table A-2. X-ray powder diffraction data for $Ce_{12}Ga_4Sb_{23}$.[a]

hkl	d_{obs} (Å)	d_{calc} (Å)	I/I_0 [b]	hkl	d_{obs} (Å)	d_{calc} (Å)	I/I_0 [b]
0 1 1	——	15.746	6	0 5 11	2.058	2.059	14
1 0 3	——	3.876	5	0 10 0	1.950	1.951	6
0 5 3	3.584	3.573	16	0 0 14	1.905	1.903	6
1 3 2	3.478	3.467	8	0 9 7	1.883	1.884	9
0 0 8	3.339	3.333	9	1 8 7	1.853	1.854	12
0 5 5	3.156	3.149	15	2 5 3	1.845	1.845	5
1 1 6	3.043	3.055	6	2 5 5	1.783	1.778	6
1 4 3	3.043	3.035	42	1 9 6	1.774	1.775	9
0 6 4	2.928	2.923	5	1 1 14	1.733	1.735	5
1 0 7	2.861	2.854	67	2 8 0	1.613	1.614	10
1 5 2	2.832	2.826	16	2 4 10	1.584	1.585	20
1 4 5	2.767	2.762	9	2 5 11	1.487	1.488	11
0 5 7	2.729	2.726	5	1 9 12	1.459	1.460	5
1 5 4	2.659	2.653	100	2 10 0	1.445	1.446	5
1 1 8	2.616	2.613	13	2 0 14	1.425	1.427	5
1 6 3	2.496	2.491	5	2 9 7	1.416	1.418	8
1 0 9	2.443	2.441	6	1 4 17	1.409	1.411	25
0 8 0	2.443	2.439	15	1 13 4	1.385	1.386	18
1 5 6	2.428	2.424	6	3 4 3	1.360	1.361	5
0 5 9	2.362	2.360	6	1 9 14	1.357	1.358	16
0 4 10	2.342	2.340	29	3 0 7	1.342	1.344	9
0 9 1	2.157	2.161	5	3 5 4	1.320	1.321	16
2 0 0	2.157	2.154	39	0 13 11	1.273	1.276	6

[a] The orthorhombic cell parameters refined from the powder pattern, obtained on a Guinier camera at room temperature, are: $a = 4.308(2)$, $b = 19.509(9)$, $c = 26.667(12)$ Å, and $V = 2241(1)$ Å^3.

[b] The intensities were calculated based on positional parameters from the crystal structure of $Pr_{12}Ga_4Sb_{23}$ with the use of the program LAZY-PULVERIX (Yvon, K.; Jeitschko, W.; Parthé, E. *J. Appl. Crystallogr.* **1977**, *10*, 73).

Table A-3. X-ray powder diffraction data for $Pr_{12}Ga_4Sb_{23}$.[a]

hkl	d_{obs} (Å)	d_{calc} (Å)	I/I_0 [b]	hkl	d_{obs} (Å)	d_{calc} (Å)	I/I_0 [b]
0 1 1	——	15.664	6	2 0 0	2.146	2.142	39
1 0 3	——	3.855	5	0 5 11	2.047	2.049	14
0 5 3	3.564	3.553	16	0 10 0	1.936	1.939	6
1 3 2	3.462	3.448	8	0 0 14	1.892	1.897	6
0 0 8	3.325	3.319	9	0 9 7	1.871	1.874	8
0 5 5	3.137	3.132	15	1 8 7	1.841	1.844	12
1 1 6	3.055	3.040	6	2 5 3	1.838	1.834	5
1 4 3	3.028	3.018	41	2 5 5	1.766	1.768	6
0 6 4	2.912	2.906	5	1 9 6	1.766	1.765	9
1 0 7	2.847	2.840	67	1 1 14	1.723	1.727	5
1 5 2	2.816	2.810	16	2 8 0	1.604	1.605	10
1 4 5	2.752	2.747	9	2 4 10	1.575	1.576	20
0 5 7	2.716	2.712	5	2 5 11	1.479	1.481	11
1 5 4	2.646	2.638	100	1 9 12	1.459	1.452	5
1 1 8	2.604	2.600	13	2 0 14	1.417	1.420	5
1 6 3	2.482	2.477	5	2 9 7	1.414	1.410	8
1 0 9	2.429	2.430	6	1 4 17	1.408	1.405	25
0 8 0	2.429	2.424	15	1 13 4	1.376	1.378	18
1 5 6	2.415	2.411	6	1 9 14	1.351	1.351	16
0 5 9	2.350	2.348	6	3 0 7	1.334	1.336	9
0 4 10	2.329	2.329	29	3 5 4	1.311	1.313	16
0 9 1	2.149	2.148	5	0 13 11	1.268	1.269	6

[a] The orthorhombic cell parameters refined from the powder pattern, obtained on a Guinier camera at room temperature, are: $a = 4.283(3)$, $b = 19.394(10)$, $c = 26.553(16)$ Å, and $V = 2206(1)$ Å^3.

[b] The intensities were calculated based on positional parameters from the crystal structure of $Pr_{12}Ga_4Sb_{23}$ with the use of the program LAZY-PULVERIX (Yvon, K.; Jeitschko, W.; Parthé, E. *J. Appl. Crystallogr.* **1977**, *10*, 73).

Table A-4. X-ray powder diffraction data for $Nd_{12}Ga_4Sb_{23}$.[a]

hkl	d_{obs} (Å)	d_{calc} (Å)	I/I_0 [b]	hkl	d_{obs} (Å)	d_{calc} (Å)	I/I_0 [b]
0 1 1	——	15.590	6	0 5 11	2.038	2.040	14
1 0 1	——	4.214	5	0 10 0	1.930	1.931	6
1 0 3	——	3.841	5	0 0 14	1.887	1.888	5
0 5 3	3.534	3.537	16	0 9 7	1.864	1.865	8
1 3 2	3.442	3.435	8	1 8 7	1.839	1.836	12
0 0 8	3.309	3.303	9	2 5 3	1.827	1.827	5
0 5 5	3.121	3.118	15	2 5 5	——	1.761	6
1 4 3	3.011	3.006	40	1 9 6	1.756	1.758	9
0 6 4	2.896	2.893	5	1 1 14	1.717	1.719	5
1 0 7	2.834	2.828	67	2 8 0	1.598	1.599	10
1 5 2	2.803	2.799	16	2 4 10	1.569	1.570	20
1 4 5	2.739	2.736	9	2 5 11	1.474	1.474	11
0 5 7	2.703	2.699	5	1 9 12	1.445	1.446	5
1 5 4	2.633	2.627	100	2 10 0	1.431	1.432	5
1 1 8	2.592	2.589	13	2 0 14	1.413	1.414	5
1 6 3	2.470	2.467	5	2 9 7	1.403	1.404	8
1 0 9	2.421	2.419	6	1 4 17	1.398	1.398	25
0 8 0	2.416	2.414	15	1 13 4	1.371	1.372	18
1 5 6	2.404	2.401	6	3 4 3	1.348	1.349	5
0 5 9	2.339	2.337	5	1 9 14	1.343	1.345	15
0 4 10	2.319	2.318	29	3 0 7	1.330	1.331	19
0 9 1	2.136	2.138	5	3 5 4	1.307	1.308	16
2 0 0	2.136	2.134	39	0 13 11	1.260	1.263	6

[a] The orthorhombic cell parameters refined from the powder pattern, obtained on a Guinier camera at room temperature, are: $a = 4.268(1)$, $b = 19.308(6)$, $c = 26.425(8)$ Å, and $V = 2177.6(8)$ Å^3.

[b] The intensities were calculated based on positional parameters from the crystal structure of $Pr_{12}Ga_4Sb_{23}$ with the use of the program LAZY-PULVERIX (Yvon, K.; Jeitschko, W.; Parthé, E. *J. Appl. Crystallogr.* **1977**, *10*, 73).

Table A-5. X-ray powder diffraction data for $Sm_{12}Ga_4Sb_{23}$.[a]

hkl	d_{obs} (Å)	d_{calc} (Å)	I/I_0 [b]	hkl	d_{obs} (Å)	d_{calc} (Å)	I/I_0 [b]
0 1 1	——	15.424	6	2 0 0	2.107	2.107	39
1 0 1	——	4.159	5	0 5 11	2.015	2.016	14
1 0 3	——	3.792	5	0 10 0	1.911	1.912	6
0 5 3	3.515	3.501	16	0 0 14	1.862	1.864	5
1 3 2	3.406	3.394	8	0 9 7	1.846	1.846	8
0 0 8	3.272	3.262	9	1 8 7	1.815	1.816	12
0 5 5	3.096	3.085	15	2 5 3	1.804	1.805	5
1 1 6	2.980	2.989	6	2 5 5	1.738	1.740	6
1 4 3	2.980	2.971	40	1 9 6	1.738	1.739	9
0 6 4	2.870	2.863	5	1 1 14	1.696	1.698	5
1 0 7	2.800	2.792	66	2 8 0	1.579	1.580	10
1 5 2	2.774	2.767	16	2 4 10	1.550	1.551	20
1 4 5	2.709	2.704	9	1 9 12	1.428	1.430	5
0 5 7	——	2.670	5	2 10 0	1.414	1.416	5
1 5 4	2.606	2.598	100	2 0 14	1.397	1.396	5
1 1 8	2.563	2.556	13	2 9 7	1.386	1.388	8
1 6 3	2.444	2.440	5	1 4 17	1.379	1.381	25
0 8 0	2.395	2.390	15	1 13 4	1.357	1.358	18
1 0 9	2.395	2.389	6	1 9 14	1.328	1.330	16
1 5 6	2.377	2.373	6	3 0 7	1.312	1.314	9
0 5 9	2.312	2.311	5	3 5 4	1.290	1.292	16
0 4 10	2.292	2.291	29	0 13 11	1.248	1.250	6
0 9 1	2.117	2.117	5				

[a] The orthorhombic cell parameters refined from the powder pattern, obtained on a Guinier camera at room temperature, are: $a = 4.213(3)$, $b = 19.120(10)$, $c = 26.099(15)$ Å, and $V = 2103(1)$ Å³.

[b] The intensities were calculated based on positional parameters from the crystal structure of $Pr_{12}Ga_4Sb_{23}$ with the use of the program LAZY-PULVERIX (Yvon, K.; Jeitschko, W.; Parthé, E. *J. Appl. Crystallogr.* **1977**, *10*, 73).

Table A-6. Anisotropic displacement parameters ^{a} ($\mathring{A}^2$) for $La_{13}Ga_8Sb_{21}$ and $Pr_{12}Ga_4Sb_{23}$.

Atom	U_{11}	U_{22}	U_{33}	U_{12}	U_{13}	U_{23}
			$La_{13}Ga_8Sb_{21}$			
La(1)	0.0086(4)	0.0084(6)	0.0049(4)	0.0042(3)	0	0
La(2)	0.0089(4)	0.0092(6)	0.0059(5)	0.0046(3)	0	0
La(3)	0.0276(18)	0.0276(18)	0.013(2)	0.0138(9)	0	0
Ga(1)	0.0186(15)	0.0140(17)	0.055(8)	0.0070(9)	0.009(2)	0
Ga(2)	0.0077(18)	0.0077(18)	0.017(6)	0.0038(9)	0	0
Sb(1)	0.0112(5)	0.0070(7)	0.0062(6)	0.0035(3)	0	0
Sb(2)	0.0117(6)	0.0091(7)	0.0090(7)	0.0046(3)	0	0
Sb(3)	0.0091(5)	0.0081(7)	0.0325(8)	0.0041(3)	0	0
Sb(4)	0.0115(7)	0.0075(10)	0.0062(8)	0.0037(5)	0	0
			$Pr_{12}Ga_4Sb_{23}$			
Pr(1)	0.0084(2)	0.0059(2)	0.0097(3)	0	0	−0.00044(2)
Pr(2)	0.0086(2)	0.0060(2)	0.0087(2)	0	0	−0.00081(2)
Pr(3)	0.0086(3)	0.0068(3)	0.0093(4)	0	0	0
Pr(4)	0.0111(3)	0.0070(3)	0.0105(4)	0	0	0
Ga(1)	0.0562(13)	0.0046(8)	0.0068(8)	0	0	0
Ga(2)	0.011(3)	0.008(3)	0.019(3)	0	0	0
Ga(3)	0.0088(6)	0.0241(9)	0.0073(7)	0	0	0
Sb(1)	0.0142(3)	0.0100(3)	0.0213(4)	0	0	0.0039(2)
Sb(2)	0.0092(3)	0.0068(3)	0.0114(3)	0	0	0.0020(2)
Sb(3)	0.0098(3)	0.0067(3)	0.0097(3)	0	0	−0.0003(2)
Sb(4)	0.0101(3)	0.0066(3)	0.0105(3)	0	0	−0.0004(2)
Sb(5)	0.0091(4)	0.0107(4)	0.0089(4)	0	0	0
Sb(6)	0.0225(4)	0.0088(4)	0.0080(4)	0	0	0
Sb(7)	0.0110(4)	0.0139(5)	0.0091(4)	0	0	0
Sb(8)	0.0092(5)	0.0085(6)	0.0085(6)	0	0	0

^{a} The form of the anisotropic displacement parameter is: $exp[-2\pi^2(h^2a^{*2}U_{11} + k^2b^{*2}U_{22} + l^2c^{*2}U_{33} + 2hka^*b^*U_{12} + 2hla^*c^*U_{13} + 2klb^*c^*U_{23})]$.

Table A-7. X-ray powder diffraction data for orthorhombic LaGaSb$_2$.[a]

hkl	d_{obs} (Å)	d_{calc} (Å)	I/I_0 [b]	hkl	d_{obs} (Å)	d_{calc} (Å)	I/I_0 [b]
0 2 0	11.617	11.387	5	2 4 1	1.861	1.860	5
0 6 0	3.812	3.796	5	0 12 1	1.746	1.747	5
0 4 1	3.535	3.518	15	2 8 0	1.737	1.736	5
1 5 0	3.168	3.158	9	1 7 2	1.698	1.699	6
1 3 1	2.903	2.894	100	2 8 1	1.618	1.619	9
0 8 0	2.852	2.847	21	2 0 2	1.565	1.565	16
1 7 0	2.615	2.612	23	1 11 2	1.434	1.436	13
1 5 1	2.586	2.580	37	1 15 0	1.434	1.435	5
0 8 1	2.404	2.402	14	1 3 3	1.387	1.388	14
0 0 2	2.240	2.237	12	2 8 2	1.371	1.372	8
0 2 2	2.199	2.195	7	1 15 1	1.365	1.366	10
2 0 0	2.199	2.191	15	2 12 1	1.365	1.366	5
0 4 2	2.084	2.082	5	1 15 1	1.365	1.366	13
0 6 2	1.928	1.927	10	1 5 3	1.347	1.348	7
1 3 2	1.921	1.927	6	3 5 1	1.328	1.328	6
2 6 0	1.899	1.898	6	3 11 0	1.192	1.193	6
1 11 0	1.870	1.872	7				

[a] The cell parameters refined from the powder pattern, obtained on a Guinier camera at room temperature, are: $a = 4.382(3)$, $b = 22.775(13)$, $c = 4.474(3)$ Å, and $V = 446.5(4)$ Å^3.

[b] The intensities were calculated based on positional parameters from the crystal structure of SmGaSb$_2$ with the use of the program LAZY-PULVERIX (Yvon, K.; Jeitschko, W.; Parthé, E. *J. Appl. Crystallogr.* **1977**, *10*, 73).

Table A-8. X-ray powder diffraction data for tetragonal $CeGaSb_2$.[a]

hkl	d_{obs} (Å)	d_{calc} (Å)	I/I_0 [b]	hkl	d_{obs} (Å)	d_{calc} (Å)	I/I_0 [b]
0 0 4	11.431	11.266	5	1 0 23	1.787	1.788	7
0 0 12	3.769	3.755	5	2 0 16	1.726	1.727	7
1 0 7	3.632	3.616	9	2 1 15	1.638	1.638	9
1 0 9	3.304	3.293	15	2 1 17	1.573	1.573	6
1 1 6	2.866	2.858	100	2 0 20	1.568	1.569	6
0 0 16	2.820	2.817	21	2 2 0	1.545	1.545	16
1 0 13	2.721	2.716	14	1 0 29	1.462	1.464	5
1 1 10	2.554	2.549	37	2 1 21	1.444	1.445	10
1 0 15	2.479	2.476	22	2 1 23	1.383	1.384	11
2 0 0	2.190	2.185	27	3 1 6	1.359	1.359	27
2 0 4	2.139	2.145	10	2 2 16	1.355	1.355	9
2 0 8	2.040	2.037	8	1 1 30	1.350	1.351	10
1 0 21	1.926	1.926	7	3 1 10	1.321	1.321	13
2 0 12	1.889	1.889	17	3 0 23	1.168	1.169	5
2 1 7	1.872	1.870	7				

[a] The cell parameters refined from the powder pattern, obtained on a Guinier camera at room temperature, are: $a = 4.3708(16)$, $c = 45.07(2)$ Å, and $V = 860.9(6)$ Å^3.

[b] The intensities were calculated based on positional parameters from the crystal structure of $NdGaSb_2$ with the use of the program LAZY-PULVERIX (Yvon, K.; Jeitschko, W.; Parthé, E. *J. Appl. Crystallogr.* **1977**, *10*, 73).

Table A-9. X-ray powder diffraction data for tetragonal $PrGaSb_2$.[a]

hkl	d_{obs} (Å)	d_{calc} (Å)	I/I_0 [b]	hkl	d_{obs} (Å)	d_{calc} (Å)	I/I_0 [b]
0 0 4	11.362	11.202	5	1 0 23	1.778	1.779	7
0 0 12	3.750	3.734	5	2 0 16	1.719	1.720	7
1 0 7	3.620	3.603	10	2 1 15	1.632	1.633	9
1 0 9	3.289	3.280	15	2 1 17	1.567	1.567	6
1 1 6	2.856	2.850	100	2 0 20	1.562	1.562	6
0 0 16	2.804	2.801	21	2 2 0	1.541	1.541	16
1 0 13	2.707	2.704	14	1 0 29	1.455	1.456	5
1 1 10	2.542	2.540	37	2 1 21	1.439	1.439	10
1 0 15	2.465	2.464	22	2 1 23	1.377	1.378	11
2 0 0	2.182	2.180	27	3 1 6	1.355	1.356	27
2 0 4	2.141	2.140	10	2 2 16	1.350	1.350	9
2 0 8	2.032	2.031	8	1 1 30	1.343	1.344	10
1 0 21	1.918	1.917	7	3 1 10	1.317	1.318	13
2 0 12	1.884	1.883	16	3 0 23	1.163	1.165	5
2 1 7	1.867	1.865	7				

[a] The cell parameters refined from the powder pattern, obtained on a Guinier camera at room temperature, are: $a = 4.3599(16)$, $c = 44.81(2)$ Å, and $V = 851.8(5)$ Å^3.

[b] The intensities were calculated based on positional parameters from the crystal structure of $NdGaSb_2$ with the use of the program LAZY-PULVERIX (Yvon, K.; Jeitschko, W.; Parthé, E. *J. Appl. Crystallogr.* **1977**, *10*, 73).

Table A-10. X-ray powder diffraction data for tetragonal $NdGaSb_2$.[a]

hkl	d_{obs} (Å)	d_{calc} (Å)	I/I_0 [b]	hkl	d_{obs} (Å)	d_{calc} (Å)	I/I_0 [b]
0 0 4	11.270	11.136	5	1 0 23	1.768	1.769	7
0 0 12	3.728	3.712	5	2 0 16	1.712	1.712	7
1 0 7	3.600	3.587	10	2 1 15	1.625	1.625	9
1 0 9	3.273	3.264	15	2 1 17	1.560	1.560	6
1 1 6	2.844	2.838	100	2 0 20	1.554	1.555	6
0 0 16	2.788	2.784	21	2 2 0	1.535	1.535	16
1 0 13	2.692	2.690	14	1 0 29	1.447	1.448	5
1 1 10	2.531	2.528	37	2 1 21	1.431	1.432	10
1 0 15	2.452	2.451	23	2 1 23	1.371	1.371	11
2 0 0	2.174	2.171	27	3 1 6	1.350	1.350	28
2 0 4	2.133	2.131	10	2 2 16	1.344	1.344	9
2 0 8	2.025	2.023	8	1 1 30	1.335	1.337	10
1 0 21	1.907	1.906	7	3 1 10	1.312	1.312	13
2 0 12	1.876	1.874	16	3 0 23	1.158	1.159	5
2 1 7	1.857	1.857	7				

[a] The cell parameters refined from the powder pattern, obtained on a Guinier camera at room temperature, are: $a = 4.3427(15)$, $c = 44.545(19)$ Å, and $V = 840.1(5)$ Å^3.

[b] The intensities were calculated based on positional parameters from the crystal structure of $NdGaSb_2$ with the use of the program LAZY-PULVERIX (Yvon, K.; Jeitschko, W.; Parthé, E. *J. Appl. Crystallogr.* **1977**, *10*, 73).

Table A-11. X-ray powder diffraction data for orthorhombic $SmGaSb_2$.[a]

hkl	d_{obs} (Å)	d_{calc} (Å)	I/I_0 [b]	hkl	d_{obs} (Å)	d_{calc} (Å)	I/I_0 [b]
0 2 0	11.310	11.060	5	2 4 1	1.819	1.819	6
0 6 0	3.700	3.687	5	2 8 0	1.701	1.698	5
0 4 1	3.421	3.404	15	0 12 1	1.695	1.696	5
1 5 0	3.097	3.085	8	1 7 2	1.648	1.647	7
1 3 1	2.825	2.818	100	2 8 1	1.578	1.580	9
0 8 0	2.769	2.765	21	2 0 2	1.524	1.524	16
1 7 0	2.552	2.547	24	1 15 0	1.397	1.395	5
1 5 1	2.515	2.511	38	1 11 2	1.390	1.393	13
0 8 1	2.331	2.329	14	1 3 3	1.341	1.343	14
0 0 2	2.162	2.160	12	3 3 1	1.336	1.339	14
2 0 0	2.152	2.152	16	2 8 2	1.333	1.335	9
0 2 2	2.124	2.120	7	2 12 1	1.330	1.332	5
0 4 2	2.014	2.012	5	1 15 1	1.324	1.328	10
1 3 2	1.865	1.868	6	1 5 3	1.303	1.305	7
0 6 2	1.865	1.864	9	3 5 1	1.299	1.301	7
2 6 0	1.859	1.859	6	3 11 0	1.169	1.168	6
1 11 0	1.819	1.822	8				

[a] The cell parameters refined from the powder pattern, obtained on a Guinier camera at room temperature, are: $a = 4.304(3)$, $b = 22.121(13)$, $c = 4.320(3)$ Å, and $V = 411.3(3)$ $Å^3$.

[b] The intensities were calculated based on positional parameters from the crystal structure of $SmGaSb_2$ with the use of the program LAZY-PULVERIX (Yvon, K.; Jeitschko, W.; Parthé, E. *J. Appl. Crystallogr.* **1977**, *10*, 73).

Table A-12. Anisotropic displacement parameters [a] (Å^2) for $SmGaSb_2$ and $NdGaSb_2$.

Atom	U_{11}	U_{22}	U_{33}	U_{12}	U_{13}	U_{23}
			$SmGaSb_2$			
Sm	0.0075(18)	0.00632(17)	0.00895(17)	0	−0.0006(4)	0
Ga	0.0311(8)	0.0087(5)	0.0297(7)	0	0	0.0054(6)
Sb(1)	0.0076(2)	0.0095(2)	0.0094(2)	0	−0.0005(6)	0
Sb(2)	0.0075(2)	0.0071(2)	0.0092(2)	0	−0.0002(5)	0
			$NdGaSb_2$			
Nd	0.0092(3)	0.0083(3)	0.0097(3)	0	0	0
Ga	0.0356(13)	0.0534(17)	0.0146(10)	0	0	0.0057(11)
Sb(1)	0.0097(3)	0.0093(3)	0.0134(3)	0	0	0
Sb(2)	0.0094(3)	0.0094(3)	0.0112(4)	0	0	0
Sb(3)	0.0089(3)	0.0089(3)	0.0109(4)	0	0	0

[a] The form of the anisotropic displacement parameter is: $exp[-2\pi^2(h^2a^{*2}U_{11} + k^2b^{*2}U_{22} + l^2c^{*2}U_{33} + 2hka^*b^*U_{12} + 2hla^*c^*U_{13} + 2klb^*c^*U_{23})]$.

Table A-13. X-ray powder diffraction data for $FeGe_{0.80}Sb_{0.20}$.[a]

hkl	d_{obs} (Å)	d_{calc} (Å)	I/I_0 [b]	hkl	d_{obs} (Å)	d_{calc} (Å)	I/I_0 [b]
1 0 1	5.550	5.538	3	3 1 3	1.664	1.664	4
0 0 2	3.992	3.986	13	3 0 4	1.574	1.574	5
2 0 1	3.468	3.466	3	4 1 2	1.548	1.548	9
1 1 2	2.971	2.968	27	2 2 4	1.483	1.484	4
3 0 0	2.569	2.566	42	3 3 0	1.483	1.481	9
1 0 3	2.515	2.512	5	3 3 2	1.388	1.389	5
2 2 0	2.224	2.222	32	4 1 4	1.283	1.284	10
3 0 2	2.159	2.158	21	6 0 0	1.283	1.283	29
0 0 4	1.994	1.993	18	6 0 2	1.220	1.221	3
2 1 3	1.964	1.962	3	3 3 4	1.188	1.189	3
2 2 2	1.943	1.941	100	3 0 6	1.178	1.180	19
1 1 4	1.818	1.819	13				

[a] The cell parameters refined from the powder pattern, obtained on a Guinier camera at room temperature, are: $a = 8.888(2)$, $c = 7.973(3)$ Å, and $V = 545.5(3)$ Å^3.

[b] The intensities were calculated based on positional parameters from the crystal structures of $FeGe_{0.80}Sb_{0.20}$ with the use of the program LAZY-PULVERIX (Yvon, K.; Jeitschko, W.; Parthé, E. *J. Appl. Crystallogr.* **1977**, *10*, 73).

Table A-14. X-ray powder diffraction data for $FeGe_{0.67}Sb_{0.33}$.[a]

hkl	d_{obs} (Å)	d_{calc} (Å)	I/I_0 [b]	hkl	d_{obs} (Å)	d_{calc} (Å)	I/I_0 [b]
1 0 1	5.567	5.558	10	2 2 2	1.958	1.958	100
0 0 2	3.965	3.960	13	1 1 4	1.812	1.812	17
2 0 1	3.499	3.499	10	3 2 1	——	1.746	6
1 1 2	2.975	2.974	27	3 1 3	1.672	1.674	14
2 1 1	2.765	2.764	8	4 0 3	——	1.569	5
3 0 0	2.602	2.601	45	4 1 2	1.566	1.564	9
1 0 3	2.502	2.500	16	3 3 0	1.501	1.502	9
2 2 0	2.253	2.252	36	3 3 2	——	1.404	5
3 0 2	2.175	2.174	20	2 1 5	——	1.395	5
0 0 4	1.978	1.980	15	6 0 0	1.299	1.300	28
2 1 3	1.967	1.967	12	4 1 4	1.289	1.291	13

[a] The cell parameters refined from the powder pattern, obtained on a Guinier camera at room temperature, are: $a = 9.009(3)$, $c = 7.919(3)$ Å, and $V = 556.7(3)$ Å^3.

[b] The intensities were calculated based on positional parameters from the crystal structures of $FeGe_{0.67}Sb_{0.33}$ with the use of the program LAZY-PULVERIX (Yvon, K.; Jeitschko, W.; Parthé, E. *J. Appl. Crystallogr.* **1977**, *10*, 73).

Table A-15. Anisotropic displacement parameters [a] (Å^2) for $FeGe_{0.80}Sb_{0.20}$ and $FeGe_{0.67}Sb_{0.33}$.

Atom	U_{11}	U_{22}	U_{33}	U_{12}	U_{13}	U_{23}
$FeGe_{0.80}Sb_{0.20}$						
Fe(1)	0.0076(6)	0.0103(8)	0.0104(7)	0.0051(4)	−0.0014(3)	−0.0029(7)
Fe(2)	0.0061(9)	0.0109(12)	0.0106(10)	0.0055(6)	−0.0008(4)	−0.0016(8)
Ge(1)	0.0135(7)	0.0120(7)	0.0092(6)	0.0073(5)	0	0
Ge(2)	0.0055(6)	0.0055(6)	0.0186(15)	0.0028(3)	0	0
Ge(3)	0.0057(15)	0.0057(15)	0.006(4)	0.0029(8)	0	0
Sb(1)	0.0055(6)	0.0055(6)	0.0186(15)	0.0028(3)	0	0
Sb(2)	0.0057(15)	0.0057(15)	0.006(4)	0.0029(8)	0	0
$FeGe_{0.67}Sb_{0.33}$						
Fe(1)	0.0058(3)	0.0070(4)	0.0056(5)	0.0035(2)	−0.00001(1)	0.0000(3)
Fe(2)	0.0065(5)	0.0074(7)	0.0083(8)	0.0037(4)	0	0
Ge(1)	0.0086(4)	0.0054(4)	0.0062(5)	0.0027(2)	0	0
Ge(2)	0.0082(4)	0.0109(5)	0.0057(5)	0.0055(2)	0	0
Sb(1)	0.0046(2)	0.0046(2)	0.0111(4)	0.00228(11)	0	0
Sb(2)	0.0049(3)	0.0049(3)	0.0094(6)	0.00244(17)	0	0

[a] The form of the anisotropic displacement parameter is: $exp[-2\pi^2(h^2 a^{*2} U_{11} + k^2 b^{*2} U_{22} + l^2 c^{*2} U_{33} + 2hka^*b^*U_{12} + 2hla^*c^*U_{13} + 2klb^*c^*U_{23})]$.

Table A-16. Anisotropic displacement parameters ^{a} (Å^2) for $\text{Ti}_{0.5}\text{Fe}_6\text{Ge}_5\text{Sb}$, $\text{Cr}_{0.8}\text{Fe}_{5.3}\text{Ge}_{5.2}\text{Sb}_{0.8}$, and $\text{Mn}_{1.8}\text{Fe}_{4.6}\text{Ge}_{4.9}\text{Sb}_{1.1}$.

Atom	U_{11}	U_{22}	U_{33}	U_{12}	U_{13}	U_{23}
			$\text{Ti}_{0.5}\text{Fe}_6\text{Ge}_5\text{Sb}$ ^{b}			
$M(1)$ ^{c}	0.0066(6)	0.0104(9)	0.0064(7)	0.0052(4)	−0.0001(3)	−0.0003(6)
$M(2)$ ^{c}	0.0074(9)	0.0113(14)	0.0064(10)	0.0056(7)	0	0
Ge(1)	0.0104(7)	0.0063(8)	0.0050(6)	0.0032(4)	0	0
Ge(2)	0.0082(7)	0.0097(9)	0.0044(6)	0.0048(4)	0	0
$X(1)$ ^{d}	0.0083(7)	0.0083(7)	0.0202(9)	0.0042(3)	0	0
$X(2)$ ^{e}	0.0050(8)	0.0050(8)	0.0101(10)	0.0025(4)	0	0
			$\text{Cr}_{0.8}\text{Fe}_{5.3}\text{Ge}_{5.2}\text{Sb}_{0.8}$ ^{b}			
$M(1)$ ^{c}	0.0066(5)	0.0107(7)	0.0049(5)	0.0053(3)	−0.0004(2)	−0.0009(3)
$M(2)$ ^{c}	0.0066(7)	0.0106(11)	0.0063(7)	0.0053(6)	0	0
Ge(1)	0.0116(6)	0.0090(7)	0.0046(6)	0.0045(4)	0	0
Ge(2)	0.0095(5)	0.0122(7)	0.0046(6)	0.0061(4)	0	0
Ge(3)	0.0063(6)	0.0063(6)	0.0193(16)	0.0032(3)	0	0
Ge(4)	0.0055(7)	0.0055(7)	0.012(2)	0.0028(3)	0	0
$X(1)$ ^{d}	0.0063(6)	0.0063(6)	0.0193(16)	0.0032(3)	0	0
$X(2)$ ^{e}	0.0055(7)	0.0055(7)	0.012(2)	0.0028(3)	0	0
			$\text{Mn}_{1.8}\text{Fe}_{4.6}\text{Ge}_{4.9}\text{Sb}_{1.1}$ ^{b}			
$M(1)$ ^{c}	0.0054(4)	0.0106(6)	0.0103(8)	0.0053(3)	−0.0005(2)	−0.0009(4)
$M(2)$ ^{c}	0.0074(7)	0.0095(10)	0.0069(11)	0.0047(5)	0	0
Ge(1)	0.0090(5)	0.0059(6)	0.0062(8)	0.0030(3)	0	0
Ge(2)	0.0090(5)	0.0118(7)	0.0080(8)	0.0059(3)	0	0
$X(1)$ ^{d}	0.0057(4)	0.0057(4)	0.0246(10)	0.0029(2)	0	0
$X(2)$ ^{e}	0.0058(5)	0.0058(5)	0.0120(9)	0.0029(3)	0	0

^{a} The form of the anisotropic displacement parameter is: $exp[-2\pi^2(h^2a^{*2}U_{11} + k^2b^{*2}U_{22} + l^2c^{*2}U_{33} + 2hka^*b^*U_{12} + 2hla^*c^*U_{13} + 2klb^*c^*U_{23})]$.

^{b} Sites $R(1)$ and $R(2)$ were refined isotropically.

Table A-16. Anisotropic displacement parameters (Å^2) for $Ti_{0.5}Fe_6Ge_5Sb$. $Cr_{0.8}Fe_{5.3}Ge_{5.2}Sb_{0.8}$, and $Mn_{1.8}Fe_{4.6}Ge_{4.9}Sb_{1.1}$ (continued).

[c] Sites $M(1)$ and $M(2)$ contain 100% Fe in $Ti_{0.5}Fe_6Ge_5Sb$; 11% Cr, 89% Fe in $Cr_{0.8}Fe_{5.3}Ge_{5.2}Sb_{0.8}$; and 23% Mn, 77% Fe in $Mn_{1.8}Fe_{4.6}Ge_{4.9}Sb_{1.1}$. These ratios were fixed at compositions determined by EDX analysis.

[d] Site $X(1)$ contains 60(2)% Ge, 40(2)% Sb in $Ti_{0.5}Fe_6Ge_5Sb$; 30(2)% Ge, 36(2)% Sb (and 34% vacancies) in $Cr_{0.8}Fe_{5.3}Ge_{5.2}Sb_{0.8}$; 53(2)% Ge, 47(2)% Sb in $Mn_{1.8}Fe_{4.6}Ge_{4.9}Sb_{1.1}$.

[e] Site $X(2)$ contains 36(2)% Ge, 64(2)% Sb in $Ti_{0.5}Fe_6Ge_5Sb$; 32(3)% Ge, 54(2)% Sb (and 14% vacancies) in $Cr_{0.8}Fe_{5.3}Ge_{5.2}Sb_{0.8}$; 21(2)% Ge, 79(2)% Sb in $Mn_{1.8}Fe_{4.6}Ge_{4.9}Sb_{1.1}$.